Fast, Accurate Force and Position Control of Shape Memory Alloy Actuators

A thesis submitted for the degree
of Doctor of Philosophy of
The Australian National University

Yee Harn Teh

Department of Information Engineering

ANU College of Engineering and Computer Science

June 2008

This thesis contains no material which has been accepted for the award of any other degree or diploma in any university. To the best of the author's knowledge and belief, it contains no material previously published or written by another person, except where due reference is made in the text.

Yee Harn Teh

June 2008

Acknowledgements

There are many people who have made contributions, both directly and indirectly, towards the completion of this thesis. I would like to name a few.

First and foremost, I would like to express my sincerest gratitude to my supervisor, Dr. Roy Featherstone. Roy's help has been extremely enormous, and his enthusiasm has sparked my own in this wonderful work. This work would never have been completed without his advice and guidance.

Apart from Roy, I would also like to thank Dr. Zbigniew Stachurski and Dr. Robert Mahony for being on my Ph.D. supervisory panel. Roy and Zbigniew especially, thank you for the wonderful coffees and brilliant discussions together.

I would also like to express my gratitude to my parents, and my three brothers, who provided me with unconditional advice, support and love. They have never been far from my heart.

And finally to Aya, my partner, thank you.

Abstract

Shape memory alloy (SMA) actuators have great potential in niche applications where space, weight, cost and noise are crucial factors. Despite many of the advantages, they remain mostly as experimental actuators due to their perceived slow response speed, low accuracy and controllability. Especially in situations where there is a moving link or an external payload, the problem of limit cycles has been pursued by various researchers but never fully solved. In this thesis, practical, effective control systems are applied to achieve fast and accurate force and position control of SMA wire actuators.

Investigations into very high-frequency responses from SMAs are initially explored, which produce surprising results of audio frequency responses. This discovery has led us towards using high-bandwidth control systems as a possible method of eliminating limit cycles. Frequency response analysis of SMA actuators have also been carried out. Based on the results, linear force models for single SMA wires as well as for an actuator comprising of an antagonistic pair of SMA wires have been developed. A position model for an antagonistic SMA-actuated robotic joint has also been developed based on the force models. These models are integral in the design, tuning and simulation of various control systems for SMA actuators.

High-bandwidth PID control has been employed in the force control of single SMA wire actuators. More importantly, it forms the main control component in the differential force control architecture for antagonistic SMA actuators. Other components are the anti-slack mechanism, the rapid-heating mechanism and the anti-overload mechanism. The closed loop response is fast and accurate, even in the presence of external motion disturbances. There is generally no limit cycles in the actuator's differential force output; and the performance is unaffected by large load inertias. This thesis also presents a two-loop architecture for position control, in which a position feedback loop is added to the force control architecture. Experimental results demonstrate highly accurate position control with no limit

cycles in the presence of external loads.

The accomplishments reported in this thesis represent a significant development in making SMA actuators faster, more accurate and effective. It is aspired that the results and control methods in this work can be utilised in enabling practical SMA technologies for robotic and commercial applications.

List of Source Publications

Most of the discussions and results presented in this thesis are based on the following publications. Several passages in this thesis contain materials that have been copied verbatim, or with some adaptation, from these publications. All such copied materials were originally written by myself.

i. R. Featherstone and Y. H. Teh. Improving the Speed of Shape Memory Alloy Actuators by Faster Electrical Heating. In *Proceedings of the 9th International Symposium on Experimental Robotics*, Singapore, 18-21 June 2004.

ii. Y. H. Teh and R. Featherstone. A New Control System for Fast Motion Control of SMA Actuator Wires. In *The 1st International Symposium on Shape Memory and Related Technologies*, Singapore, 24-26 November 2004.

iii. Y. H. Teh and R. Featherstone. Experiments on the Performance of a 2-DOF Pantograph Robot Actuated by Shape Memory Alloy Wires. In *Proceedings of the 6th Australasian Conference on Robotics and Automation*, Canberra, Australia, 6-8 December 2004.

iv. Y. H. Teh and R. Featherstone. Experiments on the Audio Frequency Response of Shape Memory Alloy Actuators. In *Proceedings of the 7th Australasian Conference on Robotics and Automation*, Sydney, Australia, 5-7 December 2005.

v. Y. H. Teh and R. Featherstone. Accurate Force Control and Motion Disturbance Rejection of Shape Memory Alloy Actuators. In *Proceedings of the IEEE International Conference on Robotics and Automation*, Rome, Italy, 10-14 April 2007.

vi. Y. H. Teh and R. Featherstone. An Architecture for Fast and Accurate Control of Shape Memory Alloy Actuators. *International Journal of Robotics Research*. Submitted for review, May 2007.

vii. Y. H. Teh and R. Featherstone. Frequency Response Analysis of Shape Memory Alloy Actuators. In *Proceedings of the International Conference on Smart Materials and Nanotechnology in Engineering*, Harbin, China, 1-4 July 2007.

Claims of Originality

In this thesis the following original contributions are presented:

   i. Observations and investigations of the audio frequency mechanical response of SMA wires of up to 2000 Hz.

  ii. Small-signal frequency response analysis conducted on SMA wire actuators with force responses of up to 100 Hz.

 iii. Force models for a single SMA wire and for an antagonistic pair of SMA wires based on the frequency response analysis.

 iv. An extended position model, based on the force models, of a robotic joint application actuated by an antagonistic pair of SMA wires.

  v. A high-bandwidth PID controller applied to the force control of a single SMA wire, which is also integral in the differential force control architecture of an antagonistic SMA wire actuator.

 vi. Actuator damage avoidance from overheating and overstressing based on the rapid-heating and anti-overload control mechanisms, as well as SMA wire slack prevention based on the anti-slack mechanism.

 vii. A two-loop control architecture for the continuous position control of an antagonistic SMA wire actuator with no signs of limit cycles under heavy external loads.

viii. Experimental results that are a significant step forward for fast, accurate force and position control of SMA actuators.

Contents

List of Figures

xiv

List of Tables

CHAPTER 1

Introduction

There has been a continuing trend in technology towards ever-smaller scales for mechanical, optical as well as electro-mechanical devices. Actuators, which are the driving mechanism and usually the moving part of these devices, must therefore undergo similar miniaturisation in design and construction. Following this trend, factors such as power consumption, work density, costs and space constraints gain increased importance in the selection of suitable technologies. However, conventional actuators, including electric motors, pneumatic and hydraulic actuators, suffer a large reduction in power that they can deliver as they are scaled down in size and weight. These constraints have led to the emergence and development of novel actuator technologies such as piezoelectric actuators, electrostatics, magnetostrictive materials and shape memory alloys (SMAs).

Among all the presently known actuation principles, shape memory alloys show one of the highest work densities at $10^7 \, \text{Jm}^{-3}$, which is a factor of 25 times greater than the work density of electric motors [37]. A NiTi (nickel-titanium) wire actuator with a diameter of $1 \, \text{mm}$, which is a typical SMA actuator, can produce large forces sufficient to lift a mass of $15 \, \text{kg}$. Currently few actuator technologies can match that.

SMAs are generally considered a type of 'smart' materials because they have, aside from actuation functions, temperature sensing, electrical or structural functions and so enable compact and multifunctional features. SMAs are also potentially attractive for niche applications, where large forces or displacements are required for small masses and in tight spaces. These include micro-robotics, surgical devices and micro-electromechanical (MEMS) applications. With recent advances in SMA production and materials improvement, many more engineering and commercial applications will be accessible to SMA technologies.

This chapter will provide a brief introduction of shape memory alloys, followed by their advantages and limitations in terms of actuator applications. The motivations behind our research and the research objectives of this thesis will

then be covered. Finally, the chapter will end with a general outline of the entire thesis.

1.1 Shape Memory Alloys

Shape memory alloys are a group of metallic alloys that have the special ability to 'remember' or to retain a specific shape or size prior to deformation, by undergoing a heating process. They accomplish this shape memorisation via a temperature dependent phase transformation process between two crystal structures, the higher temperature austenite phase and the lower temperature martensite phase. This phenomenon is known as the shape memory effect.

Austenite, the high-temperature phase, is relatively hard and has a much higher Young's Modulus; whereas the martensite phase is softer and more malleable. When cool and in the martensite phase, the SMA can be easily stretched by applying a small external force. To recover its original length, the alloy is heated beyond a certain temperature, causing it to contract and transform into the austenite structure. Heating the SMA can be done via Joule heating, which is resistively heating the material using electric current.

Of all the SMAs that have been discovered so far, NiTi shape memory alloys, also known as Nitinol, have proven to be the most flexible and successful in engineering applications. One of the ways SMAs are commonly used is in the form of wires. In our research, Flexinol, which is a commercially produced NiTi, has been used in wire form for all the modelling and control experiments.

1.2 Advantages and Limitations

The advantages of using SMAs as an actuation mechnanism are:

i. High power-to-weight ratio — Ikuta [32] compared different types of actuator technologies and found that at low weights (less than $100\,g$), SMA actuators offer the highest power-to-weight ratio. This property makes SMA actuators highly attractive for miniature applications.

ii. Mechanical simplicity and compactness — An SMA actuator only uses the shape recovery of the alloy and it can be actuated directly via Joule heating. It does not require any reduction gear system nor other moving parts. Due to mechanical simplicity and the small size of the actuator, there are other benefits such as reduced material, production and maintenance costs.

iii. Easy miniaturisation — SMAs can be used as 'direct drive linear actuators' requiring little or no additional motion reduction or amplification hardware [59]. This permits easy miniaturisations of simple actuator systems.

iv. Clean and silent operation — Because SMA actuators do not require friction mechanisms such as reduction gear, it avoids the production of dust particles, sparks and noise. These merits make SMA actuators extremely suitable for areas such as microelectronics, biotechnology and medical applications.

Aside from the general advantages listed above, NiTi SMA has other characteristics which make it stand out from other SMA materials. They include greater ductility, more recoverable motion, excellent corrosion resistance, stable transformation temperatures and high bio-compatibility [80].

Despite the above advantages, SMA actuators are not free from limitations and drawbacks. They are:

i. Low energy efficiency — The maximum theoretical efficiency of SMAs is of the order of $10\,\%$ based on the Carnot cycle, according to [78]. In reality, the efficiency is often less than $1\,\%$, since the SMA actuator can be considered a heat engine operating at low temperatures. This means that the conversion of heat into mechanical work is very inefficient. Most of the heat energy is lost to the environment. Hence SMA actuator applications must be limited to areas where energy efficiency is not an issue.

ii. Degradation and fatigue — The long-term performance and reliability of SMA actuators depend on a number of factors, including maximum temperature, stress, strain and the number of transformation cycles achieved. Care should be taken to prevent overheating and overstressing of the actuators for long durations. However, advancement in materials development and processing can reduce degradation and fatigue. For example, Flexinol has been specially trained to exhibit the shape memory effect over millions of cycles.

iii. Slow speed and inaccuracy — SMA actuators have generally been considered to have slow response due to restrictions in heating and cooling, and also due to the inherent thermal hysteresis. The common method in actuation is by electrical heating. Although applying larger electrical currents can increase the speed, this may also overheat and damage the actuator

without monitoring. The large hysteresis loop, as well as the nonlinear characteristic of the phase transformations, also make SMA actuators difficult to control accurately. Most research so far has investigated SMA position control at generally low tracking speeds of less than 1 Hz. Rise times for step responses usually took more than 1 second, and accuracies were mediocre, with error amplitudes greater than 1% of the working range.

1.3   Research Objectives and Approach

Shape memory alloy actuators have generally been considered to be slow, inaccurate and difficult to control continuously. Their actuator applications have so far been very limited commercially, and in areas where they are applied, usage is often restricted to passive or on-off applications.

The primary objective of this research is to demonstrate that **faster and more accurate control of SMA actuators can be achieved compared with the current state-of-the-art**. This can be accomplished via the design and implementation of practical and effective control systems.

The approach that has been adopted for this research initially involves investigating the high-frequency response of SMA actuators. If small-signal responses can be detected, it means that very fast responses can be induced, despite the existence of hysteresis and nonlinearities in the large-signal responses of SMAs. It is then possible, and perhaps practical, to control such small-signal responses using high-bandwidth control systems operating at frequencies higher than the controllers that are currently used by others. The aim of this is to improve actuator controllability and tracking accuracy.

Modelling, force control simulations and experiments are conducted first for a simple actuator consisting of a single SMA wire. Modelling experiments based on frequency response analysis have been carried out to determine a simple SMA force model that captures the overall behaviour essential to control. This model relates the input heating power to output force response for a single SMA wire actuator, and it successfully demonstrates good comparison between simulation and experimental force control results.

The next step in this research is to develop high-performance differential force control systems for an actuator which consists of two SMA wires in antagonistic arrangement. To improve the speed of response, a control algorithm known as the rapid-heating mechanism has been included in the force control architecture.

Coupled with the anti-slack and anti-overload mechanisms, optimum performance of the SMA actuator can be achieved while ensuring actuator reliability and preventing damage. Simulations for the differential force control system have also been implemented.

Finally, a position control architecture for an antagonistic pair of SMA wires will be investigated. To this end, an extended position model based on the force model will be built. This SMA position model not only takes into account the input heating power, but also strain variations due to wire contractions and extensions. This can be accomplished using frequency response analysis to investigate the effects of small, continuous strain changes to the SMA dynamic behaviour. The model has been used for simulation and control design. The proposed position control system contains a fast, inner force loop based on the differential force controller and a slower, outer position loop. This two-loop control design is aimed at eliminating limit cycles and inaccuracies due to large, external load dynamics on the plant.

It is hoped that the accomplishments of the modelling and control experiments conducted in this research can be utilised in enabling SMA technologies for practical actuator and robotic applications.

1.4   Thesis Outline

This thesis is organised in the following manner.

Chapter 2 begins with some background information on SMAs, including more detailed descriptions of their phases and the phase transformations, as well as the various arrangements illustrating how SMAs are used as actuators. The chapter also contains a review of the literature, including past work on modelling and control of SMA actuators.

Chapter 3 discusses our investigations into the high-frequency response of SMA actuators. The motivation behind the research for this chapter, which is to determine if audio frequency response exists in SMAs, will first be discussed. A discussion of the experimental loudspeaker setup used to detect SMA mechanical response together with the results will then be provided.

Modelling experiments and frequency response analysis results will be presented in Chapter 4. Firstly, the experimental test bed used for modelling as well as the subsequent force and motion control experiments will be presented. A detailed description and discussion of modelling using frequency response analy-

sis will next be provided together with the experimental procedures and results. The power to force relationship for an SMA wire actuator that is independent of wire stresses and strains is extracted based on the frequency response data. Force models for both a single SMA wire and a pair of antagonistic SMA wires will be presented in this chapter.

Chapter 5 will explore the force control of a single SMA wire actuator. A PID controller is first applied to the single-wire force model from Chapter 4 and then fine-tuned on the actual system to control the force of an SMA wire. The simulation as well as the experimental force control results will be presented and compared. The chapter also addresses the motion disturbance rejection ability of the force feedback control system.

The differential force control of an antagonistic SMA wire actuator pair is discussed in Chapter 6. Several important issues and problems of the differential force control architecture will first be addressed. This will be followed by a section on various control system designs aimed at solving the problems and improving the performance of the controller. The improvements include the anti-slack mechanism, the rapid-heating mechanism and the anti-overload mechanism. The high-bandwidth PID differential controller, together with the additional mechanisms, demonstrates fast and accurate force control for an antagonistic SMA actuator pair. Performance over continuous operations, as well as external motion and load disturbance rejection are also addressed in this chapter.

Chapter 7 discusses the challenges in continuous motion control applications involving the influence of a large external load and the work that has been done in this area. A dynamic position model of an antagonistic SMA-actuated joint application that takes into account the stress, strain and input power relationships of the SMA wires will first be presented. This model is integral in the design and testing of the proposed two-loop position control architecture. This control architecture will be further described and explained, followed by a comprehensive discussion of the experimental results for various types of position commands. It will be seen that the control system achieves highly accurate position control with no signs of limit cycles, and also at an acceptable level of speed.

Finally in Chapter 8, a summary of our research achievements and contributions will be provided together with some discussion of future work.

CHAPTER 2

Shape Memory Alloys

In this chapter, background information as well as the state-of-the-art of shape memory alloy research are presented. Section 2.1 explains the phases of SMA and the mechanisms of phase transitions from a mechanical and materials perspective. It also discusses the different configurations of SMA actuator applications. Section 2.2 basically provides an overview of past and current work on SMAs in terms of experimental and commercial applications, modelling, actuator designs and control systems. The literature review places more emphasis on research of SMA actuators, rather than the non-actuator applications.

2.1 SMA Background

The term 'shape memory' refers to the special ability of certain materials to remember shape, usually induced thermally but may also be initiated mechanically. A number of material and biological systems that exhibit the shape memory properties are described in Table 2.1. This chapter is only concerned with shape memory metal alloys. For detailed information on other shape memory materials, readers are directed to [55].

Although the shape memory effect was first observed in metal alloys as early as the 1930s, the real significance of this phenomenon has only been understood since its discovery in NiTi alloys in the 1960s. At present, NiTi remains the most successful shape memory alloy.

2.1.1 The Phases of SMA

In SMAs, the shape memory mechanism is based on a reversible, solid-state phase transformation between the high-temperature austenite phase and the low-temperature martensite phase. This phase transition is also known as martensitic transformation. There are other transformations associated with shape memory,

7

Systems	Examples
Metals	NiTi-based alloys:
	NiTi, NiTiCu, NiTiPd, NiTiFe, ...
	Cu-based alloys:
	CuZn, CuZnAl, CuAlNiMn, ...
	Fe-based alloys:
	FePt, FeMnSi, FeNiC, ...
Polymers	e.g., PTFE (polytetrafluoroethylene)
Ceramics	e.g., ZrO_2
Biological Systems	e.g., bacteriophages

Table 2.1: Systems with shape memory properties [37].

such as rhombohedral (R-) and bainitic transformations. This overview is restricted to martensitic transformations.

In terms of practical applications, a NiTi SMA can exist in three different crystal structures or phases — martensite, austenite and stress-induced martensite — as noted by [52]. At low temperature, the alloy exists as martensite. It is weak, malleable and can be easily stretched. Once heated to a high temperature, the alloy contracts and reverts to the austenite phase and becomes stronger and more rigid. Stress-induced martensite forms if the alloy is in the austenite phase and an external stress is applied. If the stress is removed, the material reverts back into austenite. This effect is known as 'pseudoelasticity' and will be covered in detail in Section 2.1.3.

The stress-strain curves of the two primary SMA phases, martensite and austenite, are depicted in Figure 2.1.

When an external stress is applied to the alloy when fully martensitic, the alloy deforms elastically (Figure 2.1(a) curve 1). If the stress exceeds the martensite yield strength, a large non-elastic deformation will result, which allows a large strain in the material with a small increase in external stress. The martensite is strain recoverable up until this stage (Figure 2.1(a) curve 2). However, further increase in stress causes the material to again behave elastically up to the point where the external stress begins to break the atomic bonds between the martensite layers, resulting in permanent plastic deformation ((Figure 2.1(a) curves 3 and 4). The strain at which this permanent deformation occurs in NiTi material is 8%. Most applications will restrict strains to 4% or lower.
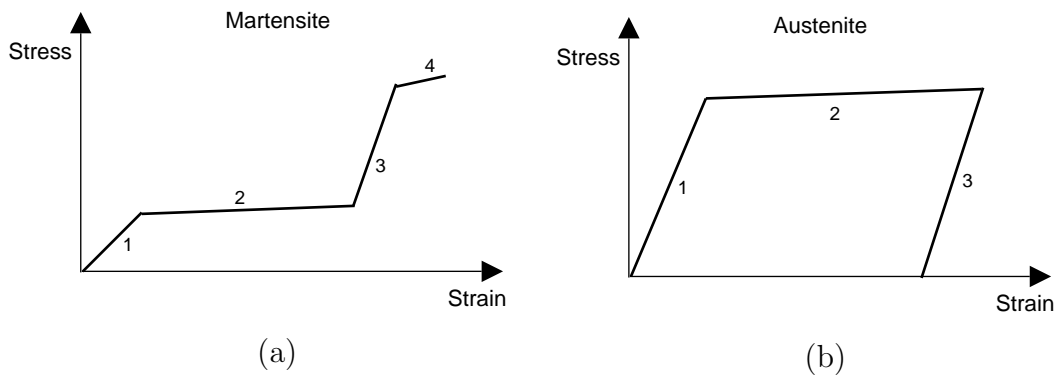
Figure 2.1: Stress-strain curves for the two primary phases of SMA, (a) martensite and (b) austenite.

For the austenite phase however, it has a higher yield strength compared to martensite. Initially, the alloy will behave elastically (Figure 2.1(b) curve 1) until the stress exceeds its yield strength. From this point onwards, plastic deformation will ensue causing unrecoverable stretching upon unloading (Figure 2.1(b) curves 2 and 3).

The martensitic phase transformations of the alloy can be characterised by four transformation temperatures:

i. A_s, the austenite start temperature,
ii. A_f, the austenite finish temperature,
iii. M_s, the martensite start temperature,
iv. M_f, the martensite finish temperature.

This reversible phase transformation is depicted in Figure 2.2.

Starting at the left of the curve in Figure 2.2, with a temperature less than M_f, the NiTi alloy consists only of the martensite phase. As the temperature is
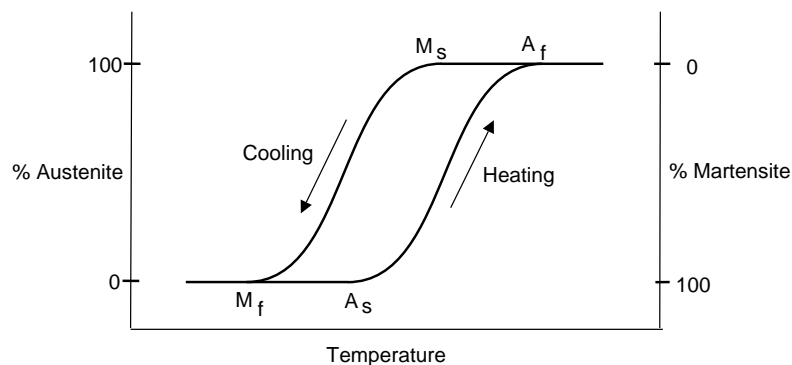
Figure 2.2: The hysteresis curve of SMA.

9

increased beyond A_s, austenite begins to form in the alloy and when the temperature exceeds A_f, the alloy is primarily in the austenite phase. As the alloy cools, martensite begins to form when the temperature drops below M_s, and when the temperature reaches M_f, the alloy is again fully martensitic.

As can be seen in Figure 2.2, this transition between the austenite and martensite phases can be characterised by a wide thermal hysteresis loop. The hysteresis varies according to the alloy system. For NiTi alloys, the temperature hysteresis is generally between 30 – 50°C.

During phase transitions between martensite and austenite, most of the physical properties of SMAs vary. These include Young's Modulus, electrical resistance, heat capacity and thermal conductivity. Some of these properties for NiTi SMAs are listed in Table A.2 of Appendix A. In the possible range where both martensite and austenite co-exist, nonlinearities and hysteresis are prominent, and they are influenced by material composition, processing and the number of activated cycles [27].

2.1.2   The Shape Memory Effect

In addition to common shape change effects such as elastic and plastic deformations, as well as thermal expansion and contraction, SMAs also exhibit three shape memory characteristics, which can be categorised as follows:

  i.   One-way shape memory effect — After the removal of an external force, the material shows permanent deformation. It can recover its original shape upon heating. Subsequent cooling does not change the shape unless it is stressed again.
 ii.   Two-way shape memory effect — In addition to the one-way effect, shape change occurs upon cooling and without the applying of external stress.
iii.   Pseudoelasticity — Mechanical loading at temperatures beyond A_f stretches the alloy and upon unloading, it reverts to its initial shape. No thermal process is involved.

The above three effects can be demonstrated using simplified 2-dimensional crystal structure models and stress-strain-temperature curves.

The one-way shape memory effect forms the basis of SMA actuators. The shape recovery and the high forces generated as a result of the phase transformation to austenite can be used for continuous actuation and to perform work. The one-way effect of SMAs is depicted in Figure 2.3.
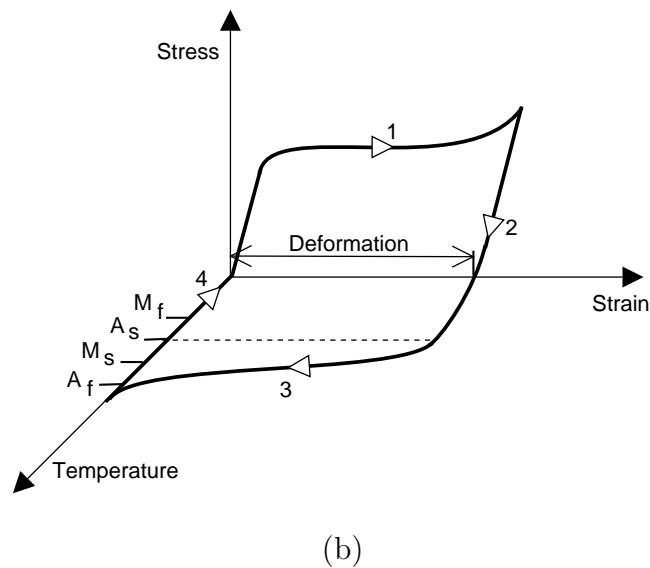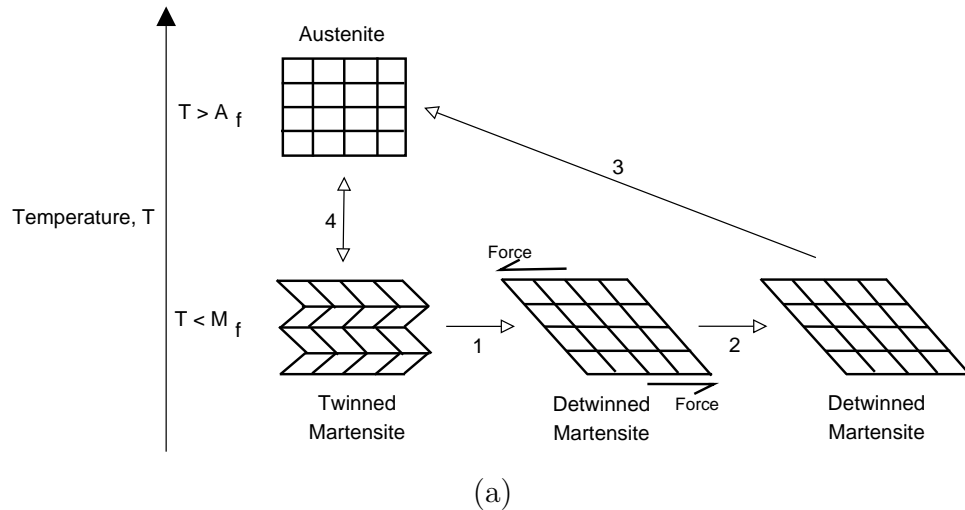
Figure 2.3: One-way shape memory effect shown using (a) 2D crystal structure model of SMAs, and (b) stress-strain-temperature curve.

Based on the 2D model of Figure 2.3(a), it can be seen that as the temperature of the austenite decreases, martensite begins to form. Note that no shape change occurs during cooling (also depicted as Figure 2.3(b) curve 4). The martensite in this form is said to be 'twinned' with each layer separated by a twinning boundary. Martensite in this state is highly malleable and has a very low elastic limit.

Applying external stress to the martensite will result in curve 1 in both Figures 2.3(a) and 2.3(b). The alloy initially behaves elastically followed by a recoverable pseudoplastic deformation of up to several percent. Martensite in this state is said to be 'detwinned'. Further stressing causes unrecoverable strain up to fracture. With relaxation in the recoverable strain range, depicted as curve 2
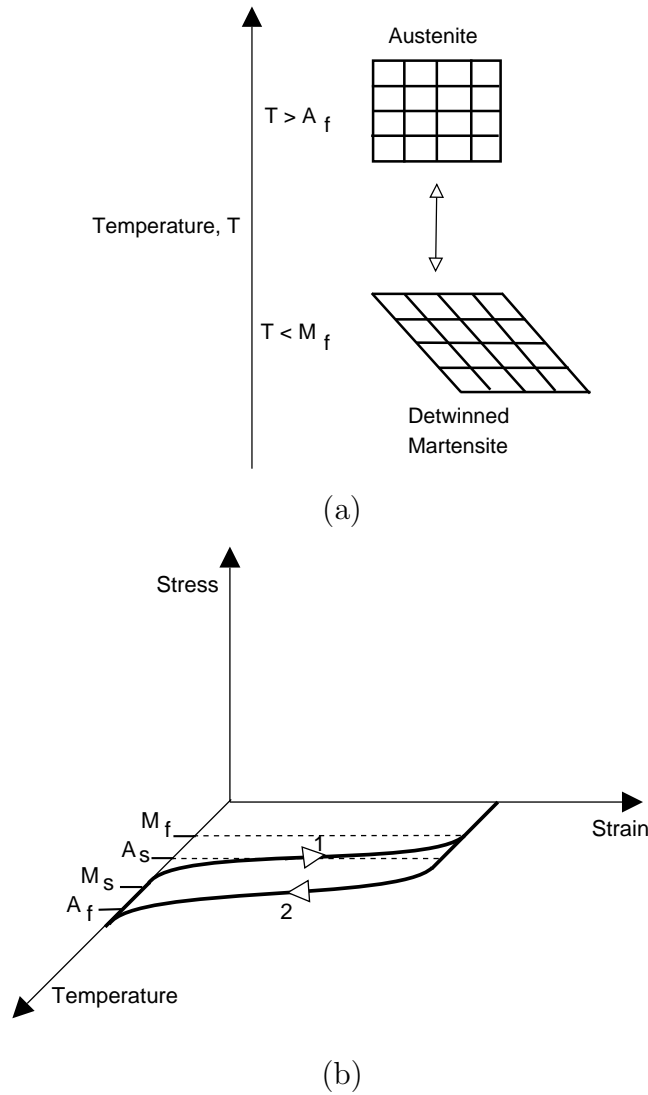
Figure 2.4: Two-way shape memory effect shown using (a) 2D crystal structure model of SMAs, and (b) stress-strain-temperature curve.

in Figure 2.3, the alloy maintains the deformed shape.

By heating the deformed martensite past A_s, the austenite start temperature, austenite begins to form and the material begins to contract (Figure 2.3(b) curve 3). Full shape recovery can be achieved by heating above A_f, where the alloy is completely in the austenite phase again. As this shape recovery only occurs in one direction, it is referred to as the one-way shape memory effect. This effect can be repeated over many cycles following the process in Figure 2.3. It can also be observed that a large hysteresis loop exists in this phenomenon.

The two-way shape memory effect is less pronounced than the one-way effect and usually requires training. It can be defined as the reversible shape change upon thermal cycling in the temperature range of martensitic transformations

without requiring any external load. This results in the direct transformations between austenite and detwinned martensite in Figure 2.4(a). It can also be described using the curves located only in the strain-temperature plane, as shown in Figure 2.4(b). Hysteresis is also prominent in the two-way effect.

SMAs can be trained to exhibit the two-way effect using two methods, which are spontaneous and external load-assisted induction [4]. However, the shape change obtained is in practice less than that of the one-way effect.

2.1.3 Pseudoelasticity

(a)

(b)
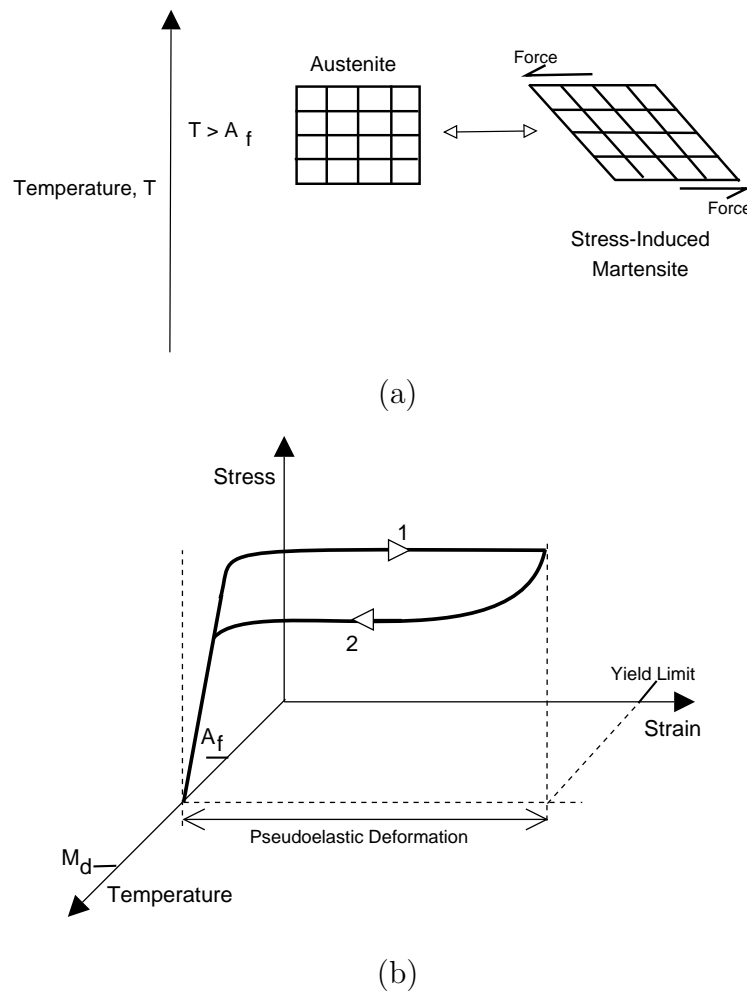
Figure 2.5: Pseudoelasticity shown using (a) 2D crystal structure model of SMAs, and (b) stress-strain-temperature curve.

Pseudoelasticity, also known as 'superelasticity', is the shape recovery associated with mechanical loading and unloading of SMAs at temperatures above A_f. Figure 2.5 presents the 2D model and the stress-strain-temperature curve depicting pseudoelasticity of SMAs.

There is no temperature change required for pseudoelastic behaviour. Therefore, the strain characteristic can be described using only the stress-strain plane of Figure 2.5 (b). By applying external stress above A_f, the austenite initially behaves in an elastic manner followed by a plateau in which highly nonlinear deformation occurs up to a virtual yield limit. Upon unloading, the curve returns via the lower hysteresis loop for complete strain recovery.

The plateau region is a result of the formation of stress-induced martensite from austenite. External stress on the material increases the phase transformation temperatures [34]. This relationship is fairly linear, as can be seen in Figure 2.6, although A_s and A_f behave nonlinearly at low stress levels.
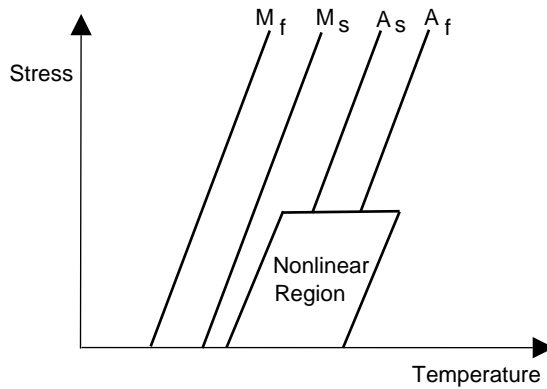
Figure 2.6: Stress dependence of transformation temperatures.

This stress dependence of the four transformation temperatures can be approximately represented as:

$$\frac{d\sigma}{dT} = \frac{1}{c_m},$$ (2.1)

or equivalently,

$$T(\sigma) = c_m \sigma + T_o,$$ (2.2)

where $1/c_m$ is the stress rate, $T(\sigma)$ is the stress dependent transformation temperature and T_o is the zero stress transformation temperature [34].

If the external stress causes M_s, the martensite start temperature, to increase beyond the current temperature, martensite will form. This makes the alloy malleable under small increase in stress. Once the stress is removed, the transition temperatures decrease and the alloy returns to the austenite phase.

There is an upper temperature limit, M_d, to which the formation of stress-induced martensite can exist. At temperatures in the range of $A_f > T > M_d$, pseudoelastic behaviour can occur. Beyond M_d, the alloy behaves like a normal material with elastic behaviour followed by plastic deformation up to fracture.

2.1.4 SMA Actuators

A shape memory alloy element works against a constant or varying force to perform work. Upon heating, the SMA uses the one-way shape memory effect to generate force and motion, which can be harnessed for actuator applications. SMA actuators can be used in various configurations including helical springs, cantilever strips, straight wires, torsion tubes and torsion springs [80].

The advantages of SMA actuators include a high work output, silent and clean operation, simplicity of design and ease of miniaturisation. NiTi alloys currently have the greatest potential as actuators because they also have other qualities such as biocompatibility, reliability over millions of cycles under appropriate training, more recoverable motion compared to other SMAs and they can also be electrically heated, simplifying the mechanism and reducing the overall number of parts.

According to [11], the primary actuator joint applications can be divided into two types, linear or prismatic joints, and revolute or rotary joints. SMA actuators can be used in both joint applications, as shown in Figure 2.7.

Because SMA actuators utilise the one-way effect and can only contract in one direction, it is necessary to provide a biasing force to return to the neutral position. This can be accomplished using a dead weight, a bias spring, or another SMA element in a differential arrangement. In practice, the latter two arrangements are usually used, as demonstrated in Figure 2.7.

In the SMA actuator with bias spring arrangement, only one SMA is heated and cooled, so the hysteresis effect has quite a significant influence on control performance. The differential, or antagonistic SMA actuator arrangement, which heats one actuator while the other cools, can reduce the hysteresis effect [33, 41]. Another advantage of using the antagonistic actuator configuration over a bias spring is, instead of providing passive biasing force or motion, both directions can be actively controlled. This increases the range of controllable actuation.
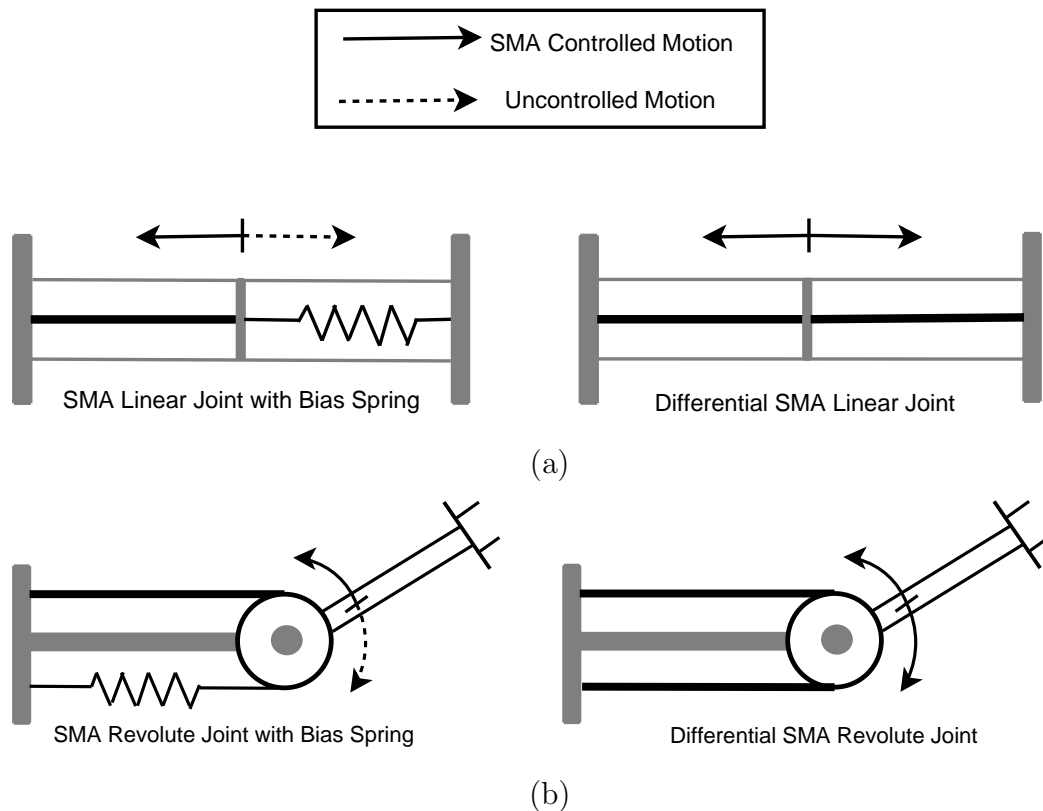
Figure 2.7: (a) SMA linear joint configurations. (b) SMA revolute joint configurations.

2.2 Literature Overview

2.2.1 History and Applications

In 1932, a Swedish physicist by the name of Arne Olander discovered an interesing 'rubber-like' behaviour when working with gold-cadmium alloys. He observed that the Au-Cd alloy could be plastically deformed when cool, and when heated, it returned to its original configuration. This was the first reported observation of the shape memory effect. However, it was not until twenty years later that the phenomena of shape memory and pseudoelasticity really began to be fully understood. In 1951, Chang and Read presented a clear description of the rubber-like effect as well as the observations of reversible phase transformations. It was also in the 1950's that similar effects were observed in alloys of Cu-Zn, In-Tl, and Cu-Al-Ni. Although these discovered SMAs had captured the interest of researchers, their practical and industrial applications were not realised due to high costs, the complexity of manufacturing technologies as well as their unattractive mechanical

properties at the time.

It was only around 1962–63, with the discovery of the shape memory effect in NiTi (nickel-titanium) alloys, also known as Nitinol, that earnest interests began to accumulate for industrial use of SMAs. The discovery of NiTi SMA was led by William Buehler at the US Naval Ordnance Laboratory, hence the term 'Nitinol' (**NI**ckel-**TI**tanium **N**aval **O**rdnance **L**aboratory). Nitinol alloys have better mechanical properties, are cheaper to produce, are easier and less dangerous to work with compared to other existing SMAs at that time. The 1960's and 1970's saw the emergence of commercially available and potential SMA products, mostly involving Nitinol. According to [4], these include the following major industrial areas: 1) simple applications involving once-off shape memory change, such as for thermomechanical couplings and sealings; 2) the construction of space device platforms and self-unfolding devices sparked by rapid development of astronautics in the USSR and USA; and 3) temperature-sensitive and actuating applications.

The potential of Nitinol SMAs in medical applications began to show in the early 1980's. Major areas of expansion include minimally invasive endovascular medical applications and orthodontic applications. Although more costly than stainless steel, Nitinol, which is biocompatible and can be manufactured to provide body temperature response and shape change, proves to be more attractive for medical applications [46]. It was also around the late 1980's and 1990's that saw the beginning of SMA research into robotic and actuator applications.

SMAs are rapidly gaining commercial importance. According to Waram [80], technical problems on the fabrication of SMAs have largely been overcome, and there are numerous specialised companies around the world that supply these materials in special order and stock amounts. Semi-finished SMAs in various shapes and forms such as wires, rods, tubes and ribbons are now available. Finished SMAs such as helical springs and wire actuators can also be easily purchased. Companies now exist, such as MIGA Motor Company,[1] that manufacture linear, compact actuators from SMAs.

There are currently numerous commercial SMA products for passive applications including pipe couplings, fasteners, superelastic materials for eye glass frames, antennas for mobile phones, as well as medical applications including orthodontic wires, medical stents, implants and arterial clips [46, 53, 78]. The dynamic applications of SMAs as actuators are lagging behind and are mostly

---

[1]http://www.migamotors.com

in the research stage despite many of their advantages. However, research into the applications and control of SMA actuators is still active and growing. Actuator applications of SMA include linear actuators, micro-switches, micro-valves, robotic grippers, vibration control and active damping of structures, medical endoscopes and micro-electro-mechanical systems (MEMS) [18, 33, 37, 44, 78].

2.2.2 Modelling

There have been numerous models proposed to capture or explain the characteristics of SMAs, most notably in terms of their thermomechanical relations and the hysteresis effects, in order to simulate the behaviour of SMAs and as a control design aid. By far the majority of these models are phenomenological models. These are models based on the input-output relationship of SMAs which are described by internal state variables such as martensite fraction, strain and temperature. Phenomenological models are widely used for engineering and control applications because they avoid parameters that are difficult to measure, such as free energy, and they use clearly defined engineering material constants.

Some of the earlier phenomenological models that were used for control purposes include: Kuribayashi's model based on experimentally identified relations [40], the sub-layer models of Ikuta et al. [29, 34], and Tanaka's constitutive model [69].

In his experiments, Kuribayashi observed a linear relationship between very small variations in the force and strain of an SMA wire. Under constant strain, the relationship between the force and supplied voltage was also observed to be approximately linear. Hence, the following static mathematical model can be obtained by considering the small variations of force, voltage and strain as Δf, Δu and Δx respectively:

$$\Delta f = \alpha_0 \Delta u + \beta_0 \Delta x, \tag{2.3}$$

where α_0 and β_0 are gain constants. Equation 2.3 can be regarded as the steady state of a dynamic system. Kuribayashi presented a dynamic model by adding first order terms $G(s)$ and $H(s)$ in the Laplace domain as follows:

$$\Delta f(s) = \alpha_0 G(s) \Delta u(s) + \beta_0 H(s) \Delta x(s). \tag{2.4}$$

The above force model resulted in a summation of two first-order terms with different time constants, and Kuribayashi extended it to a position model by

considering the SMA plant as a mass-damper system. Both his force and position models were used for control simulations.

Ikuta et al. [29] first introduced the two-phase model for SMAs using the sub-layer model, a commonly used method in solid mechanics to describe nonlinear stress-strain relationships. In 1991, they proposed a new variable sub-layer model that takes into account the two conventional martensite and austenite phases, as well as the newly discovered rhombohedral phase (R-phase). The model considers the SMA to be composed of parallel sub-layers of the different phases with their respective mechanical properties. This is combined with a model of transformation kinetics based on thermodynamics to form the variable sub-layer model. Ikuta et al. applied the model to SMA coil spring theory and it had been verified experimentally. Madill and Wang [47] extended their work for a new SMA actuator model that is capable of modelling minor hysteresis loops.

Tanaka [69] proposed a thermomechanical law that governs the stress-strain behaviour of the SMA element. He assumed that the thermomechanical behaviour of SMA can be fully described by three state variables: strain, temperature and martensite fraction, and he proposes the following governing constitutive relation in the rate form:

$$\dot{\sigma} = D\dot{\epsilon} + \Theta\dot{T} + \Omega\dot{\xi}, \qquad (2.5)$$

where σ is the Piola-Kirchhoff stress, ϵ the Green strain, T the temperature, and ξ the martensite ratio. The material parameters D, Θ and Ω are the elastic modulus, the thermoelastic tensor and the transformation tensor respectively. In general, D, Θ and Ω are functions of ϵ, T and ξ, but Tanaka assumed them to be constant.

The phase transformation kinetics law is the most critical part of the model as it defines the hysteresis behaviour of the material. The martensite ratio ξ is an internal variable used to account for the phase change of SMA, and is dependent on the applied stress and temperature. It is the ratio of martensite to austenite varying from complete martensite, $\xi = 1$, to complete austenite, $\xi = 0$. Tanaka proposed the following exponential functions relating martensite ratio to stress and temperature to describe the transformation kinetics. During the heating process,

$$\xi_{M \to A} = e^{[A_a(T - A_s) + B_a \sigma]}, \qquad (2.6)$$

and for the cooling process,

$$\xi_{A \to M} = 1 - e^{[A_m(T - M_s) + B_m \sigma]}, \tag{2.7}$$

where A_a, A_m, B_a and B_m are material constants in terms of transition temperatures, A_s, A_f, M_s and M_f.

Liang and Rogers [5], Brinson [6] and Elahinia [13] improved upon Tanaka's model using different transformation kinetic equations relating the martensite fraction to the stress and temperature.

In particular, Elahinia [13] proposed a model of an SMA actuator which consists of four sub-models: a heat transfer model, an SMA thermomechanical model, a phase transformation kinetics model and a dynamic/kinematic model.

Elahinia's heat transfer model is based on the heat transfer law for an SMA element proposed by Shahin et al. [64], which have been widely used by many researchers for SMA modelling. It relates the heating current to the temperature based on Joule heating and free convection cooling. During the heating process, this is given by:

$$mc_p \frac{dT}{dt} - m\Delta h \frac{d\xi}{dt} = I^2(t)R - h(T - T_o), \tag{2.8}$$

where m is the mass of the SMA, c_p the constant-pressure specific heat, Δh the latent heat of transformation, I the heating current, R the SMA resistance, h the heat convection coefficient and T_o the ambient temperature. The term $-h(T - T_o)$ corresponds to heat loss to the surrounding.

When the current input is zero, the alloy cools according to:

$$mc_p \frac{dT}{dt} - m\Delta h \frac{d\xi}{dt} = -h(T - T_o). \tag{2.9}$$

The dynamic/kinematic law relates the forces applied by the SMA element and any external forces or torques to the strain or position of the actuator, based on the dimensions of the system. Elahinia presented a nonlinear dynamic model of an SMA-actuated robotic arm relating the torques from the SMA wire actuator, gravitational loads and spring to the angular position:

$$I_c \ddot{\theta} + \tau_g + \tau_s + c\dot{\theta} = \tau_w, \tag{2.10}$$

where τ_w, τ_g and τ_s are the resulting torques from the SMA wire, gravitational loads and spring respectively, I_c the effective mass moment of inertia of the arm and the payload, and c the torsional damping coefficient.

He also described a kinematic model relating angular position of the robotic arm to the strain of the SMA wire, given as:

$$\dot{\epsilon} = -\frac{2r\dot{\theta}}{l_o},$$ (2.11)

where r is the pulley radius and l_o the SMA wire initial length.

By combining the above equations with Tanaka's thermomechanical law and an improved transformation kinetics law, Elahinia obtained the complete position model of the SMA actuator system.

Because of the hysteresis effects, the kinetics laws that have been proposed so far have a heating and a cooling equation for each phase transformation process. Grant [23] also based his SMA force model on Tanaka's constitutive relations. He proposed a force model for an SMA wire based a single, explicit equation between the output force, F, and the input current:

$$F = \frac{a_f n}{K_g} K_p [\int_0^t I^2(t) R dt + C_i],$$ (2.12)

where K_p is a parameter dependent on a number of SMA physical properties, n the number of SMA wires in an actuator, K_g the actuator displacement gain, a_f the wire cross-sectional area, I the input current per wire, R the wire resistance, and C_i the integration constant.

Grant first considered the constrained case for an SMA wire, so Tanaka's model of Equation 2.5 can be reduced to:

$$\dot{\sigma} = \Theta\dot{T} + \Omega\dot{\xi}.$$ (2.13)

For the kinetics law, Grant did not consider the hysteresis effect. Because he used an antagonistic arrangement of SMA actuators, he assumed that the hysteresis effect in such a system had been minimised. So he proposed a single, linear transformation kinetics equation which simplifies the model:

$$\xi_{M \to A} = \begin{cases} 1 & \text{if } T < A_s; \\ \dfrac{A_f - T}{A_f - A_s} & \text{if } A_f \geq T \geq A_s; \\ 0 & T > A_f. \end{cases}$$ (2.14)

Including the effects of the applied stress on the transformation temperatures using Equation 2.1, the transformation equation of Equation 2.14 can be written as:

$$\xi_{M \to A} = \begin{cases} 1 & \text{if } T < c_m\sigma + A_{so}; \\ \dfrac{c_m\sigma + A_{fo} - T}{A_{fo} - A_{so}} & \text{if } c_m\sigma + A_{fo} \geq T \geq c_m\sigma + A_{so}; \\ 0 & T > c_m\sigma + A_{fo}. \end{cases} \qquad (2.15)$$

where c_m is the inverse of the stress rate, and A_{fo} and A_{so} are the stress free transformation temperatures.

Taking the derivatives of the above Equation 2.15 for the martensite ratio during heating with respect to time, the following relationship is obtained:

$$\dot{\xi} = K_m c_m \dot{\sigma} - K_m \dot{T}, \qquad (2.16)$$

where the constant $K_m = 1/(A_{fo} - A_{so})$.

Substituting Equation 2.16 into Tanaka's model for the constrained case, Equation 2.13, the dependence of Equation 2.13 on martensite ratio ξ can be eliminated. Solving for $\dot{T}$ results in:

$$\dot{T} = \frac{(1 - \Omega K_m c_m)}{(\Theta - \Omega K_m)}\dot{\sigma}. \qquad (2.17)$$

Equation 2.17 relates the temperature to the stress for a single SMA wire. Combining Equations 2.13 and 2.17 with Shahin's heat transfer Equation 2.8 and neglecting the heat loss term during heating, the following relationship is obtained:

$$\dot{\sigma} = \frac{(\Theta - K_m\Omega)}{m[c_p(1 - K_m c_m\Omega) + \Delta h K_m(1 - c_m\Theta)]}I^2(t)R. \qquad (2.18)$$

Further integration with time gives the following stress σ to current I relation:

$$\sigma = K_p \int_0^t I^2(t)R\,dt + C_i, \qquad (2.19)$$

where C_i is an integration constant and K_p is given by:

$$K_p = \frac{(\Theta - K_m\Omega)}{m[c_p(1 - K_m c_m\Omega) + \Delta h K_m(1 - c_m\Theta)]}. \qquad (2.20)$$

Taking into account the number and arrangement of SMA wires in the actuator resulted in the SMA input current-output force relationship of Equation 2.12 for the constrained case. Grant also proposed a position model for an SMA actuator by adding a second order mass-spring-damper term in series with the force model.

Preisach modelling of SMA hysteresis has also been investigated by various researchers, including [9, 21, 31, 38, 39, 48]. The Preisach model is one of the most successful mathematical models of hysteretic effects. Originally, it was developed to represent the hysteresis in magnetic materials. Hughes and Wen [31] demonstrated experimentally that piezoceramics and shape memory alloys satisfied two crucial characteristics for Preisach hysteresis modelling: the minor loop property and the wiping out property. These properties are discussed in detail in [21].

The main assumption about Preisach modelling is that the system can be thought of as a parallel summation of various weighted relay hystereses $\gamma_{\alpha\beta}$. This is illustrated in Figure 2.8. The value $\mu(\alpha, \beta)$ represents the weighting of the relay $\gamma_{\alpha\beta}$. Each relay is characterised by the pair of switching values (α, β), with $\alpha \geq \beta$, such that there is a unique representation of the collection of relays as points in the half-plane $P = \{(\alpha, \beta) \mid \alpha \geq \beta\}$, as shown in Figure 2.9. The vertical segments of the relays are irreversible; they can only traversed in one direction. The horizontal segments are reversible.
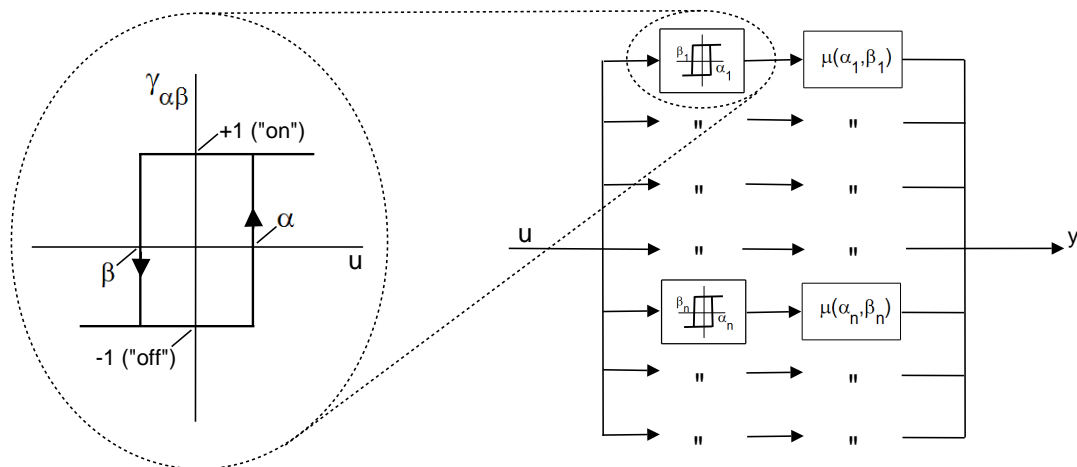
Figure 2.8: Schematic of the Preisach model (adapted from [21]).

The behaviour of these relays, and hence the Preisach model, is only defined for continuous inputs u. As u varies with time, each individual relay adjusts its output according to the current input value. Hence the standard Preisach model has the expression:

$$y(t) = \int\int_P \mu(\alpha, \beta)\gamma_{\alpha\beta}[u(t)]d\alpha d\beta, \tag{2.21}$$

23
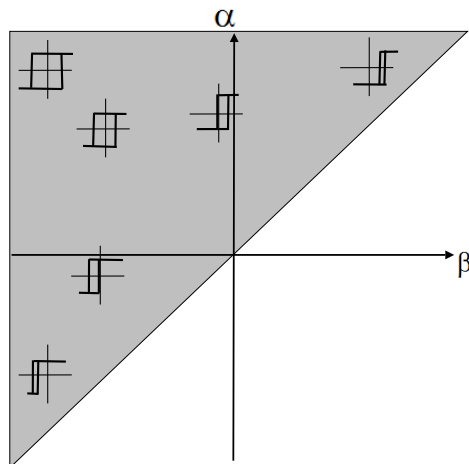
Figure 2.9: The Preisach plane (adapted from [21]).

where $y(t)$ is the measured output, $u(t)$ the input, $\gamma_{\alpha\beta}[u(t)]$ the relay hysteresis operator, and $\mu(\alpha, \beta)$ the weighting function that describes the distribution of the operator $\gamma_{\alpha\beta}[u(t)]$.

Mayergoyz [51] proposed a Preisach model identification method to determine the Preisach weighting function $\mu(\alpha, \beta)$ from experimental data. The method involves collecting a set of 'first-order descending curves', generated from major and minor hysteresis curves, and using the set to estimate $\mu(\alpha, \beta)$. Gorbet [21] conducted both major and minor hysteresis loop identification for SMAs, which produced very accurate Preisach models that closely matched experimental data. However, this identification method is time-consuming due to its mathematical complexity, and a large amount of experimental data must be obtained to identify $\mu(\alpha, \beta)$ precisely.

Some researchers attempted to simplify the Preisach modelling identification procedure. Ktena et al. [38, 39] proposed matching only the major hysteresis loops using a least-squares parameter fitting procedure to determine the weighting functions; Choi and Lee [9] used the almost proportional relationship of the major loop for modelling the hysteresis nonlinearity of an SMA; Instead of obtaining and matching hysteresis curves, Majima et al. [48] obtained the weighting functions using the stress-temperature relationship of the SMA.

There are other SMA models that have been investigated, including models based on thermodynamics and derived from a free energy formulation [50], microscopic physical models such as [36], which considers atomic interactions of different alloys in the shape memory material, as well as geometric models based on matching of experimentally obtained curves of stress-strain-temperature rela-

tionships that exclude any material physics [77].

In this thesis, force and position models of SMA actuators have been proposed using the method of small-signal frequency response analysis. The force model is described in Chapter 4; and the position model in Chapter 7.

2.2.3 Actuator Designs

Since the 1980's, research into using SMA actuators for robotic and control applications has been growing steadily. Many of the actuator applications involve the use of long, straight SMA wires, including those reported in [14, 15, 19, 40, 74]; Others use SMA coils or springs in their research to achieve larger displacements compared to SMA wires [32, 33, 34, 44, 48].

Several different actuator designs and configurations had been proposed over the years. Grant and Hayward [24] designed and built a novel type of SMA actuator for their control experiments. Their SMA actuator comprised of twelve 100-μm Nitinol wires in a helical arrangement that produced larger strains than long, straight SMA wires, was more efficient than SMA springs, but at the expense of reduced force outputs compared with straight SMA wires.

In 2001, Mosley and Mavroidis [54] proposed an SMA wire bundle actuator as a platform for developing large-scale robotic manipulators that are strong, lightweight, compact and dexterous. It consisted of 48 SMA wires mechanically bundled in parallel, and was capable of lifting up to 45.4 kg, which is approximately 300 times its weight.

Various researchers had implemented SMA actuators in robotic hands and grippers, including [8, 30, 75, 83]. In 2006, Sugiyama and Hirai [68] proposed a soft robot prototype that was capable of crawling and jumping. The wheel-like robot was composed of 8 SMA coils attached to the inside of a circular rubber shell. Motion was achieved by deformation of the SMA coils in various heating sequences. Thin-film SMAs had also been investigated by [18, 42, 65] for microactuator and MEMS applications.

Almost all of the SMA actuator applications involve electrical heating; but there are other methods of actuating the SMA elements. Selden et al. [63] presented another approach using the Peltier Effect. This was achieved by thermally heating the SMA using Peltier Modules. In 2006, an article in New Scientist by Cho [7] reported an alternative method of heating SMA actuators, using liquid fuel to convert chemical energy into heat energy. The researchers aim to design

artificial muscles that can mimic the functions of biological muscles.

2.2.4 Control Systems

The control research of SMAs can generally be divided into three categories: pulse width modulation (PWM) control, linear control, and nonlinear control. PWM control had been implemented by some of the early SMA researchers including [30, 33, 40, 70] and more recently by [68, 82]. Linear control schemes that have been explored by researchers include P, PI and PID control. Some of the more notable work include [19, 20, 32, 60, 74].

Ikuta [32] investigated a new feedback control scheme which combined position feedback and electrical resistance feedback using PID control. His experimental results showed that the stiffness of an SMA spring is a linear function to normalised electrical resistance. This allowed him to experiment with direct stiffness control as well as indirect force control using resistance feedback. Troisfontaine et al. [74] proposed two control schemes for SMA micro-actuators: position and temperature control. Their position controller was based on a two-stage (P and PI control) structure to minimise errors; and the temperature feedback controller used PID control.

More recently, nonlinear control schemes have also been employed for SMA actuator systems. Pons et al. [58] compared PI control based on direct strain feedback linearisation and feedforward approach to the conventional PI controller. It was shown that feedforward control achieved the best overshoot reduction. Other comparisons with linear controllers include Lee and Lee [43] who investigated time delay control on SMA actuators, and Ahn and Nguyen [1] who experimented with self-tuning fuzzy PID controllers.

Grant and Hayward [25] presented a two-stage variable structure control (VSC) scheme. The VSC scheme switched between a high and a low current level based on a boundary layer, with the parameters of the controller determined empirically. Other work on VSC included Elahinia et al. [13, 14, 15].

Van der Wijst [77] proposed a model-based control law consisting of open and closed loop parts for SMA wire actuators. The open loop controller determined a control input, based on a constitutive model of the SMA actuator, which was added to the closed loop PI controller. His results showed better performance than pure PI control. Selden et al. [63] presented an alternative approach of controlling SMA actuators based on segmented binary control. Instead of controlling

the overall displacement of an SMA wire, their method is a digital approach which controls the SMA wire segment-by-segment with separate on-off controllers. Experiments verified that this approach was feasible for discrete positioning of an SMA actuator, and demonstrated considerable load disturbance rejection.

Although there have been a lot of research on SMA actuator control, their successes have been constrained mainly by speed and accuracy issues. SMA actuators have nonlinearities such as backlash-like hysteresis and saturation effects, which make precise control difficult. SMAs have also been regarded widely as slow actuators due to their thermal responses.

Some researchers have attempted to improve the performance of SMA actuators. One of the earliest attempts at improving SMA actuator speed is by Kuribayashi [40]. His method involved using miniature thermocouples to measure the temperatures of 0.5 mm antagonistic SMA wires and determining the heating currents based on a temperature threshold to prevent overheating. Improvements were demonstrated with moderate settling times of 0.2 s for step responses, and stable sine responses at up to 0.4 Hz, for angular displacements of 15° magnitude. Russell and Gorbet [19, 61] worked on two fronts of the speed problem — rapid heating and improved cooling — of SMA wires in antagonistic arrangement. To allow rapid heating without the danger of overheating, they used a non-contact infra-red temperature sensing unit instead of a thermocouple to measure the temperature and determine the currents to be delivered to the actuators. To improve cooling, they attached a mobile heat sink to help cool the passive actuator.

Grant and Hayward [23, 25, 26] have made significant contributions in improving the speed and accuracy of SMA actuators. Using their novel helical SMA actuators in antagonistic arrangement, they investigated the use of two-stage VSC relay control. The results demonstrated fast and accurate force and position responses with 0.1 s rise times for large force steps of 7 N and position steps of 2.5 mm, as well as stable tracking of both 2 N and 1.5 mm amplitude sine commands at 2 Hz. However, there was no consideration about the overheating and overstressing of the actuators. Another major problem they faced was the existence of limit cycles, or oscillations, due to the discontinuous switching of the relay controller . Under 'no load' conditions, the results showed small but high-frequency limit cycles; and in the presence of a load disturbance, the oscillations were significantly worse.

Ashrafiuon et al. [2] further investigated the use of variable structure control in SMA position control. Their test bed consisted of a 3-link SMA actuated robot

with a heavy payload. Their results showed accurate position control, but with a slow rise time of 1s for a 70° magnitude step. Wellman et al. [81] designed a small, prototype tactile shape display using 75-μm SMA wires. Using careful mechanical design and liquid cooling combined with a proportional controller and current feedforward, they achieved a 40 Hz bandwidth.

At the micro-actuator scale, Shin et al. [65] investigated the high-frequency response of thin-film NiTi membrane using three different fluid mediums (air, silicon oil and de-ionised water) to improve cooling. Their results showed that a 40 Hz response with approximately 70 μm contraction could be achieved. A more recent work by these researchers in 2005 [66] involved the development of a prototype SMA-actuated micro-pump in a linear hydraulic actuator. The micro-pump achieved actuation response of 100 Hz, which allowed the hydraulic actuator to lift a bias weight of 10 kg at a velocity of 5.85 mms^{-1}.

2.3   Chapter Summary

This chapter provides essential background information on shape memory alloys and their actuator applications. The current state-of-the-art of SMA research and applications has also been described. It should be clear now that despite its wonderful properties and potential, there remains obstacles in developing SMA technologies and applying them to commercial or industrial actuator applications. The most crucial limitations of SMAs in actuator applications are their apparent slow speed and the difficulty of accurate and continuous control, as well as energy inefficiency. Some work have been done on this front, but successes have been constrained.

This dissertation aims to provide some groundwork on practical control strategies in achieving faster and more accurate SMA responses. In the following chapters, results and significant work that have been accumulated during this Ph.D. research will be documented and described in depth. It is hoped that this thesis will be useful for further development of SMA actuator technologies.

CHAPTER 3

Investigation of SMA High-Frequency Response

There have been some discussions over the years as to whether shape memory alloys can respond very quickly. As noted in the literature review of Chapter 2, researchers have attempted to improve upon the controllable speed of SMA actuators. Some of the results are quite significant, especially in the small or micro-actuator scale.

In this chapter, we will investigate the possibility of SMA actuators having very fast and detectable responses when subjected to audio-frequency cyclic heating and cooling. The investigation involves resistively heating Flexinol wires using electric current modulated at high frequencies. The mechanical response, which has the same frequency as the heating current, is detected by connecting the wire to a diaphragm and measuring the emitted sound.

The motivations for this investigation into high-frequency responses of SMA will first be explained, followed by a discussion of the different perspectives on the factors limiting SMA speed. In Section 3.2, the experimental setup as well as the experimental procedures will be described. The results of the experiments are presented in Section 3.3. Due to the very high frequency nature of the response, some evidence is provided to demonstrate that the shape memory effect is the main cause of the response, rather than thermal expansion and contraction. Some discussions of the repeatability and variability of the experiments are also presented.

3.1 Introduction

3.1.1 Experiment Motivations

The objectives of the experiments described in this chapter are to determine, firstly, if high-frequency mechanical response of SMAs can be induced, and secondly, if the response is attributable to the shape memory effect. It is useful to find out if the detectable responses in an SMA wire can be produced by very small, high-frequency variations in temperature induced by changes in heating current. The results of this investigation will be important for SMA control system design.

Specifically, $20-30\,\mathrm{Hz}$ limit cycles have been observed in our previous work [71], by Grant [23] at approximately $100-200\,\mathrm{Hz}$, as well as by van der Wijst [77], due to the inertia of external loads. To eliminate these limit cycles, one method is to design and implement a small-signal high-bandwidth controller capable of running at frequencies higher than that observed in the limit cycles. For such a control system to be feasible, it is crucial to know if SMAs are capable of such high-frequency responses.

3.1.2 Background

There have been diverging results and opinions, as to whether shape memory alloys can respond rapidly. Part of the debate involves the different views on the factors limiting the speed of SMAs. Some proposed that it is due to the heat transfer characteristics of shape memory alloys [61, 65]; while others observed that the rate of phase transformation is the limiting factor [45, 79].

Shape memory alloys undergo martensitic transformations between a high-temperature austenite phase and a lower-temperature martensite phase accompanied by reversible shape changes. Martensitic transformation has generally been considered athermal, which is rate independent, and the speed of phase transformation has always been considered 'instantaneous', limited only by the speed of sound in the material [3, 12, 56]. The formation energy for the critical size nucleus for martensitic transformations is small [73]. Moreover, if the transformation is not reversed fully to its completion then residual nuclei remain, and therefore, there should be no nucleation barrier to repeated phase transformations (in a cyclic fashion) caused by small cyclic changes of temperature close to the martensite transformation temperature.

Athermal transformations do not depend explicitly on time, but depend only on the values of the external parameters, such as temperature, stress, etc. It follows from the above that reversible martensitic transformation can be induced as fast as possible by changing the driving external parameter, i.e., temperature. However, scientists have questioned this 'instantaneous' phase transformation speed. [56] has shown that martensitic transformations can exhibit both athermal and isothermal characteristics, depending on the characteristic times associated with the driving field and nucleation. In isothermal transitions, the amount of resulting phase depends on values of external parameters, but also depends explicitly on time. [45] has observed the slow rate of phase transformation between the austenite and martensite phases. Using in-situ transmission electron microscopy, they observed a slow phase growth rate of about $0.3\,\mu\mathrm{ms}^{-1}$ in NiTi shape memory alloy thin films.

Regardless of the above debate, the aim of the experiments is to determine if SMA high-frequency response is possible. It is observed that the resulting responses from SMA Flexinol wires are surprisingly fast, compared with published results which imply that the response speed of SMA is very limited because of slow heat transfer characteristics [61, 65] and the long transient associated with the phase transformation process [45, 79]. The results show that only a very short duration, a millisecond or less, is required for a small change in heating power to produce a detectable response in SMA wires. This information is important for high-bandwidth control system design of SMA actuators.

3.1.3 Experimental Design

The objective is to design an experiment that distinguishes between the shape memory effect and normal thermal expansion. Figure 3.1 depicts the curve of sound output plotted against the input power that would be expected for a normal metal wire if the response is due to thermal expansion and contraction. It should be noted that the sound is emitted by the diaphragm, which is connected to the wire. To record a sound output data point on the graph, the wire undergoes cyclic heating and cooling at the same frequency as the positively varying heating current, [1] and the sound output is averaged over a suitable duration. The input power is the mean AC power over the same duration, and it provides an approximate indication of the wire's temperature, due to the difficulty of directly

---

[1]Note that the heating current is proportional to the square root of the heating power, per unit length of wire.
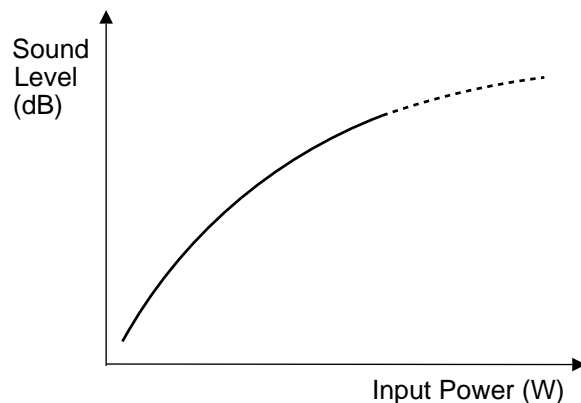
Figure 3.1: Expected sound output curve due to thermal expansion and contraction for a normal wire.

measuring the temperature of the thin wire.

For an ordinary metal wire, the sound level output should increase steadily with the input power, as suggested in Figure 3.1. Note that the y-axis is given in logarithmic scale, whereas the x-axis is linear. This is because ordinary metals undergo thermal expansion when heated, and they contract when cooled. The higher the input power, the hotter the wire becomes, leading to a bigger temperature difference between the wire and its surroundings. The result is a faster cooling rate, and hence a larger temperature swing in the wire about its equilibrium average temperature. This produces a louder sound output at the same frequency as the input power. We emphasise that the sound output is at the same frequency as the input power modulation because there is another mechanism by which a martensite phase change can cause acoustic emissions at a different frequency [57, 67]. Thus, if the sound were due to cyclic thermal expansion and contraction, then the graph would show a steady rise in sound level with increasing input power.

For an SMA wire, we would expect the sound output curve, when plotted against the heating power, to look as shown in Figure 3.2. The sharp rise and fall in sound output at low power magnitudes occurs during the phase transformation temperature range of the SMA, and is evidence for the shape memory effect.

Indeed, the results and the graphs of the experiments show similar patterns compared to the sound output curves of Figure 3.2, which proves that the high-frequency results cannot be solely due to normal thermal expansion and contraction. To further support the hypothesis that the observed high-frequency response is due to the shape memory effect, the following additional evidence is
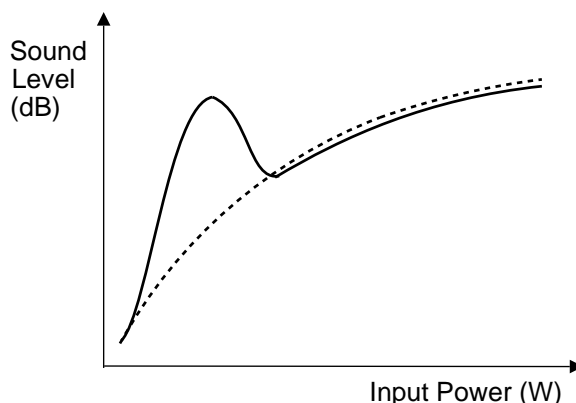
Figure 3.2: Expected sound output curve for an SMA wire (solid line), compared to a normal wire (dashed line).

presented:

  i. The response has been observed to occur in the phase transformation temperature range of the SMA.

 ii. This effect is found to be sensitive to thermal history, and some degree of hysteresis has been observed.

iii. A control experiment has also been conducted using an SMA wire which has been annealed at high temperature to undo the training of the shape memory effect. The recorded high-frequency response is found to have diminished significantly.

Details of the experiments and the results will be presented in the following sections.

3.2   Experimental Setup

3.2.1   Hardware

The actual SMA loudspeaker setup as well as its schematic diagram are shown in Figure 3.3 and Figure 3.4 respectively. The loudspeaker consists of a wooden base with two terminal posts at the rear and a bridge at the front. A 60-cm long Flexinol wire is connected so that the two ends are fixed to the posts, and the middle passes through a tiny hook attached to one end of a lightweight plastic diaphragm. The other end of the diaphragm is attached to a chord via two elastic bands, and the chord runs over the bridge to a dangling weight that sets the tension on the wire. This experiment design was chosen as it is easy to set
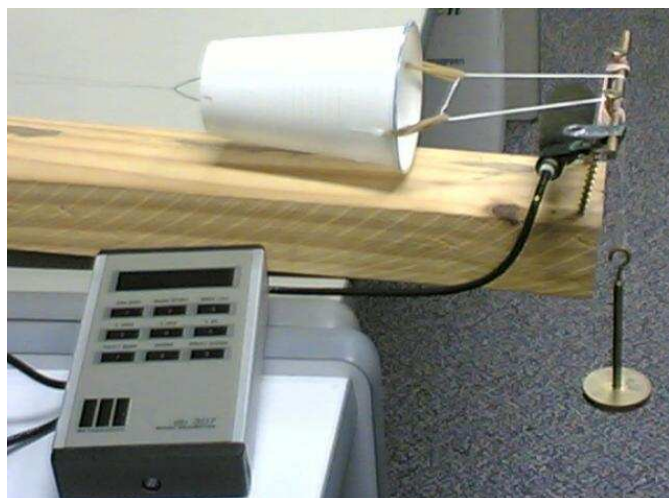
Figure 3.3: The SMA loudspeaker setup.
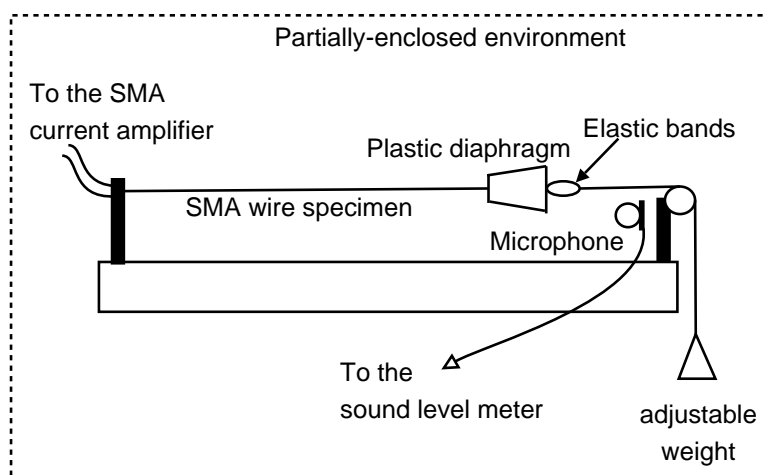
Figure 3.4: Schematic diagram of the SMA loudspeaker.

up, sufficient to prove the existence of a high-frequency response, and we had a calibrated sound level meter available for sound measurement.

Flexinol wires are commercially produced NiTi alloy wires,[2] which have been trained to exhibit the shape memory effect over millions of cycles without fatigue, provided the working strain is limited to 4%. We used Flexinol wires with an austenite finish temperature (A_f) of 90°C and a diameter of $100\,\mu$m. Two wires were used in the experiments: an untreated Flexinol wire, and a Flexinol wire annealed at 300°C for 15 hours which serves as a control. The annealing process undoes the training, and reduces the wire's shape memory response to thermal cycling.

---

[2]Flexinol wires are available from Dynalloy Inc. http://www.dynalloy.com.

To measure the sound output from the loudspeaker, it is placed in an enclosure made of sound-absorbing material. This serves partly to block external ambient noise, and partly to shield the SMA wire from external air movements. The measuring instrument is a db-307 sound level meter, manufactured by Metrosonics. Its microphone is fixed to a point approximately 8 cm in front of the plastic diaphragm. The db-307 features a 95 dB dynamic range from 45 to 140 dB. The sound levels reported in this paper are sound levels averaged over 10 seconds. Note that the proximity of the microphone to the sound source means that the recorded sound intensity will be more than 20 dB higher than if the microphone had been placed at a standard distance of 1 metre. However, the sound outputs from the experiments could still be heard from $2-3$ metres away. [3]
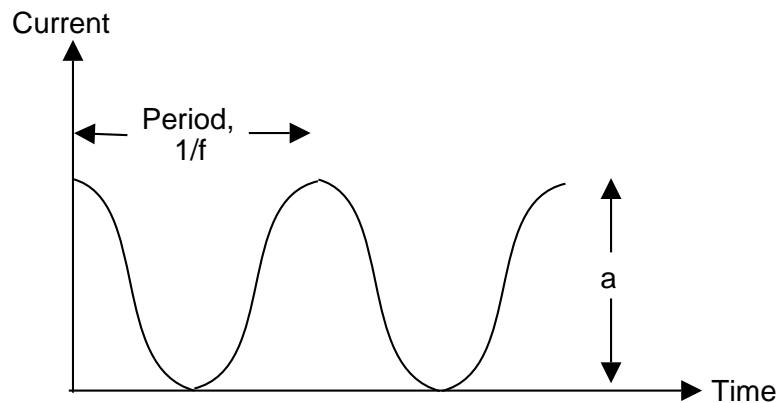
Figure 3.5: General input current signal of the form $\frac{a}{2}(\sin(2\pi ft) + 1)$.

Figure 3.5 depicts the input current signal used to heat the SMA wire. It has the formula $\frac{a}{2}(\sin(2\pi ft) + 1)$, where a is the peak amplitude of the signal, f the frequency in Hertz, and t the time in seconds. The signal is synthesised digitally on a dSPACE DS1104 real-time control board, and sent to a custom-built transconductance (voltage-in, current-out) amplifier that delivers the current to the SMA wire. The amplifier also measures the voltage across the wire, so that the RMS heating power can be calculated. The bandwidth of this amplifier is sufficiently high to be irrelevant.

---

[3]A sample of the SMA loudspeaker's audio output is available at http://users.rsise.anu.edu.au/~roy/SMA/index.html.

3.2.2 Experimental Procedures

Type of Wire	Operating Frequency (Hz)			
	500	1000	1500	2000
Normal Flexinol	150 g	50 g	150 g	150 g
		100 g		
		150 g		
		200 g		
Annealed Flexinol	150 g	50 g	150 g	150 g
		100 g		
		150 g		
		200 g		

Table 3.1: Experimental parameters used for both the normal and annealed Flexinol SMA wire specimens.

A series of experiments were conducted, in which the following parameters were varied: the average tension on the wire, the frequency of the sine wave, and the heating power. Table 3.1 lists every combination of the load mass and frequency that was tested. As the wire is effectively doubled-up, the wire tension is half the load. For each combination, the power was stepped up progressively from zero to a maximum power of about 2.5 W, and then stepped back down again. After each step, the wire was allowed a period of 5 seconds to settle to a steady state, and then an average sound measurement over 10 s was taken. A heating power of 2.5 W is enough to heat the wire significantly above its A_f.

3.3 Results and Discussions

3.3.1 SMA Flexinol Wire

Figure 3.6 shows the sound level measurements obtained using the normal Flexinol wire with an input modulation frequency of 1 kHz. Figure 3.6(a) shows the measurements obtained during the heating cycle; that is, the measurements made as the RMS heating power was stepped up progressively from 0 W to 2.5 W. Likewise, Figure 3.6(b) shows the measurements obtained during the cooling cycle, in which the RMS heating power was stepped back down to zero. Each graph shows four curves, one for each load used. Recall that the wire tension is half the load.
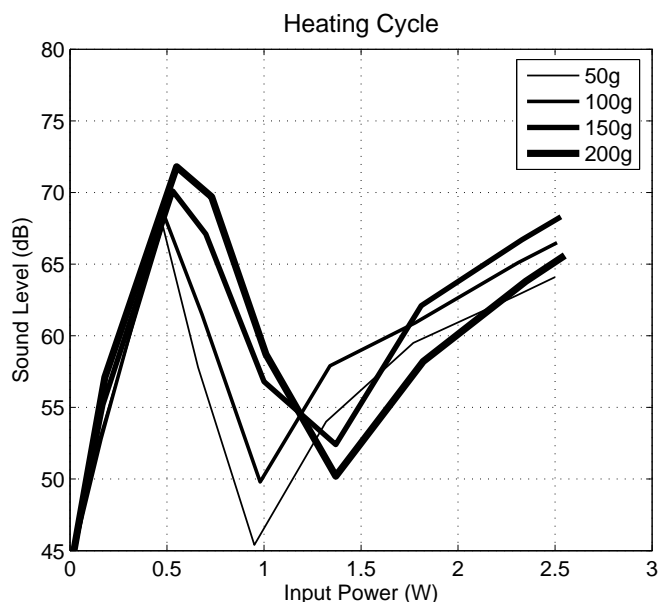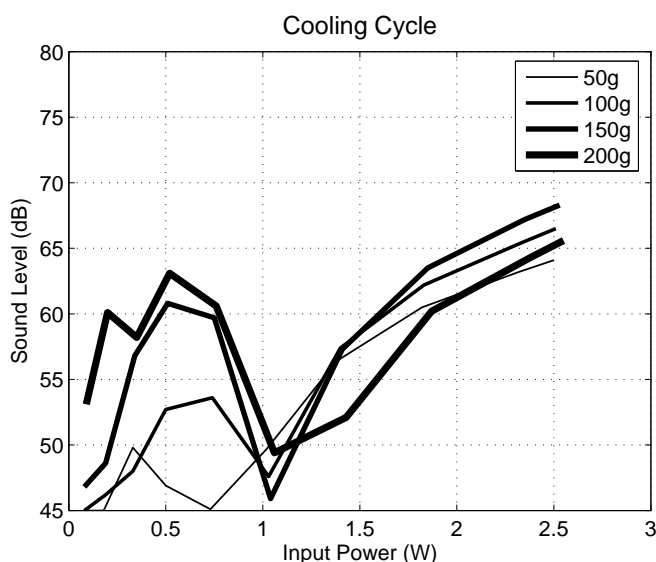
Figure 3.6: Sound level output from the loudspeaker actuated by a normal Flexinol SMA wire using incremental loads of 50 g respectively to a sine-wave input of 1 kHz during (a) the heating cycle and (b) the cooling cycle.

Figure 3.6(a) clearly shows that the sound level first rises and drops sharply, followed by a more gradual rise, as the input power is increased. The sharp rise and fall occur at power levels that heat the wire to its phase transformation temperature range; that is, the temperature range at which the shape memory effect occurs. The power required to heat the wire to its A_f temperature varies with load, but is somewhere near 1.5 W. The shape of this graph suggests the follow-
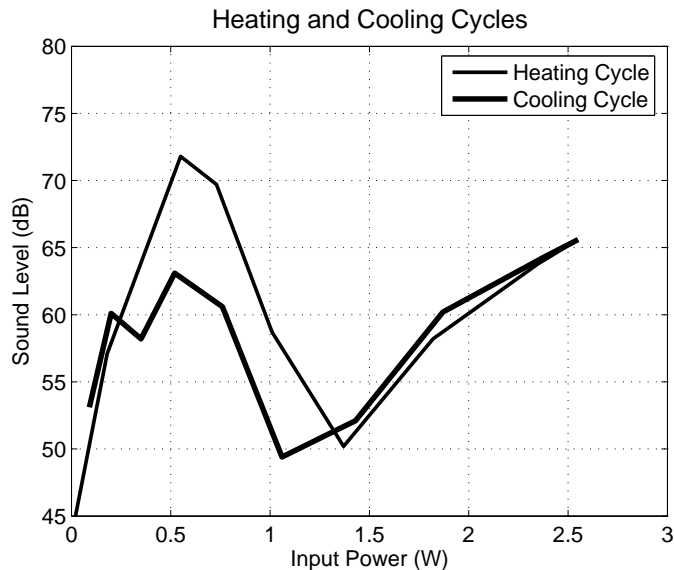
Figure 3.7: Sound level output from the loudspeaker during both the heating and cooling cycles for a normal Flexinol wire with a 200 g load and a 1 kHz input signal.

ing hypothesis: at low power levels, where the temperature is in the transition range, the shape memory effect is mainly responsible for the sound emission; but at higher power levels, where the temperature is above A_f, the wire begins to behave like an ordinary metal, and the sound emission is mainly due to the thermal expansion and contraction of the wire as its temperature varies according to the input signal frequency.

Several observations support this hypothesis. First, the sharp drop occurs at progressively higher power levels (and therefore higher temperatures) as the load is increased. This agrees with the well-known property of the shape memory effect that the phase transformation temperatures rise as the stress on the material is increased (See Chapter 2, Section 2.1.3). Second, it can be seen from Figure 3.6(b) that the behaviour of the wire during the cooling cycle is qualitatively the same, but quantitatively different at low power levels. In other words, the behaviour at low power levels depends on the thermal history of the material. This is a property of the shape memory effect, but not of normal thermal expansion and contraction. Third, a degree of hysteresis is evident in the response. In particular, the rise in sound level as the power is decreased on the cooling cycle occurs at a lower power level than the drop in sound output on the heating cycle. Figure 3.7 superimposes the heating cycle and cooling cycle curves for the 200 g test case, to show the hysteresis more clearly. Again, thermal hysteresis is a property

of the shape memory effect. Finally, the peak sound output in Figure 3.6(a), which occurs at around 0.5 W, is an order of magnitude higher than the sound output at 1.5 W. Therefore, whatever is causing the sound emission at 0.5 W must involve a much larger strain change per degree of temperature change than thermal expansion and contraction. This, too, is a property of the shape memory effect.

To look at how the SMA responds to different input signal frequencies, the normal Flexinol wire is subjected to input signals at frequencies of 0.5 kHz, 1 kHz, 1.5 kHz and 2 kHz respectively. A constant load of 150 g is applied throughout all of the experiments.

The results of heating the Flexinol wire are presented in Figure 3.8. At frequencies of 0.5 kHz and 1 kHz, the responses are similar, both following the trend of a sharp rise and fall in sound output at lower input powers followed by a more gradual rise in sound output at higher input powers. The peak sound output at both frequencies is approximately 72 dB. Although similar trends are observed at frequencies of 1.5 kHz and 2 kHz, the magnitude of sound output is considerably lower. The peak sound output for the 1.5 kHz results is approximately 53 dB. The sound from the diaphragm is barely audible throughout the experiment.
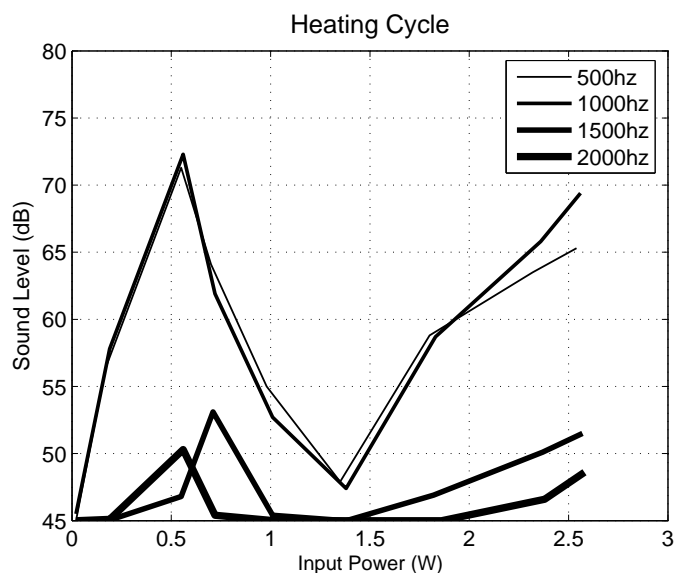
Figure 3.8: Sound level output from the loudspeaker to sine-wave inputs of 0.5 kHz, 1 kHz, 1.5 kHz and 2 kHz respectively for a normal Flexinol SMA wire during the heating cycle at a fixed load of 150 g.

3.3.2 Annealed Flexinol Wire — Control Experiment

To further strengthen the hypothesis that the shape memory effect plays a role in the observed high-frequency response, the experiment is repeated using an annealed Flexinol wire. This serves as a control experiment. It should be noted
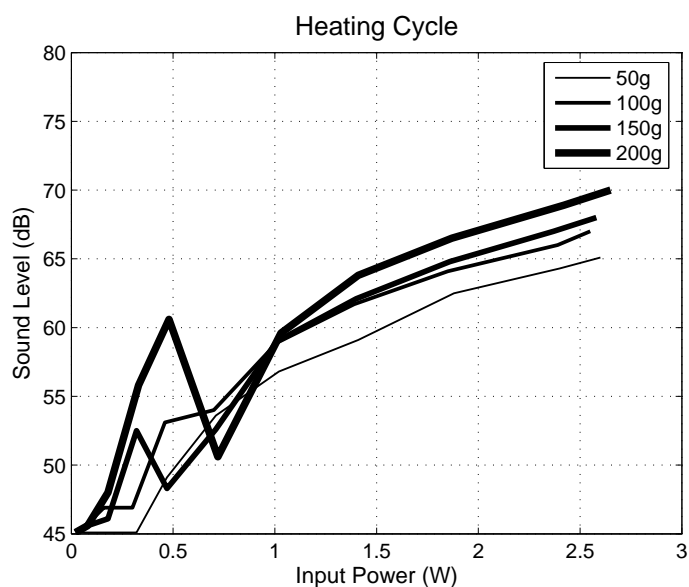
(a)
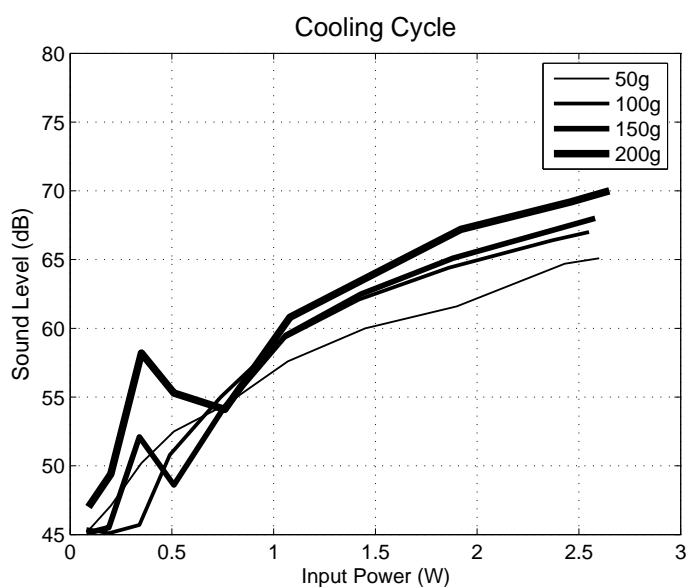
(b)

Figure 3.9: Sound level output from the loudspeaker actuated by an annealed Flexinol SMA wire (at 300°C for 15 hours) using incremental loads of 50 g respectively to a sine-wave input of 1 kHz during (a) the heating cycle and (b) the cooling cycle.

that the annealing process does not destroy the shape memory effect completely, but substantially reduces its magnitude along the length of the wire, while causing no other significant change. Therefore, if the sound is due to the shape memory effect, then a large reduction in the sound output can be expected at low input powers, but with no significant change at high powers.

Figure 3.9 presents the sound level measurements using the annealed Flexinol wire at the input frequency of 1 kHz. Figure 3.9(a) shows results obtained during the heating cycle of the wire, whereas Figure 3.9(b) shows the measurements from the cooling cycle. The important observation made from these graphs is the significant reduction in sound level measurements at low input powers. This feature is more evident in the results obtained using lower wire tensions.

At 50 g and 100 g load weights, the sound output increases steadily at progressively higher input power. Likewise, in the cooling cycle, the sound output drops steadily as the input power is decreased. No sharp rise and fall in sound output at low input powers are observed using these loads. At 150 g and 200 g load weights, a peak in sound output at low input powers is observed, but the magnitude is noticeably smaller compared to the measurements from a normal flexinol wire in Figure 3.6. The peak at low input powers indicates that the annealing process has reduced, but not completely destroyed, the effect as seen in Figure 3.6. This observation in the annealed wire results further supports the hypothesis.
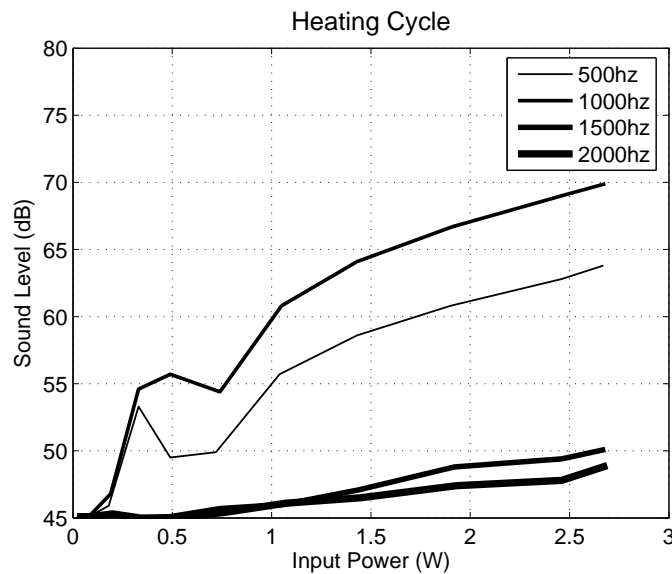
Figure 3.10: Sound level output from the loudspeaker to sine-wave inputs of 0.5 kHz, 1 kHz, 1.5 kHz and 2 kHz respectively for an annealed Flexinol SMA wire (at 300°C for 15 hours) during the heating cycle at a fixed load of 150 g.

The annealed Flexinol wire is also subjected to input signals at different frequencies of 0.5 kHz, 1 kHz, 1.5 kHz and 2 kHz at a constant load of 150 g. The results are shown in Figure 3.10. Compared to the untreated Flexinol wire results of Figure 3.8 ,the sound level measurements have noticeably lower magnitudes at low heating powers. At frequencies of 0.5 kHz and 1 kHz, the initial peaks are approximately 18 dB lower compared to the normal Flexinol under similar test conditions. At higher frequencies, the sound level meter barely detects any audible sound from the loudspeaker. Again, this supports the above hypothesis.

3.3.3 Repeatability of Experiments
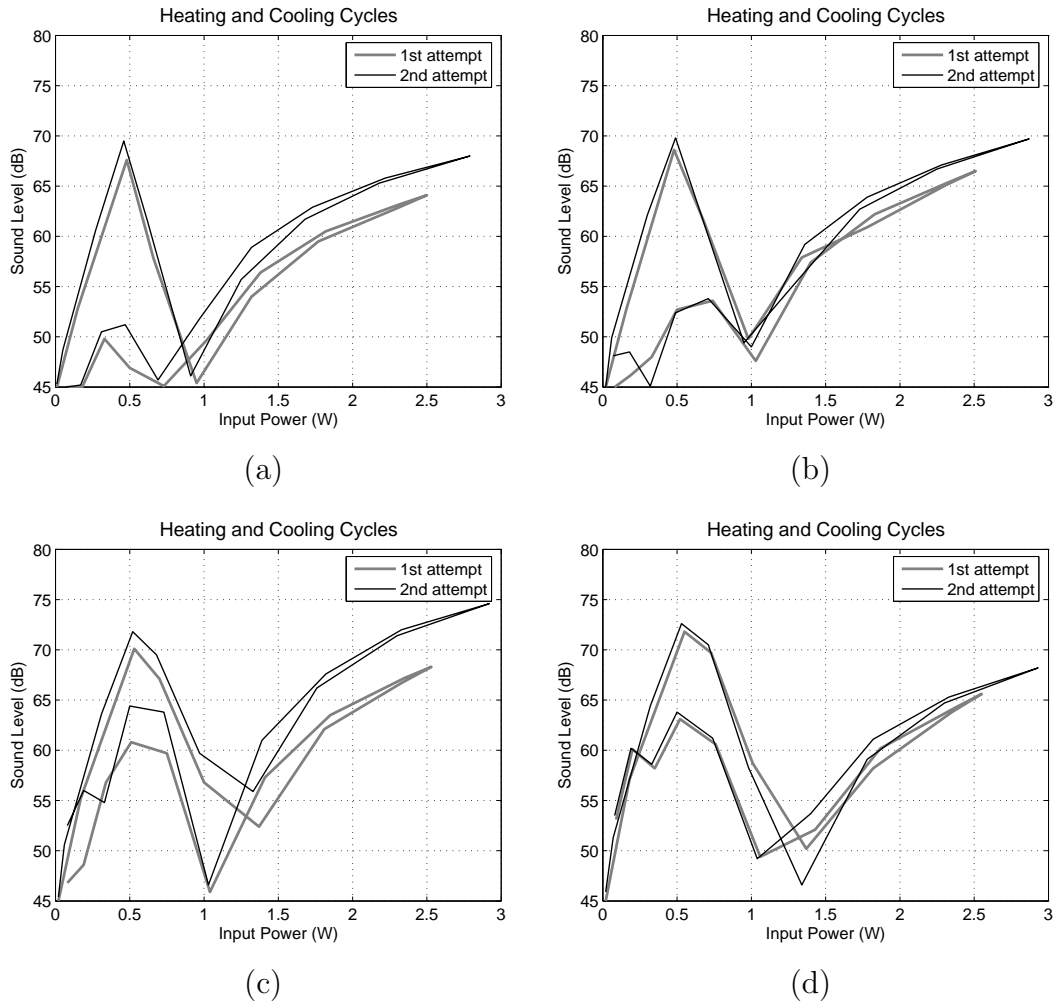
Figure 3.11: Two sets of sound level output results from the loudspeaker produced by a normal Flexinol wire at a frequency of 1 kHz, with weights of (a) 50 g, (b) 100 g, (c) 150 g, and (d) 200 g respectively.

During the experiments, it is observed that, under some combinations of power, load and frequency, the sound level could fluctuate by as much as 15 dB. The presence of these fluctuations was the reason the sound level readings were taken as an average over a 10-second period, which is long enough to average them out.

The experiments were repeated several times, in order to get statistics on the variability of the results. Figure 3.11 and Figure 3.12 show two sets of results for each experiment conducted using the normal Flexinol wire under different wire tensions and input frequencies. It can be observed from these graphs that individual measurements from different runs of the same experiment could differ by as much as 5 dB. However, the magnitude of variability is insufficient to invalidate the results. The experimental graphs remain in agreement with the hypothesis.
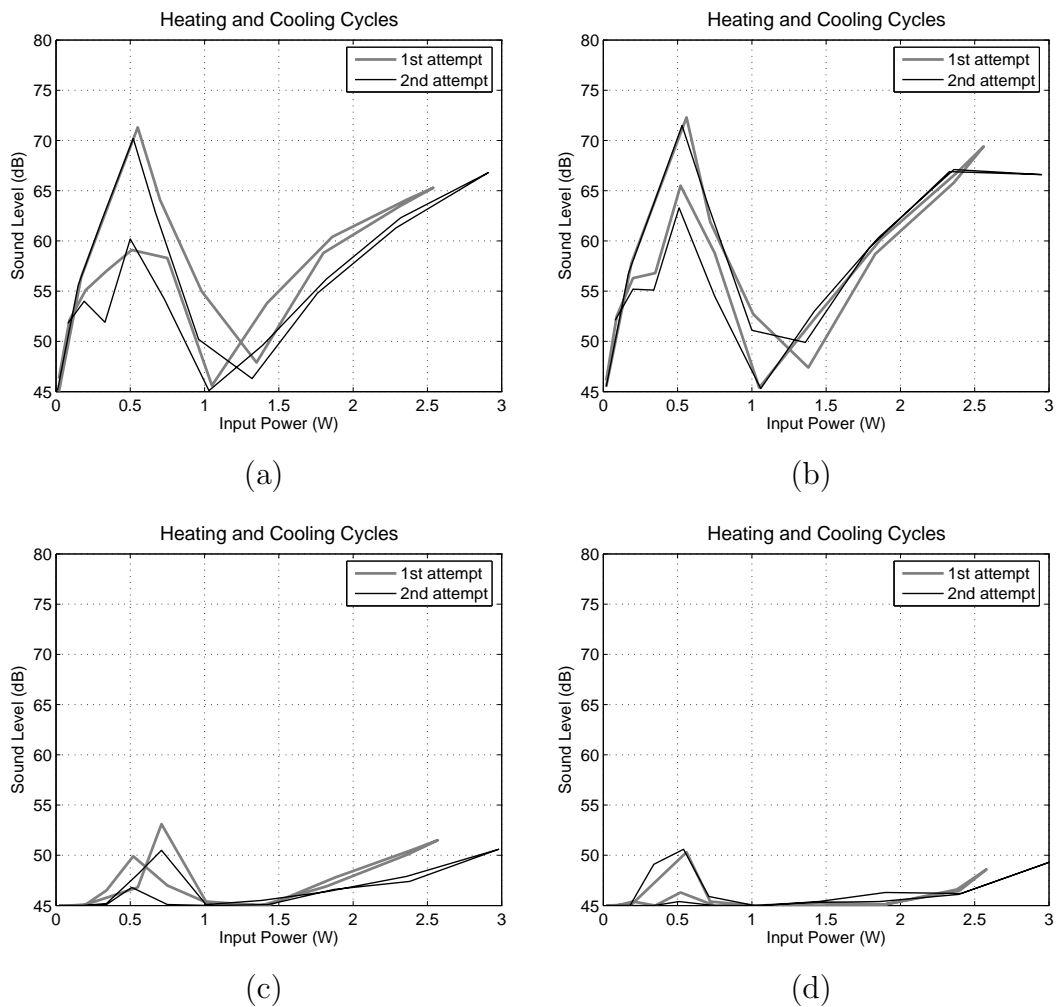
Figure 3.12: Two sets of sound level output results from the loudspeaker to sine-wave inputs of (a) 0.5 kHz, (b) 1 kHz, (c) 1.5 kHz, and (d) 2 kHz respectively for a normal Flexinol SMA wire at a fixed load of 150 g.

However, it is conceded that in repeating the experiments, the SMA wire has not been heated to the same level, as can be seen in Figure 3.11 and Figure 3.12. This may lead to different thermal histories. Future experimental design should ensure that all repeat experiments produce the same thermal history for better comparison.

To improve upon the loudspeaker experiment, a more controlled environment and a better sound level meter are required. It must also be stated that the measurements made during the experiments are not precise, and the sound output measurements are only indirect and amplified measurements of the SMA response. Direct temperature or wire strain measurements will be more conclusive, but sensors with sufficient resolution and accuracy will be required.

3.4 Chapter Summary

It has been demonstrated in this chapter that a $0.1\,\mathrm{mm}$ diameter NiTi SMA wire can respond to a time-varying heating current at frequencies as high as $2\,\mathrm{kHz}$ when suspended in still air at room temperature. We have observed sound emitted from the loudspeaker diaphragm connected to the SMA wire, which is heated by an electric current modulated at different audio frequencies. The sound outputs are produced by small movements of the diaphragm, caused by bulk contraction and lengthening of the wire as it heats and cools down, and they have the same frequency as the heating current. The evidence strongly suggests that the SMA wires are capable of high-speed actuation, although at very small displacements. This suggests that the delay between the change in input current and an observable response is very short.

Experiments at various tensions and heating powers indicate that the sound output first rises, then falls, then rises again as the power is ramped up, and follows a quantitatively similar pattern as the power is ramped back down. Furthermore, the response at the lower power levels depends on the thermal history of the material, and is greatly reduced by annealing the wire. These results suggest that the shape memory effect plays a significant role in the observed response. Given that the temperature fluctuations in the wire must be very small at such high frequencies, these observed responses are very surprising and contrary to past work.

Based on the results, it is proposed that some form of small-signal high-bandwidth controller may be capable of improving stability and eliminating limit

cycles in the response of SMA actuators. An SMA force feedback control system may be suitable for this purpose. In the next chapter, an experimental test bed which allows accurate measurement of SMA wire forces will be described, followed by modelling experiments which aim to quantitatively measure and model the high-frequency small-signal force responses of SMA wires. The model will be used for force control simulations and controller design.

CHAPTER 4

SMA Force Modelling

When it comes to designing feedback control systems, having a model of the plant to be controlled is very valuable. This is especially so if the aim is to obtain a high-performance control system. For most applications in general, it is easier to implement and test controllers in simulation, rather than running experiments on actual plants. If the plant requires a more complicated control system to improve performance, the process of choosing and tuning control systems becomes more difficult and empirical. An accurate model will assist in selecting and optimally tuning the best control system. Modelling and simulation can help reduce design cost and effort, as well as minimise damage due to sub-optimal controllers.

SMA models that have been proposed in the past are generally phenomenological models, which attempt to capture or describe the complex nature of SMAs, especially in terms of their thermomechanical behaviour and the hysteretic effects. These studies usually concentrate on the large-signal behaviour of SMAs, which are quite nonlinear, hysteretic and often not repeatable. Furthermore, some of the internal state variables of SMAs may be irrelevant to control, including equations relating to temperature or martensite ratio. Actual measurements of these variables are often difficult, even impractical.

For SMA control, it is helpful to have a dynamic model of the SMA plant relating the observed output to the applied input. Almost all control and actuator applications of SMAs use the resistive heating method to drive the actuators. Therefore, the heating power supplied to the SMA can be regarded as the control input rather than the temperature, and the output response is usually a force or a position. In this chapter, a dynamic model of the SMA wire actuator relating the force output of the wire to the applied heating power is developed. The proposed method for obtaining such an SMA force model is the frequency response analysis. It allows us to study the small-signal response of SMA wires over a suitable frequency range, which has been observed to be very repeatable and also exhibits very little hysteresis.

This chapter will begin by presenting in Section 4.1 the experimental setup that is used for the force modelling experiments. The frequency response analysis will be further explained and the obtained results presented in Section 4.2. Constrained force models for a single SMA wire as well as for an actuator comprising of two SMA wires in antagonistic arrangement will be given in Section 4.3. The modelling method as well as the force models will then be used to derive a position model for the antagonistic case in Chapter 7.

4.1   Experimental Setup

(a)   (b)
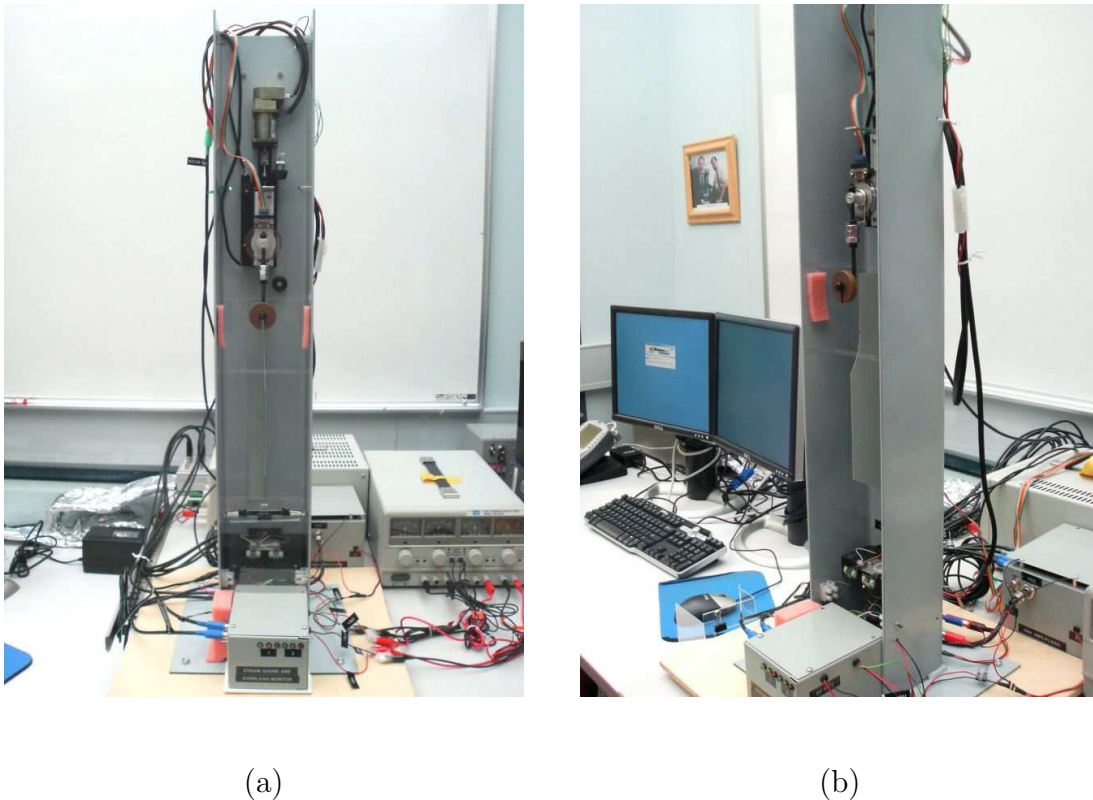
Figure 4.1: (a) Front view, and (b) side view of the SMA experimental test bed.

The experiments and results reported in this and later chapters are conducted using the SMA experimental test bed which has been custom-designed, commissioned and housed in the research lab of the Department of Information Engineering of the Australian National University. The experimental test bed is shown in Figure 4.1. Basically, the test bed consists of a steel column that can house an antagonistic pair of SMA wires with a pair of load cells for SMA force measurements near the bottom, and a pulley on a servo-controlled linear slide near the
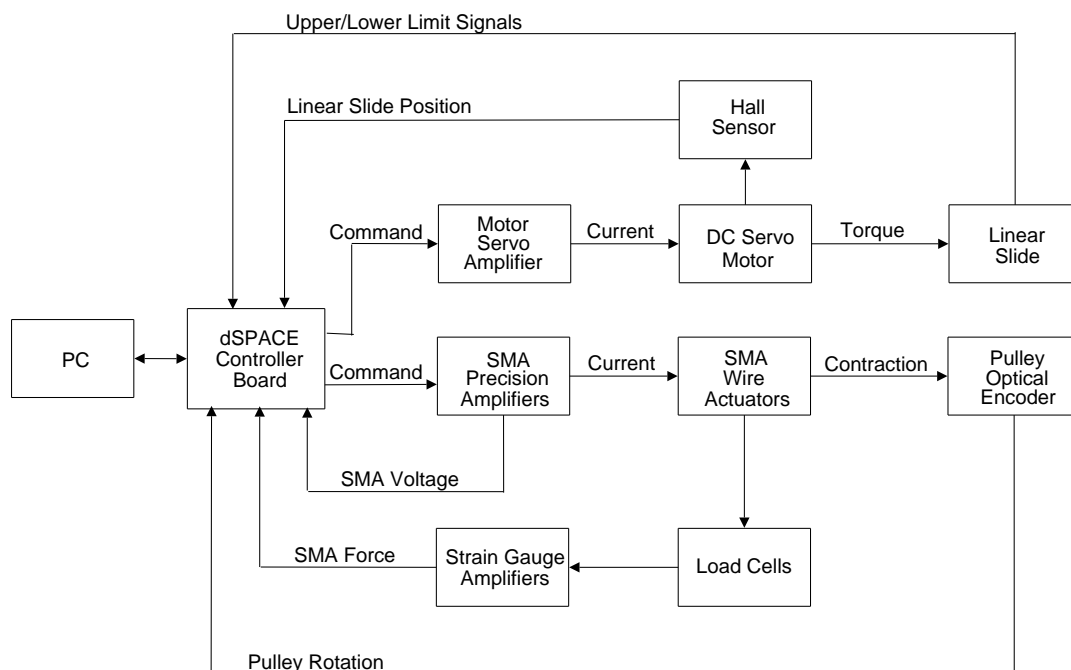
Figure 4.2: Simplified schematic diagram of the experimental setup.

top. In addition to the test bed, the experimental setup includes a PC as well as a dSPACE hardware and software system that allows us to program and run experiments and control systems on the test bed. A schematic diagram showing the major components of the setup is shown in Figure 4.2.

4.1.1 dSPACE System

A PC running MATLAB/Simulink is used to program and implement experiments and control systems on the SMA actuator test bed. In addition, a DS1104 system from dSPACE[1] which consists of (1) ControlDesk Standard, the experimental software, (2) Real-Time Interface (RTI), the implementation software, and (3) hardware including a DS1104 Controller Board and a CP1104 Connector Panel, is installed on the PC. ControlDesk Standard is a graphical user interface that provides the functions to control, monitor and automate experiments and make the development of controllers more efficient; and the RTI forms the interface between Simulink and the dSPACE Controller Board hardware. It is used to build, download and execute real-time codes on the Controller Board. The DS1104 Controller Board is a complete real-time microprocessor based on a 603 PowerPC processor at 250 MHz; and the CP1104 Connector Panel provides the

---

[1]DS1104 system from dSPACE obtained via http://www.ceanet.com.au.

input/output hardware interface between the Controller Board and the test bed.

4.1.2 Experimental Test Bed

<p align="center">(a)   (b)</p>
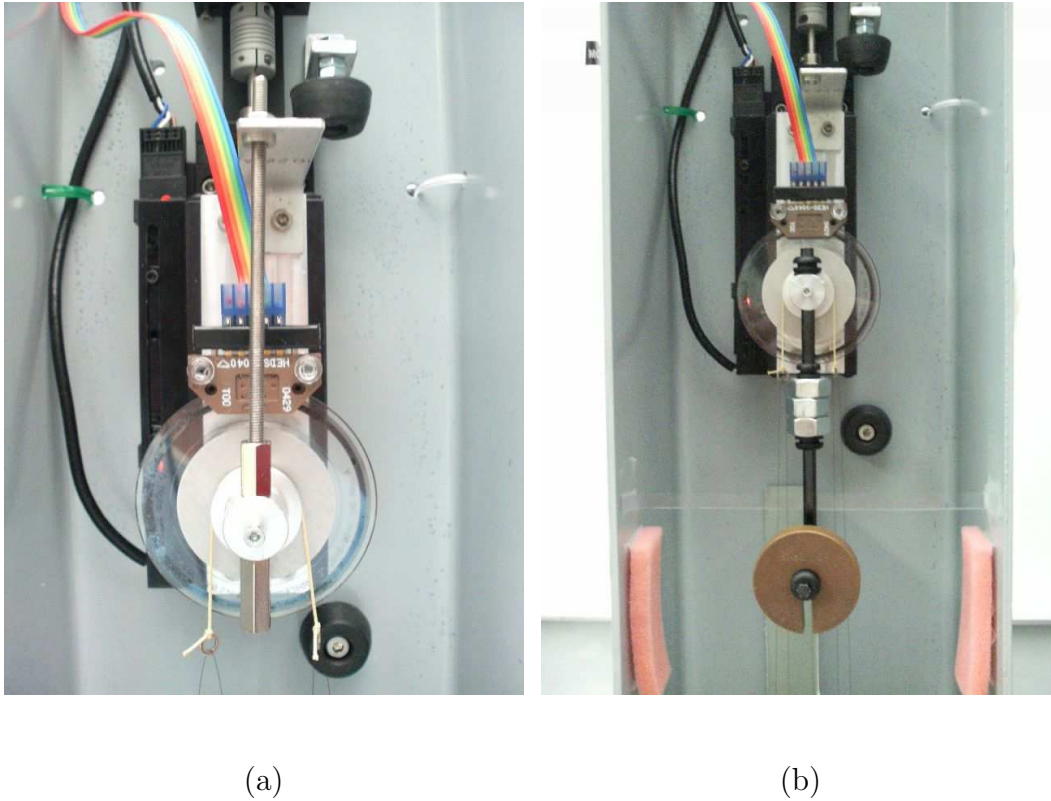
Figure 4.3: Close-up views of the pulley and optical shaft encoder mounted on the linear slide with (a) the pulley-locking pin, and (b) a pendulum load attached to the freely rotating pulley.

Close-up views of the pulley and the load cells appear in Figure 4.3 and Figure 4.4 respectively. The pulley is mounted on a precision linear slide from Deltron,[2] and is directly actuated by a Pittman brushless DC servo motor.[3] The linear slide has adjustable upper and lower limit switches, and can provide up to 75 mm travel with high linear accuracy and repeatability of 2.5 μm per 25 mm of travel. It can be used to simulate any desired strain profiles or to induce motion disturbances to the SMA wire(s). Depending on the type of experiment to be performed, the pulley can either be locked in a single orientation, or allowed to rotate freely with an optical shaft encoder for rotation measurement. In the latter case, an inertial load can also be attached to the pulley. In the following force control chapters, except for Section 6.5 of Chapter 6, the pulley is locked for

---

[2]Mini Posi-Drive Stage obtained from Del-Tron Precision Inc. http://www.deltron.com.
[3]Pittman brushless DC servo motor obtained from http://www.clickautomation.com.

constrained wire length; whereas in Section 6.5 of Chapter 6 as well as Chapter 7 for position control, the pulley is free to rotate. Figure 4.3(b) shows a pendulum load attached to the pulley, whereas Figure 4.3(a) shows the pulley locked. The optical shaft encoder module on the pulley has a resolution of 8192 bits per revolution, [4] and the pulley has a groove diameter of 1.6 cm. Thus, one encoder bit equates to approximately 0.04° (or 6 μm) pulley rotation.
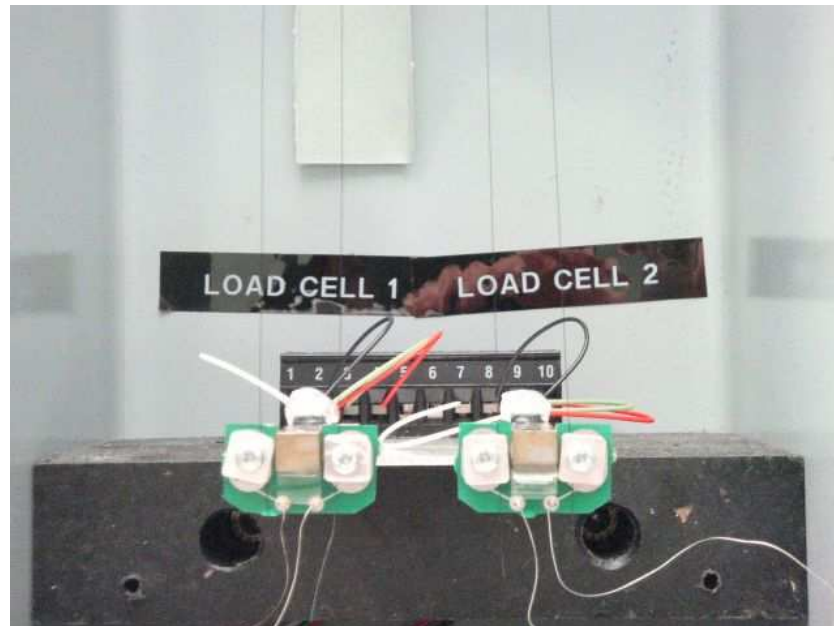
Figure 4.4: Close-up view of the load cells and SMA wires.

The test bed can accommodate two SMA wires in an antagonistic arrangement. The left-hand wire is connected so that its two ends are fixed to load cell 1, and its middle passes through an eyelet that is connected to the left-hand side of the pulley via a short aramid chord. The two ends of the wire are held by clamping from the screws between the small printed circuit board and two aluminium plates. This prevents slippage of the SMA wire during contraction. The right-hand wire is similarly connected between load cell 2 and the right-hand side of the pulley. Thus, the left-hand wire can exert a counter-clockwise moment on the pulley, and the right-hand wire a clockwise moment. The two wires are just visible in Figure 4.4.

The SMA Flexinol wires used in this test bed are 80 cm long, but they are doubled up, so a 4% strain equates to a 16 mm movement at the eyelets. For the modelling experiments reported in this chapter, three different diameters of

---

[4]HEDS optical shaft encoder module and 2-inch encoder disk obtained from US Digital, http://www.usdigital.com.

Flexinol wires are tested: $75\,\mu$m, $100\,\mu$m and $125\,\mu$m. In later chapters, only $100\,\mu$m Flexinol wires are used for force and motion control experiments. The $100\,\mu$m SMA wires have a rated pulling force of $1.5\,$N, which becomes $3\,$N when they are doubled up.

The load cells are S215 single point force sensors obtained from Strain Measurement Devices Inc.[5] They can measure forces in the $\pm 9\,$N range with a bandwidth of up to $140\,$Hz. A resolution of $0.3\,$mN is achieved based on the strain gauge amplifier and the 16-bit ADC.

Other components of the test bed include precision transconductance (voltage-in, current-out) amplifiers that can deliver heating currents of up to $0.8\,$A to the SMA wires, and strain gauge amplifiers that amplify the voltage signals corresponding to the measured forces from the load cells before being processed on the PC.

4.1.3 Safety Features

There are several safety and damage concerns about the experimental setup, involving especially the linear slide, the SMA wires and the load cells. Accidents or human errors may damage these components. The following safety features have been implemented on the experimental setup:

   i. Mechanical upper and lower rubber end-stops have been installed in the test bed column to prevent linear slide run-off at the end of travel.

  ii. A hard plastic cover shields the load cells from accidental striking.

 iii. Cardboard is placed between the two SMA wires as a physical separation to prevent short-circuit.

 iv. An overload monitor electronic circuit with LED displays measures and monitors the state of the load cells.

  v. A software load cell overload mechanism overrides any running experiment or control system when either load cells exceeds the threshold of $9\,$N. It automatically switches off input power to the SMA wires and moves the linear slide downwards until it touches the lower rubber end-stop to remove any residual forces on the load cells.

 vi. Adjustable upper and lower limit switches on the linear slide can be used to override any running operation on the test bed when the linear slide travel exceeds the normal range.

---

[5]S215 load cells obtained from http://www.smdsensors.com.

Further information about the test bed, including safety aspects, the initialisation procedures for the linear slide, the bandwidths of the linear slide and the load cells can be found in Appendix B.

4.2　Modelling Experiments

Consider an actuator made of an SMA wire that produces a force in response to a commanded signal with the constrained length condition. The SMA actuator is heated electrically and it attempts to contract, and forcefully increases the tension on the actuator. If the output force is to track a desired force command accurately, then a force sensor is required, and a feedback control system like the one shown in Figure 4.5 is needed to determine the heating power to the SMA. For control design and simulation, it is useful to obtain a model of the SMA plant; and in this case, a model relating the heating power to the output force of the SMA wire. The frequency response analysis is proposed to develop an SMA force model for these purposes.
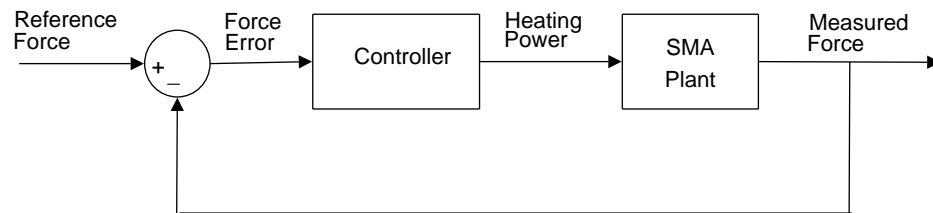
Figure 4.5: A force feedback control system for an SMA actuator.

4.2.1　Frequency Response Analysis

The frequency response analysis is aimed at finding the response of a linear system by applying test signals (usually sinusoids) to the input and looking at the output to see how it responds. By measuring the output amplitude and phase over a range of frequencies of the input sine wave, a measure of the dynamic response of the linear system can be built [17]. For SMA actuator modelling, the input signal is kept small so as to measure the small-signal response of the plant. This is important because the large-signal behaviour of SMA is highly nonlinear and hysteretic, but its small-signal behaviour is relatively linear and exhibits relatively little hysteresis, as have also been observed by Kuribayashi [40, 42].

When it comes to large-magnitude commands, such as step commands, the large-signal behaviour of the SMA dominates, and the feedback controller attempts to deliver as much heating power to the actuator as is possible in order to reduce the errors, within certain limitations to prevent overheating and actuator damage. Once the response enters into the region of close proximity to the commanded signal, accuracy and small-signal responses dominates, rather than the large-signal behaviour and the speed of response. This small-signal behaviour, and the ability to model and simulate it, are crucial for achieving high accuracy in force or position control systems. The frequency response analysis is a modelling method capable of capturing the small-signal behaviour over the frequency range of interest that is relevant for control.

A model can then be constructed in the form of a transfer function that matches the measured gain and phase data over the frequency range of interest. Such a model describes only the AC behaviour of the wire, not its large-signal DC behaviour. However, we have found that this is actually an advantage, as the AC behaviour is more repeatable, and therefore more reliable, than the DC behaviour.

The obtained small-signal force model has been shown to accurately predict closed-loop stability and the onset of limit cycles to within 10% of the true values of the actual plant, despite some limitations for large-scale responses. The model has also proven to be useful as a design aid for control systems and has been used to simulate single-wire SMA force control and the differential force control of an SMA antagonistic wire pair in Chapters 5 and 6. Results from these chapters show that the response of the actuator under feedback control can be fast and very accurate.

4.2.2 Experimental Procedures

The small-signal frequency response analysis has been conducted using the experimental test bed described in Section 4.1. The test bed can accommodate a pair of SMA wires arranged antagonistically about a rotating pulley and shaft housing. For the purpose of this analysis, only single SMA wires are used. Three different diameters of Flexinol wires are tested in these experiments: $75\,\mu$m, $100\,\mu$m and $125\,\mu$m. For the experiments described in this chapter, the pulley on the linear slide is locked mechanically.

Figure 4.6 presents a simplified block diagram of the experimental arrange-
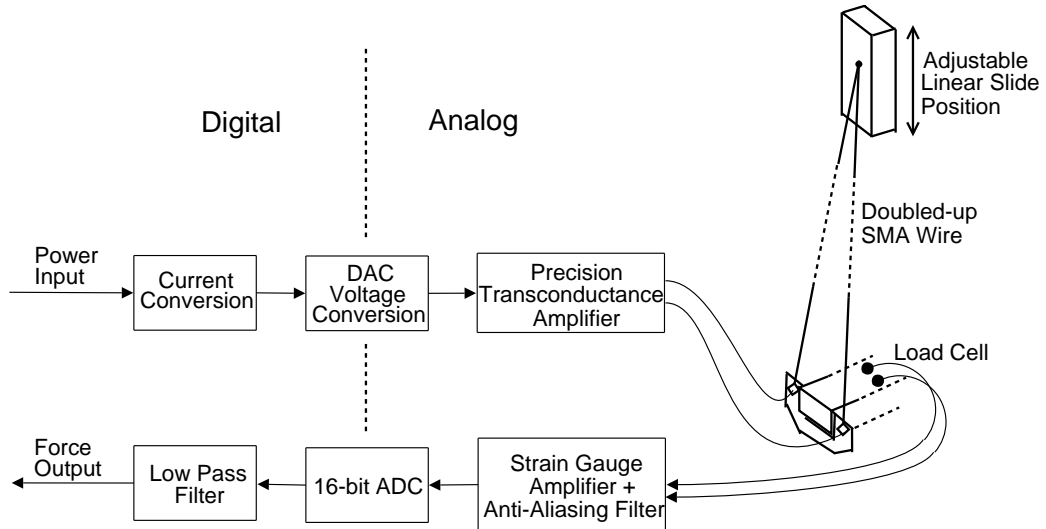
Figure 4.6: Experimental arrangement.

ment. Firstly, a power signal of the form $a + b\sin(\omega t)$ is generated, where $a \geq b$. This signal represents the heating power to be applied to the wire. a is the mean power, and b the magnitude of the sinusoidal component. This signal is converted to a current signal using a nominal value for the wire's electrical resistance, and is then converted to an analog voltage and sent to the precision transconductance amplifier, which drives the SMA wire. The measured force response, which has the same frequency as the heating power, is obtained from the load cell using a 16-bit analog-to-digital converter and is low-pass filtered to remove high-frequency noise. Once steady-state is achieved, the force signal is recorded for a sufficient length of time to allow an accurate measurement of the magnitude and phase of the sine-wave component at the driving frequency, ω. The above procedure is repeated for suitable spot frequencies over the $0.1 - 100\,\mathrm{Hz}$ range. For the experiments reported in this chapter, the dSPACE system ran at a sampling rate of $10\,\mathrm{kHz}$.

It should be noted that the mean (DC) value of the input power signal is kept constant over the frequency range so that the mean force output is fairly constant, although the magnitude of the AC input signal is varied. At the lowest frequency, the magnitude of the sinusoid is kept small, so that only small temperature variations result; but the magnitude is increased at higher frequencies so that there is still a detectable force signal. Strictly speaking, it is the temperature fluctuation that is the small signal, not the heating power. However, input power is used as the experimental parameter instead of temperature because of the difficulty of measuring rapidly-varying temperature for a thin wire. The SMA

55

wire is also shielded within the test bed to reduce the effects of air movements on wire temperature.

The next step is to extract the sine-wave component in the recorded data at the driving frequency ω, and measure its magnitude and phase. This is accomplished using a recursive parameter identification method based on a least-squares algorithm [35]. The algorithm is sufficiently robust to reject the noise and harmonic distortion present in the force signal, and the estimates have been averaged over many cycles.

The parameter identification method is briefly described as follows. Consider the recorded force data,

$$y(t) = A \cos\left(\omega t + \varphi\right), \tag{4.1}$$

which has a sinusoidal form with a known frequency $\omega = 2\pi f$, with f the frequency in Hz, but an unknown phase φ and an unknown force amplitude A. The force signal $y(t)$ and driving frequency ω are known, and the objective is to estimate A and φ. Using the trigonometric identity $\cos\left(A + B\right) = \cos A \cos B - \sin A \sin B$, we obtain

$$y(t) = A \cos\varphi \cos\omega t - A \sin\varphi \sin\omega t. \tag{4.2}$$

Equation 4.2 now has the same form as the following parametric model,

$$z(t) = \theta^{\star T}\phi(t), \tag{4.3}$$

with $z(t) = y(t)$, $\theta^{\star} = [A_1, A_2]^T$ and $\phi\left(t\right) = [\cos\omega t, -\sin\omega t]^T$, where $A_1 = A\cos\varphi$ and $A_2 = A\sin\varphi$. This parametric model is fully described in [35]. Notice that the unknown parameters which we wish to estimate have been lumped in the vector $\theta^{\star}$.

Next, we set up an estimation model $\hat{z}(t)$, in the same form as the parametric model, but with estimate θ instead of $\theta^{\star}$:

$$\hat{z}(t) = \theta^T(t)\phi(t). \tag{4.4}$$

We also define an estimation error, $\epsilon(t)$, which reflects the distance between the estimate θ and the unknown $\theta^{\star}$:

$$\epsilon(t) = z(t) - \hat{z}(t). \tag{4.5}$$

An adaptive algorithm, in this case a least-squares algorithm, is then used to generate the estimate $\theta(t)$ online. The adaptive law is fed by the estimate error $\epsilon(t)$ and is a differential equation of the form

$$\dot{\theta}(t) = H(t)\epsilon(t), \tag{4.6}$$

where $H(t)$ is a time-varying gain vector that depends on the measured signals. The least-squares algorithm fits a mathematical model to a sequence of observed data by minimising the sum of the squares of the difference between the observed and computed data. Once $\theta^\star$ has been estimated as $\theta = [\hat{A}_1, \hat{A}_2]^T$, we can obtain the estimates $\hat{A}$ and $\hat{\varphi}$ of force amplitude A and phase φ as

$$\hat{A} = \sqrt{\hat{A}_1^2 + \hat{A}_2^2}, \tag{4.7}$$

$$\hat{\varphi} = \tan^{-1}\left(\frac{\hat{A}_2}{\hat{A}_1}\right). \tag{4.8}$$

The estimation of the force amplitude and phase is conducted using the *Adaptive Control Toolbox* in MATLAB/Simulink. At the end of this process, a set of magnitude and phase data in the $0.1 - 100\,\text{Hz}$ range for one SMA wire diameter, at one particular strain and average stress condition, has been obtained.

The procedure is then repeated using different mean values, a, of the input power signal and varying linear slide positions to produce a variety of stresses and strains in the wire. The whole experiment is finally repeated using wires of different diameters.

Figure 4.7 demonstrates the coverage of the allowable stresses and strains for different wire diameters. The safe maximum pull forces for the $75\,\mu\text{m}$, $100\,\mu\text{m}$, and $125\,\mu\text{m}$ Flexinol wires are approximately $0.8\,\text{N}$, $1.5\,\text{N}$ and $2.3\,\text{N}$ respectively, as can be seen in Table A.1. Recall that the SMA wires are doubled-up in the test bed. Therefore the maximum rated force for each wire will be doubled to $1.6\,\text{N}$, $3.0\,\text{N}$ and $4.6\,\text{N}$ respectively; whereas a 4% strain corresponds to a $16\,\text{mm}$ movement of the linear slide. The frequency response data has covered nearly the full span of allowable stresses and strains of each wire diameter, as shown in Figure 4.7. Notice that there are a few irregular data points (such as the $1\,\text{W}$ and $1.25\,\text{W}$ data at the slide position of $2\,\text{mm}$ in Figure 4.7(c), and the $1.39\,\text{W}$ data at the slide position of $0\,\text{mm}$ in Figure 4.7(e)) that are slightly deviated compared to the rest of the data. The reason for this is not known, but several possible causes can be experimental noise and error, or varying environmental conditions during the experiments.
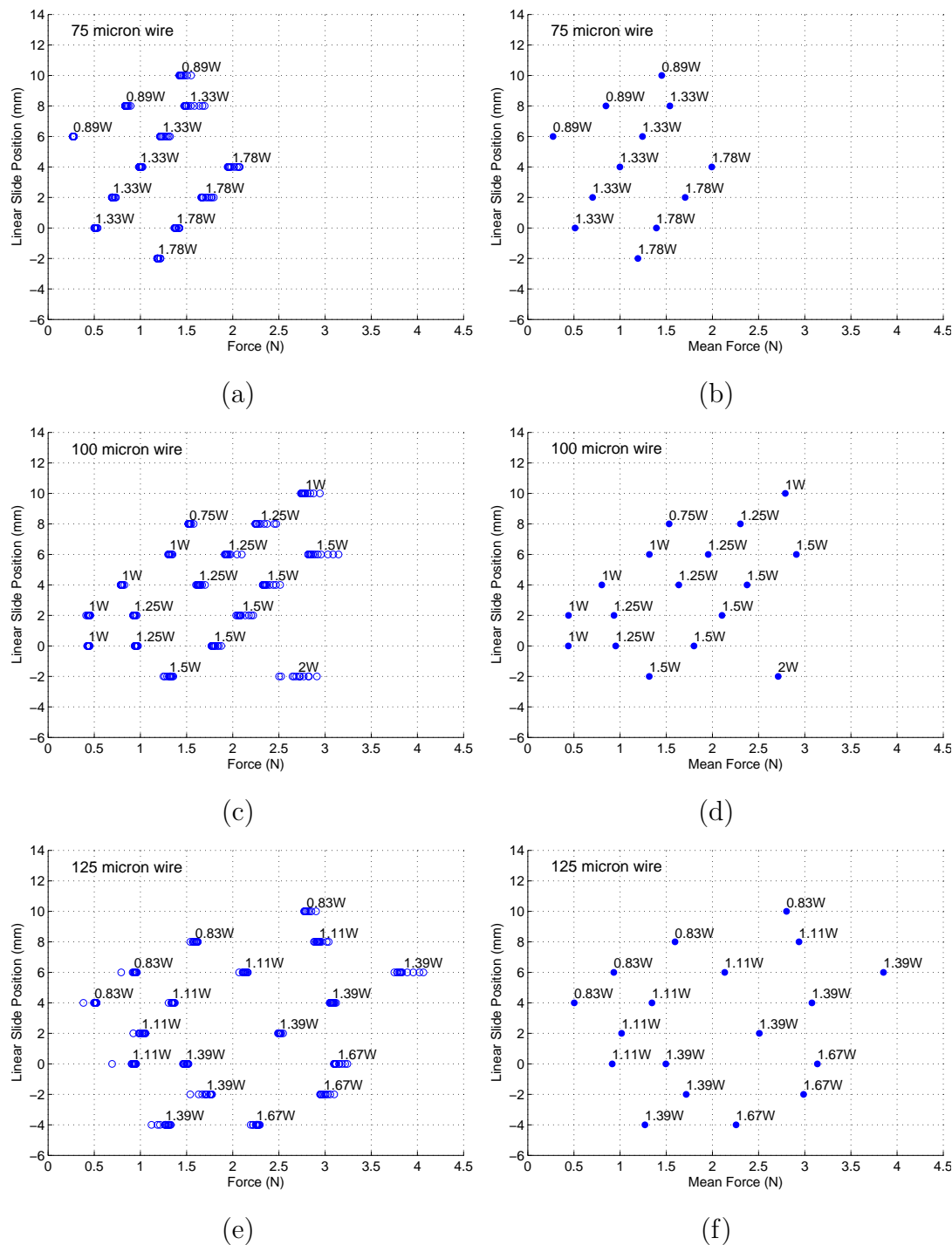
Figure 4.7: Sets of frequency response data spanning nearly the full range of stresses and strains at various mean input power a for different Flexinol wire diameters. Graphs on the left show the spread of force data recorded at different frequencies between $0.1 - 100$ Hz; whereas graphs on the right show the mean force data over the frequency range.

4.2.3 Results and Discussions

Figure 4.10 shows the experimental Bode plots of the system using different wire diameters of $75\,\mu$m, $100\,\mu$m and $125\,\mu$m under varying stress and strain conditions. Each curve represents one stress-strain combination. The magnitude in decibels (dB)[6] is given by:

$$\text{Magnitude} = 20\log\frac{\text{Force Amplitude}}{\text{AC Power}}, \tag{4.9}$$

where the force amplitude is the least-squares estimate calculated using the best-fit sinusoid and the AC power is the parameter b mentioned in Section 4.2.2. The phase in degrees ($°$) is the phase shift between the best-fit sinusoid and the input power signal.

As a final processing step, the magnitude and phase data of Figure 4.10 have been adjusted to compensate for the known effects of the experimental arrangement. Figure 4.8 presents the various physical subsystems that needs to be compensated in the frequency response data. The three effects are: the measured mechanical resonance ($280\,$Hz) of the load cell, the analog anti-aliasing filter, and the digital low-pass filter. The transfer function for each of them has been determined, and their bode plots are shown in Appendix B.
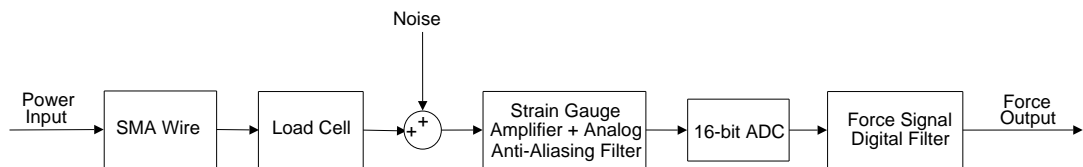
Figure 4.8: Experimental open loop SMA force system.

The mechanical resonance of the load cell can be measured by subjecting the load cell to a mechanical impulse, measuring the force output signal, and examining its force signal power spectrum. It has been observed that the force signal exhibits decaying oscillations, which are characteristic of an underdamped 2nd-order system. Therefore the transfer function of the load cell resonance, $R(s)$, can be given as

$$R(s) = \frac{\omega_n^2}{s^2 + 2\zeta\omega_n s + \omega_n^2}, \tag{4.10}$$

---

[6]The decibel is usually a ratio of two quantities having the same dimensions, making it a dimensionless quantity. However, in this thesis, it is used to express a ratio of quantities having different physical dimensions, such as force and power. The value of such a ratio depends on the units being used.

where ζ is the damping ratio, and ω_n the undamped natural or resonant frequency.

The analog anti-aliasing filter is effectively two analog RC circuits in series, thereby making it a 2nd-order low-pass filter, with a transfer function, $A(s)$, of the form

$$A(s) = \frac{1}{R_1 R_2 C_1 C_2 s^2 + (R_1 C_1 + R_2 C_2 + R_1 C_2)s + 1}, \qquad (4.11)$$

where R_1, R_2, C_1 and C_2 are calculated from the measured resistances and capacitances of the analog filter and strain gauge bridge, with the subscripts referring to the first or the second RC circuit in series. The actual anti-aliasing filter is shown in Figure 4.9(a) and its equivalent of two cascading RC circuits in Figure 4.9(b). The resistance and capacitance values have been measured, of which $R_1 = 10\,\mathrm{k\Omega}$, $R_2 = 11.2\,\mathrm{k\Omega}$, and $C_1 = C_2 = 33.6\,\mathrm{nF}$.

The force signal digital filter is a 2nd-order low-pass Butterworth filter with a cut-off frequency, ω_c, of $150\,\mathrm{rad\,s^{-1}}$. Its transfer function, $D(s)$, is given by
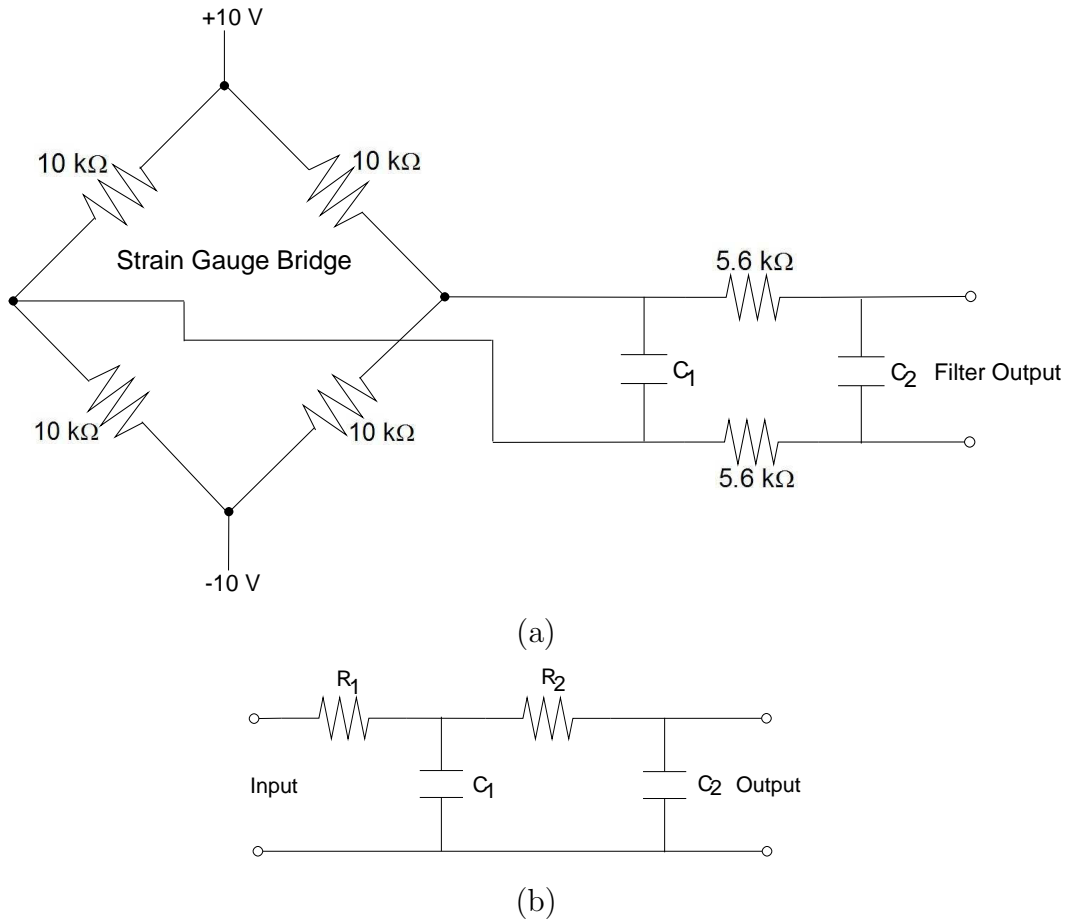
Figure 4.9: The actual analog anti-aliasing filter (a) and its equivalent (b).

$$D(s) = \frac{1}{\frac{1}{\omega_c^2}s^2 + \frac{\sqrt{2}}{\omega_c}s + 1}. \tag{4.12}$$

The plots appearing in Figure 4.10 have been processed to remove the effects of this digital filter.

The most striking feature of Figure 4.10 is that the phase response is independent of stress and strain for each wire diameter. If we plot the three sets of phase curves in a single graph, as in Figure 4.11, then it can be seen that they are shifted horizontally relative to each other, and that they converge to a phase lag of 90° at high frequencies. This is the behaviour that one would expect of a linear, first-order, low-pass filter with a cut-off frequency that decreases with increasing wire diameter.

The variations in phase curves for different diameters are plausible, due to the effects of wire dimensions on the heat transfer time constants. One would expect that a thicker SMA wire would respond slower, and therefore have a larger phase lag compared to that of a thinner wire at the same frequency. This is exactly what the phase responses suggest. For example, at a frequency of $1\,\mathrm{rad\,s^{-1}}$, phase plots from the $75\,\mu$m wire have a lag of approximately 30°; whereas the results of the $100\,\mu$m wire show a larger lag of approximately 42°; and the $125\,\mu$m wire results show a much larger lag of approximately 54°. It can also be seen that at the highest recorded frequencies, the curves tail off to more than 90° phase lag, and there is also more electrical noise. At these frequencies, the signal power is lower compared with lower frequency signals, resulting in a reduction of the signal-to-noise ratio.

The magnitude response graphs show a different picture. For any given diameter, the curves all have almost the same shape, but are vertically shifted relative to each other within a window of approximately $7\,\mathrm{dB}$. This shows that any change in stress or strain has approximately the same effect at all frequencies. The magnitude response curves for the $75\,\mu$m-diameter wire are almost horizontal at the lowest frequencies, but switch to a slope of approximately $-20\,\mathrm{dB}$ per decade at a frequency of about $2\,\mathrm{rad\,s^{-1}}$. The frequency at which the change of slope in magnitude occurs is known as a pole. The magnitude responses for the other two diameters are the same, except that the pole appears at progressively lower frequencies as the diameter is increased. This pole probably marks the boundary between frequencies at which the wire is substantially at thermal equilibrium and frequencies at which it is not. The magnitude responses for the three wire diam-

eters collectively suggest that only a single pole exists in the $0.1 - 100\,\mathrm{Hz}$ range. This supports the observation from the phase curves, that the SMA frequency response is similar to that of a first-order linear system.
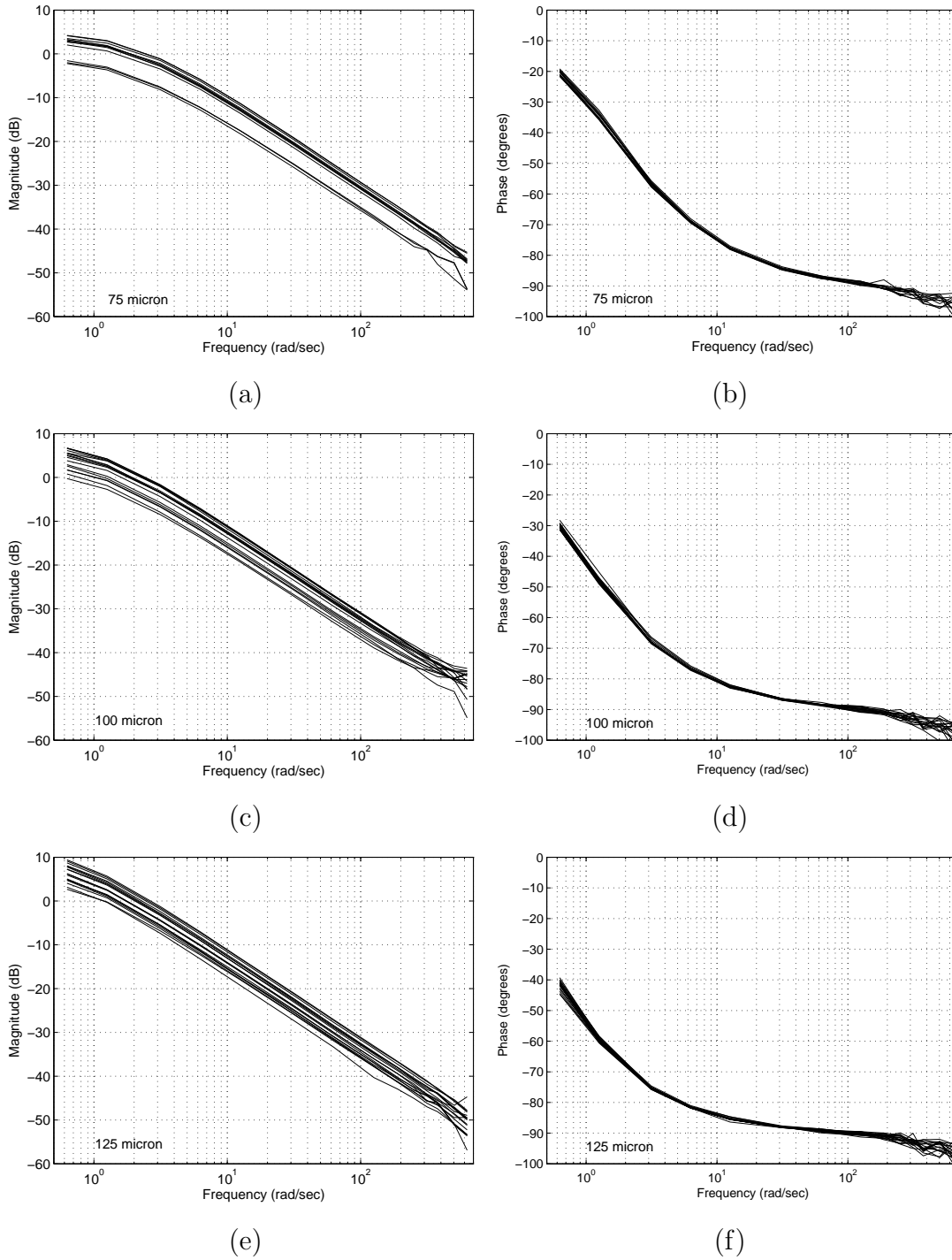
Figure 4.10: Bode magnitude and phase plots for Flexinol wires having diameters of $75\,\mu\mathrm{m}$, $100\,\mu\mathrm{m}$, and $125\,\mu\mathrm{m}$.

A narrow range of Flexinol wire diameters has so far been investigated in this chapter, although there are Flexinol wires with many different diameters readily available. Therefore at other wire diameters that have not been tested, it is difficult to speculate on their frequency response behaviour. However, it is possible to reason that the behaviour will follow similar patterns observed in Figure 4.10 and Figure 4.11: the pole will continue to increase as the wire diameter decreases below $75\,\mu$m, and decreases as the diameter increases above $125\,\mu$m. It is therefore worthwhile to investigate the frequency response of a larger range of Flexinol wire diameters, as well as other types of SMA wires, to see how their frequency responses will compare with the results in this chapter.
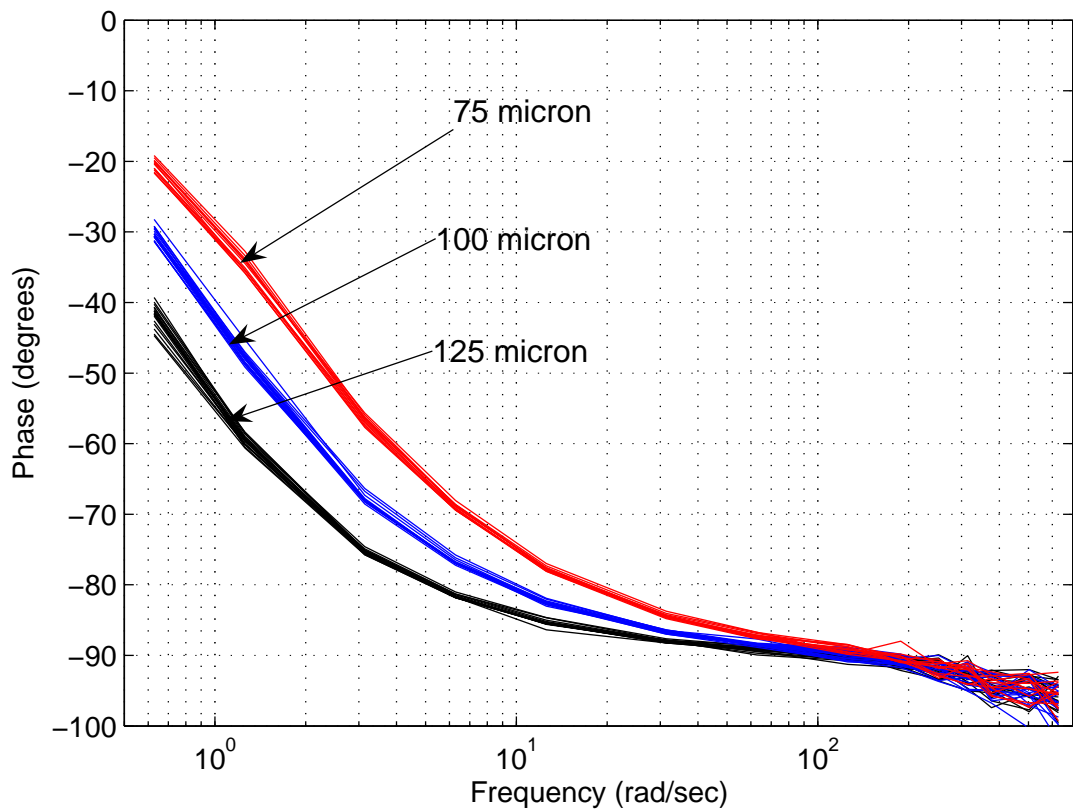
Figure 4.11: Superimposed phase plots for Flexinol wires of different diameters.

4.3　SMA Force Model

4.3.1　Power to Force Relationship for an SMA Wire

An SMA input power to output force model, in terms of a transfer function, can be obtained directly from the Bode diagrams in Section 4.2.3. This method of determining a transfer function model from the frequency response data is widely used in practice [17].

Let $P(s)$ and $F(s)$ denote the Laplace transforms of the heating power and measured force signals, respectively. The dynamic behaviour of an SMA wire can be modelled by a transfer function, $G(s)$, which satisfies

$$F(s) = G(s)P(s). \tag{4.13}$$

The experimental Bode diagrams show the existence of a single frequency pole, and the convergence to a phase lag of 90° at high frequencies. These observations strongly suggest that a first-order linear system can be used to model the dynamic response of SMA wires. In the case of the $100\,\mu$m wire data in Figure 4.10, a first-order linear transfer function with the following analytical expression is selected,

$$G(s) = \frac{K}{Ts + 1}, \tag{4.14}$$

and a suitable transfer function that fits the experimental data is

$$G(s) = \frac{1.7}{0.7579s + 1}. \tag{4.15}$$

Kuribayashi [40], as well as Grant and Hayward [23, 26] had also observed and modelled similar first-order behaviour in their SMA actuator response. The Bode magnitude and phase plots for the model of Equation 4.15 are shown as the dashed black curves in Figure 4.12. The model can be observed to accurately match the experimental Bode plots over the entire frequency range. Similar models can be determined for other wire diameters.
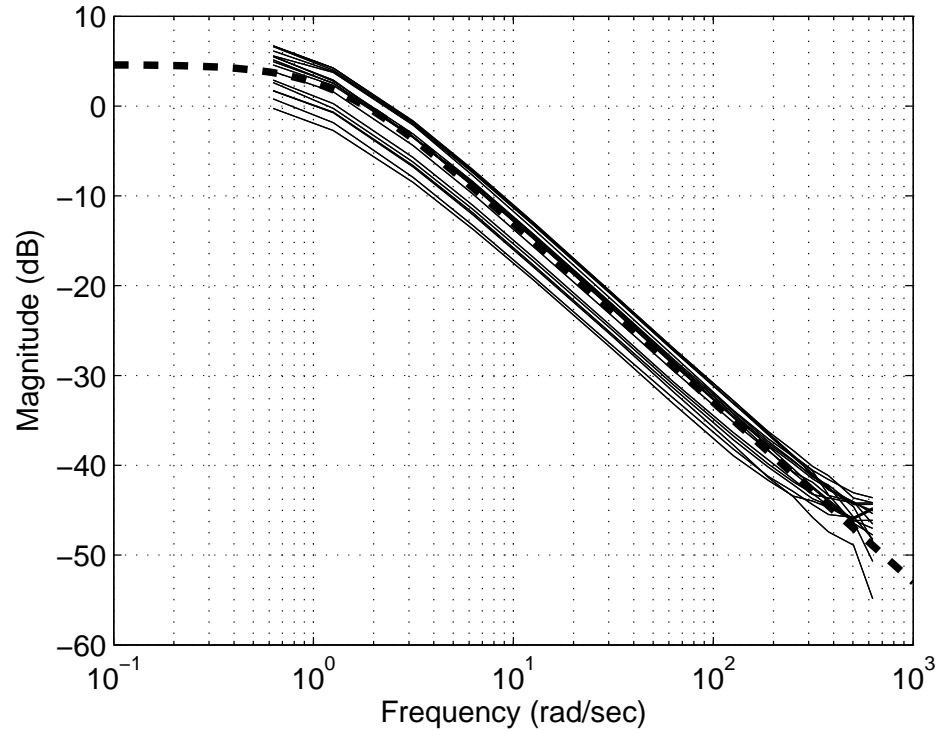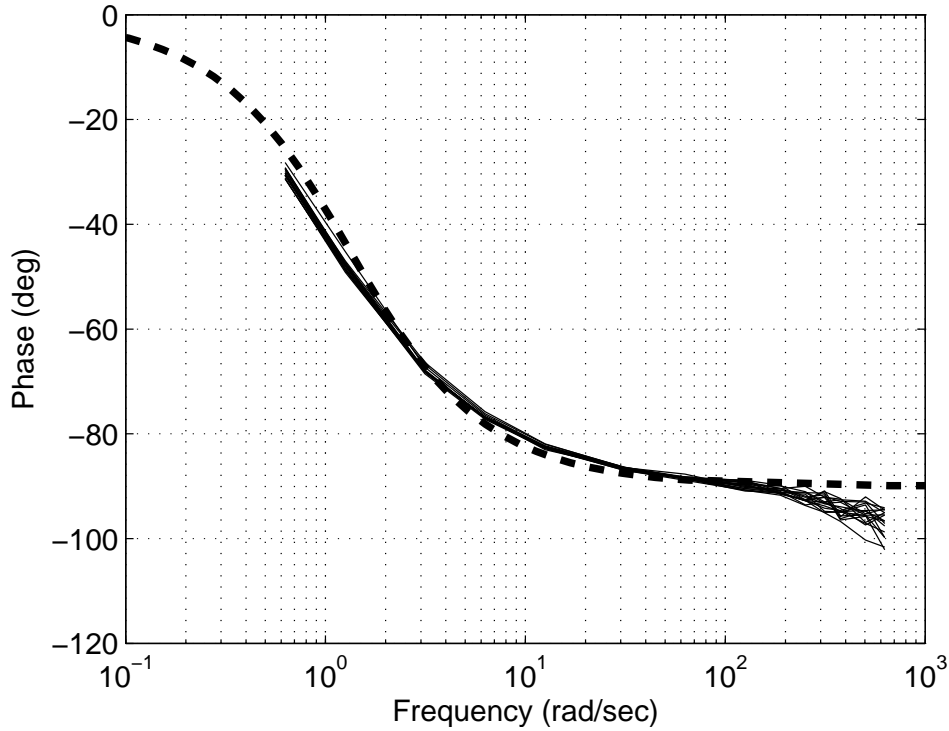
Figure 4.12: Bode magnitude and phase plots of the $100\,\mu$m-diameter Flexinol wire frequency response data and the derived power-force model, $G(s)$. Solid black lines = experimental data. Dashed black line = model.

4.3.2 Force Model for an SMA Wire

A block diagram of the open loop force model of a single SMA wire used for simulation and force control design is given in Figure 4.13. The transfer function $G(s)$, modelled as a first-order system previously, represents the *actual* force model of the SMA wire plant, because it has compensated for various effects including the load cell mechanical resonance, the analog anti-aliasing filter and the digital low-pass filter of the force signal. In order to provide a useful simulation comparable to the actual plant, the simulation model should also take into consideration these physical effects. It can be seen in Appendix B that the anti-aliasing filter and the load cell mechanical resonance have negligible effects in the frequency range at which the force controller operates ($< 100\,\text{Hz}$). Therefore, they can be omitted from the simulation model.

A digital 4th-order low-pass Butterworth filter with a cut-off frequency of $600\,\text{rad}\,\text{s}^{-1}$ (or approximately $100\,\text{Hz}$) is used in the force control experiments of later chapters to remove high-frequency noise from the load cell (rather than the 2nd-order low-pass Butterworth filter in the modelling experiments). Because it affects the magnitude and phase of the response within the controller operating frequency range, this filter is included in the simulation force model as shown in Figure 4.13.
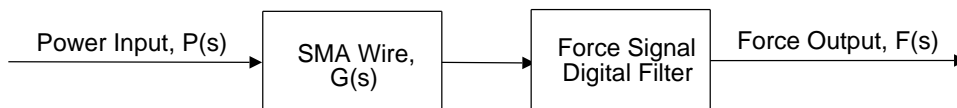
Figure 4.13: Open loop SMA force model used for simulation.

4.3.3 Force Model for an Antagonistic SMA Wire Pair

An SMA force actuator model which consists of a constrained antagonistic pair of SMA wires is proposed in this section. Figure 4.14 represents the block diagram of the open loop model for the antagonistic force system. This antagonistic pair of SMA wires is considered as an SMA force actuator, in which the actuator force output is a differential force, obtained as the difference between individual SMA wire forces.

SMA Wire 1

Power Input

SMA Wire, $G_1(s)$

Force Signal Digital Filter

$F_1(s)$

Differential Force

Power Input

SMA Wire, $G_2(s)$

Force Signal Digital Filter

$F_2(s)$
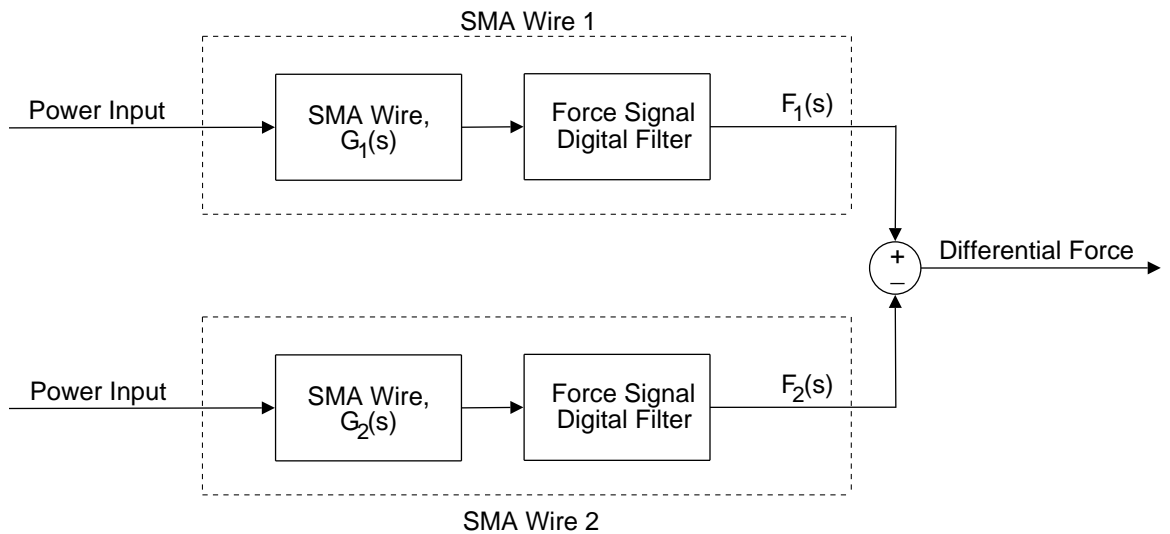
SMA Wire 2

Figure 4.14: Open loop force model for an antagonistic pair of SMA wires.

4.4 Chapter Summary

In this chapter, a new method of characterising the dynamic behaviour of SMA actuators based on small-signal frequency response analysis has been described. Over the frequency range of $0.1\,\text{Hz}$ to $100\,\text{Hz}$, detectable force responses from SMA wires are recorded and then processed to produce sets of Bode diagrams for different wire diameters of $75\,\mu\text{m}$, $100\,\mu\text{m}$ and $125\,\mu\text{m}$. The experimental results show several invariant properties of the magnitude and phase responses, which allow a dynamic force model of the SMA wire actuator to be determined. The force model takes the form of a first-order linear system, relating the heating power to the output force, and is given by the following transfer function:

$$G(s) = \frac{K}{Ts + 1}. \tag{4.16}$$

The force model is particularly useful for the design and simulation of force feedback control systems for SMA actuators. This will be fully discussed in Chapter 5. The force model has also been extended for an antagonistic pair of SMA wires, and the differential force architecture for such an SMA actuator arrangement will be described in Chapter 6.

68

CHAPTER 5

Force Control of Single SMA Wire

For practical SMA actuator applications, simple, effective and easily adapted control designs should be employed. In this case, a small-signal high-bandwidth controller in the form of a high-gain PID controller has been applied in the force feedback control of an SMA wire actuator. The control system has been successful in achieving excellent performance and stability of the SMA force response. The force model from Chapter 4 has been instrumental in the simulation and tuning of the control system.

This chapter will begin by considering possible SMA force control applications. The proposed force control system utilising PID control for a single SMA wire will then be presented in Section 5.1.2, followed by a description of the actual control system implementation in Section 5.1.3.

In Section 5.2, the control system will be applied to the force model of Chapter 4, as well as to the experimental test bed of Figure 4.1. The step response, the ramp response and the tracking response to sine-wave commands will be investigated. Simulation and experimental results will be compared, where discrepancies between the model and the actual plant will also be addressed. In Section 5.3, experimental responses of the SMA force control system in the presence of external motion disturbances will also be considered, where the results will demonstrate good external disturbance rejection.

5.1 Force Control

5.1.1 Background

SMA actuators are well adapted for flexible and miniaturised force control applications due to their high force-to-weight ratio, mechanical compactness and simplicity. These force control applications include robotic grippers and force contact applications.

Zhong and Yeong [83] experimented with SMA wire actuated robot gripper for miniature applications. They showed that cheap SMA actuators compared to other technologies such as piezoelectric actuators can produce large gripping forces reliably over millions of cycles. Other works on force control and robot gripping of SMA actuators include [10, 26, 28, 32]. Of these papers, Grant and Hayward [26] were very successful in achieving fast and accurate constrained force control with SMA actuators. However, their results showed low magnitude limit cycles at steady state, mainly due to the switching nature of the relay controller. Other research in position control of SMA under the influence of heavy external loadings, including [23, 25, 71, 77], have also resulted in significant limit cycles.

Using accurate and high-resolution load cells, the high-frequency force responses of SMA actuators have been demonstrated in Chapter 4, thereby opening the way for small-signal high-bandwidth force control. Using such a force controller, it is possible to prevent these limit cycles, and to achieve fast and accurate responses. This has potential commercial applications such as in camera anti-shake mechanisms, vibration control, and other micro-actuator applications [37, 44, 49]. Electric motors may not be suitable in these miniaturised applications due to cost, weight and space problems, and other alternative actuator technologies cannot generate sufficiently large motions or forces.

In this chapter, results that illustrate fast and accurate force control of a single SMA wire actuator will be presented. Our extended efforts to cover the differential force control and position control of an antagonistic pair of SMA wires will be presented later in Chapter 6 and Chapter 7 respectively.

5.1.2 PID Control

The force feedback control of an SMA Flexinol wire is investigated using a proportional-integral-derivative (PID) controller as shown in Figure 5.1. In past research, PID controllers were considered to be inadequate for SMA actuator
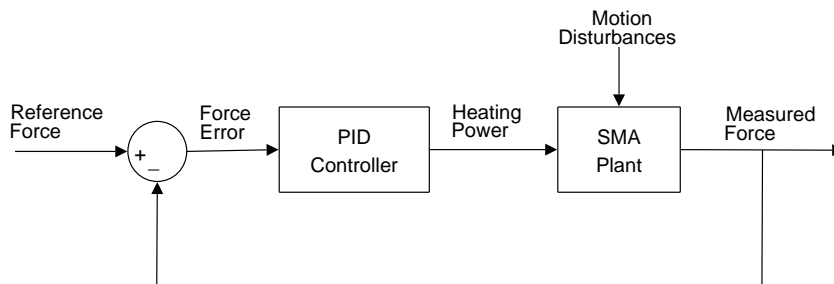
Figure 5.1: Closed loop force control system for a single SMA wire actuator.

control [1, 13, 43, 48]. SMA actuators were generally thought to be slow, so PID controllers with high gains were never investigated. This resulted in slow and inaccurate performance. In this chapter, we experiment with high-gain PID force control to achieve better performance.

PID control is the most widely adopted and well-understood class of feedback controllers in industrial and commercial applications. In fact, it is observed that such a controller is suitable for SMA force control. Our experimental results show fast and accurate tracking of force commands with no sign of limit cycles. In contrast to more complicated control algorithms, PID controllers are often simple, effective, and can be adjusted and tuned easily without advanced mathematics. This makes them suitable for practical control applications of SMA actuators. In the following section, the implementation of the force controller will be described.

5.1.3 Implementation

The force control system for a single SMA wire actuator consists of a PID controller, an integrator anti-windup scheme and a constant saturation block, as depicted in Figure 5.2. A power saturation limit, max, of $5\,\mathrm{W}$ is applied to the control system in both simulation and the experiment. [1] The lower limit of $min = 0$ prevents negative power inputs. The anti-windup scheme prevents integrator overshoot during periods of saturation.

The PID controller transfer function is given by

$$D(s) = K_P(1 + \frac{1}{T_I s} + T_D s), \tag{5.1}$$

where K_P, T_I and T_D are the proportional, integral and derivative time constants respectively.

---

[1]The recommended heating power for the length of Flexinol wire used is approximately $3\,\mathrm{W}$ (based on data sheet values in Table A.1). However, the heating power of $5\,\mathrm{W}$ is insufficient to cause thermal damage.
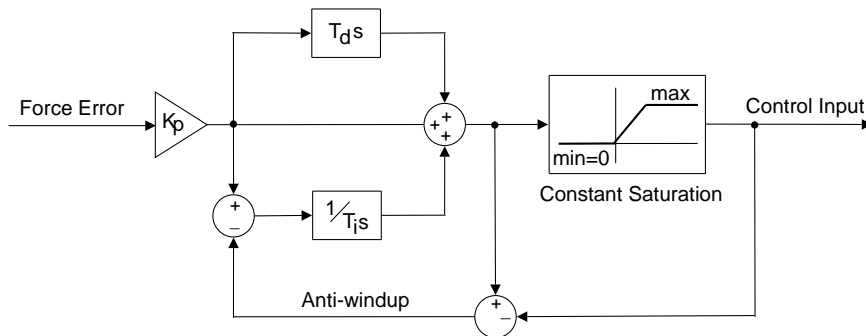
Figure 5.2: PID ontroller with integrator anti-windup scheme and constant saturation.

The internal details of the actual SMA plant is shown in Figure 4.6 of Chapter 4. The power input from the PID controller is first converted to a current signal, based on the power-current relationship, $P = I^2 R_{nom}$, where R_{nom} is a constant approximately equal to the resistance of the hot SMA wire. The DAC (Digital-to-Analog Converter) voltage is calculated from the current signal and the known gain of the transconductance amplifier which drives the SMA wire. The current signal may be used to calculate the SMA electrical resistance, as will be seen in Chapter 6 for the rapid-heating control algorithm. The measured SMA force is conditioned using an analog anti-aliasing filter and determined from the strain gauge amplifier before digital conversion via a 16-bit ADC. The signal is then filtered using a digital 4th-order low-pass Butterworth filter with a cut-off frequency of $600\,\mathrm{rad\,s^{-1}}$ to remove unwanted high-frequency noise. The length of the SMA wire is constrained (with the pulley locked), although external motion disturbances could be instigated by the motion of the test bed linear slide.

Figures 5.3(a) and 5.3(b) show the FFT plots of the load cell electrical noise (at zero load) before and after applying the digital 4th-order low-pass Butterworth filter; whereas Figures 5.3(c) and 5.3(d) show the load cell force signals (pre- and post-filtered respectively). It can be seen that the filter is mostly removing high-frequency noise spikes from the force signals.

Using the force model of Figure 4.13 from Chapter 4 in simulation, the feasibility of using PID control for SMA force control is investigated and a set of control parameters obtained. The PID controller is then implemented and fine-tuned online to obtain better results. The final parameter values are $K_P = 70$, $T_I = 0.0115$ and $T_D = 0.003$. The same PID controller parameters are used in both simulation and experiment. To illustrate the accuracy of the SMA force model, it was found that the model predicts the limit of stability based on the
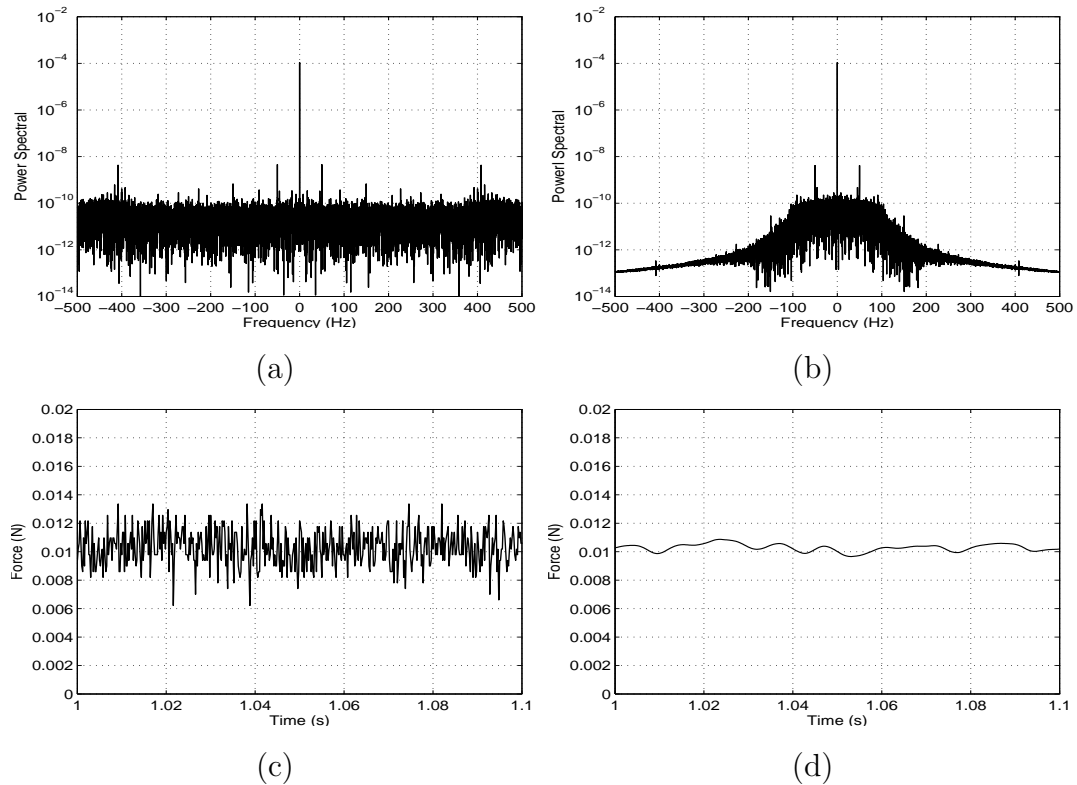
Figure 5.3: FFT plots of the electrical noise of the load cell with no load: (a) before digital filtering and (b) after digital filtering. (c) and (d) are samples of the load cell force signals before and after digital filtering respectively.

second Ziegler-Nichols tuning method (tuning by evaluation at limit of stability; see also [17]) with a limit cycle period of $0.019\,\mathrm{s}$ as K_P is increased to 150; and the value at which limit cycles occur in practice is when $K_P = 135$, with a limit cycle period of $0.023\,\mathrm{s}$. The model manages to predict the onset of limit cycles to within 10% of the actual system.

All simulations are implemented in MATLAB/Simulink, and experiments implemented using the test bed shown in Figure 4.1, with a dSPACE servo rate of $5\,\mathrm{kHz}$ and the pulley locked mechanically. To produce the smooth experimental graphs as seen in this chapter, all experimental responses have been postconditioned with a fourth-order, zero-phase, digital low-pass Butterworth filter ($\omega_c = 200\,\mathrm{rad\,s^{-1}}$) to remove the high-frequency electrical noise of the load cell. The electrical noise originally has a peak-to-peak magnitude of approximately $0.01\,\mathrm{N}$ at non-zero force setpoints. The accuracy claims that follow, such as the claim of $0.001\,\mathrm{N}$ steady-state accuracy in Section 5.2.1, are based on the postconditioned force signals. Downsampling by a factor of 8 has also been applied.

5.2   Results and Discussions

5.2.1   Step Response
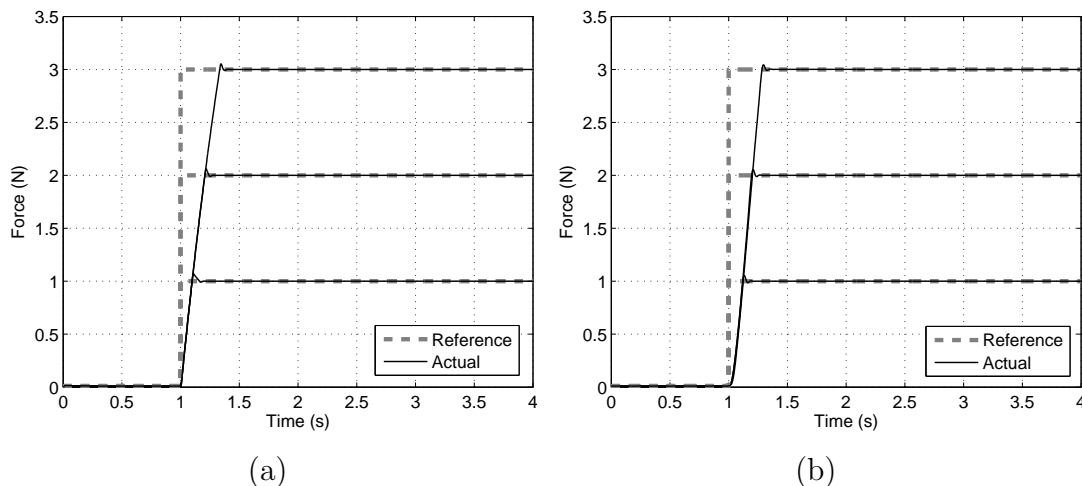
Figure 5.4: (a) Simulated, and (b) experimental force responses for 1, 2 and 3 N steps.

Both the simulated and experimental responses to a series of force step inputs from 1 N to 3 N are shown in Figure 5.4. It should be noted that 3 N is the maximum rated pulling force for a doubled-up 100μm-diameter Flexinol wire.

In Figure 5.4(a), the simulated response rise times are observed to be approximately 0.1 s, 0.2 s and 0.33 s respectively for step inputs of 1 N, 2 N and 3 N. The experimental response to a similar series of desired step inputs can be seen in Figure 5.4(b). Examining Figure 5.4(b), it is observed that the experimental force response resembles that of the simulation. The experimental response rise times are observed to be approximately 0.12 s, 0.2 s and 0.29 s respectively. Maximum overshoot is less than 5%. The simulated and experimental force tracking errors are not shown; but these errors are measured to be less than 0.001 N at steady state, and no limit cycle is observed. An error amplitude of 0.001 N is 0.033% of the 3 N force range of the actuator.

The Flexinol wires tested in the experiments are observed to develop a behaviour known as the *two-way shape memory effect* during use. These wires contract when heated, and extend upon cooling even in the absence of external stress. This causes the wires to become slack during cooling. This behaviour has been described in Chapter 2. In the force control experiments, the SMA wire in use will respond slower due to its slack configuration. Therefore in the experi-

ments, an initial desired force input of $0.01\,\mathrm{N}$ has been applied before time $= 1\,\mathrm{s}$ so that the SMA wire will not start out slack in the test bed. Since the wire is already warm, this taut configuration allows it to contract faster. As we shall see later in Chapter 6, the two-way shape memory effect becomes more problematic in the differential force control of antagonistic pair of SMA wires, which requires the implementation of an 'anti-slack mechanism' in the control system.

5.2.2   Ramp Response
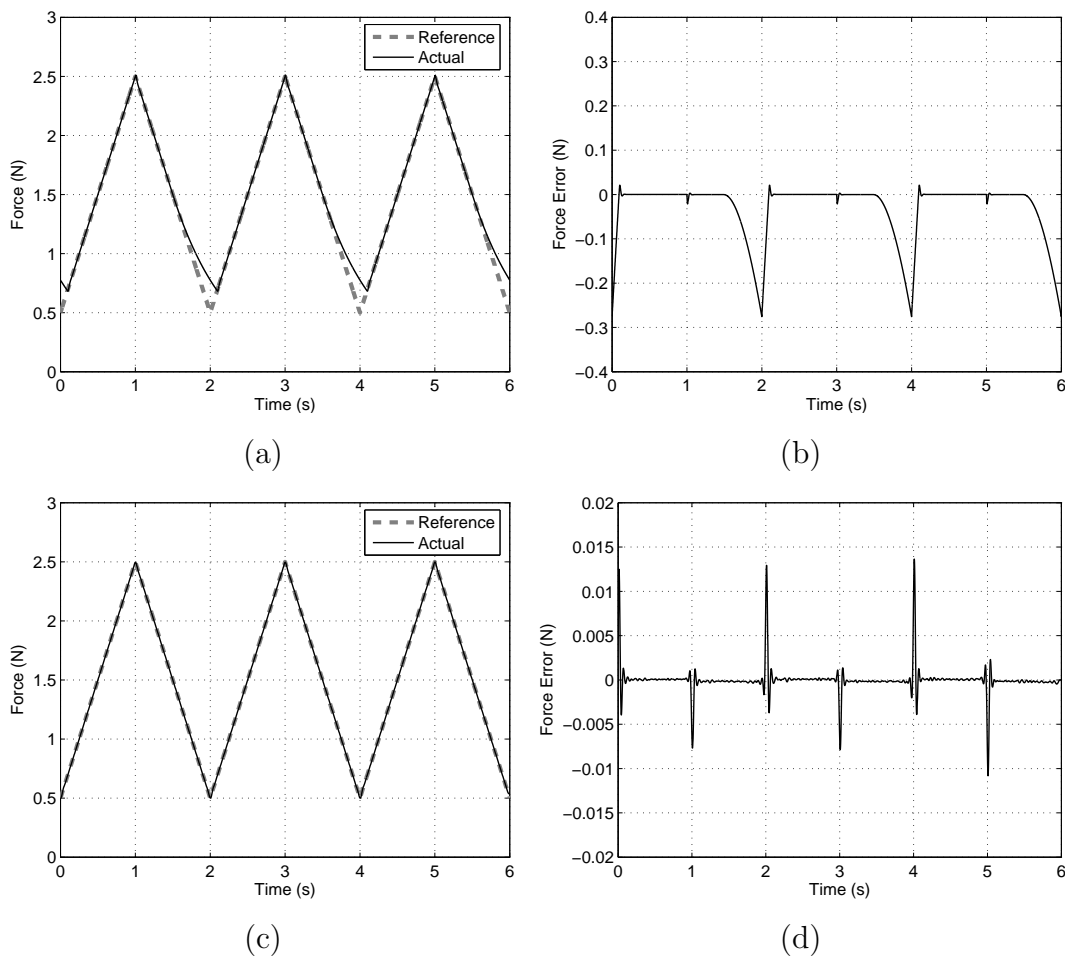
Figure 5.5: Force ramp responses with $2\,\mathrm{N}$ magnitude and ramp rates of $\pm2\,\mathrm{Ns}^{-1}$. (a) Simulated force ramp response, and (b) its corresponding force errors. (c) Experimental force ramp response, and (d) its corresponding force errors.

The force response to $2\,\mathrm{N}$ magnitude ramp commands are simulated and examined experimentally in Figure 5.5. The ramps have slopes of $\pm2\,\mathrm{Ns}^{-1}$.

It is clear that the simulated response of Figure 5.5(a) manages to track the upward ramp accurately, but it fails to follow the downward ramp, especially at

75

the minimum force values. This is because the force model is a poor predictor of the SMA large-signal behaviour. The simulated response of Figure 5.5(a) clearly shows that it underestimates the SMA cooling rate. However, the experimental results of Figure 5.5(c) achieves accurate tracking of the large ramps with error amplitudes of less than 0.001 N generally in Figure 5.5(d). The changes in slopes produce the narrow error spikes in Figure 5.5(d). It is also observed, however, that the control system can rapidly correct the errors.

(a)   (b)
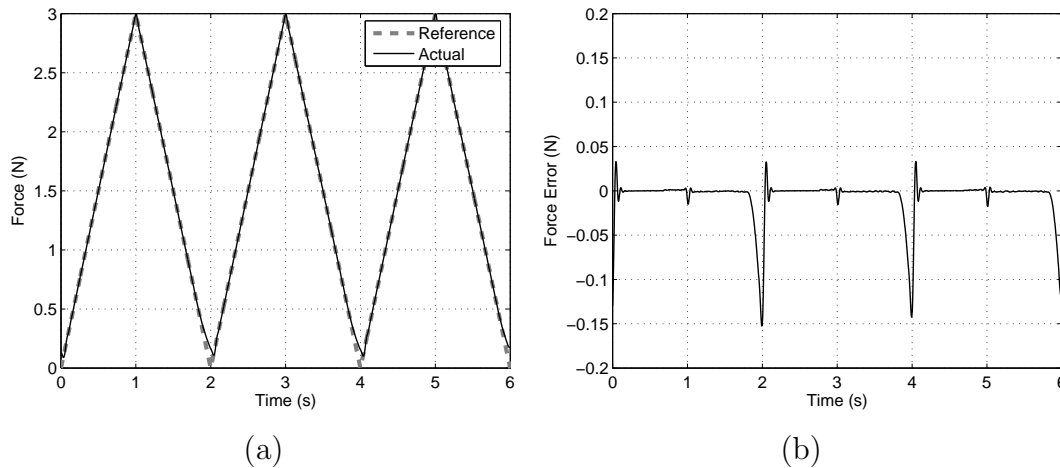
Figure 5.6: Force ramp responses with $3\,\mathrm{N}$ magnitude and ramp rates of $\pm\,3\,\mathrm{Ns}^{-1}$. (a) Experimental force ramp response, and (b) its corresponding force errors.

Figure 5.6 depicts the experimental force response to a series of $3\,\mathrm{N}$ ramps with larger force rates of $\pm3\,\mathrm{Ns}^{-1}$. The controller manages to track the command accurately most of the time except at values close to $0\,\mathrm{N}$. This is due to the slow cooling rate of the SMA wire.

5.2.3   Sine Response

Using the same controller parameters, the simulated and experimental closed loop tracking responses are examined. Responses to sinusoidal force commands at two different frequencies, $f \in \{1,2\}\,\mathrm{Hz}$, have been investigated. They are of the form $c + 0.2\sin\left(2\pi f t\right)\mathrm{N}$ with $c \in \{1,2\}$ for $f = 1\,\mathrm{Hz}$, and $c + 0.1\sin\left(2\pi f t\right)\mathrm{N}$ with $c \in \{1,2\}$ for $f = 2\,\mathrm{Hz}$. Figures 5.7(a) and 5.7(b) depict the sinusoidal force commands.

Figures 5.7(c) and 5.7(e) show the force tracking errors in response to force commands of the form $c + 0.2\sin\left(2\pi f t\right)\mathrm{N}$, with $c \in \{1,2\}$ respectively and $f = 1\,\mathrm{Hz}$. Both simulated and experimental results are presented. Despite the different force command DC offsets, the results in Figures 5.7(c) and 5.7(e) are
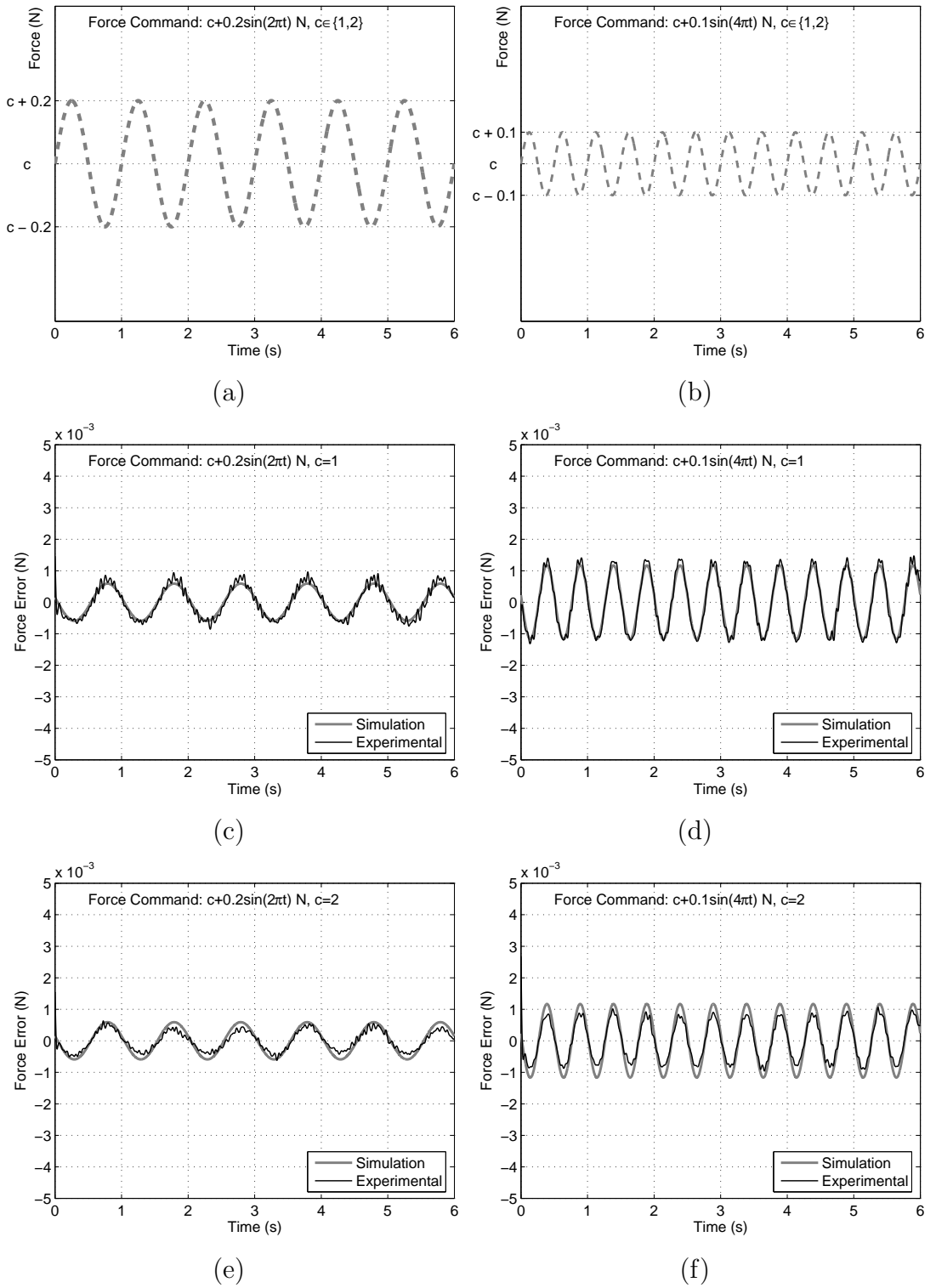
Figure 5.7: (a) Force command $c + 0.2\sin(2\pi f t)\,\mathrm{N}$, its corresponding tracking errors in (c) and (e), with $c \in \{1, 2\}$ and $f = 1\,\mathrm{Hz}$. (b) Force command $c + 0.1\sin(2\pi f t)\,\mathrm{N}$, its corresponding tracking errors in (d) and (f), with $c \in \{1, 2\}$ and $f = 2\,\mathrm{Hz}$.

similar. Both simulation and experimental results show a tracking error of less than 0.001 N, and the two curves are in phase. A tracking error of 0.001 N is 0.033% of the 3 N force output range of the actuator.

Figures 5.7(d) and 5.7(f) show the tracking errors in response to force commands of the form $c + 0.1 \sin(2\pi f t)$ N, with $c \in \{1, 2\}$ respectively and $f = 2$ Hz. Once again, the curves in Figures 5.7(d) and 5.7(f) are very similar, indicating that the DC offset makes little difference. The model predicts a peak tracking error of about 0.0012 N, and the experimental results show similar tracking errors in Figure 5.7(d), but a smaller error of 0.001 N in Figure 5.7(f). However, both simulated and experimental curves are again in phase.

5.3   Motion Disturbance Rejection

To investigate how the control system performs under the influence of motion disturbances, the SMA wire is subjected to strain changes by vertically servoing the linear slide to follow two types of motion commands: a sudden 1 mm-magnitude impulse signal, and a slow, continuous 4 mm-magnitude sinusoidal command at 0.25 Hz. The 4 mm disturbance constitutes 25% of the SMA strain range under normal conditions. Since the 80 cm long SMA wire is doubled up, its effective strain range is 1.6 cm.

First, the force tracking results of a $1 + 0.2 \sin(2\pi f t)$ N signal at $f = 1$ Hz, under the 1 mm impulse motion disturbance, is shown in Figure 5.8. The impulse disturbances affect the tracking performance significantly, because of the sudden stretching and relaxing of the SMA wire due to the linear slide movement. However, it can be seen that the control system can rapidly correct the errors. Peak tracking errors (after the controller has settled) are usually less than 0.001 N, similar to the experimental curves in Figures 5.7(c) and 5.7(e).

Force tracking performance of a $1 + 0.2 \sin(2\pi f t)$ N signal at $f = 1$ Hz, under the 4 mm sinusoidal disturbance throughout the experiment, is next presented in Figure 5.9. The strain disturbance clearly degrades the response compared to Figure 5.7(c). The force error graph in Figure 5.9(b) shows very small errors due to the 1 Hz force command, as well as larger, high-frequency error spikes. The force error spikes are caused by position error spikes in the linear slide motion control system, shown in Figure 5.9(d). These spikes have been observed to occur at every 30° rotation of the servo motor, and are caused by a mechanical effect in the linear slide. Further discussions of the linear slide error spikes can be found
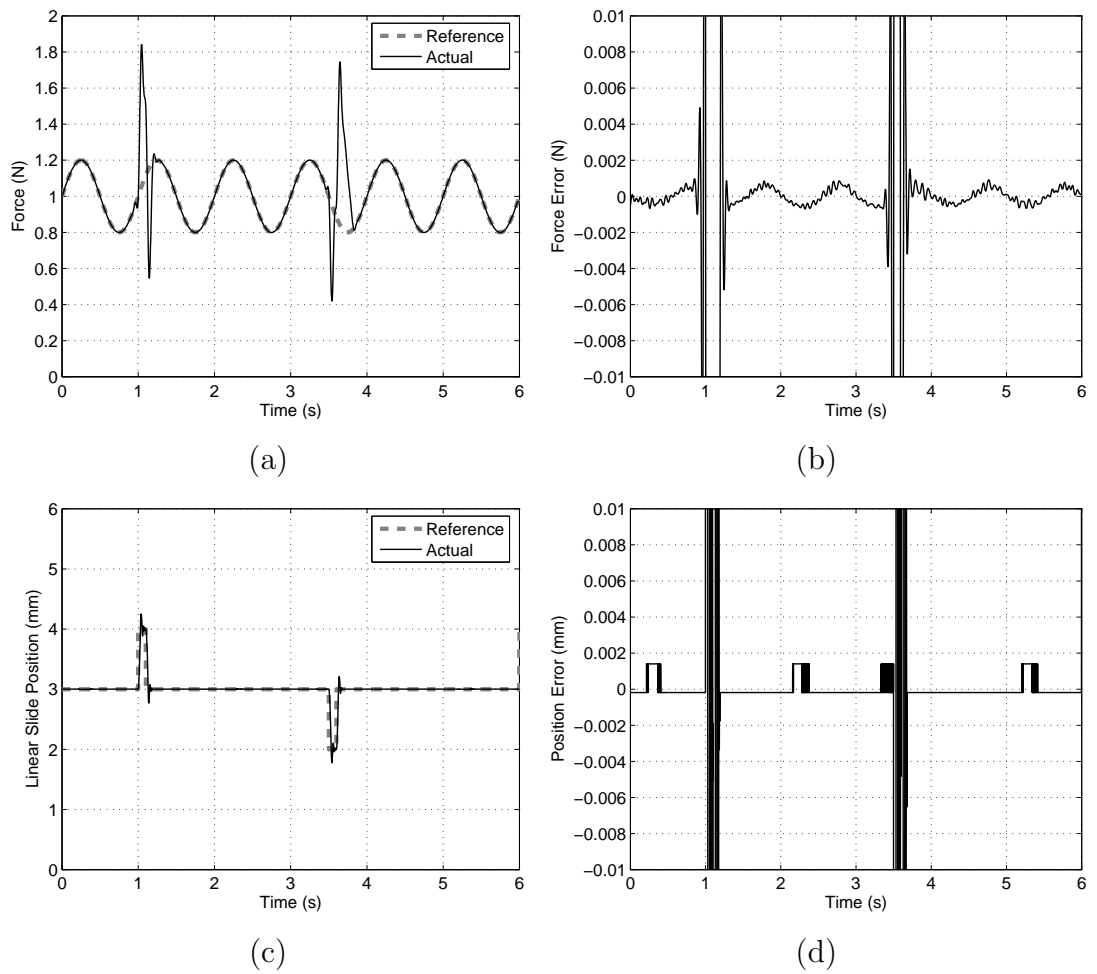
Figure 5.8: Experimental force tracking response under 1 mm magnitude impulse motion disturbances. (a) Force tracking of 1 Hz command, (b) its corresponding force errors, (c) linear slide position simulating impulse motion disturbances, and (d) linear slide position errors.

in Appendix B. The force controller cannot completely eliminate the effects of the sharp position spikes due to their high-frequency nature.

Although the performance of the closed loop response has been affected, its accuracy is fairly good. The response is stable and is able to reject the 0.25 Hz motion disturbances throughout the experiment. The force tracking error of Figure 5.9(b) has a maximum amplitude of 0.002 N or less, except for a few of the biggest spikes.
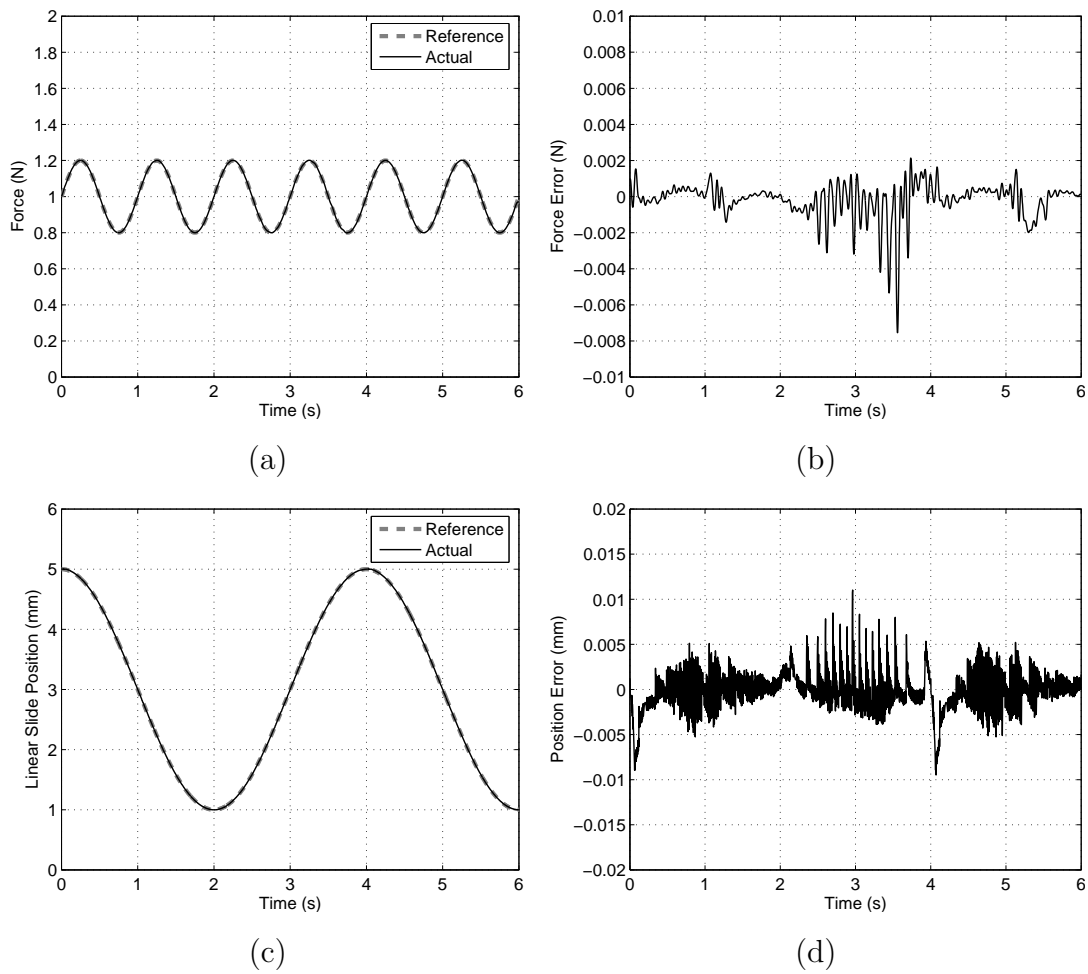
Figure 5.9: Experimental force tracking response under a 4 mm magnitude sinusoidal motion disturbance of 0.25 Hz. (a) Force tracking of 1 Hz command, (b) its corresponding force errors, (c) linear slide position simulating sinusoidal motion disturbance, and (d) linear slide position errors.

5.4   Chapter Summary

Force control for a single SMA wire actuator using high-gain PID control was presented in this chapter. The small-signal SMA force model, which was described in Chapter 4, has been used to aid the design of the PID controller and also used to simulate SMA closed loop responses. The PID controller is then fine-tuned online and force control experiments are carried out on actual SMA wires.

The simulation results show that the model accurately predicts the stability and small-signal tracking accuracy of the SMA wire's closed-loop response under PID control; but it underestimates the large-signal cooling rates of the wire. Nevertheless, running simulations with the model is a necessary step as it allows the testing of control system designs prior to online implementation which may adversely affect or damage the actual system. The usefulness of the model in simulation will be more apparent when the design of high-performance controllers becomes more complicated and effort-consuming, due to our aim of controlling an antagonistic pair of SMA wires rather than only one, and due to the incorporation of control algorithms such as the anti-slack, rapid-heating and anti-overload mechanisms. These will be discussed in later chapters.

The experimental results indicate that the SMA wire actuators are able to control force both rapidly and accurately using PID control. The system is shown to be capable of rapidly changing the setpoint over the $3\,\mathrm{N}$ force range of the SMA wire. It achieves excellent setpoint accuracy with no limit cycles, with an error amplitude of less than $0.001\,\mathrm{N}$, or 0.033% of the $3\,\mathrm{N}$ range. Reasonably fast response has also been demonstrated with good tracking of a $2\,\mathrm{Hz}$ sine-wave force command. The experimental error amplitudes are observed to be $0.0012\,\mathrm{N}$, which is only 0.04% of the $3\,\mathrm{N}$ force range. Finally, the results also demonstrate accurate tracking of force commands in the presence of large motion disturbances.

In the next chapter, the SMA force model will be used for simulation and control design in the differential force control of an antagonistic pair of SMA wires. Experimental results will also show fast and accurate response of the system using the differential force control architecture.

CHAPTER 6

Differential Force Control of Antagonistic SMA Wires

Building on the work from the previous chapter, differential force control of an SMA actuator, which consists of an antagonistic pair of Flexinol wires, will be investigated. This chapter will begin by considering some control design challenges when dealing with an antagonistic SMA wire pair instead of a single SMA wire. In Section 6.2, the complete force control architecture will be described. It employs a differential controller based on PID control to track the differential force output from the SMA actuator, which will be discussed in Section 6.2.2. The soft-saturation algorithm, which aims to provide smooth transitions between wire switchings, will also be presented in Section 6.2.3.

To further improve the performance of the actuator, various additional control algorithms are incorporated in the force control architecture. Section 6.3.1 describes the anti-slack mechanism which sets a lower force threshold on the SMA wires to keep them warm and taut for better response. In Section 6.3.2, a rapid-heating mechanism is employed on both wires to allow faster heating without the risk of overheating. Its principle of operation and algorithm will be described. Next, Section 6.3.3 presents the anti-overload mechanism, which limits the upper forces on the SMA wires to prevent overstressing. For all of the above, simulation results are first presented for verification, followed by experimental results, which demonstrate improved performances with each addition of the control algorithms. A set of experimental results which demonstrates the overall excellent performance of the differential force control architecture will also be given in Section 6.4.

Finally, Section 6.5 presents the motion disturbance and load inertia rejection of the complete force controller. The experimental results are also discussed in detail. They show that the controller is very robust against external influences, and this may be useful in eliminating large position limit cycles when applied to

a position controller under the influence of large load inertias.

It should also be stated here that the *SMA actuator* in this chapter refers to an antagonistic pair of SMA wires, not to be confused with the single SMA wire arrangement of the previous chapter.

6.1 Control Challenges

Although the high-gain PID controller is straight forward to design and tune for the force control of a single SMA wire, the desired antagonistic arrangement of two SMA wires will raise some control design concerns. For one, the design of a suitable controller for such an SMA actuator will become more complicated. This is because we will be looking at the differential force, which is the difference between the two forces of the SMA wires. Instead of controlling one SMA wire, measurements of forces from two SMAs are now necessary and there will be more actuator and sensor data in such a system.

To successfully control the antagonistic SMA actuator for rapid and accurate response in real-time applications, a simple computational feedback scheme is required. A simple feedback control is also necessary to enable practical and feasible SMA actuator applications. For this to be possible, high-gain PID control has been employed in the differential force controller. As discussed in Chapter 5, PID control has a number of advantages including simplicity and ease of implementation, both computationally and physically. It has also been observed to produce very accurate force response from SMAs.

However, when we consider the antagonistic arrangement of practical SMA actuators, several control challenges emerge that require addressing. First, we need to consider achieving faster response without the fear of overheating. There are two ways to achieve this — faster heating and cooling. A rapid heating algorithm has been employed and the details are discussed in Section 6.3.2. A second challenge is the possibility of overstressing the SMA actuator and damaging the shape memory effect. It is necessary to ensure that a maximum safe force threshold is upheld at all times. This can be accomplished using an anti-overload mechanism. Another important issue is the effect of the two-way shape memory effect on the SMA wires, which causes slack and may lead to slower response and wire entanglement. This will be addressed as well in this chapter.

These control challenges require the incorporation of various control algorithms to enhance the performance of SMA actuators. They pose a very compli-

cated practical control problem to be solved. This makes modelling and simulations especially important as these controllers can be tested off-line before actual implementation on the SMA test bed in order to save time, effort and unnecessary damages to the SMAs.

6.2 Differential Force Control Architecture

6.2.1 Control Architecture
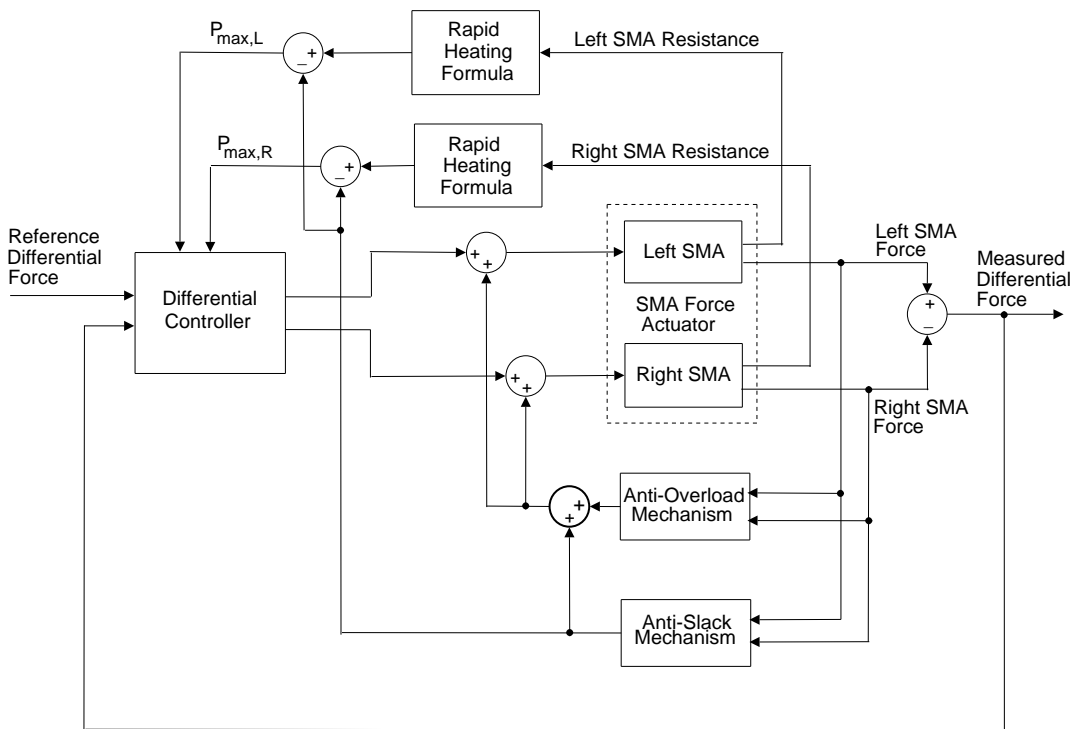
Figure 6.1: Overview of the force control system for an SMA actuator composed of an antagonistic pair of SMA wires.

Figure 6.1 shows the architecture of the force control system to produce fast, accurate responses from the SMA actuator. The main features of this control architecture can be summarised in the following:

i. The actuator's output is the difference between the two individual SMA forces, i.e. the differential force. This differential force is arbitrarily determined as the left SMA force minus the right SMA force. The control system has therefore been organized into two channels: the differential channel and the common channel.

ii. The differential channel is maintained by the differential controller, which is responsible for making the actuator's differential force output track the command input. PID control is used in the differential controller to determine the required heating power to the SMA actuator. This power input is a differential signal. If the power input is positive, it is sent to the left SMA wire; otherwise it is sent to the right SMA wire. Generally, the accuracy of the overall system depends on the performance of this controller.

iii. The common channel is maintained by the anti-slack mechanism and the anti-overload mechanism. The former applies heating power to keep the wires taut and warm; whereas the latter reduces heating power to prevent overstressing.

iv. Finally, the entire control system operates within heating power limits that are calculated separately for each SMA wire, based on its electrical resistance. For each wire, a rapid-heating formula determines the maximum safe heating power based on the measured resistance; and these limits are fed back into the differential controller. This rapid-heating mechanism increases the actuator's maximum speed without the problem of overheating.

These components are described individually in the sections that follow. It should be noted that the differential force output of the actuator is arbitrarily defined as the left SMA wire force minus the right SMA wire force.

The two blocks in Figure 6.1 labelled 'Left SMA' and 'Right SMA' represent the actuator plant, and the internal details of one of these blocks is shown in Figure 6.2. It is very similar to the SMA plant described in Chapter 4, with the addition of the SMA electrical resistance measurement. This resistance value is estimated by combining a measurement of the voltage across the SMA wire with the current signal. It is used for the rapid-heating calculations.

Similar to the results of Chapter 5, all experimental force data have been processed offline with a 4th-order, zero-phase, low-pass Butterworth filter ($\omega_c = 200\,\mathrm{rad\,s^{-1}}$), and downsampled by a factor of 8. The original noise level of the
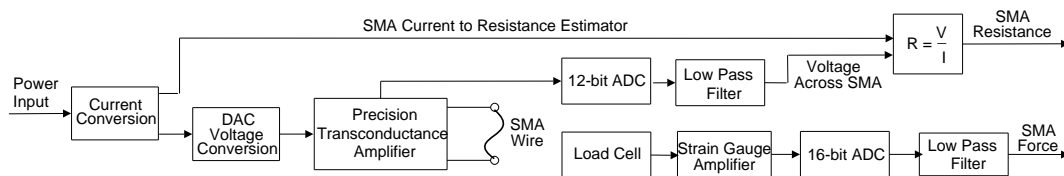
Figure 6.2: SMA Plant.

load cells was $\pm 0.005\,\mathrm{N}$. All accuracy measurements presented in this chapter are based on the post-conditioned force results.

As will be reported in later sections, the differential force control system has a setpoint accuracy of better than $1\,\mathrm{mN}$, which is one part in 6000 (0.017%) of the $6\,\mathrm{N}$ safe differential force range of the actuator (from $-3\,\mathrm{N}$ to $+3\,\mathrm{N}$). Tracking errors are also small, as can be seen from the graphs in this chapter, and there are no limit cycles. The best comparable results in the literature can be found in Grant's and Hayward's work [23, 26], which implemented variable structure control. Their results showed setpoint error amplitudes of $40\,\mathrm{mN}$ from the $14\,\mathrm{N}$ force range (from $-7\,\mathrm{N}$ to $+7\,\mathrm{N}$) available from their SMA actuators. This translates to a setpoint accuracy of 0.29%, which is more than an order of magnitude worse than our accuracy measure.

6.2.2 Differential Controller

Figure 6.3 depicts the block diagram of the differential controller. As can be seen, it consists of a PID controller, a dynamic saturation block, [1] and an anti-windup circuit for the integrator.

The PID controller transfer function is given by

$$D(s) = K_P(1 + \frac{1}{T_I s} + T_D s), \tag{6.1}$$

where K_P, T_I and T_D are the proportional, integral and derivative time constants respectively. The PID parameter values are $K_P = 70$, $T_I = 0.0115$ and $T_D = 0.003$. The choice of a PID controller and the parameter values draws on our work in Chapter 5, which are the results of an on-line tuning process that started with the parameter values suggested by the simulator.

The dynamic saturation block prevents the output from exceeding the power levels determined by the rapid-heating formulae, and it allows the power levels, $P_{max,L}$ and $P_{max,R}$, to be set independently for the two SMA wires. $P_{max,L}$ and $P_{max,R}$ are the maximum power limits determined by the rapid-heating mechanism for the left and right SMA wires respectively. It should be noted that the dynamic saturation levels also take into account the power signal from the anti-slack mechanism when incorporated in the control architecture. The anti-windup circuit works correctly with the time-varying saturation levels to reduce integrator overshoot and the control effort in the feedback system.

---

[1]The saturation levels are allowed to vary with time, and are determined by the 'min' and 'max' inputs. Note that $min = -P_{max,R}$ and $max = P_{max,L}$.

The output signal, P_{diff}, is a signed power signal. If P_{diff} is positive then it is sent to the left SMA, otherwise $-P_{diff}$ is sent to the right SMA.
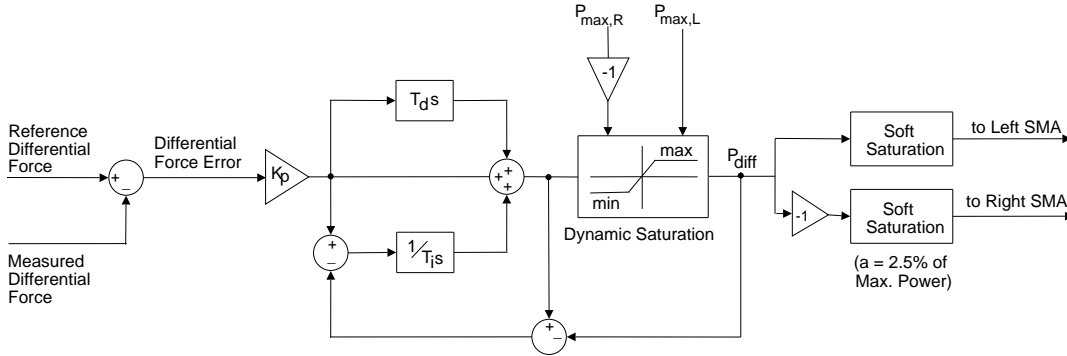
Figure 6.3: Differential PID controller with integrator anti-windup scheme and dynamic saturation.

6.2.3 Soft Saturation
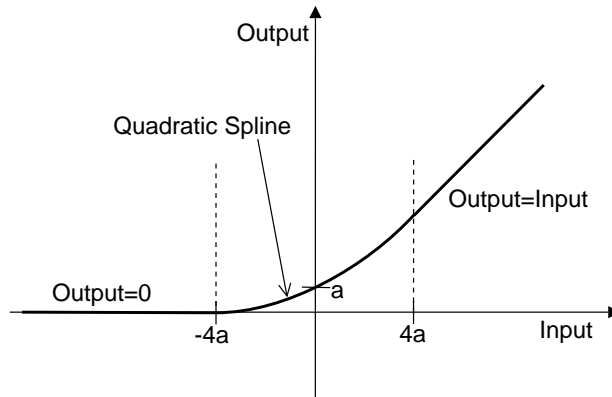
Figure 6.4: Soft saturation curve: a quadratic spline ensures continuity of slope.

To avoid discontinuity in slope at $P_{diff} = 0$, soft-saturation blocks have been implemented in the differential controller as shown in Figure 6.3. They have the following equation to calculate the power to each wire based on a quadratic spline:

$$P_{out} = \begin{cases} 0 & \text{if } P_{in} \leq -4a; \\ \dfrac{1}{16a}(P_{in} + 4a)^2 & \text{if } -4a < P_{in} \leq 4a; \\ P_{in} & P_{in} > 4a. \end{cases} \qquad (6.2)$$

where P_{out} and P_{in} are the output and input powers of the block respectively, and a is an empirical constant. The algorithm provides smooth transitions in the $-4a$

to $+4a$ boundary layer to prevent force spikes during wire heating activations. The soft-saturation transfer function is graphically depicted in Figure 6.4.

6.2.4 Initial Results

(a)

(b)

(c)

(d)
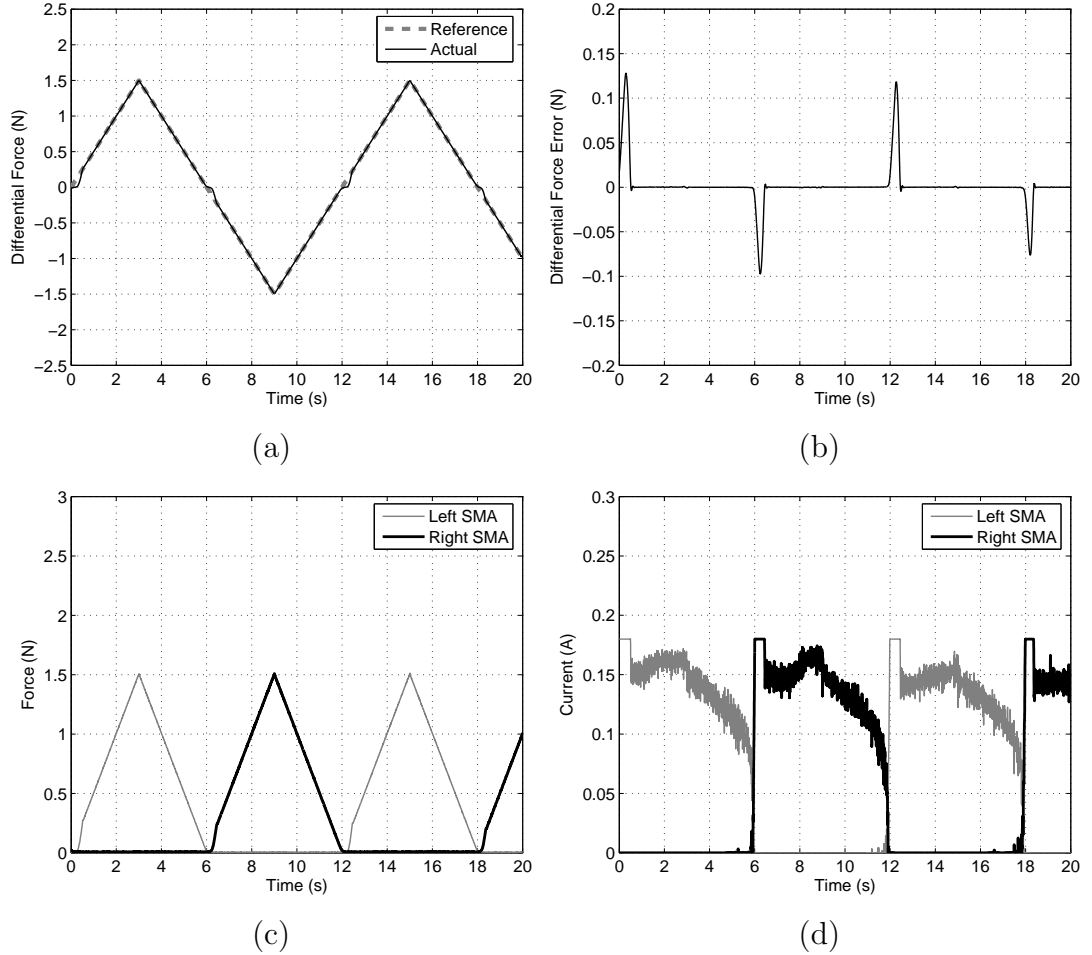
Figure 6.5: Experimental differential force response for $\pm1.5\,\mathrm{N}$ ramps with only the differential controller. (a) Differential force ramp response, (b) its corresponding force errors, (c) individual SMA forces, and (d) individual SMA heating currents.

This section describes some initial experimental results based on the differential controller. Figure 6.5 presents the experimental response to $\pm1.5\,\mathrm{N}$ ramps with only the differential controller of Figure 6.3. The power levels of the dynamic saturation block ($P_{max,L}$ and $P_{max,R}$) are initially set to datasheet recommended levels (corresponding to $0.18\,\mathrm{A}$ current). As can be seen in Figure 6.5(d), at any instant, only one wire is being heated, while zero power is sent to the other wire (the passive wire). Recall that the Flexinol wires used in the experiments have
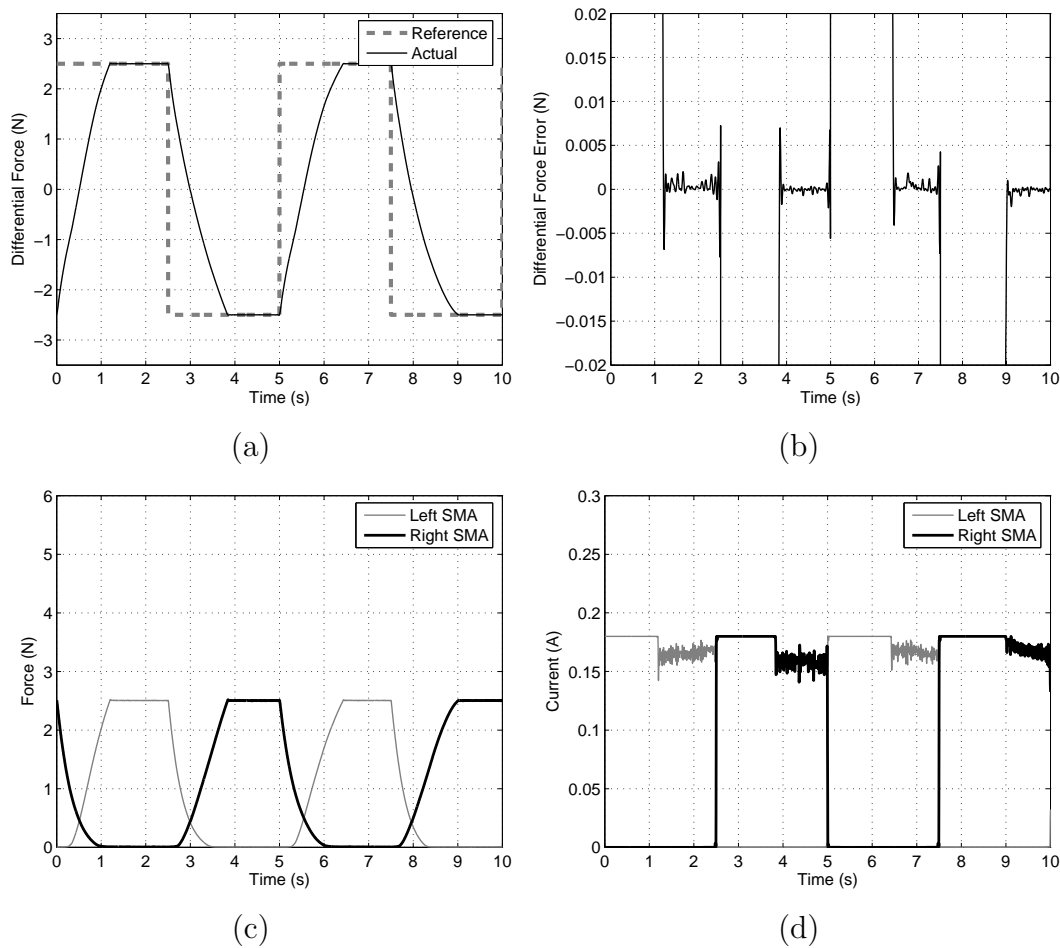
Figure 6.6: Experimental differential force response for steps of $\pm 2.5\,\mathrm{N}$ with only the differential controller. (a) Differential force ramp response, (b) its corresponding force errors, (c) individual SMA forces, and (d) individual SMA heating currents.

been observed to develop the two-way shape memory effect during use. The passive wire becomes slack as it cools, and will therefore not begin to pull in response to heating current until it has contracted enough to become taut. This delay causes substantial tracking errors, which can be seen as kinks in Figure 6.5(a) and large spikes in Figure 6.5(b).

Figure 6.6 shows the experimental step response based on the differential controller. It can be seen from Figure 6.6(a) that the rise time for the step command is more than 1 s, as the slack configuration of the wires causes slower actuator response speed. This delay can be reduced using the anti-slack mechanism described in the next section.

6.3 Improvements in Control System

6.3.1 Anti-Slack Mechanism

When the two-way shape memory behaviour becomes entrained, the wires actively lengthen when cooled, even if the tension on them is zero. The end result is that the passive wire (the one that is not being heated) can develop a few millimetres of slack as it cools. This is a drawback for the control system — if a wire has gone slack then it cannot begin to pull until it has contracted enough to remove the slack. Slack in the wires can also lead to mechanical problems inside the actuator, such as entanglement, and possibly electrical short-circuits.
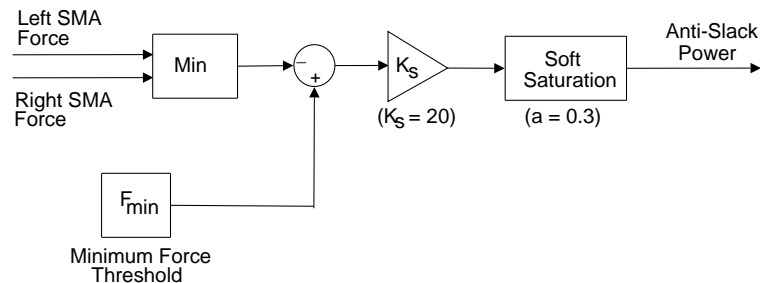
Figure 6.7: Anti-slack mechanism

To prevent the wires from becoming slack, the control architecture employs the anti-slack mechanism shown in Figure 6.7. It consists of a simple proportional feedback algorithm that uses the force outputs of the individual SMA wires, compares the minimum of the two forces to a minimum force threshold, F_{min}, and appropriately determines an anti-slack power signal to make sure the lesser of the two SMA wire forces does not drop significantly below F_{min}. The soft-saturation block, similar to the ones shown in Figure 6.3, allows for a smoother transition during the activation of the anti-slack mode. The anti-slack power is a common-mode signal as it is delivered to both SMA wires.

By keeping both wires warm, the anti-slack mechanism effectively raises the temperature of the wires, which increases the speed of response. The anti-slack mechanism is an improvement compared to a previous open loop method of keeping the wires taut by means of a small positive bias power sent to each wire [71]. Figure C.5 of Appendix C shows that the actual control system used in the experiments incorporates the anti-slack power in the dynamic saturation loop of the differential controller.

To test the effectiveness of the anti-slack mechanism, it is first implemented in
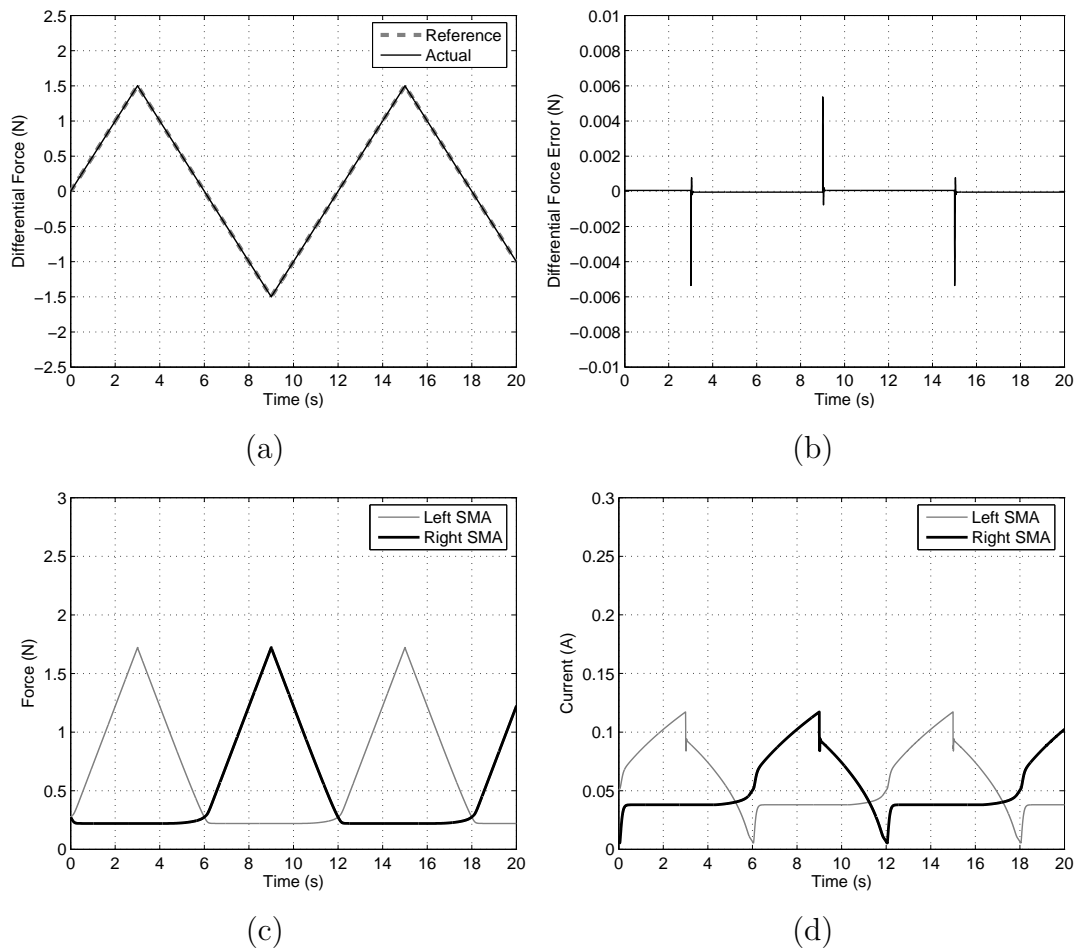
Figure 6.8: Simulated differential force response for $\pm 1.5\,\text{N}$ ramps with anti-slack mechanism implemented. (a) Differential force ramp response, (b) its corresponding force errors, (c) individual SMA forces, and (d) individual SMA heating currents.

simulation. Figure 6.8 presents the simulated response to ramps with a $3\,\text{N}$ peak-to-peak magnitude with F_{min} set to $0.2\,\text{N}$, proportional gain K_s at 20 and soft-saturation parameter a at 0.3. The simulation is able to demonstrate the proper functioning of the anti-slack mechanism, with the $0.2\,\text{N}$ lower force threshold maintained by the passive wire as shown in Figure 6.8(c). To keep the passive wire *warm*, a current of approximately $0.04\,\text{A}$ is needed as shown in Figure 6.8(d). This method can eliminate the force error spikes caused by slack in the wires as observed in Figure 6.5. It also predicts very accurate force tracking, except for small force errors of $0.006\,\text{N}$ at the change of slopes.

Following this, the mechanism is experimentally tested on the SMA actuator. Figure 6.9 illustrates the improvements in experimental response to similar ramps with the anti-slack mechanism implemented. Recall that the anti-slack force
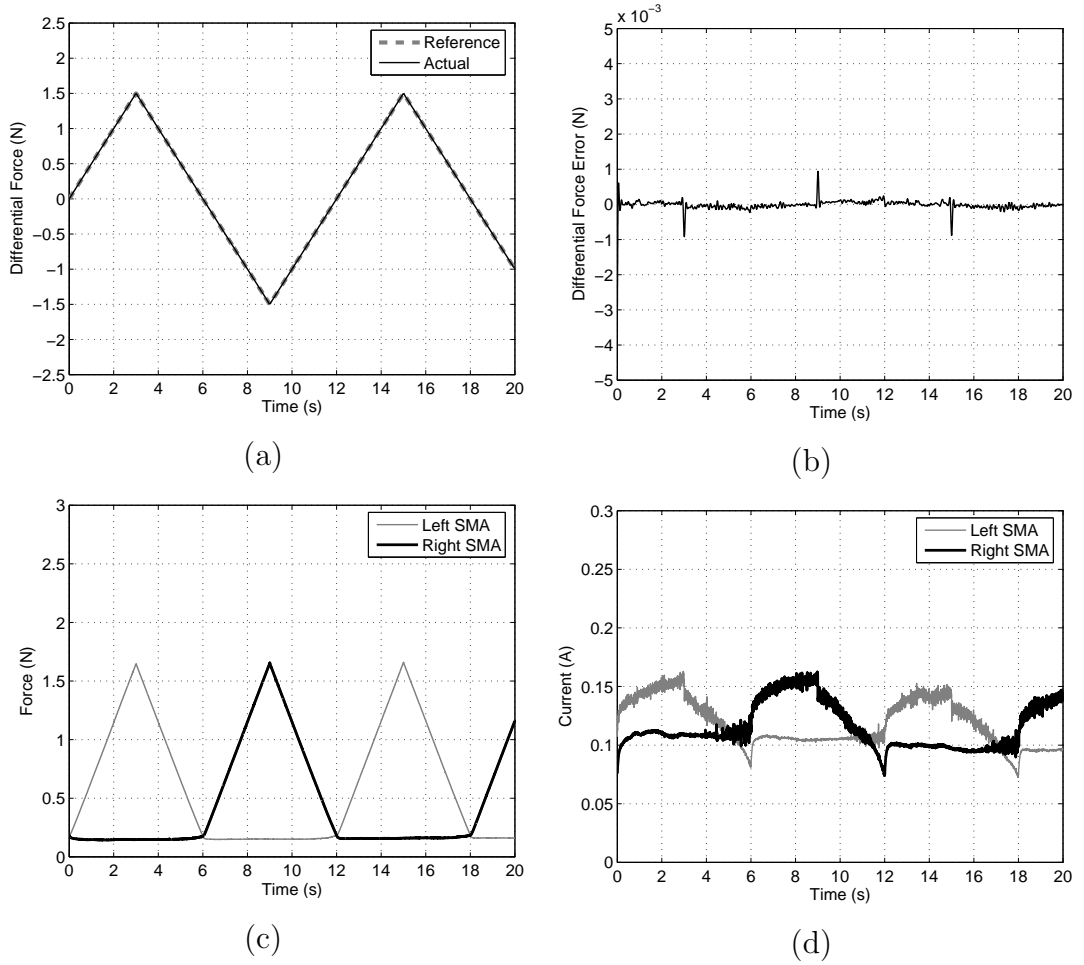
Figure 6.9: Experimental differential force response for $\pm 1.5\,\mathrm{N}$ ramps with anti-slack mechanism implemented. (a) Differential force ramp response, (b) its corresponding force errors, (c) individual SMA forces, and (d) individual SMA heating currents.

threshold is set at $0.2\,\mathrm{N}$. Compared to the experimental results of Figure 6.5, there are no large inaccuracies due to the passive wire becoming slack. High tracking accuracy with an error amplitude of less than $0.001\,\mathrm{N}$ is achieved, which is 0.017% of the $6\,\mathrm{N}$ safe differential force range of the SMA actuator. The error spikes of $0.001\,\mathrm{N}$ are caused by the change in slopes. The anti-slack mechanism has demonstrated its effectiveness experimentally. The mechanism kicks in when the force on the cooling wire falls below $0.2\,\mathrm{N}$. Instead of heating only one wire at any instant, as in Figure 6.5(d), a current of approximately $0.1\,\mathrm{A}$ is required to keep the wires warm and taut as can be seen in Figure 6.9(d). It is observed that the simulation of Figure 6.8 predicts smaller heating current levels to track the differential force command, as well as to keep the passive wire taut. This suggests that the model underestimates the cooling rate of the actual plant.
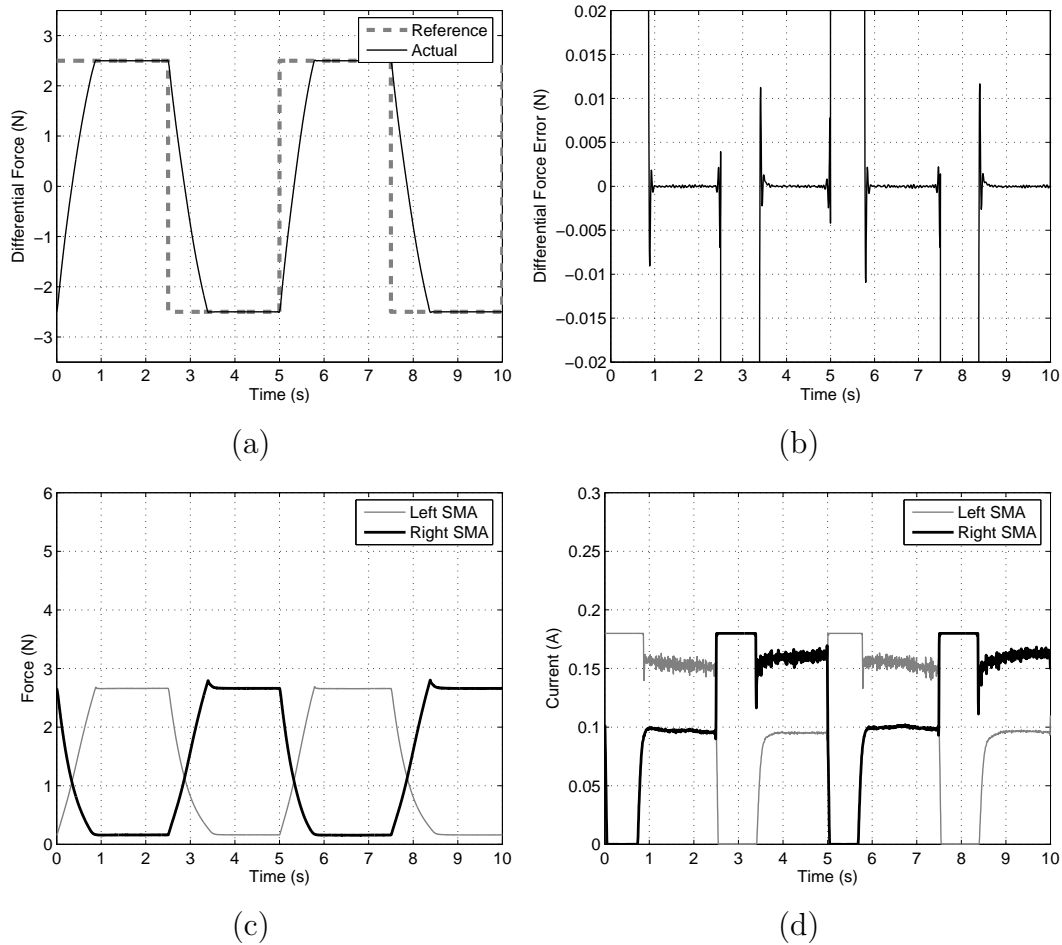
Figure 6.10: Experimental differential force response for steps of $\pm 2.5\,$N with anti-slack mechanism implemented. (a) Differential force ramp response, (b) its corresponding force errors, (c) individual SMA forces, and (d) individual SMA heating currents.

Figure 6.10 illustrates the experimental step response with the implementation of the anti-slack mechanism. Comparing it with the experimental response of Figure 6.6 without the anti-slack mechanism, it can be observed that the response in Figure 6.10(a) is smoother and faster than Figure 6.6(a), without anti-slack. Figure 6.10(d) clearly shows the anti-slack mechanism kicking in to heat the passive right SMA wire after 0.8 s, then the passive left SMA wire after 3.5 s, and so on. Despite the high accuracy at the steady-state, the speed of response of the actuator is slow, with rise times of about 0.8 s for 5 N peak-to-peak magnitude steps. This is an average force rate of only $6.25\,$Ns^{-1}. The limiting factor is the safe current level of 0.18 A.

In the next section, the rapid-heating mechanism described is able to increase this safe current limit to very high levels in order to substantially increase the

actuator speed of response, while protecting the actuator from overheating using an algorithm based on the SMA electrical resistance.

6.3.2 Rapid-Heating Mechanism

This section presents a complete description of how the rapid-heating mechanism works. Some of our past work on the rapid-heating mechanism can be found in [16, 71, 72]. These papers, in addition to describing the rapid-heating mechanism, showed experimentally the implementation and the improved speed of response of SMA actuators using this control algorithm.

The rapid-heating mechanism sets an upper limit to the heating power that can be applied to each wire. The upper limit is calculated separately for each wire, and is a function of the wire's measured electrical resistance. The idea is to allow rapid heating of the wires, via large heating powers, whenever it is safe to do so, because rapid heating increases the speed of the actuator. The rapid-heating mechanism consists of the two blocks labelled 'rapid heating formula' in Figure 6.1, which calculate the power limits from the measured resistance, and the dynamic saturation block in Figure 6.3, which imposes the power limits on the controller.

The speed of an SMA actuator is determined partly by the rate at which the wires are heated, and partly by the rate at which they cool. According to the technical data sheet for Flexinol wires in Appendix A, the cooling rates for the thinnest wires are faster than the heating rates using the recommended heating currents. [2]   An excerpt of the data sheet is shown in Table 6.1. It is therefore possible to produce a substantial increase in the speed of an SMA actuator simply by using heating currents above the recommended values. However, the use of larger heating currents can raise the temperatures of the wires far above the transformation temperature range, with two adverse consequences: the wires take longer to cool, and they may suffer thermal damage.

An early attempt to solve this problem is by Kuribayashi [41]. Kuribayashi proposed using miniature thermocouples to measure the temperatures of an antagonistic SMA wires and determining the heating currents based on a temperature threshold to prevent overheating. If the temperature is below a certain threshold, then a large heating current is allowed; otherwise, the current is switched off. In this thesis, the proposed rapid-heating mechanism similarly

---

[2]Specifying a heating current is equivalent to specifying a heating power per unit length of wire.

Wire Diameter (inches)	Current at Room Temp. (mA)	Contraction Time (second)	Off Time 70°C Wire (second)	Off Time 90°C Wire (second)
0.003	100	1	0.5	0.2
0.004	180	1	0.8	0.4
0.005	250	1	1.6	0.9
0.006	400	1	2.0	1.2

Table 6.1: Heating and cooling times for several Flexinol wires.

improves the actuator response speed while preventing overheating, but without the use of a temperature sensor. Instead, it uses the SMA's electrical resistance as an indirect measurement of its temperature.

Figures 6.11, 6.12 and 6.13 show how the method works. Figure 6.11 shows a typical resistance-versus-temperature curve for a Nitinol wire. The physical explanation for this curve is that the resistivity of the martensite crystal phase (in Nitinol) is about $15-20\%$ higher than the resistivity of the austenite phase. As a result, the resistance of the wire is about $15-20\%$ higher when it is cold than when it is hot. Furthermore, the resistance varies with the martensite ratio, so it drops smoothly as the wire is heated, and rises smoothly again as it cools. The hysteresis shown in this figure is a consequence of the thermal hysteresis in the phase transformation.
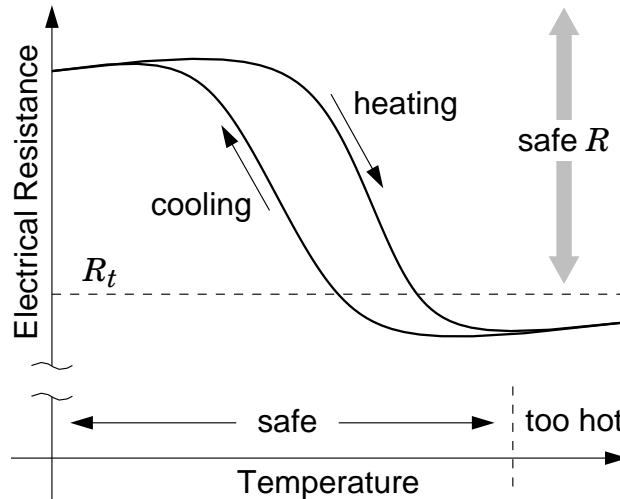
Figure 6.11: Electrical resistance of Nitinol wire versus temperature

Figure 6.12 presents an actual graph of resistance-versus-heating-power for the $100\,\mu$m Flexinol wire which is $80\,$cm long. Since there is no practical temperature measurement method available, the input heating power to the SMA is used as a proxy for temperature. It should also be stated that at very low input

power levels ($< 0.1\,\mathrm{W}$), resistance measurements, which are based on the voltage measurements from the SMA driving amplifier, are not very accurate. Starting from a resistance value of $94\,\Omega$, it can be seen from the graph that as the wire is heated, the resistance decreases smoothly to a value of approximately $81.4\,\Omega$. The resistance value at the start of the heating cycle is 15% higher than at the end of the cycle. When the wire cools, the resistance value of the wire increases, but with a significant hysteresis.
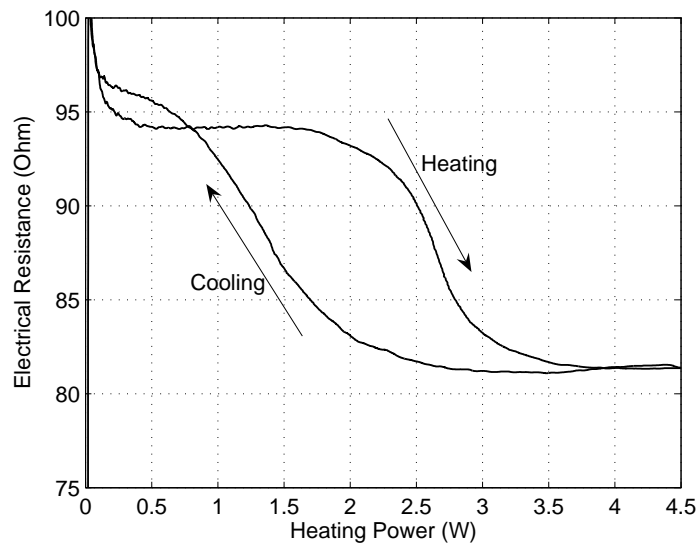
Figure 6.12: Actual result of electrical resistance versus heating power for a $100\,\mu\mathrm{m}$ Flexinol wire $80\,\mathrm{cm}$ long.

The interesting feature during the cooling cycle is the cross-over of the initial $94\,\Omega$ resistance value, which occurs at $0.8\,\mathrm{W}$. This cross-over suggests the presence of a third phase, the R-phase, in addition to the austenite and martensite phases. It has been reported in [62, 76] that the R-phase has higher electrical resistivity compared to both austenite and martensite; then it is possible to deduce that the higher electrical resistance values reached during cooling compared to the initial $94\,\Omega$ is due to the R-phase. The existence of the R-phase in Flexinol has not been reported in the data sheets provided by Dynalloy Inc. However, this unexpected cross-over observation during the cooling cycle has also been made by others [22, 76]. Readers are directed to these papers for further discussions of the R-phase.

Due to the presence of large hysteresis in the resistance versus temperature, or heating power relationship, it is therefore not possible to deduce the exact temperature of the wire from its electrical resistance. Nonetheless, a threshold

resistance, R_t (see Figure 6.11), can be calculated and identified, such that if the measured resistance is greater than R_t then it can be certain that the wire is not overheated. In practice, a small safety margin should be built into the chosen value of R_t, so as to account for measurement errors and the variation of resistance with strain. In our experiments, a safety margin of 5% has been used.
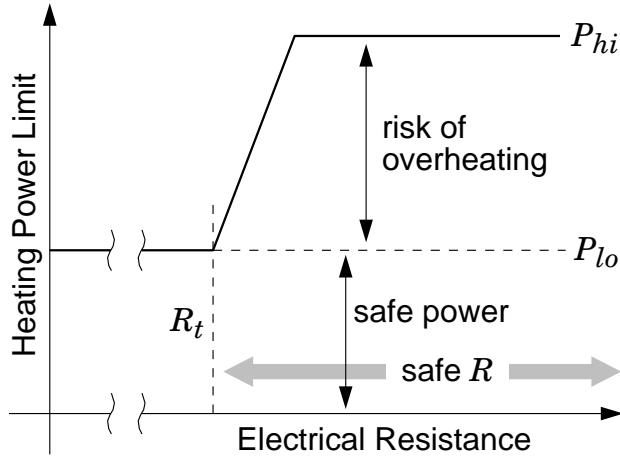
Figure 6.13: Heating power limit versus measured electrical resistance

First, let P_{max} denote the maximum heating power for a single SMA wire. Figure 6.13 illustrates the calculation of P_{max} based on the measured electrical resistance, R. If $R < R_t$ then it is not possible to tell from the resistance whether the wire is overheating. Therefore, P_{max} is set to a relatively low power level, P_{lo}, which is sufficiently low that it will not overheat the wire, even if applied indefinitely. Typically, P_{lo} is calculated from the data sheet recommended heating current and the length of the wire. If $R \geq R_t$, it can be certain that the wire is not overheating. It is therefore safe to apply a larger heating power. In this case, P_{max} is ramped up to a higher power, P_{hi}. The purpose of the ramp is to make P_{max} a continuous function of time, as a step change in P_{max} can disturb the tracking accuracy of the differential controller. The value of P_{hi} is determined by the maximum power available from the power supply, the maximum power that the power regulator can handle, or the maximum power that is reasonable for a particular application. Generally, P_{hi} is much higher than P_{lo}. If R_{ramp} is the resistance value at the top of the ramp, then the formula for calculating P_{max} is

$$P_{max} = \begin{cases} P_{lo} & \text{if } R < R_t \\ P_{lo} + \dfrac{(P_{hi} - P_{lo})(R - R_t)}{R_{ramp} - R_t} & \text{if } R_t \leq R < R_{ramp} \\ P_{hi} & \text{otherwise.} \end{cases} \quad (6.3)$$

(a)

(b)

(c)

(d)
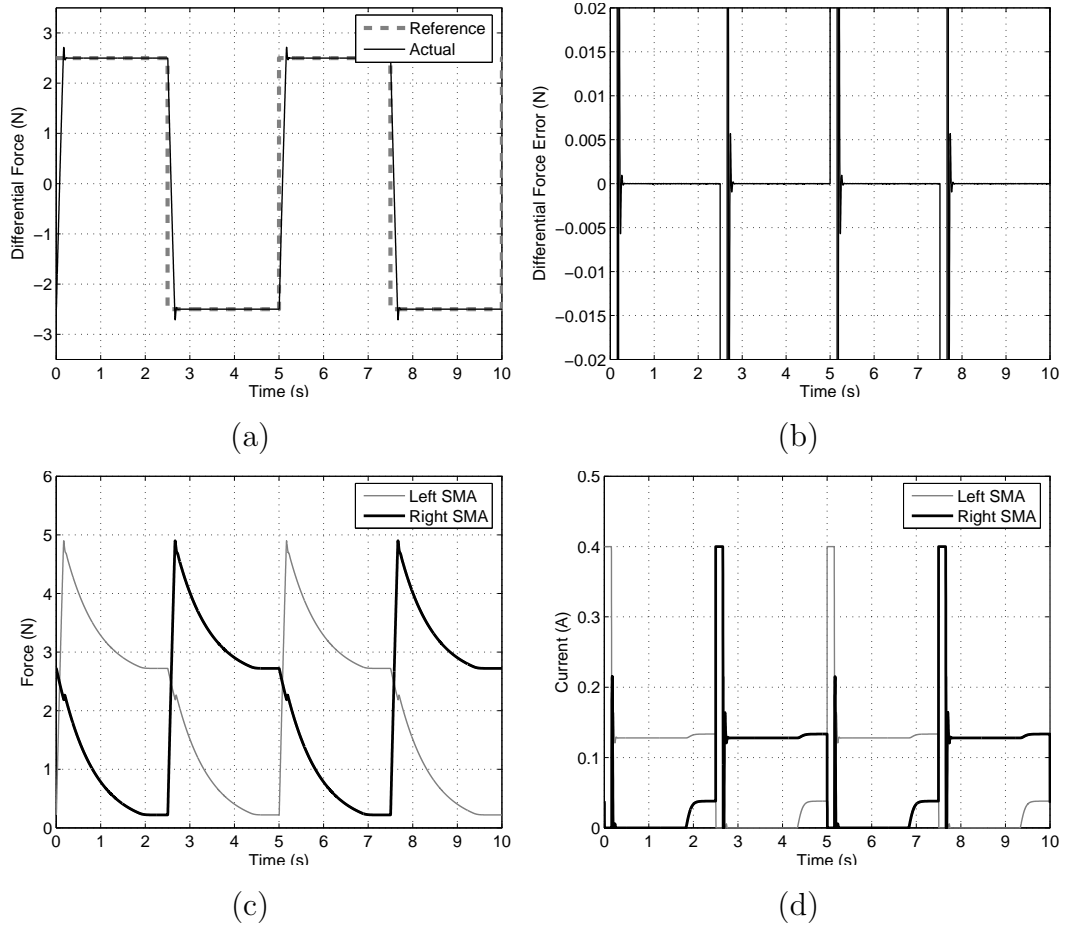
Figure 6.14: Simulated differential force response for steps of $\pm 2.5\,\text{N}$ with P_{hi} set at $14.4\,\text{W}$ (corresponding to a current of $0.4\,\text{A}$). (a) Differential force step response, (b) its corresponding force errors, (c) individual SMA forces, and (d) individual SMA heating currents.

Depending on the individual rapid-heating calculations for the left and right SMA wires, there will be two calculated values of P_{max} corresponding to $P_{max,L}$ and $P_{max,R}$ of the dynamic saturation block.

The rapid-heating mechanism cannot be directly simulated as the force model does not contain a temperature behaviour of the SMA for resistance estimation. This force model only provides the relationship between the input power and the output force of an SMA wire. However, it is useful to see what the simulation predicts when higher P_{max} values are used, and if increased inputs can adversely affect the anti-slack mechanism as well as the force output of the actuator. A simulation using increased P_{hi} values corresponding to currents of $0.4\,\text{A}$ (more than double the recommended $0.18\,\text{A}$ level) for $\pm 2.5\,\text{N}$ step responses is shown in Figure 6.14. Based on the simulation, a rise time of $0.1\,\text{s}$ for a step with $5\,\text{N}$ peak-to-peak magnitude is predicted. This is an average force rate of $50\,\text{Ns}^{-1}$.

Note that minimum individual forces of 0.2 N are still maintained by the anti-slack mechanism. The simulation also predicts peak individual forces of almost 5 N by both SMA wires, exceeding the 3 N force range of individual SMA wires.

Figure 6.15 illustrates the speed improvement which may be achieved for sinusoidal responses at 1 Hz using a larger heating power than the safe recommended level in simulation. The results also show the individual SMA forces exceeding the 3 N safe threshold, with mean forces of 2.5 N in Figure 6.15(c), and 4 N in Figure 6.15(d). It is known from the previous chapter that the model underestimates the cooling rate of the wires, thereby keeping the mean forces high. The experimental results are expected to produce lower forces at steady-state.

The experimental results for ± 2.5 N step commands with rapid heating are presented in Figure 6.16. In the experiments, the following parameters are used: $P_{lo} = 2.92$ W, $P_{hi} = 14.4$ W, $R_t = 85\,\Omega$, and $R_{ramp} = 90\,\Omega$. P_{lo} and P_{hi} correspond to current levels of 0.18 A and 0.4 A respectively.

The rapid-heating mechanism greatly improves the speed of response, with a rise time of only 0.1 s for a 5 N magnitude step. This corresponds to an average force rate of 50 Ns^{-1}, a factor of 8 improvement compared to the experimental force rate of 6.25 Ns^{-1} from Figure 6.10. Results also show no loss of setpoint accuracy, as the steady-state error is still less than 0.001 N. The incorporation of the rapid-heating mechanism does not adversely affect the anti-slack mechanism, as can be seen from the 0.2 N minimum force maintained by both wires in Figure 6.16(c). However, the results show peak individual forces of approximately 4.8 N on both SMA wires. This exceeds the 3 N safe force range of the SMA. The overstressing poses a problem as it can damage the actuator. The experimental response also shows that the anti-slack mechanism is activated for a longer duration than the simulation in Figure 6.14. This is due to the model underestimating the cooling rate of the wires.

The rapid-heating mechanism can also improve the tracking speed to sinusoidal commands significantly. Figure 6.17 presents a comparison between experimental tracking responses to a 1 Hz force sinusoid without rapid heating and with the mechanism implemented. As can be seen in Figure 6.17(e), without rapid heating, the heating current is saturated at 0.18 A, which limits the speed of response shown in Figure 6.17(a). Better tracking is achieved using the larger currents allowed by the rapid-heating algorithm. In addition, the individual wire forces of the experimental results also show mean values of 1 N and 2 N in Figures 6.17(c) and 6.17(d) respectively. This is significantly lower compared with
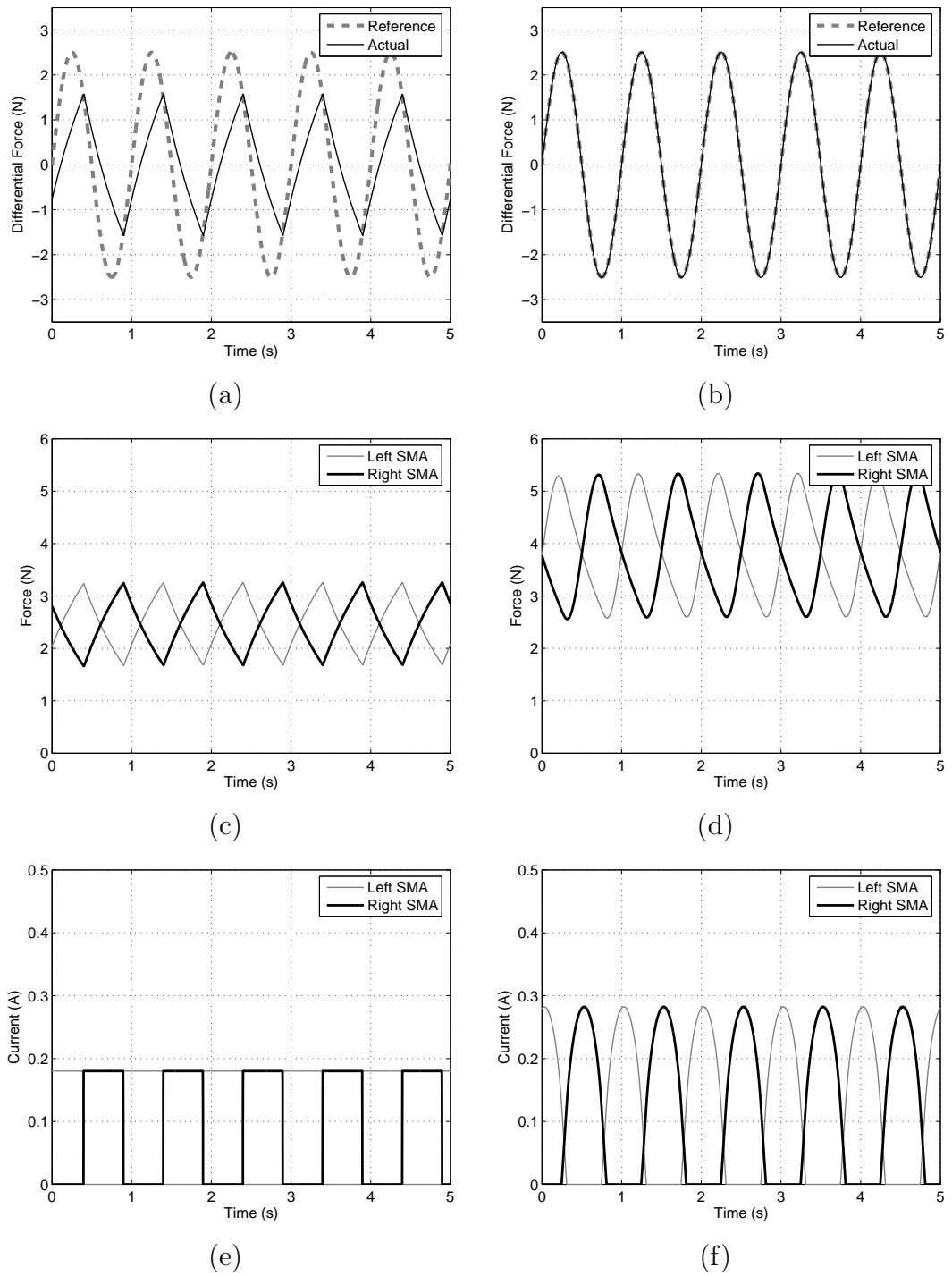
Figure 6.15: Comparison of simulated differential force tracking response at 1 Hz with $P_{hi} = 2.92\,\mathrm{W}$ and $P_{hi} = 14.4\,\mathrm{W}$. (a) Differential force tracking response with $P_{hi} = 2.92\,\mathrm{W}$, (c) its corresponding individual SMA forces, and (e) individual SMA heating currents. (b) Differential force tracking response with $P_{hi} = 14.4\,\mathrm{W}$, (d) its corresponding individual SMA forces, and (f) individual SMA heating currents.

the simulation of Figure 6.15. The differential force error amplitudes for the response of Figure 6.17(b) have been measured to be 0.002 N, which is 0.033% of the 6 N range.

Figure 6.18 shows that the experimental response can accurately track a 2 Hz force command with the rapid-heating mechanism. The force tracking errors have an amplitude of 0.02 N, which is 0.33% of the 6 N range, as can be observed in Figure 6.18(b). This is comparatively better than the 2 Hz sine tracking results in [23, 26]. However, this tracking accuracy is only possible if the SMA wires exceed the 3 N safe force. Due to the limited rate of cooling under ambient air, the mean SMA forces are approximately 4.5 N (see Figure 6.18(c)). The force drift is due to free convection around the actuator.

(a)

(b)

(c)

(d)
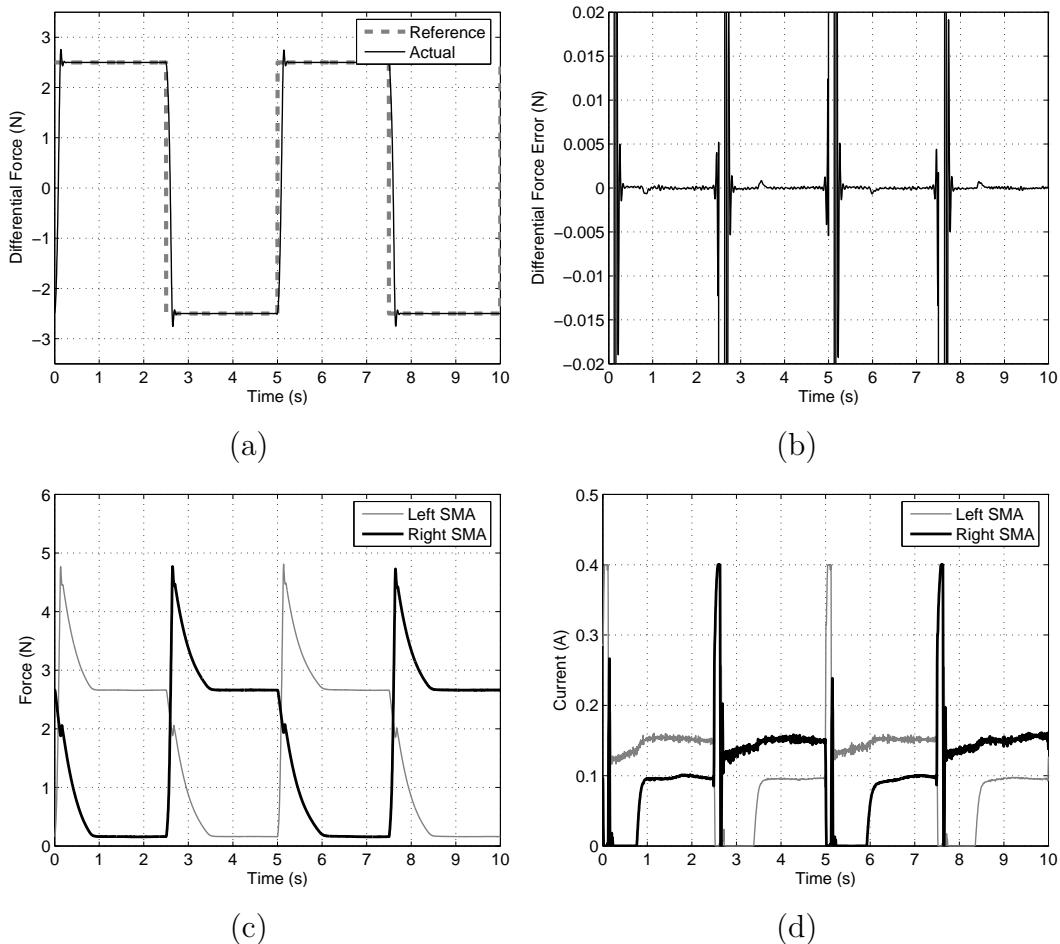
Figure 6.16: Experimental differential force response for steps of ±2.5 N with rapid-heating mechanism implemented. (a) Differential force step response, (b) its corresponding force errors, (c) individual SMA forces, and (d) individual SMA heating currents.
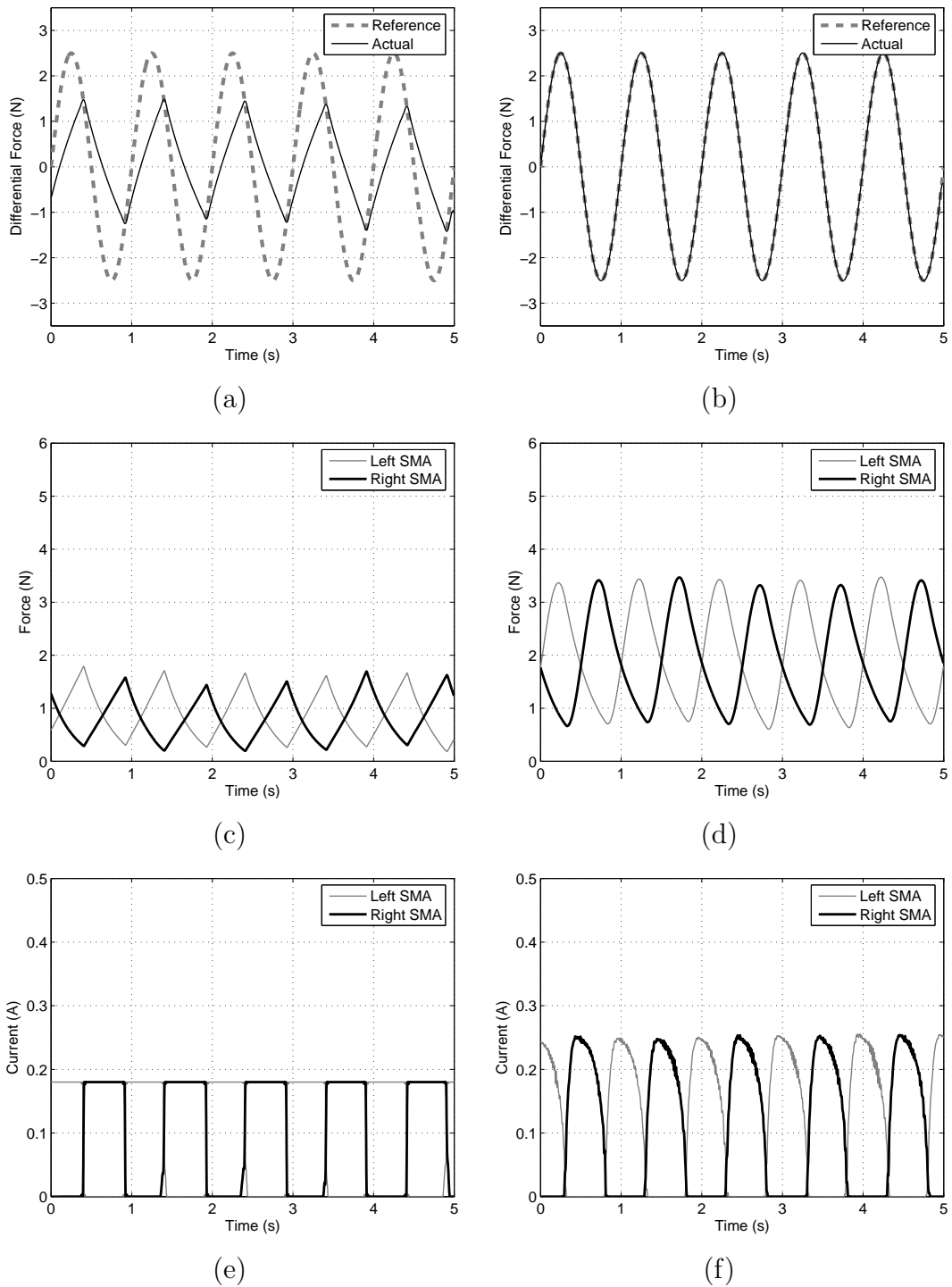
Figure 6.17: Comparison of experimental differential force tracking response at 1 Hz with and without rapid-heating mechanism. (a) Differential force tracking response without rapid heating, (c) its corresponding individual SMA forces, and (e) individual SMA heating currents. (b) Differential force tracking response with rapid heating, (d) its corresponding individual SMA forces, and (f) individual SMA heating currents.
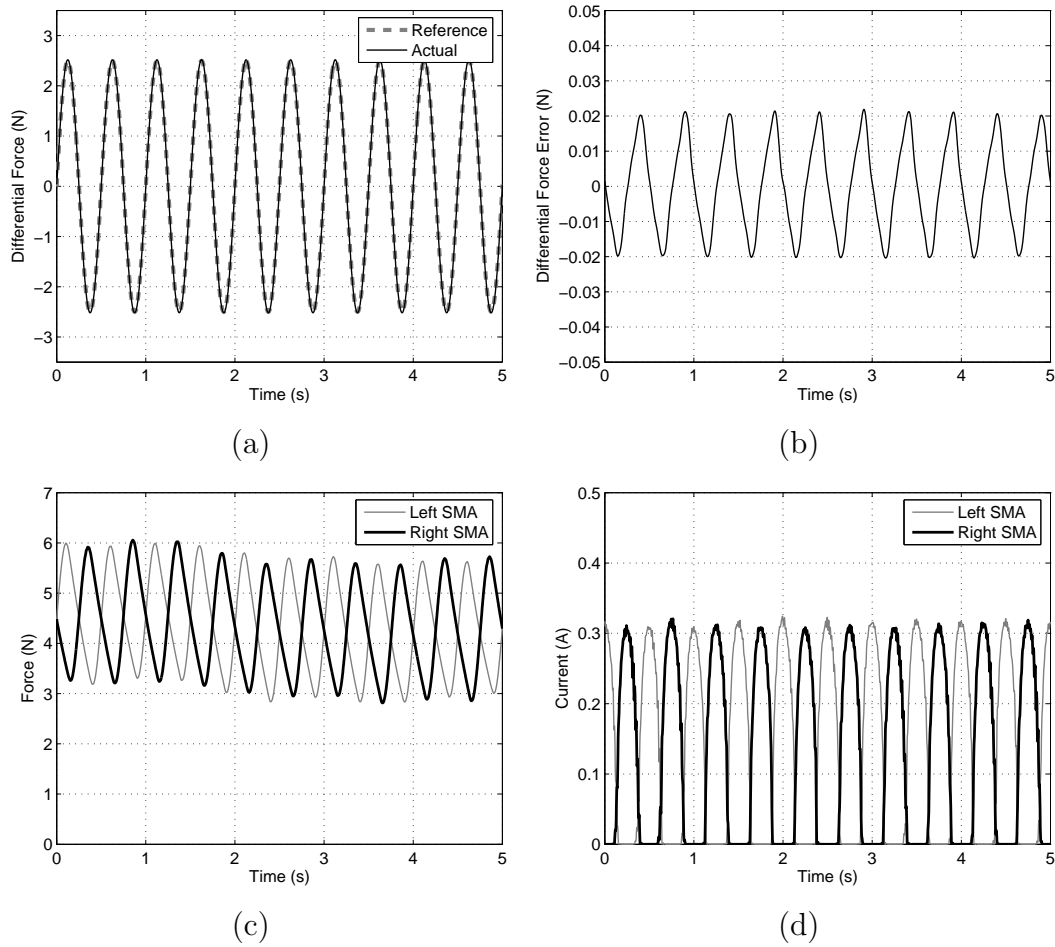
Figure 6.18: Experimental differential force tracking response at 2 Hz with rapid-heating mechanism implemented. (a) Differential force tracking response, (b) its corresponding force errors, (c) individual SMA forces, and (d) individual SMA heating currents.

6.3.3 Anti-Overload Mechanism

When the differential force command is large or the rapid-heating algorithm delivers large currents to the active SMA wire, it runs the risk of overstressing. This is undesirable as it can damage the actuator. The aim of the anti-overload mechanism is to prevent overstressing of the actuator.

The anti-overload mechanism shown in Figure 6.19 is activated whenever the measured force of any SMA wire is greater than an upper force threshold, F_{max}. The mechanism is a proportional feedback algorithm that determines the maximum of the forces from the individual SMA wires, compares it to the overload force threshold and appropriately reduces the power input to the actuator. The saturation block activates the anti-overload mode only if the measured maximum force is greater than F_{max}. The anti-overload mechanism is first tested and tuned
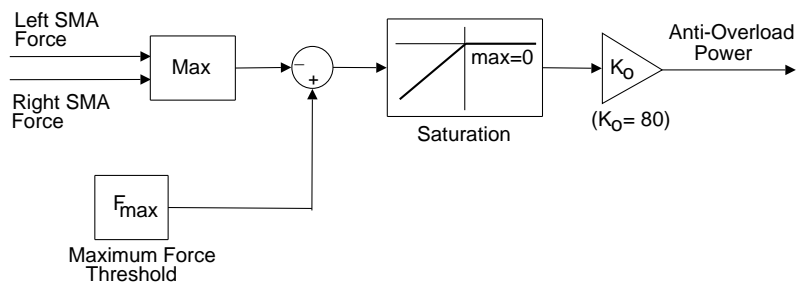
Figure 6.19: Anti-overload mechanism.

in simulation before experimental implementation. In both situations, the final anti-overload parameters are set to $F_{max} = 3\,N$, saturation limit $max = 0$, and gain $K_o = 80$. The anti-overload power is also a common-mode signal as it is delivered to both wires. Figures C.4 and C.5 of Appendix C show the anti-overload mechanism operating external to the dynamic saturation loop of the differential controller in the actual implementation.

Figure 6.20 presents the simulated response to $\pm 2.5\,$N steps with the anti-overload mechanism implemented and Figure 6.21 presents the corresponding experimental response. Both differential force graphs in Figures 6.20(a) and 6.21(a) show very similar responses. Two distinct slopes can be seen during the transients in both figures. The faster, first slope is due to the effects of rapid-heating (increased P_{max}). At the time when the response changes to the slower slope, it can be seen in Figures 6.20(c) and 6.21(c) that the individual force of the active wire has crossed the 3N threshold. The slower slope is when the anti-overload mechanism kicks in. Note that the large force overshoots previously observed in both simulation (Figure 6.14(c)) and experiment (Figure 6.16(c)) have been prevented.

Two distinctions can be made between the simulation and the experimental responses. Firstly, the simulation predicts a slower transient response than the experiment, due to its underestimation of large-signal responses. Secondly, where the simulation predicts smooth response during the period the anti-overload mechanism is activated, the experimental results show rapid switchings in the heating currents of Figure 6.21(d) and in the individual SMA forces of Figure 6.21(c). This indicates that the anti-overload controller is sub-optimal and requires improvement.

(a)

(b)

(c)

(d)
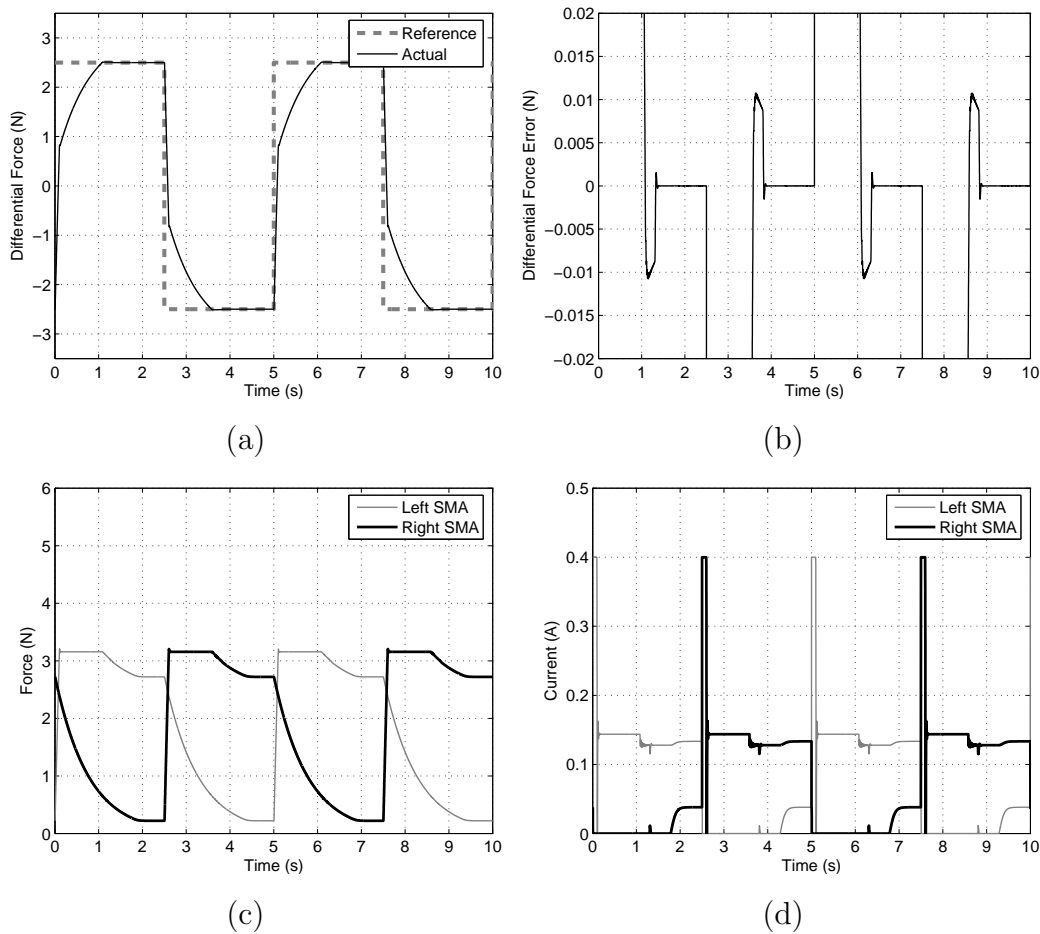
Figure 6.20: Simulated differential force response for steps of ± 2.5 N with anti-overload mechanism implemented. (a) Differential force step response, (b) its corresponding force errors, (c) individual SMA forces, and (d) individual SMA heating currents.

However, both simulation and experimental results demonstrate excellent set-point accuracy and the lack of limit cycles at steady-state. The results also show that the control system incorporating the rapid-heating, the anti-slack and the anti-overload mechanisms can achieve fast, accurate force control without the concerns of actuator damage. Furthermore, the results clearly demonstrate the compromise between response speed and overloading. To further improve speed, perhaps a slightly larger force threshold than 3 N in the anti-overload mechanism can be used, although the exact effects on the long-term performance of the actuator, if there are any, are yet to be determined. This will be investigated in Section 6.4.
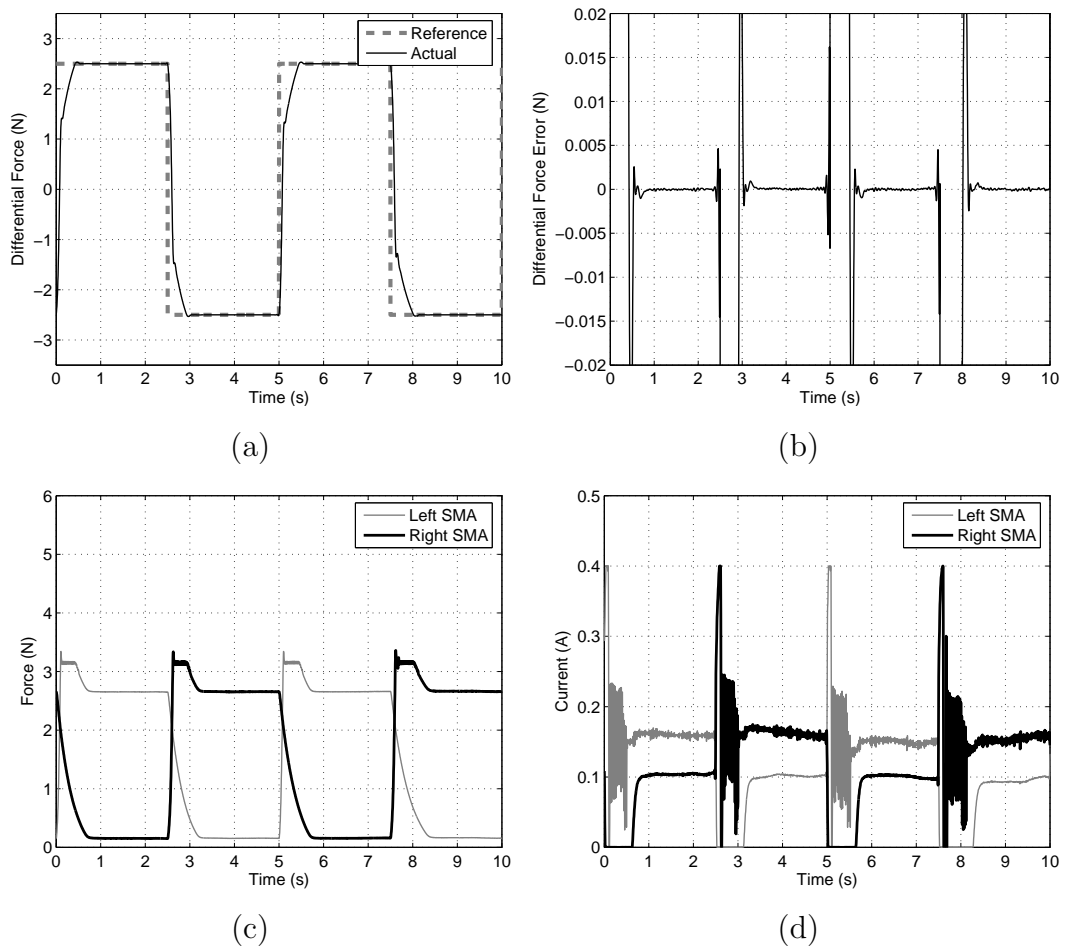
Figure 6.21: Experimental differential force response for steps of $\pm 2.5\,\mathrm{N}$ with anti-overload mechanism implemented. (a) Differential force step response, (b) its corresponding force errors, (c) individual SMA forces, and (d) individual SMA heating currents.

6.4   Performance Verification of Control System

As was mentioned in the previous sections, combining the various control sub-systems, including the anti-slack, the rapid-heating and the anti-overload mechanisms can achieve fast and accurate force response of the SMA actuator. To investigate the overall performance of the complete force controller, it is applied experimentally for a repeated force command as shown in Figure 6.22. The repeated force command consists of four types of waveforms in the following sequence: $\pm 3\,\mathrm{N}$ steps between $0-5\,\mathrm{s}$, followed by smaller $\pm 2\,\mathrm{N}$ steps between $5-7\,\mathrm{s}$, $\pm 4\,\mathrm{N}$ ramps with force rates of $\pm 3\,\mathrm{Ns}^{-1}$ between $7-13\,\mathrm{s}$, and finally, $\pm 2\,\mathrm{N}$ ramps with larger force rates of $\pm 10\,\mathrm{Ns}^{-1}$ between $13-16\,\mathrm{s}$. The following control parameter values are used: anti-slack lower threshold, F_{min} of $0.2\,\mathrm{N}$, rapid-heating

(a)

(b)

(c)

(d)
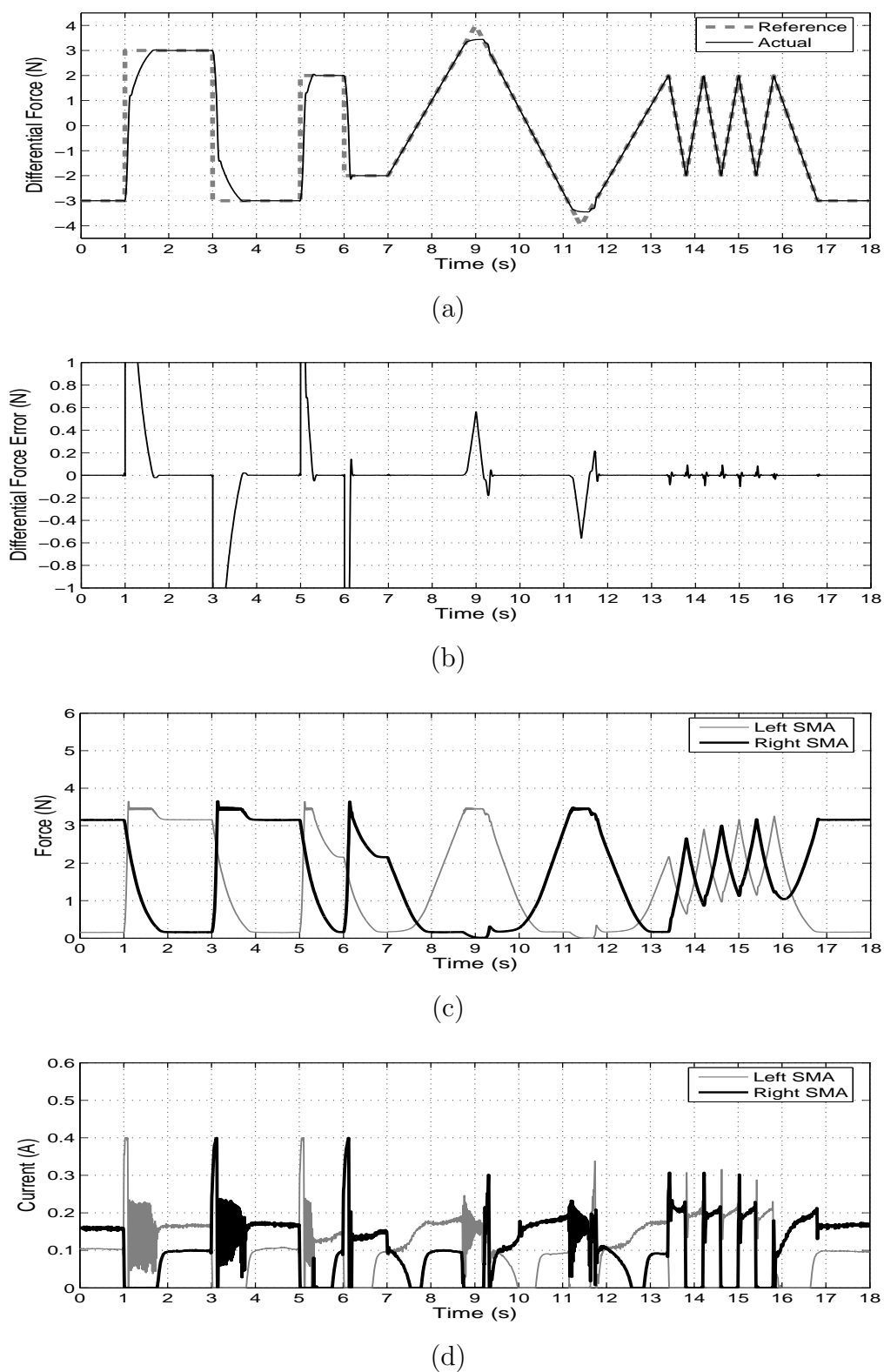
Figure 6.22: Experimental force response with complete differential force control system. (a) Differential force step response, (b) its corresponding force errors, (c) individual SMA forces, and (d) individual SMA heating currents.

P_{hi} of 14.4 W, and anti-overload upper threshold, F_{max} of 3.3 N.

The differential force response to the force command is shown in Figure 6.22(a) and the corresponding force errors in Figure 6.22(b). The response to the first command sequence of ± 3 N steps shows distinctly two transient slopes, in which the slower, latter slope is due to the activation of anti-overload when the SMA force reaches the 3.3 N limit. In the next sequence of smaller ± 2 N steps, the two transient slopes are less significant, as the anti-overload is triggered for a shorter duration. The lower F_{min} threshold has been maintained in these two step sequences. These effects are clearly shown in the individual SMA force plots of Figure 6.22(c) between $0 - 7$ s.

From the 7th second onwards, the force controller is capable of tracking the ramp waveform accurately, as can be seen in the force response of Figure 6.22(a), until the command exceeds $+3.3$ N or falls below -3.3 N. In both situations, the anti-overload kicks in, and reduces power input to the SMA actuator. From Figure 6.22(c), it can be observed that during these intervals (first around the 9th second and then around the 11th second), the measured force of the passive wire drops below the previously maintained level of 0.2 N. This is because the anti-overload power is a common-mode signal affecting both SMA wires that operates outside of the dynamic saturation loop of the differential controller; and also because reducing overload risk is a higher priority than keeping the wires taut. Therefore, as the differential controller asks for greater power inputs to track the larger command, the anti-overload mechanism works harder to reduce power inputs and keep the wire tensions down to an acceptable level. Finally between $13 - 16$ s, the controller still manages to track the final sequence of ± 2 N ramps satisfactorily even with high force rates of ± 10 Ns^{-1} in Figure 6.22(a). The change in slopes causes the 0.1 N force error spikes in Figure 6.22(b).

The experimental results of Figure 6.22 demonstrated the fast, accurate response that the force controller is capable of achieving. The concerns of overheating and overstressing the actuator have been addressed, although larger anti-overload force thresholds and larger rapid-heating power inputs can further improve its performance.

6.4.1 Continuous Operation

The control system is tested for continuous operation of at least one hour. The aim is to investigate if any degradation in the actuator performance will occur over a long period of use. The response to the same force command from the previous section, after one hour of continuous operation, is presented in Figure 6.23. This represents approximately the 200th cycle. There appears to be no adverse effects on the overall performance of the system due to continuous usage.

The experiment was continued following the recording of the results after the first hour to detect any change in performance over longer duration. However, it had been observed that both SMA wires snapped less than three hours into the experiment. The fracture point was found to be at the mid-section, where the wires meet the eyelets of the pulley housing. This is the weakest point with the highest stress concentration along the length of the wire. After repeated cycles of compression and tension, the mid-point possibly sustained the most damage and fatigue, leading to fracture. Therefore, it can be concluded that the breakage of the wires is due to sub-optimal arrangement of the wires, and that the force controller maintains its performance over continuous testing.

6.4.2 Pushing the Limits

In addition, a further experiment was conducted using larger rapid-heating power limit and anti-overload force threshold over the duration of one hour. The aim is to investigate how larger limits will affect the performance of the SMA actuator. In this case, a rapid-heating power P_{hi} of 22.5 W and an anti-overload threshold F_{max} of 5 N were used. Other parameters were unchanged.

The experimental results after one hour of continuous operation are shown in Figure 6.24. The graph of Figure 6.24(a) actually shows faster transient response to step commands compared to previous results, although larger overshoots have been observed. It also completely tracks the ramps with 4 N amplitude between the 7th and the 13th second whereas in Figure 6.22 and Figure 6.23, it could not track the peaks of the ramp due to the anti-overload threshold at 3.3 N previously.

What is more surprising, after one hour of continuous operation, is that no degradation in performance due to wire fatigue or overstress has been observed using the larger thresholds. This indicates that the maximum rated force outputs of Flexinol wires are arguably very conservative, and perhaps driving the wires at higher force levels will produce better results than expected.
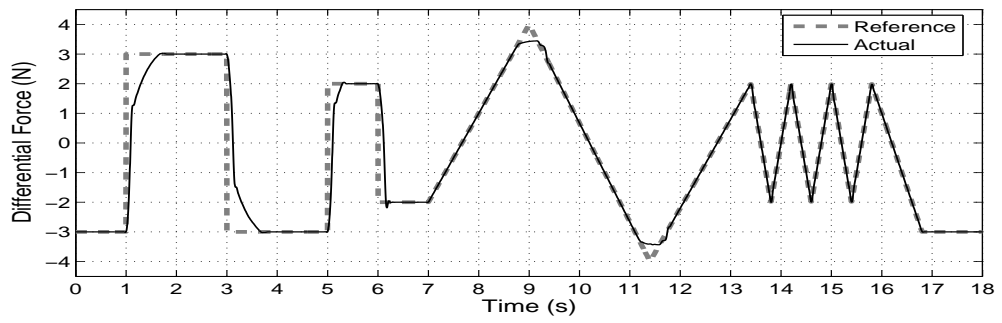
(a)
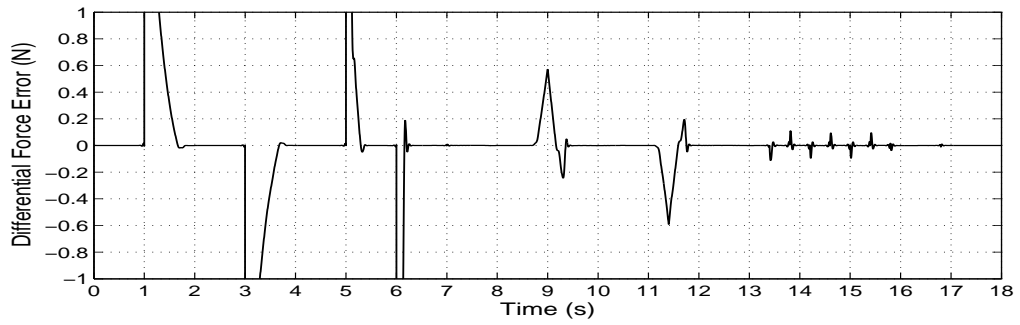
(b)
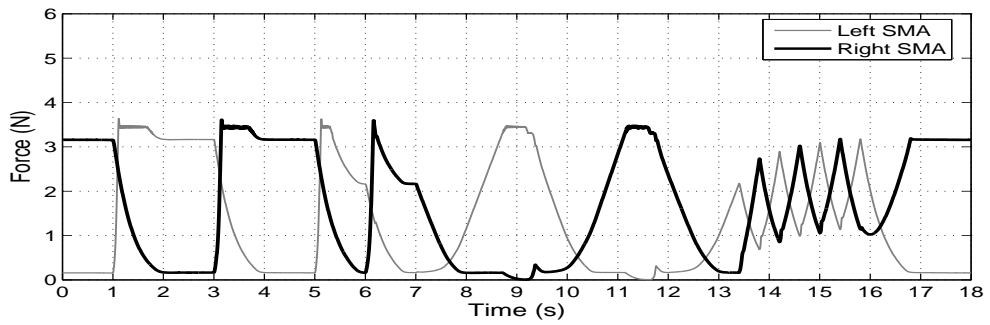
(c)
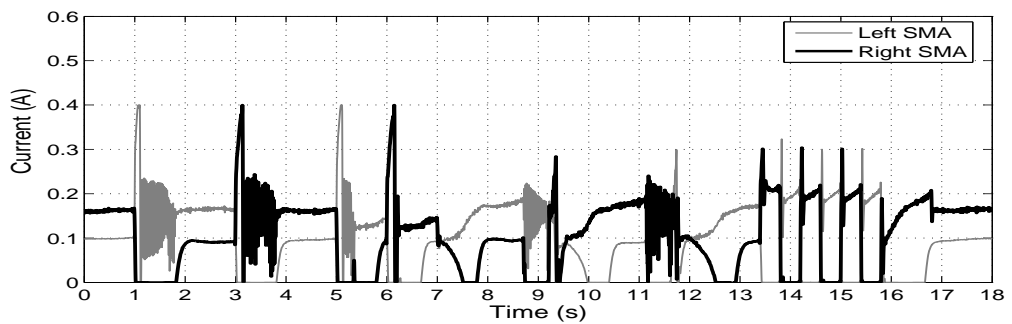
(d)

Figure 6.23: Experimental force response with complete differential force control system after continuous operation of 1 hour.
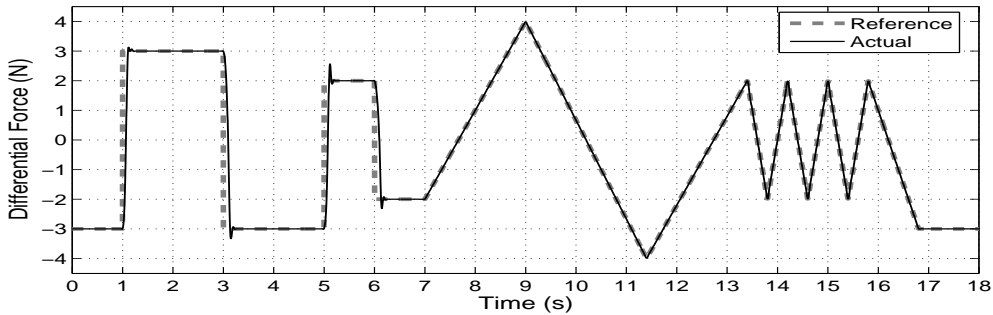
(a)
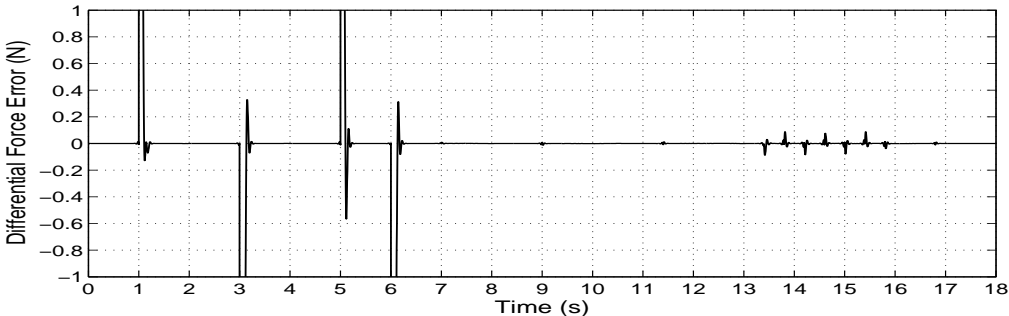
(b)
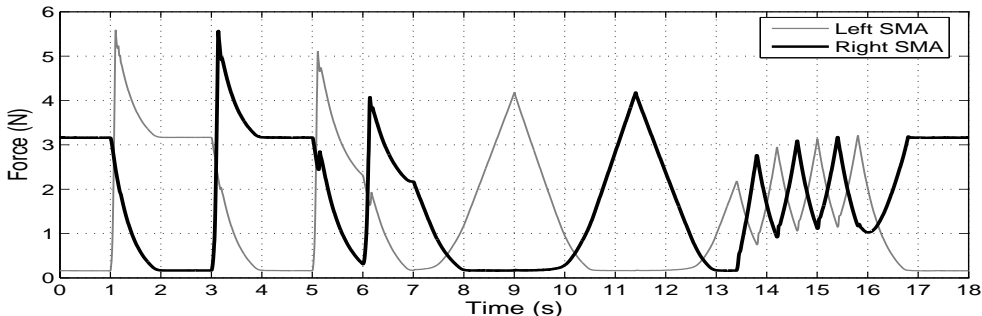
(c)
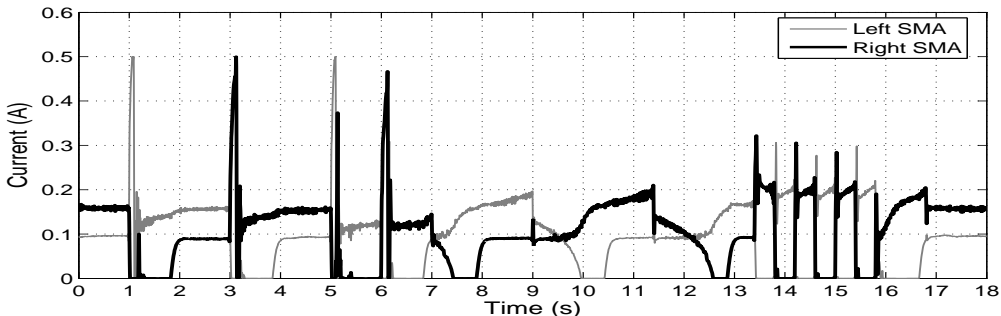
(d)

Figure 6.24: Experimental force response with $F_{max} = 5\,\mathrm{N}$ and $P_{hi} = 22.5\,\mathrm{W}$ after continuous operation of 1 hour.

6.5 Motion Disturbance and Load Inertia Rejection

In this section, we investigate how the differential force controller performs under the influence of external motion disturbances and load inertias. As a comparison, the tracking response to a trapezoidal command signal, without any external disturbances (pulley locked), is first presented in Figure 6.25. The ramps have slopes of $\pm 1\,\mathrm{Ns^{-1}}$ in Figure 6.25(a) and $\pm 2\,\mathrm{Ns^{-1}}$ in Figure 6.25(b). The sudden changes in slopes produce the narrow error spikes in Figures 6.25(c) and 6.25(d), but they are less than $0.005\,\mathrm{N}$ magnitude. The results demonstrate the good overall performance of the force control architecture.

To investigate the effects of external influences, two changes were made on the experimental test bed. First, the pulley is unlocked so that it is free to rotate. This allows motion disturbances (pulley rotation) to take place, and introduces large coupling effects between the antagonistic SMA wires, as the pulling force of one wire is transmitted to the other, and vice versa. The rotation of the pulley is measured using an optical encoder. Second, a pendulum with a mass of $79\,\mathrm{g}$, which acts like a moving robotic link, is attached to the pulley. This heavy pendulum (compared to the mass of the SMA wires) is a difficult dynamic load inertia to be controlled by the system.

When the system is subjected to these influences, the results are still generally good. They are presented in Figure 6.26. The steady-state accuracy is maintained, but the accuracy during the ramps has been affected, with peak error amplitudes of $0.04\,\mathrm{N}$ in Figure 6.26(c) and $0.08\,\mathrm{N}$ in Figure 6.26(d). These spikes occur during the change of slopes, and are caused by the activation of the anti-overload mechanism. However, it can be seen that the controller can rapidly recover from this event.

Comparison between Figure 6.25 and Figure 6.26 shows similarly good tracking responses, except for a slight degradation during the ramps and the change in slopes, which the controller can quickly correct. However, the forces on the individual wires in Figures 6.26(e) and 6.26(f) are very different from those in Figures 6.25(e) and 6.25(f). These differences can be explained as follows.

Suppose the force command is at $+2\,\mathrm{N}$, and is about to start ramping down to $-2\,\mathrm{N}$. Before the ramp starts, the left SMA wire is hot, and the right SMA wire is cool or cold. Also, the pendulum has come to rest at a position $15°$ to the right of centre (see Figure 6.27), which means that the left SMA wire is substantially

113
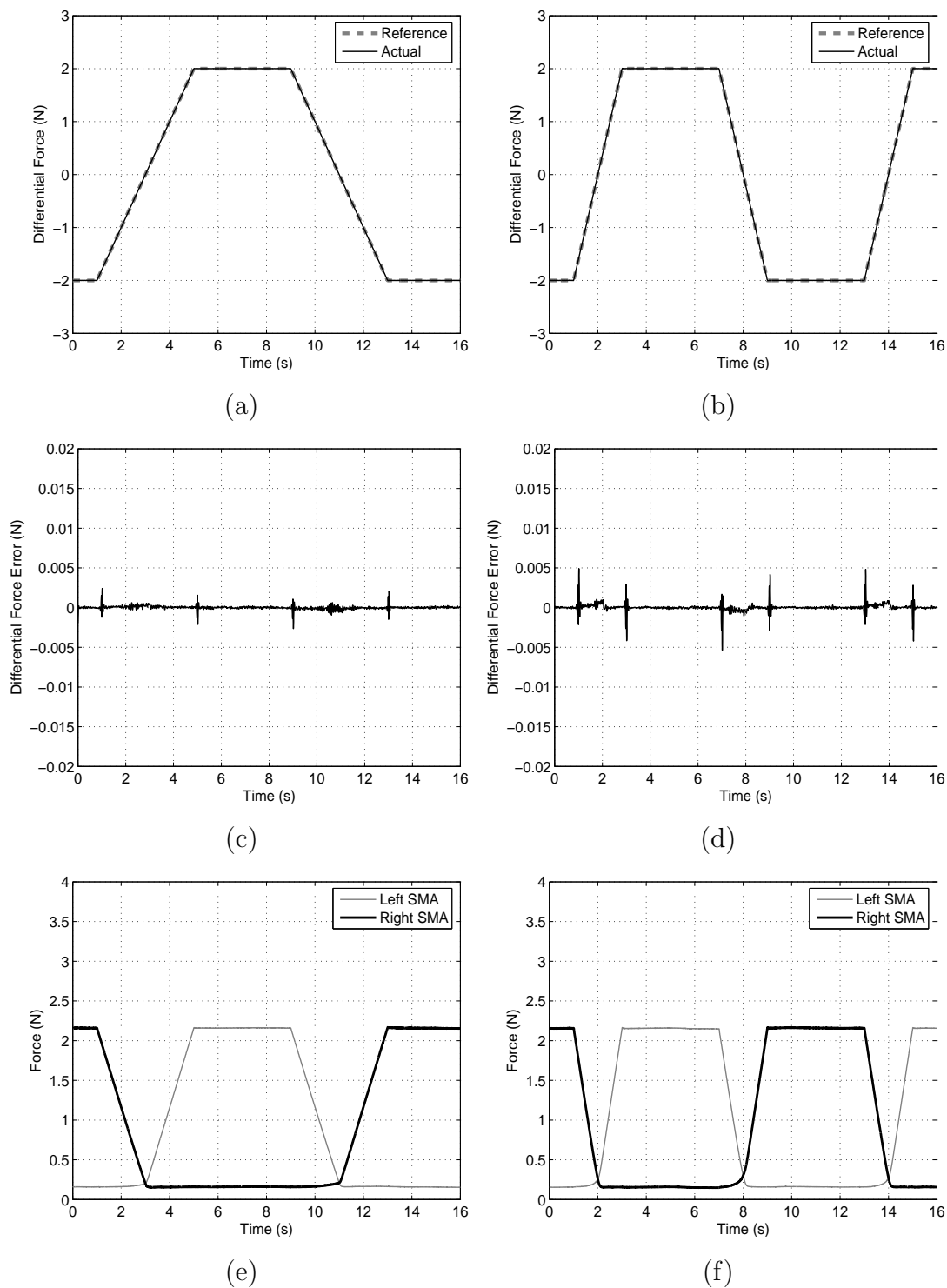
Figure 6.25: Experimental differential force ramp response with no external disturbances (pulley locked). (a) Differential force ramp response at ramp rates of $\pm 1\,\mathrm{Ns}^{-1}$, (c) its corresponding force errors, and (e) individual SMA forces. (b) Differential force ramp response at ramp rates of $\pm 2\,\mathrm{Ns}^{-1}$, (d) its corresponding force errors, and (e) individual SMA forces.

114

Figure 6.26: Experimental differential force ramp response under load and motion disturbances (pulley unlocked). (a) Differential force response at ramp rates of $\pm 1\,\mathrm{Ns}^{-1}$, (c) its corresponding force errors, and (e) individual SMA forces. (b) Differential force response at ramp rates of $\pm 2\,\mathrm{Ns}^{-1}$, (d) its corresponding force errors, and (f) individual SMA forces.

contracted, and the right SMA wire is substantially stretched. When the ramp begins, the heating power to the left SMA wire is reduced, and it begins to cool. At the same time, the pendulum begins to swing down, because the force from the actuator is reducing. This means that the left SMA is being stretched, while the stretch on the right SMA is being reduced. The latter causes the tension on the right SMA to go down, which means that the tension on the left SMA must go down even faster, so as to maintain the correct differential force. This pattern continues until the anti-slack mechanism kicks in, and stops the tension on the right SMA wire from falling below 0.2 N. From here on, the tension on the left SMA wire drops gradually to the cross-over point, and then the tension on the right SMA wire, which is now the active contracting wire, begins to rise. Due to coupling between the two wires, the left wire continues to stretch and its tension rises although more slowly than the right wire. Towards the end of the ramp, the left SMA wire approaches its maximum extension, and begins to offer some resistance. In effect, it begins to act like a spring.
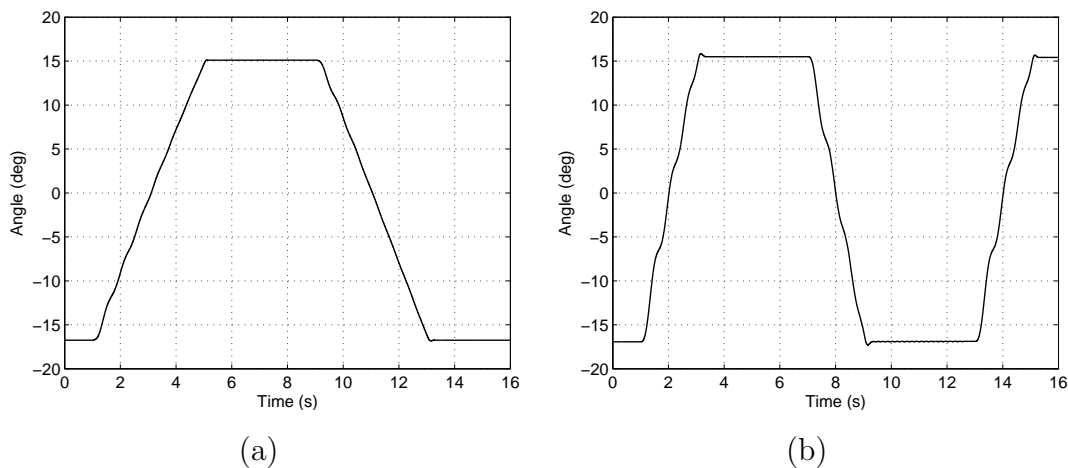
Figure 6.27: Measured pulley rotation from the experiments of Figure 6.26 showing small oscillations during transients and no limit cycles at steady-state.

Figure 6.27 presents the measured pulley rotation recorded during the two experiments of Figure 6.26. It can be seen from both Figures 6.27(a) and 6.27(b) that the sudden onset of the force ramp excites the pendulum into small oscillations during the transients, which have little effect on the tracking accuracy of the force controller. These oscillations cease at the end of each ramp, due to excellent force feedback from the controller as well as friction in the bearing.

The experiments show that the force controller remains accurate and free from limit cycles when the actuator is connected to a heavy, moving inertial load.

6.6 Chapter Summary

A differential force control architecture that produces very fast and accurate responses in an actuator consisting of an antagonistic pair of SMA wires has been presented in this chapter. The control system consists of a PID differential controller, and three additional control elements — the anti-slack, the rapid-heating and the anti-overload mechanisms.

The SMA antagonistic force model developed in Chapter 4 has been used to simulate and verify the workings of the differential force control system. The model was able to quite accurately represent the system. However, it has also been observed that the model underestimates the large-signal gains of the system, particularly the cooling rates of the SMA wires.

The experimental results indicate that the SMA actuator is capable of controlling forces both rapidly and accurately. In particular, fast setpoint tracking with a high peak force rate of $50\,\mathrm{Ns}^{-1}$ has been demonstrated. The controller also achieves high setpoint accuracy with errors as low as $0.001\,\mathrm{N}$, which is 0.017% of the $6\,\mathrm{N}$ actuator force range. In terms of tracking sinusoidal forces, the SMA actuator has a maximum tracking error amplitude of $0.02\,\mathrm{N}$ for a $2\,\mathrm{Hz}$, $5\,\mathrm{N}$ magnitude sine wave. This corresponds to an accuracy measure of 0.33% of the $6\,\mathrm{N}$ range.

In the experimental results, no steady-state errors have been observed. With the implementation of the rapid-heating and anti-overload mechanisms, actuator damage has been prevented with no overheating and overstressing of the SMA wires. However, the anti-overload mechanism introduces small limit cycles during periods of activation, but the effects on the actuator's differential force output is insignificant. Continuous operation experiments also verify that the control system can perform consistently over long durations. When subjected to motion disturbances and external loadings, the control system manages to reject these external disturbances and still performs very well.

The differential force control architecture will now be used as part of the control system for the motion control of the antagonistic SMA actuator in the presence of heavy dynamic loads in Chapter 7. However, an SMA position model will need to be determined in order to simulate the actual system. This will be presented first, followed by the motion control experiments in the next chapter.

CHAPTER 7

Position Control in the Presence of Heavy Loads

The differential force control system in the previous chapter shows that an actuator which comprises of an antagonistic pair of SMA wires can achieve very fast and accurate force tracking. However, the wires are constrained from contracting, thereby producing no motion. This is useful for gripping and force contact applications; but for practical actuator applications involving motion, such as actuating a robotic joint connected to a link or a load, continuous position control of the SMA actuator is crucial. For position control, the speed and accuracy of the response still remain the most important criteria to be addressed. However, the dynamics of the system, caused by load inertia and antagonistic wire coupling effects, cannot be ignored and must be controlled accordingly as it can produce limit cycles and may lead to instability.

This chapter will begin by investigating the position modelling of a robotic joint application actuated by antagonistic SMA wires in Section 7.1. The constrained force model of Chapter 4 is extended to take into account variations in strains due to wire contraction and extension using small-signal frequency response analysis. Once the stress, strain and heating power relationships have been determined for an SMA wire, the position model for an antagonistic SMA-actuated robotic joint moving a link can now be built. The model can then be used to simulate and test the proposed two-loop position control architecture.

In Section 7.2, position control of the system with a heavy load is examined. The two-loop position control architecture is described and explained in detail first, followed by the experimental results. The two-loop control system will be capable of stabilising the system and producing very accurate responses at acceptable speed. It will be observed that the load dynamics and wire coupling effects affect the performance, but the control system still manages to dampen and minimise these effects, with no signs of limit cycles. This is a significant ac-

complishment compared with past research in improving SMA actuator response.

7.1 Extended Position Modelling

In Chapter 4, the SMA wire is heated to produce a force. Under the constrained length case, the strain of the wire does not vary, so the modelling considers only a direct input power to output force relationship of the wire. For an SMA actuator application moving an object against an opposing force, the effects of strain variations on the required heating power and wire stress need to be considered.

A dynamic model, that relates wire strain variations to the input heating power of the SMA in order to maintain a certain level of wire stress, [1] will be presented in this section. As an example, let's assume that the aim is to maintain the wire tension at 1 N, and the length of the wire can be changed by an external device, such as the linear slide in our experimental test bed, or by another SMA wire in antagonistic arrangement. An increase in wire strain (the wire is being stretched) causes less heating power to be applied to maintain the same level of wire tension. Conversely, when the wire strain decreases (the wire becomes less taut), a larger heating power is required to maintain the wire tension. The model will be able to describe and quantify this strain-power relationship. Furthermore, combining this strain-power relationship with the force model of Equation 4.13 will allow us to fully describe the stress, strain and input power relationships for an SMA wire.

The complete model relating wire stress, strain and input power will be useful for simulating an antagonistic SMA actuator (with noticeable coupling dynamics) that acts on a rotating joint displacing a heavy link. A position model for such a robotic joint application can then be built. However, it is noted that the accuracy of the strain-power data is limited, thereby restricting the accuracy of the resulting position model. Nonetheless, the model is still useful for the design and simulation of the proposed position controller.

7.1.1 Modelling Experiments

Similar to the previous force modelling of Chapter 4, frequency response analysis is employed to investigate the relationship between strain variations to input power under constant wire stress. A single $100\,\mu$m Flexinol wire is tested using

---

[1]Specifying a level of wire stress is the same as the wire tension per wire cross-sectional area.

the same test bed for the experiments.

The experimental procedures are described as follows. To maintain a constant SMA wire tension, the PID force controller of Chapter 5 is used to accurately track the desired force command. The strain of the wire is varied by moving the linear slide to follow a sinusoidal trajectory at the appropriate test frequencies. The heating power to the SMA, determined from the force feedback controller, changes in accordance with the strain variations to accurately track the constant force command. This power signal has the same frequency as the sinusoidal strain variations. Once steady-state is achieved, the power signal is recorded over a sufficient number of cycles. This allows the magnitude and phase components of the power signal to be accurately measured later using similar least-squares parameter estimation methods from Chapter 4.

The procedure is repeated for suitable spot frequencies over the $0.1 - 10\,\mathrm{Hz}$ range. This frequency range is limited by the linear slide closed-loop bandwidth, which determines how accurately the servo-controlled slide tracks a certain trajectory, and also by the bandwidth of the PID force feedback controller. At $0.1\,\mathrm{Hz}$, a wire strain variation with a peak-to-peak magnitude of $2\,\mathrm{mm}$ is induced using the linear slide. This corresponds to a strain of 0.5% for the wire. As the frequency increases, the wire strain variation is decreased so that the force controller can still accurately track the force command. At $10\,\mathrm{Hz}$, the slide induces a wire strain variation with a peak-to-peak magnitude of only $0.02\,\mathrm{mm}$, which corresponds to a strain of 0.05%.

The procedure is then repeated at different constant wire tensions as well as different mean values of the linear slide positions to span the full range of stresses and strains in the SMA wire. The sets of frequency response data are then recorded and plotted using Bode diagrams.

7.1.2 Strain to Power Relationship for an SMA Wire

Figure 7.1 presents the experimental Bode plots of the $100\,\mu\mathrm{m}$ Flexinol wire under different stress and strain conditions.

The solid black curves represent the experimental data, whereas the dashed curve represent one possible model. The magnitude in decibels (dB) is given by:

$$\text{Magnitude} = 20\log\frac{\text{AC Power}}{\text{Wire Length Change}}, \tag{7.1}$$

where the AC power is the least-squares estimate of the SMA heating power

amplitude, and the SMA wire length change amplitude measured using the linear slide position encoders. [2] The phase in degrees (°) is the phase shift between the SMA heating power signal and the wire length variation induced by the linear slide motion. In all of the experiments, the force tracking accuracy is quite good, with tracking error amplitudes of less than $0.01\,\mathrm{N}$ generally.

The magnitude Bode diagram of Figure 7.1(a) shows all experimental plots having similar shape and curvature, although they are vertically parallel to each other within a small window of approximately $5\,\mathrm{dB}$. It indicates that the magnitude is relatively independent of different wire stress-strain conditions. At the lowest frequencies, the slope of the magnitude curves appears to be low, although not completely horizontal. Further experiments at frequencies lower than $0.1\,\mathrm{Hz}$ may yield more convincing results. At approximately $1\,\mathrm{rad\,s^{-1}}$, the curves switch to a slope of approximately $+24\,\mathrm{dB}$ per decade, which suggests the existence of a zero close to this frequency. The curves switch back to be horizontal again at approximately $40\,\mathrm{rad\,s^{-1}}$. This suggests a pole in this frequency region. In general, the magnitude plot implies that as the frequency increases, the tracking power signal increases in order to maintain the wire tension.

The phase Bode diagram of Figure 7.1(b) depicts the experimental plots as being more than 180° out of phase compared to the input strain signal. This implies that a positive strain (the wire is stretched) would cause a decrease in heating power in order to track a desired wire tension; and vice versa, a negative strain (the wire becomes more slack) induces an increase in heating power to track the desired tension. At the lowest frequencies, the phase curves exist within a window of approximately 15°, but they converge at the middle of the $0.1-10\,\mathrm{Hz}$ range, and diverges again at the higher frequencies. This indicates that the phase curves are generally similar, although not completely independent of different tested stress-strain situations. By extrapolation at frequencies lower than the tested range, the phase curves appear to be 180° out of phase, indicating the inverse relationship between strain and heating power. The curves of Figure 7.1(b) are observed to undergo a positive phase change at lower frequencies, followed by a negative phase change at the higher frequencies. This is compatible with the magnitude response, which suggests that the strain-power behaviour can be linearly modelled with a zero at low frequencies, and a pole at high frequencies. It can also be seen that at high frequencies, the phase shift

---

[2]The strain is given by $\frac{\Delta l}{l_0}$ where Δl is the peak-to-peak wire length change and l_0 is the initial wire length.
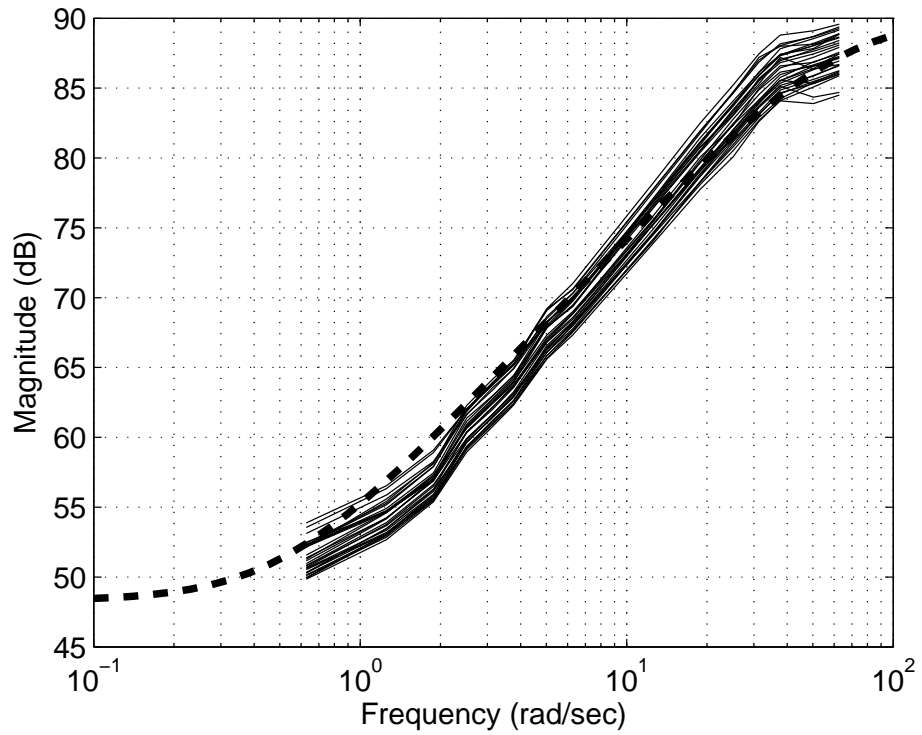
(a)
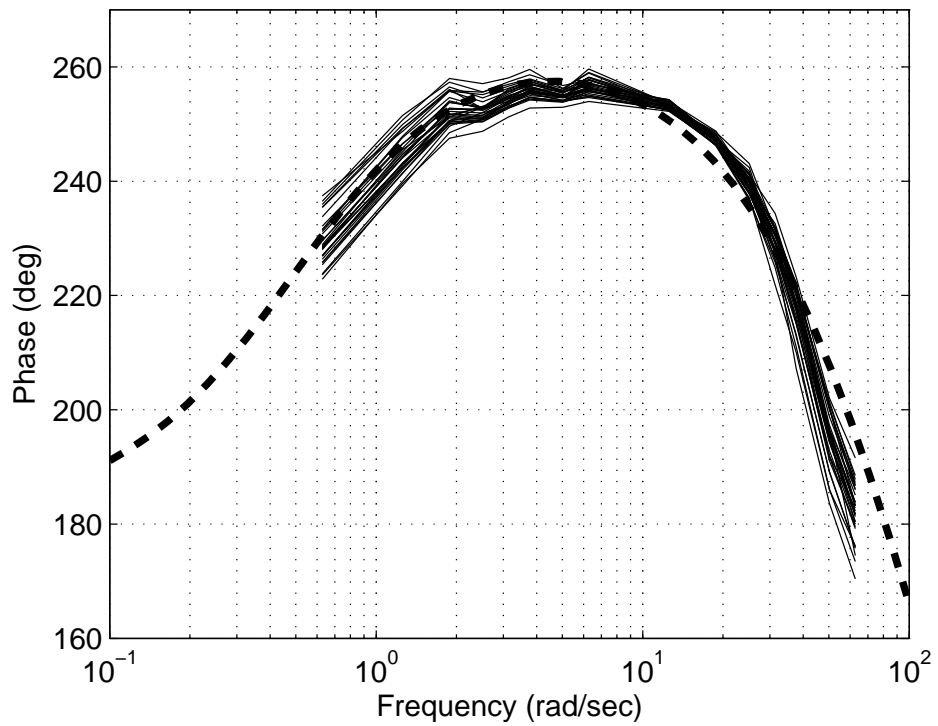
(b)

Figure 7.1: Bode magnitude and phase plots of the $100\,\mu$m-diameter Flexinol wire frequency response data and the derived strain-power model, $H(s)$. Solid black lines = experimental data. Dashed black line = model.

appears increasingly larger in proportion to the frequency with little attenuation.

Although the frequency response data for the strain-power relationship is not as conclusive and convincing as the power-force modelling results in Chapter 4, it still suggests that this dynamic behaviour can be modelled in a linear fashion. The accuracy of the resulting model is expected to be poor, but still sufficient to assist the design of a position control system.

Let $X(s)$ and $D(s)$ denote the Laplace transforms of the wire strain variations and the change in heating power signals, respectively. The strain to power relationship of an SMA wire can be modelled by a transfer function, $H(s)$, which satisfies

$$D(s) = H(s)X(s). \tag{7.2}$$

The frequency response data suggests that a single pole and zero system can be used to model the strain-power behaviour of the $100\,\mu$m Flexinol wire. In order to match the frequency response data more accurately, especially at high frequencies where excessive phase lag is observed, a time delay is added to an inverted first-order transfer function with a zero and a pole, to produce the following expression:

$$H(s) = -\frac{Ke^{-sL}(T_1 s + 1)}{(T_2 s + 1)}, \tag{7.3}$$

where the parameters are determined as $K = 260$, $L = 0.008$, $T_1 = 1.9894$, and $T_2 = 0.0159$. This model has been plotted as the dashed curve in Figure 7.1.

7.1.3   Position Model of Antagonistic SMA Actuator

For an SMA wire undergoing resistive heating in the constrained length case (no strain changes), the input power to output force relationship can be modelled as

$$F(s) = G(s)P(s), \tag{7.4}$$

which is Equation 4.13 of Chapter 4. The transfer function $G(s)$ is given in Equation 4.15.

An SMA wire undergoing various heating, stress and strain conditions can be completely described using the above Equation 7.4 rewritten as,

$$F(s) = G(s)[P(s) + D(s)], \tag{7.5}$$

where D(s) denote the input power variations due to strain changes in the Laplace domain.

Substituting Equation 7.2 into Equation 7.5, we obtain the following:

$$F(s) = G(s)P(s) + G(s)H(s)X(s). \tag{7.6}$$

The model of a revolute joint actuated by an antagonistic pair of SMA wires that moves an external link such as the one shown in Figure 4.3(b) can now be constructed. The model consists of several subsystems, each representing a part of the physical system's behaviour, as shown in Figure 7.2. It consists of the two SMA wire blocks described by Equation 7.6, one for each SMA in antagonistic arrangement, a joint dynamic model block and a joint kinematic model block. $F_1(s)$ and $F_2(s)$ denote the force outputs from the left and right SMA wires respectively.
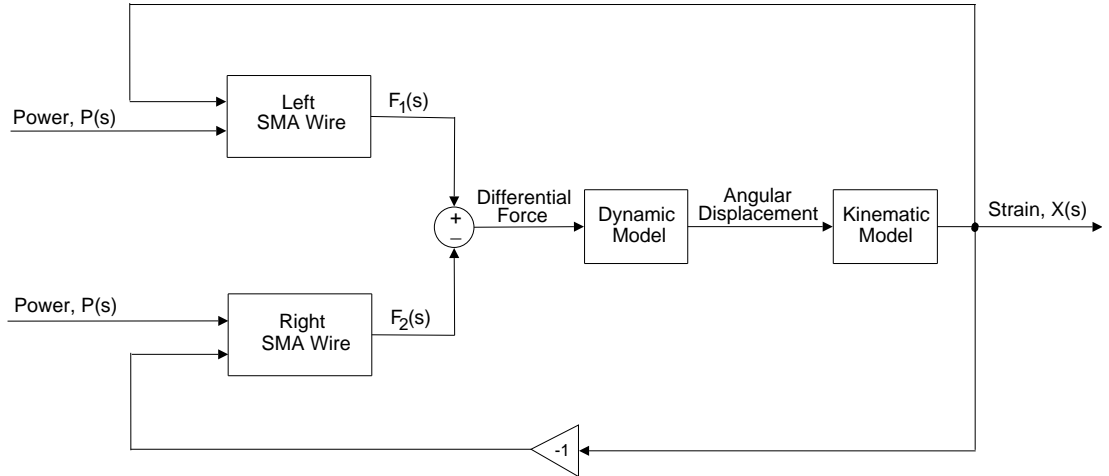
Figure 7.2: Open loop position model for robotic joint actuated by an antagonistic SMA actuator.

The nonlinear dynamic model of the robotic joint describes the relationship between the torque produced by the differential force from the SMA actuator, and the angular displacement of the moving external link (which acts like a pendulum), and it includes the payload effect of the link as well as damping in the system. This nonlinear model is given as:

$$I\ddot{\theta} + c\dot{\theta} + mgx_{cm}\sin\theta = Fr, \tag{7.7}$$

where I is the link's moment of inertia about the rotational axis, c the torsional damping coefficient, m the mass of the moving external link, g the gravitational

acceleration due to the Earth's mass, x_{cm} the distance between the link's centre of mass and the joint axis, F the differential force produced by the antagonistic SMA wires, r the radius of the pulley, and θ the angular displacement. Because there is negligible sliding contact in the system (with ball bearings used for the pulley), Coulomb friction is not considered in the model.

If the motion is assumed to be small enough, for instance, $\theta \leq \frac{\pi}{9}$ rad (or 20°), that we can let $\sin \theta \cong \theta$, then Equation 7.7 becomes a linear equation. Rewriting it in the Laplace domain, we obtain

$$\frac{\theta(s)}{F(s)} = \frac{r}{Is^2 + cs + mgx_{cm}}, \tag{7.8}$$

which is essentially a mass-spring-damper system.

The kinematic model describes the relationship between the angular displacement θ and the wire strain variation $X(s)$. Starting from the link's rest position and measuring positive angle anticlockwise, the equation is

$$X(s) = r\theta, \tag{7.9}$$

where angular displacement θ is measured in radians.

Table 7.1 lists the modelling parameters and their numerical values which have been determined empirically.

Parameter	Description	Unit	Value
I	Moving link's moment of inertia	kgm^2	0.00059
c	Torsional damping coefficient	kgm^2s^{-1}	0.007
m	Moving link's mass	kg	0.079
g	Gravitational acceleration	ms^{-2}	9.81
x_{cm}	Distance from link's centre of mass to joint axis	m	0.07925
r	Pulley radius	m	0.008

Table 7.1: Modelling parameters and their numerical values.

7.2   Position Control Architecture

7.2.1   Control Challenges

Consider a robotic joint application controlling the motion of a heavy link. This joint is actuated by two thin SMA wires which provide the rotational motion. In this case, the total mass of the two SMA wires which are each 80 cm-long is approximately 0.08 g (based on a density of $6.45\,\mathrm{g\,cm^{-3}}$); whereas the mass of the moving link is 79 g. This is close to 1000 times greater than the actuator's mass, which makes the inertia of this moving link difficult to control. In addition, the coupling effects between the SMA wires also effectively increase the magnitudes of the individual wire forces, thereby increasing the risk of overstressing. The coupling also reduces the differential force output, thus limiting the amount of torque available to the SMA actuator.

Finally, the dynamics of this pendulum-like link as well as the large coupling effects between the antagonistic SMA wires pose a difficult problem for the task of achieving fast and accurate controlled motion. Past attempts at controlling such high inertia loads have suffered from limit cycles, or oscillations around the set point.

Until now, the problem of significant limit cycles had never been completely solved. These limit cycles degrade the performance of the control system, and may even produce unstable oscillations. This problem is undesirable in robotic applications as it causes excessive wear and tear to the actuating system. Grant's research using a two-stage relay controller produced very large and high-frequency limit cycles, and even with the implementation of a variable dead band controller, limit cycles still persist [23]. Van der Wijst's work on SMA model-based position control, also did not manage to suppress the limit cycles caused by load disturbances acting on the system [77]. It is also understood that standard PID controllers in the position loop are generally inadequate to achieve both fast and accurate SMA-actuated motion control in the presence of heavy external loads.

A two-loop position control architecture is proposed in the next section. By controlling the forces of the SMA wires rapidly and accurately using a high-bandwidth inner-loop force controller, we are able to show that the dynamic response of the system can be stabilised, and that position limit cycles can be completely eliminated. Results show that closing the position loop, in addition to the inner differential force controller, produces a highly accurate SMA motion control system in the presence of heavy loads. For experiments in this chapter,

we use the same load as was used in Section 6.5 of Chapter 6: a 79 g pendulum attached to the pulley. The pendulum can be seen in Figure 4.3(b).

7.2.2 Two-Loop Position Control System
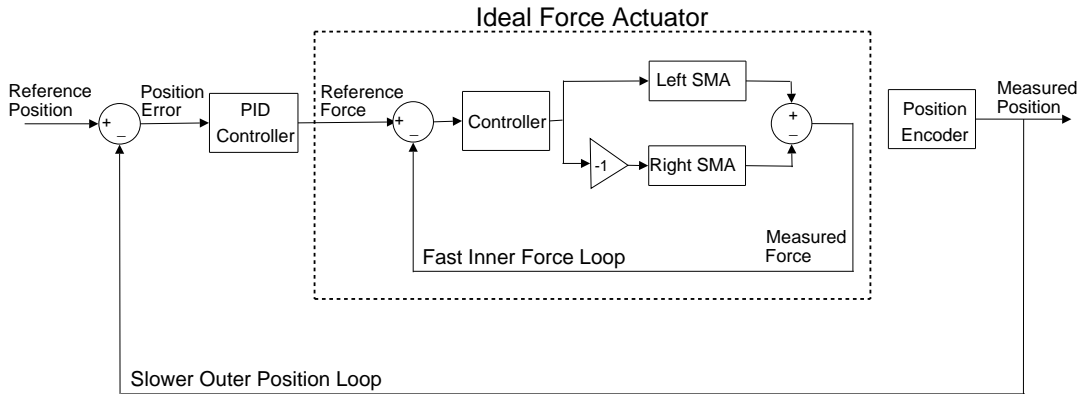
Figure 7.3: Position control system with two-loop control architecture for an antagonistic SMA actuator.

The SMA position control system adopts a two-loop control architecture as shown in Figure 7.3. It consists of a fast, high-bandwidth inner force loop, based on the control architecture in Figure 6.1, and a slower, outer position loop closed around the rotation of the joint. The outer position controller determines a control input which acts as the reference force for the inner force controller to track. The reasons for choosing this two-loop control architecture are summarised as follows:

  i.   The SMA test bed has high-bandwidth force sensors capable of providing highly accurate force measurements.

 ii.   The differential force control architecture has achieved fast, accurate force control of antagonistic SMA wires with excellent motion and load disturbance rejection. This controller is suitable for use as the inner force loop.

iii.   With the inner differential force controller, the antagonistic SMA actuator can be assumed to behave like an ideal force actuator. So whatever force commands are required within the possible range of the actuator, the inner force loop can be expected to quickly achieve the desired setpoint or response with high accuracy, and without limit cycles or steady-state errors.

 iv.   This two-loop control architecture may be able to eliminate limit cycles and compensate for external load disturbances.

Note that the rapid-heating, the anti-slack and the anti-overload mechanisms are always implemented in the inner differential force loop although not shown in the simplified diagram of Figure 7.3. The rapid-heating mechanism attempts to provide large heating power to rapidly achieve the desired differential force. The anti-slack mechanism may be affected by the coupling effects of the wires, which stretch the passive wire and increase the wire tension even when the wire is not being heated. This is especially so during constantly varying position tracking compared to setpoint tracking. Furthermore, the anti-overload threshold may also need to be increased due to this wire coupling effects.

The outer position loop also implements a PID controller which has first been tuned in simulation using the open loop position model of Section 7.1.3, and then fine-tuned online using the SMA test bed. The proportional feedback term affects the speed of response as well as the transient overshoot; the integral term aims to eliminate steady-state errors, at the expense of worse dynamic response due to the load inertia; the derivative term is used in conjunction to increase the damping and stability of the system. By combining the force controller and the outer-loop position controller, it is possible to achieve accurate SMA motion control with no limit cycles, and an acceptable level of speed response.

7.3 Results and Discussions

The experimental results based on the two-loop control architecture are presented in this section, in which the position model has been integral in designing and tuning this control system. Three categories of responses are studied: step responses, ramp responses as well as sinusoidal tracking responses. The maximum peak-to-peak rotation that can be tested is 40°. This 40° range constitutes the full working range of the pendulum, limited by the dimensions of the test bed column. Ignoring physical limitations, the maximum allowable rotation should be 115°, based on a standard 4% wire strain.

The fine-tuned parameters of the position PID controller are $K_P = 0.5$, $T_I = 0.1$ and $T_D = 0.06$, with the control input (reference force) into the inner force loop saturated at ± 3 N. The differential force PID controller parameters are set to the same values as in Chapter 6. Other control parameters used are: anti-slack threshold $F_{min} = 0.2$ N, rapid heating $P_{hi} = 14.4$ W (or equivalently 0.4 A), and anti-overload threshold $F_{max} = 6$ N. The experimental force data have also been processed offline with the same 4th-order, zero-phase, low-pass Butterworth filter

as in previous chapters. All data have also been downsampled by a factor of 8.

At the end of each subsection, some simulation results based on the above final control parameters are presented as a comparison.

7.3.1   Step Response

Figure 7.4 shows the experimental response to $\pm 10°$ step commands. The position response of Figure 7.4(a) demonstrates good speed response to the 20° peak-to-peak magnitude steps, with a rise time of 0.2 s and a settling time of approximately 1 s. The slower settling time is due to the transient response of the pendulum inertia. However, there are no limit cycles or steady-state errors, with stable setpoint tracking as can be seen in the position error results of Figure 7.4(b), while Figure 7.4(f) presents a more detailed view of the position errors, with the y-axis scale increased by a factor of 10. There are several 0.04° error spikes during steady-state due to minuscule variations in the actuator. This is caused by free convection around the actuator, as the SMA-actuated joint is placed in an open, non-temperature-controlled environment. This 0.04° error is only 0.035% of the 115° maximum range (based on the pulley dimensions and a 4% wire strain). Note also that 0.04° represents the absolute resolution of the encoder on the pulley, which means that it is possible to achieve better accuracy with a higher resolution optical encoder.

Figures 7.4(c) and 7.4(d) show the differential force tracking results and individual wire forces from the inner force loop respectively. The inner force controller has the capability to rapidly and accurately track the reference force command from the outer position loop. In terms of the individual SMA wires, peak forces of 4 N are reached due to the large heating currents allowed by the rapid-heating mechanism, and also due to the large load dynamics and wire coupling effects. It can also be observed that a low force threshold of approximately 0.2 N has been maintained for the passive wire as it cools down during steady-state.

Figures 7.4(e), 7.4(g) and 7.4(h) present detailed views of the response during one particular step between $0.5 - 2.5$ s. Starting at 0.5 s, the pendulum is maintained at the $-10°$ position (which is 10° clockwise from the rest position). During this steady-state, the right SMA wire is being heated more than the left SMA wire, i.e., the right wire is in contraction (right SMA force measuring 1.4 N in Figure 7.4(h)) whereas the left wire is being stretched (left SMA force measuring 0.2 N due to anti-slack mechanism). At 1 s, there is a step change from $-10°$

Figure 7.4: Experimental position response for steps of ±10°. (a) Position response, (b) its corresponding position errors, (c) inner-loop differential force response, and (d) individual SMA forces. (e), (f), (g) and (h) show the respective detailed views.

to $+10°$, and the control system attempts to track this command. The position controller initially demands the maximum differential force ($+3\,$N). This step change causes the left SMA wire to contract and the right SMA wire to cool and stretch. The pendulum also begins to swing from the $-10°$ to the $+10°$ position energetically due to its momentum and the torque produced by the SMA wires. The position PID controller attempts to dampen the dynamic response of the pendulum and stabilise the system to prevent unwanted oscillations. This can be seen in Figures 7.4(e) and 7.4(g), where beginning at $1.1\,$s, the position controller demands for a decreasing differential force from an initial $+3\,$N to approximately $-1\,$N, even before the pendulum reaches the $+10°$ setpoint. When the $10°$ setpoint is reached, a differential force of approximately $1.3\,$N is maintained.

For larger step responses of $\pm 20°$, the results are given in Figure 7.5. In this situation, there is more energy and momentum in the system compared to the $\pm 10°$ steps, as the range of the pendulum swing is larger, and more torque is generated by the wires to reach the larger setpoints. Oscillations and undershot are observed during the transient response, which affects the tracking speed. Figure 7.5(a) shows a larger rise time of approximately $0.5\,$s as well as a settling time of $1.5\,$s. The damping capacity of the two-loop controller necessitates the slower transient responses in order to reduce the energy and oscillations of the system. However, once the setpoints are reached, there are no limit cycles and zero position errors are observed in Figures 7.5(b) and 7.5(f). Steady-state accuracy of better than 0.035% of the $115°$ range is achieved.

The detailed views for one transient response (Figures 7.5(e), 7.5(g) and 7.5(h)) show more oscillations compared with Figure 7.4, and therefore a longer time is required to stabilise the system dynamics. It is also observed that individual SMA forces reached the anti-overload threshold of $6\,$N during the transient but gradually decreases to normal force ranges within $1\,$s (see Figures 7.5(d) and 7.5(h)). It can also be seen in Figure 7.5(c) that to keep the pendulum link at the $\pm 20°$ positions, large differential forces of approximately $\pm 2.5\,$N are required.

In Figure 7.4(d) and Figure 7.5(d), it can be seen that during the transient, force is being applied on the two SMA wires at the same time. For an antagonistic arrangement, having both wires applying high stress in the austenite state can decrease the lifetime of the material. Therefore the control system must be able to ensure that both SMA wires are not being heated at the same time during the high-temperature state.

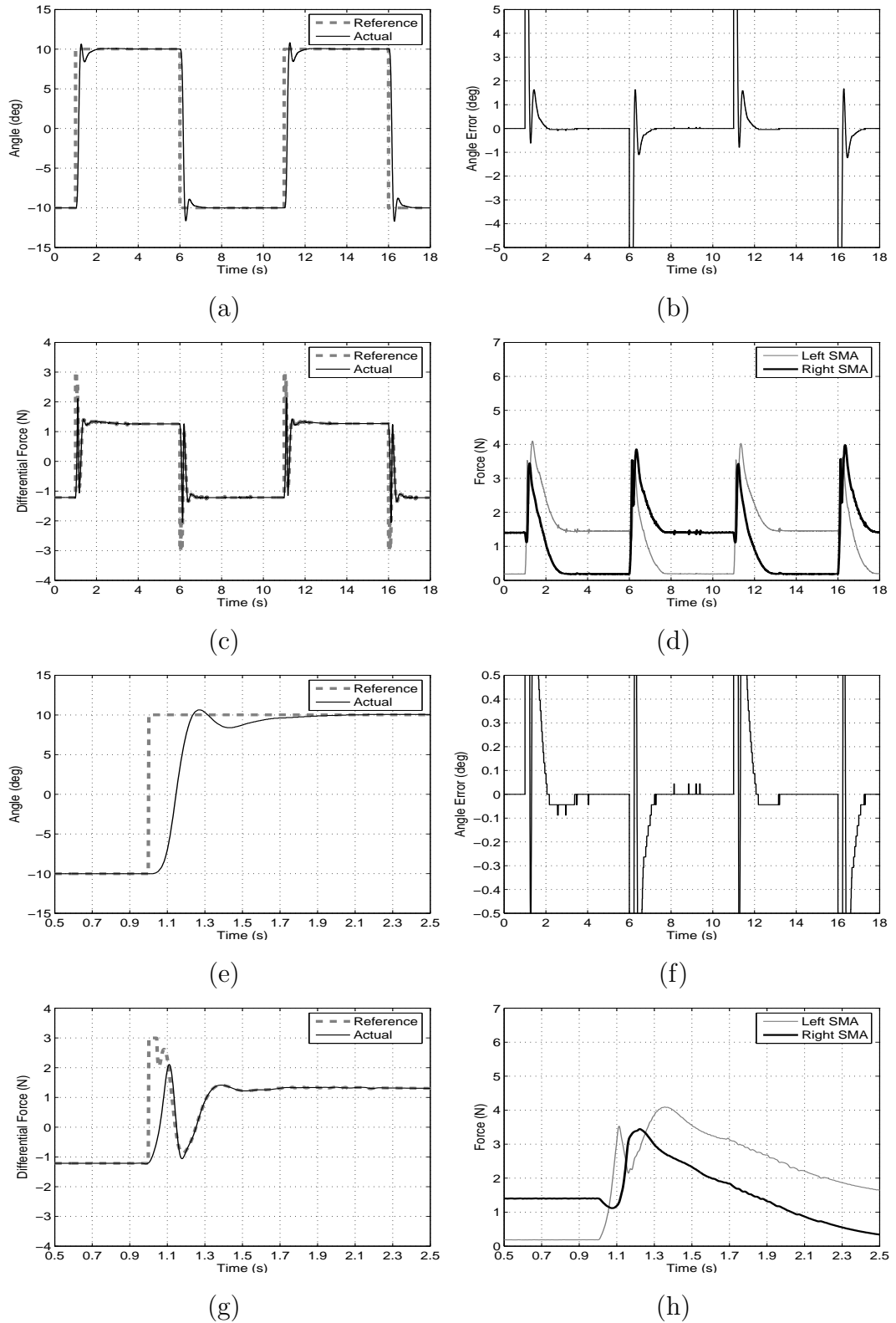Figure 7.6 shows detailed individual SMA forces and heating currents of the
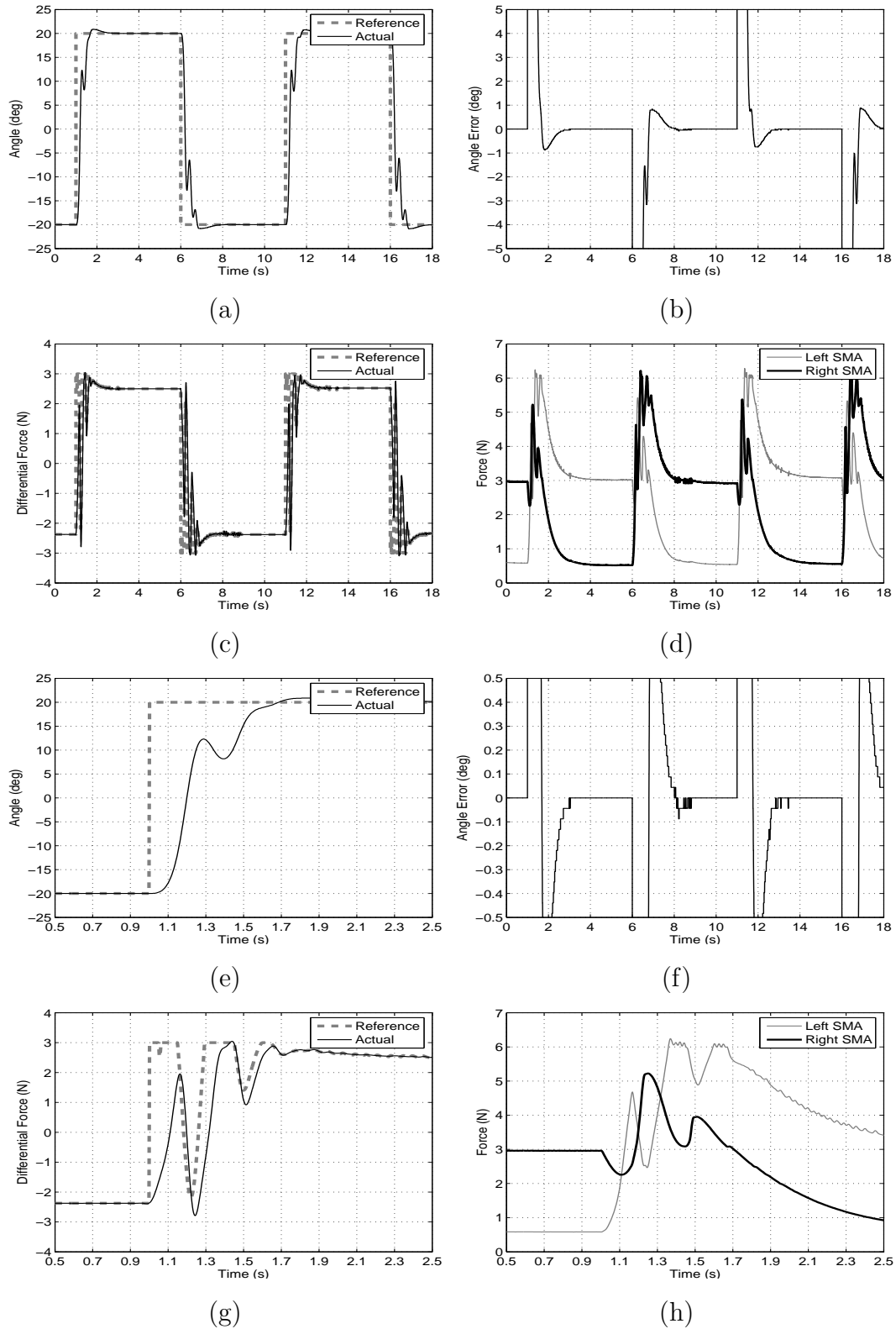
Figure 7.5: Experimental position response for steps of $\pm 20°$. (a) Position response, (b) its corresponding position errors, (c) inner-loop differential force response, and (d) individual SMA forces. (e), (f), (g) and (h) show the respective detailed views.

results from Figure 7.4 and Figure 7.5 between $0.9-1.9\,\mathrm{s}$ for a single step transition. It is evident from these graphs that during the transition, only one SMA wire is being heated at a time. Once the responses have settled to a steady-state, the wires do not need to apply high forces further and the individual SMA forces begin to decrease, whilst maintaining the differential force to track the setpoint. As the wires have cooled and are no longer in the high-temperature state, low current levels may be applied to both wires to keep the wires taut as well as to track the position setpoint. This is particular apparent in Figure 7.6(c) from approximately $1.25\,\mathrm{s}$ onwards, when the setpoint of $+10°$ has been reached.
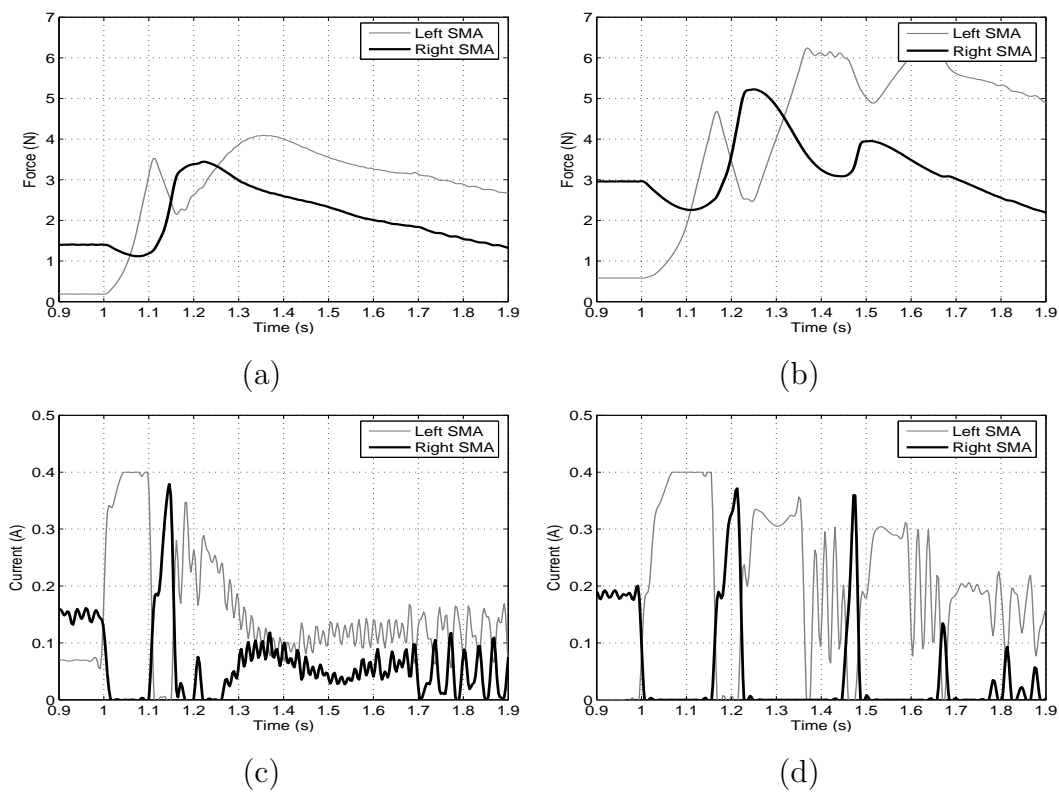
Figure 7.6: Detailed views $(0.9-1.9\,\mathrm{s})$ of (a) individual SMA forces and (c) SMA heating currents from results in Figure 7.4. Detailed views $(0.9-1.9\,\mathrm{s})$ of (b) individual SMA forces and (d) SMA heating currents from results in Figure 7.5.

Some simulated step responses are given in Figure 7.7 for comparison. Several observations can be made about the simulation. First, the simulation predicts larger overshoots in transient response based on the experimentally fine-tuned control parameters, although the rise times and settling times are similar to the experimental results. Second, the simulated differential force responses at steady-state are similar to the experimental results. The differential forces converge to $\pm 1.4\,\mathrm{N}$ and $\pm 2.7\,\mathrm{N}$ for the $\pm 10°$ and $\pm 20°$ steps respectively. The convergence
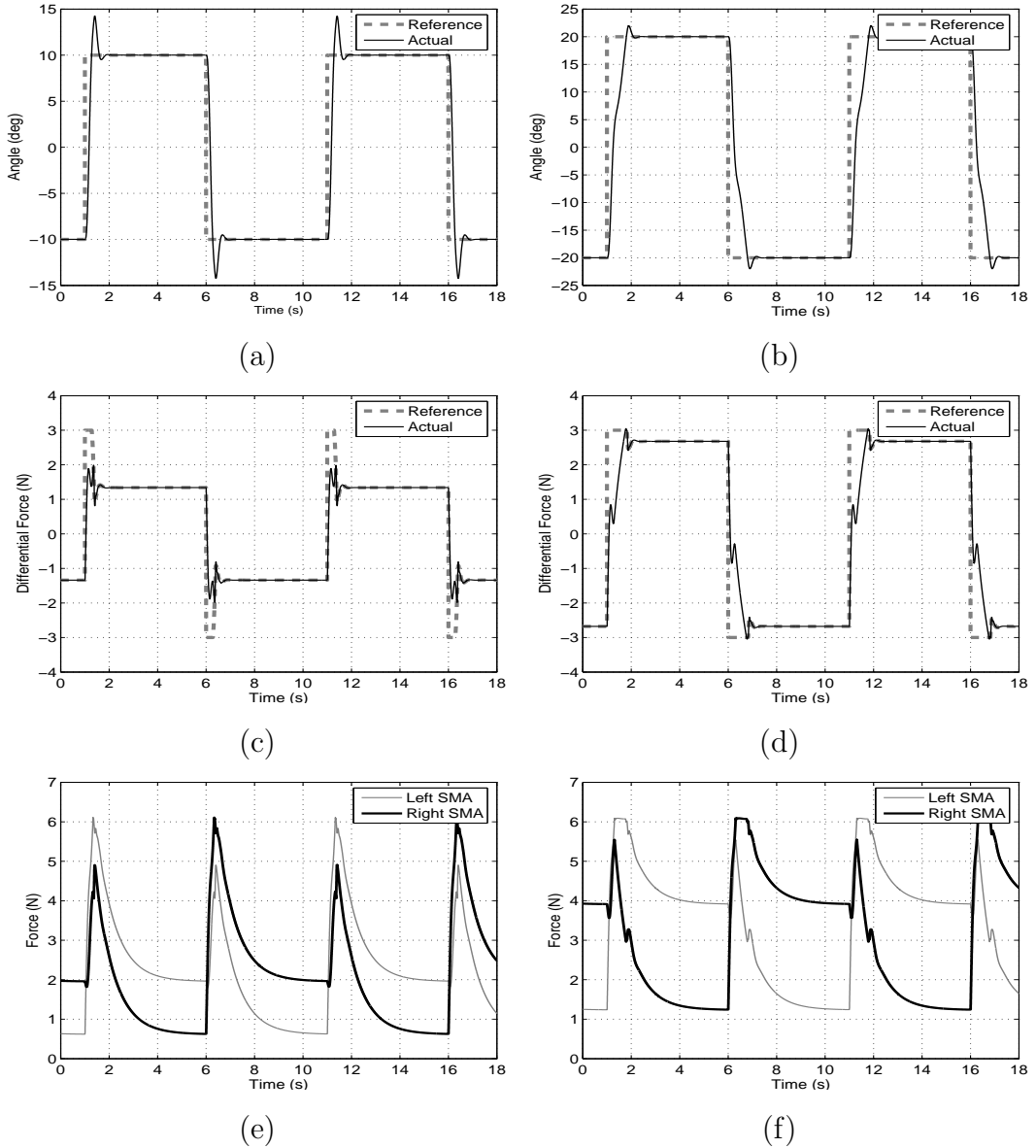
Figure 7.7: (a) Simulated position response for steps of $\pm 10°$, (c) its corresponding inner-loop differential force response, and (e) individual SMA forces. (b) Simulated position response for steps of $\pm 20°$, (d) its corresponding inner-loop differential force response, and (f) individual SMA forces.

of the simulated differential force response at steady-state, which is due to the static equilibrium of the system, demonstrates good matching of the system's physical parameters. Third, in terms of individual SMA forces, the simulation predicts slower SMA cooling rates, as can be seen in the slower decrease in the passive wire's force. This results in higher average SMA forces.

Nonetheless, the proposed two-loop control system has been able to dampen and stabilise the dynamic response of the system, at the expense of slightly slower speed. However, this speed of response is still good considering the large

mass of the load compared with the actuator. The experimental results clearly demonstrate the effectiveness of this controller. In the next two sections, the tracking performance of the control system for continuously changing commands will be examined.

7.3.2 Ramp Response
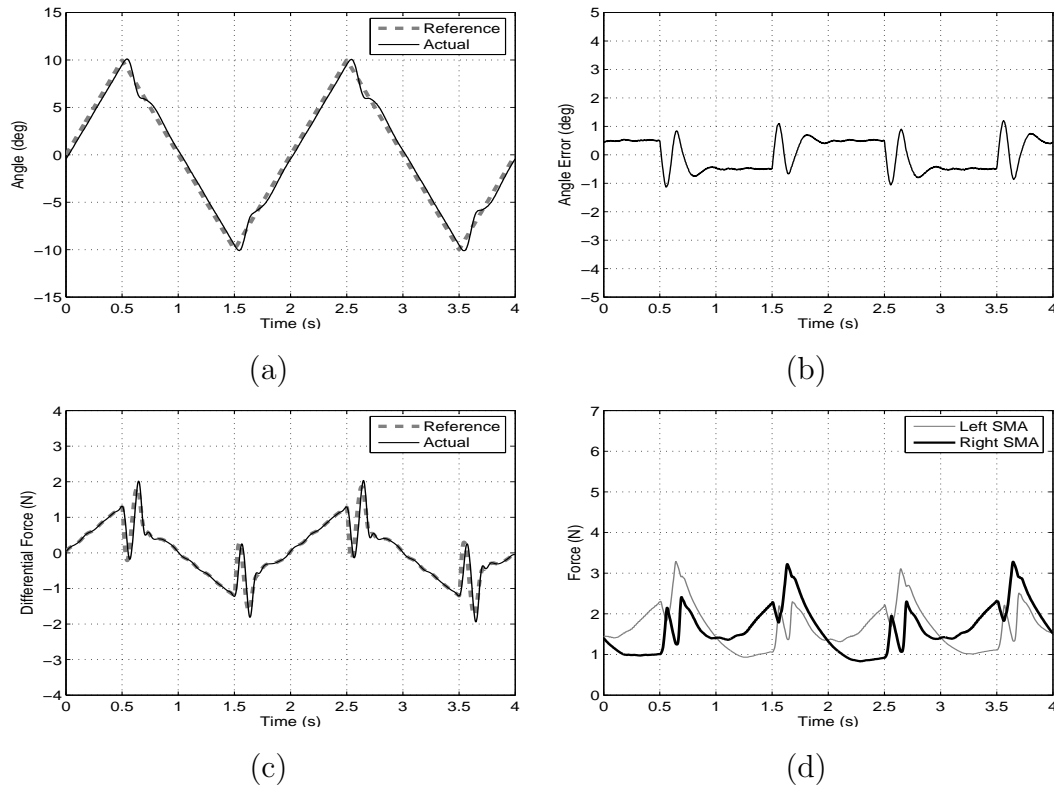
Figure 7.8: Experimental position response for $\pm 10°$ ramps with ramp rates of $\pm 20°\text{s}^{-1}$. (a) Position response, (b) its corresponding position errors, (c) inner-loop differential force response, and (d) individual SMA forces.

The experimental results for tracking various ramp commands are investigated in this section. Firstly, the response to $\pm 10°$ ramps with ramp rates of $\pm 20°\text{s}^{-1}$ is given in Figure 7.8. Physically, accurate tracking of the ramps imply that the pendulum moves from one side to the other at a constant velocity given by the ramp rate. This is compared to the situation in which the pendulum swings naturally under gravitational pull with no external force or disturbance — the pendulum accelerates as it approaches the rest position, and decelerates as it swings from the rest position. The control system needs to apply forces to the SMA wires to maintain a constant velocity for the pendulum movement.

It can be seen that the control system can produce fairly constant pendulum

velocities in order to track the position ramps, although not quite accurately at this speed. In terms of tracking errors, there are offsets of approximately $\pm 0.5°$, depending on the sign of the ramps. The start of each ramp excites the pendulum into slight oscillations, as can be observed in Figure 7.8(a), but the control system effectively dampens them out. The offsets in the tracking errors can be reduced using higher position PID gains, although this has a negative impact on the transient dynamics in step responses.

The force responses of the system (see Figures 7.8(c) and 7.8(d)) show that the wires can accurately track the differential force command from the outer position loop. The SMA forces are well within the safe range, but strong coupling effects are also observed.

Next, the tracking responses to larger $\pm 20°$ ramps at different velocities are presented in Figure 7.9. Starting at the smallest ramp velocities of $\pm 10°\text{s}^{-1}$ in Figure 7.9(a), it can be seen that the actuator manages to track the command very accurately, with position error offsets during the ramps of only $0.3°$ in Figure 7.9(b). This is only 0.26% of the $115°$ rotation range. As ramp rate increases, the tracking performance of the control system gradually degrades, as shown in experimental responses in Figures 7.9(c) and 7.9(e) with faster rates of $\pm 20°\text{s}^{-1}$ and $\pm 40°\text{s}^{-1}$ respectively. Larger position errors can be observed in Figures 7.9(d) and 7.9(f) respectively.

The SMA force responses for the $\pm 40°\text{s}^{-1}$ ramp response are presented in Figures 7.9(g) and 7.9(h). The force responses manage to track the required differential force accurately except at the peaks of the position ramps. The individual SMA forces clearly show the strong coupling effects between the wires. As the active wire is being heated to track the desired differential command, the passive wire cools down, but rather than becoming less taut, it is being stretched due to the active wire's contraction. As evident in Figure 7.9(h), the tension on both wires are kept rather high due to this effect and also because the wires may not have sufficient time to cool. Drifts in individual forces are due to air ventilation around the wires, as can be seen in Figure 7.9(h) over an extended period of 18 s.

Although at very high ramp rates, the control system did not manage to track the position commands very accurately, it is observed that unstable limit cycles are not produced. The oscillations at the beginning of the ramps in all three experimental responses have been dampened by the control system very quickly.
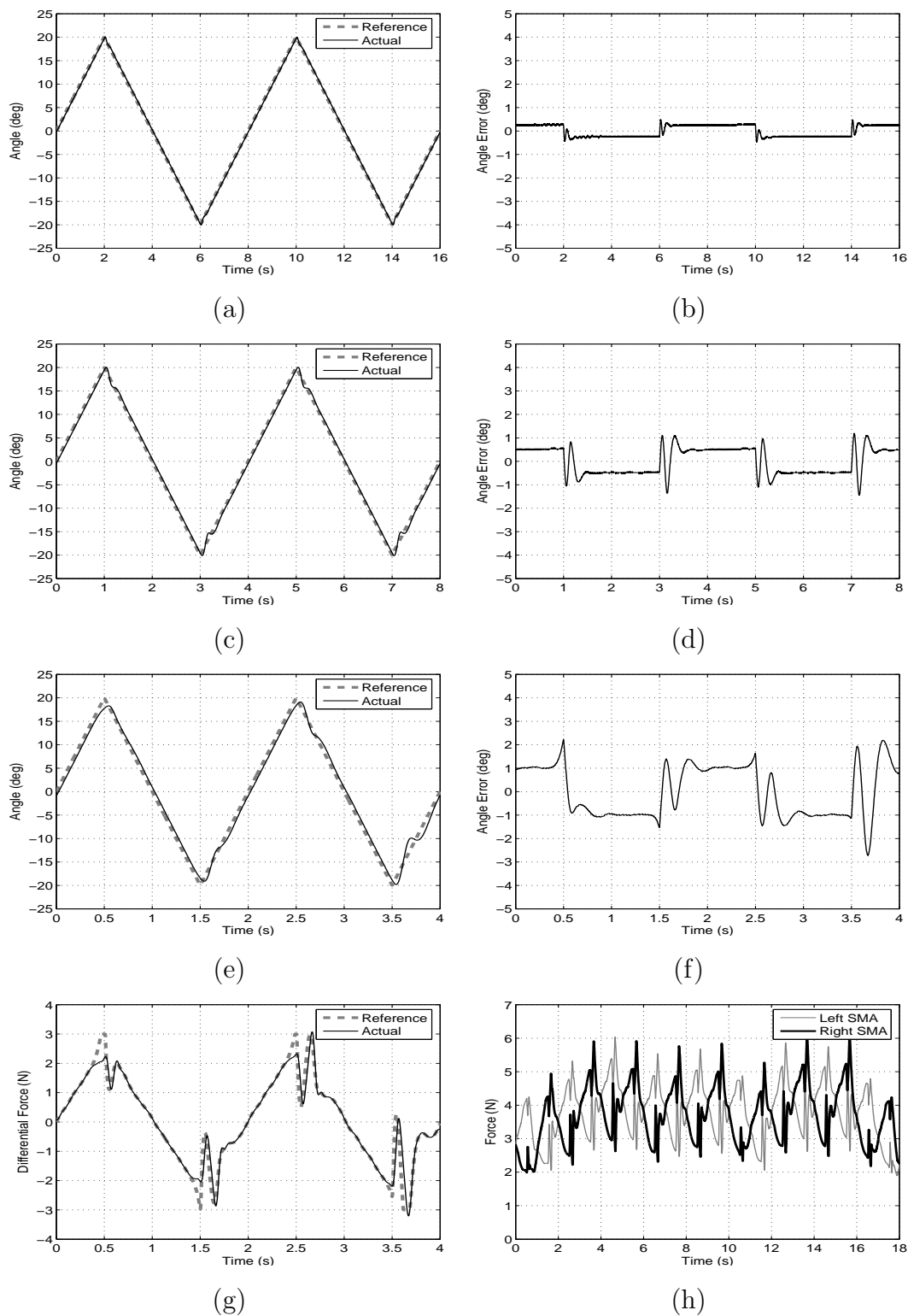
Figure 7.9: Experimental position responses for $\pm 20°$ ramps with ramp rates of (a) $\pm 10°\text{s}^{-1}$, (c) $\pm 20°\text{s}^{-1}$ and (e) $\pm 40°\text{s}^{-1}$ respectively, and the corresponding position errors in (b), (d) and (f). The inner-loop differential force response and the individual SMA forces for the results of (e) are shown in (g) and (h) respectively. Note that graph (h) is given over a period of 18 s.
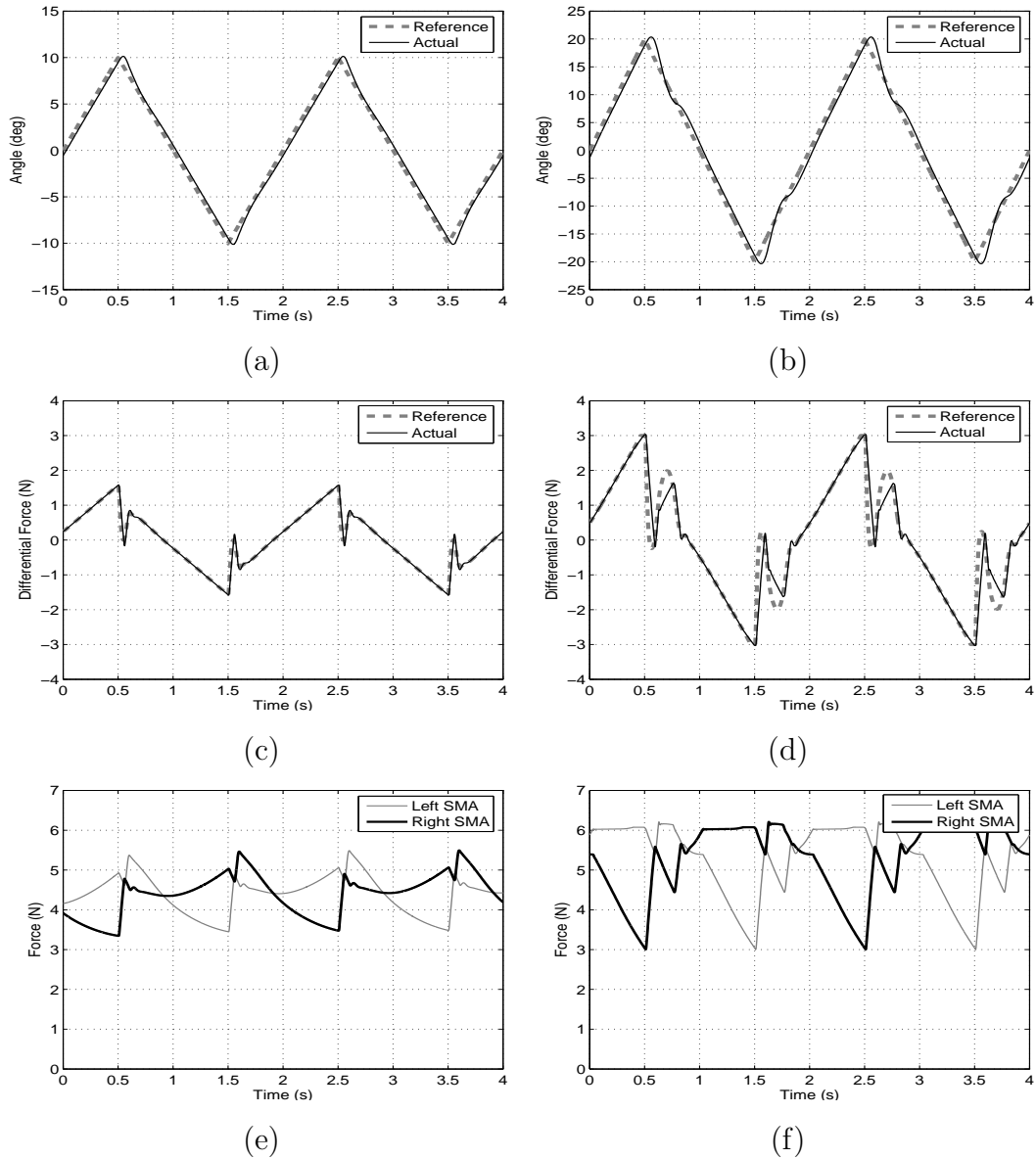
Figure 7.10: (a) Simulated position response for $\pm 10°$ ramps with ramp rates of $\pm 20°\mathrm{s}^{-1}$, (c) its corresponding inner-loop differential force response, and (e) individual SMA forces. (b) Simulated position response for $\pm 20°$ ramps with ramp rates of $\pm 40°\mathrm{s}^{-1}$, (d) its corresponding inner-loop differential force response, and (f) individual SMA forces.

Figure 7.10 presents some simulated ramp responses. Similar to the step simulations, they show the inadequacy of the model, by underestimating the cooling rates of the SMA wires. This results in higher average forces in the simulation. In terms of position responses, they are comparable to the experimental results.

7.3.3 Sine Response

In this subsection, experimental responses to various sinusoidal commands are studied. Figure 7.11 presents tracking results for a 1 Hz sine command with 20° peak-to-peak magnitude. The position response of Figure 7.11(a) shows stable tracking with no sign of limit cycles under the 79 g inertial load. However, it can be seen that the peak magnitudes of the 1 Hz sine command have not been tracked. This is due to low gains used in the position PID controller. Maximum tracking errors of 1° amplitude occur at these position peaks.

(a)   (b)

(c)   (d)
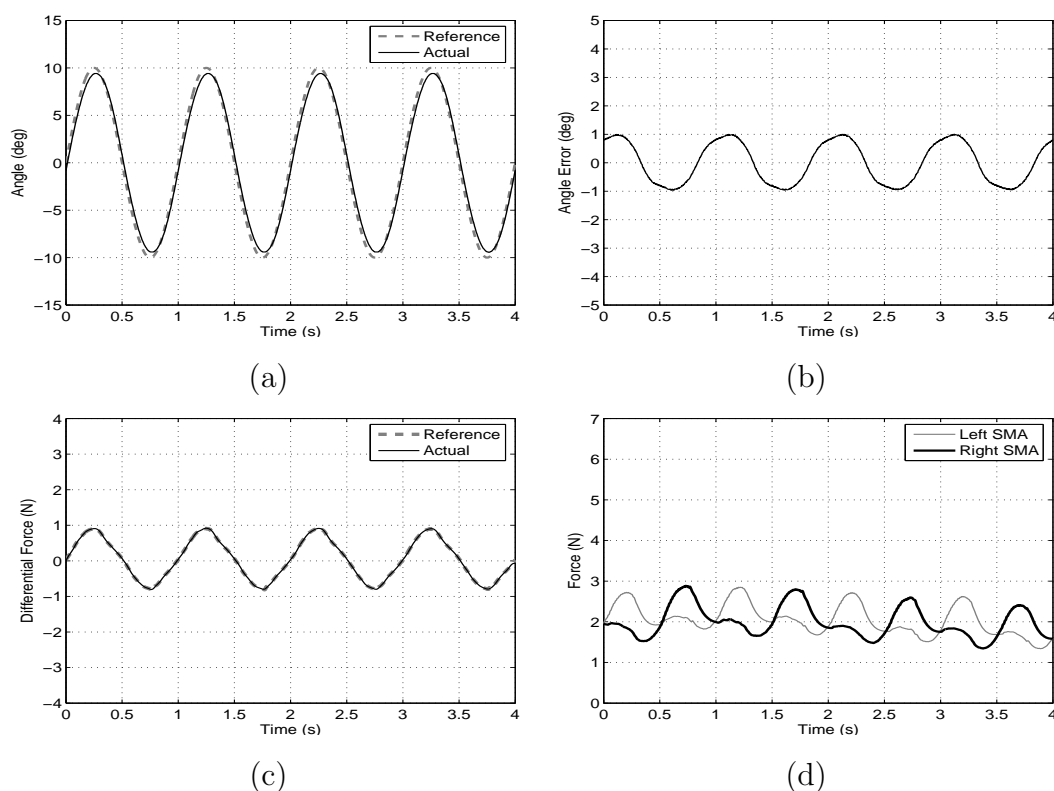
Figure 7.11: Experimental position response for a 1 Hz sine command with 20° peak-to-peak magnitude. (a) Position response, (b) its corresponding position errors, (c) inner-loop differential force response, and (d) individual SMA forces.

It can also be observed that the average SMA forces are approximately 2 N in Figure 7.11(d). This is due to wire coupling effects, which stretches the passive (less heated) wire and increases its tension. Also, the observed drifts in SMA forces are because of air ventilation around the actuator.

Figure 7.12 presents more tracking results for 40° peak-to-peak magnitude sinusoidal commands at various frequencies. In Figure 7.12(a), the sine response at 0.2 Hz produces very excellent tracking, with position errors of less than 0.3°. At a higher frequency of 0.5 Hz (see Figures 7.12(c) and 7.12(d)), the tracking
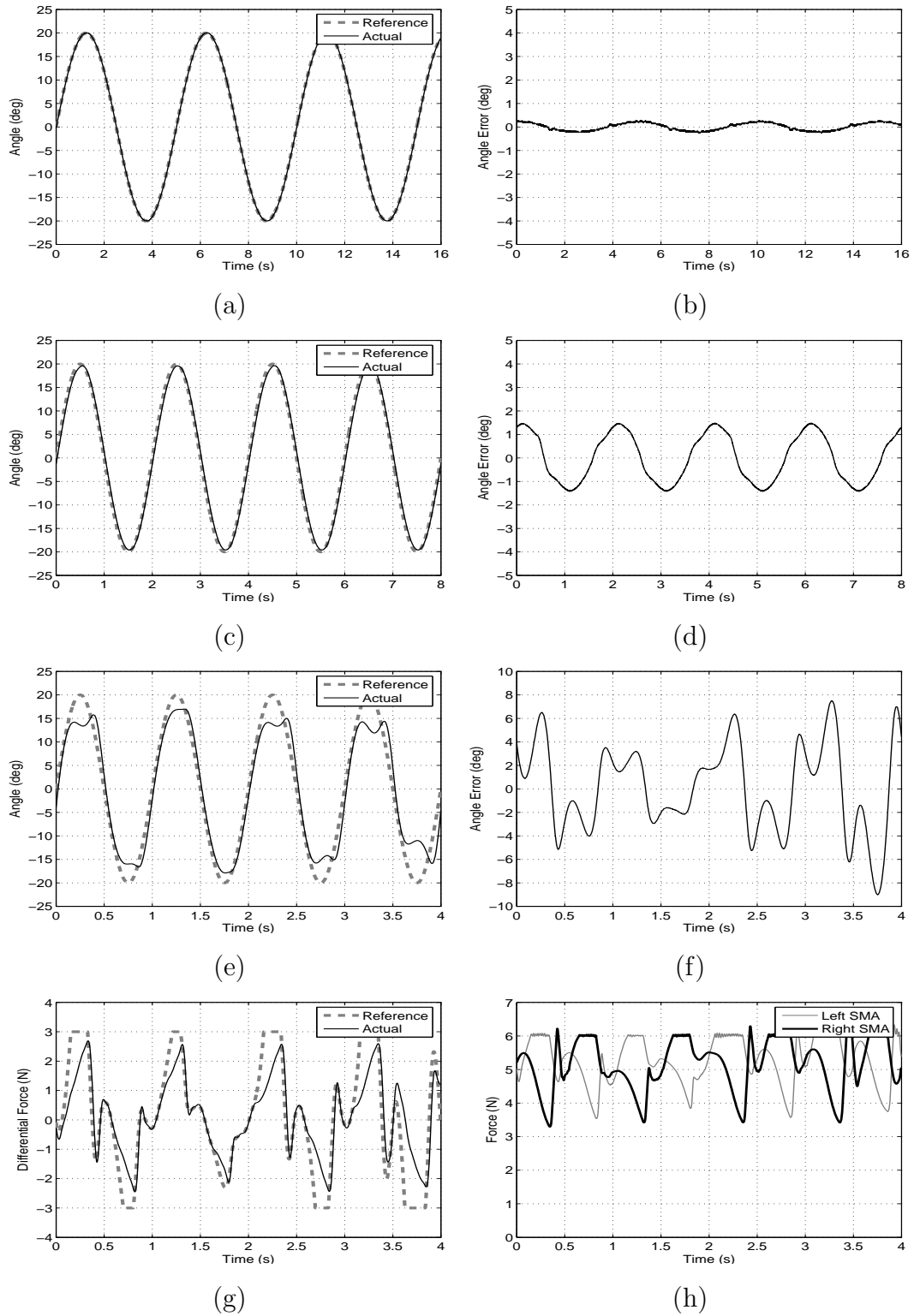
Figure 7.12: Experimental position responses for sine commands with 40° peak-to-peak magnitude at frequencies of (a) 0.2 Hz, (c) 0.5 Hz and (e) 1 Hz respectively, and the corresponding position errors in (b), (d) and (f). The inner-loop differential force response and the individual SMA forces for the results of (e) are shown in (g) and (h) respectively.

performance is affected, with increased position error amplitudes of 1.5°.

Finally, the experimental responses for a 40° peak-to-peak magnitude sine wave at a frequency of 1 Hz and its corresponding force responses are given in the Figures 7.12(e)–(h). It can be seen that the control system cannot follow the sine command completely, and misses the peak position magnitudes. This is caused by the activation of the anti-overload mechanism limiting the heating current to both wire actuators. This occurs when individual SMA forces reach 6 N, the F_{max} threshold, as can be seen in Figure 7.12(h). The wire coupling effects are very significant for this response. However, under the various tested situations, no limit cycles or unstable oscillations have been observed, due to excellent damping and force stabilisation of the two-loop control system.

The simulated sine responses are also given for comparison in Figure 7.13. Again, the slower cooling rates result in higher SMA forces. Although the 10° amplitude sine tracking is still good, for the larger 20° amplitude sine command, the simulation fails to track it completely. It clearly shows the weakness of the SMA position model in simulating the actual system for faster and larger responses. The problem lies in the underestimation of the SMA cooling rates by the model.
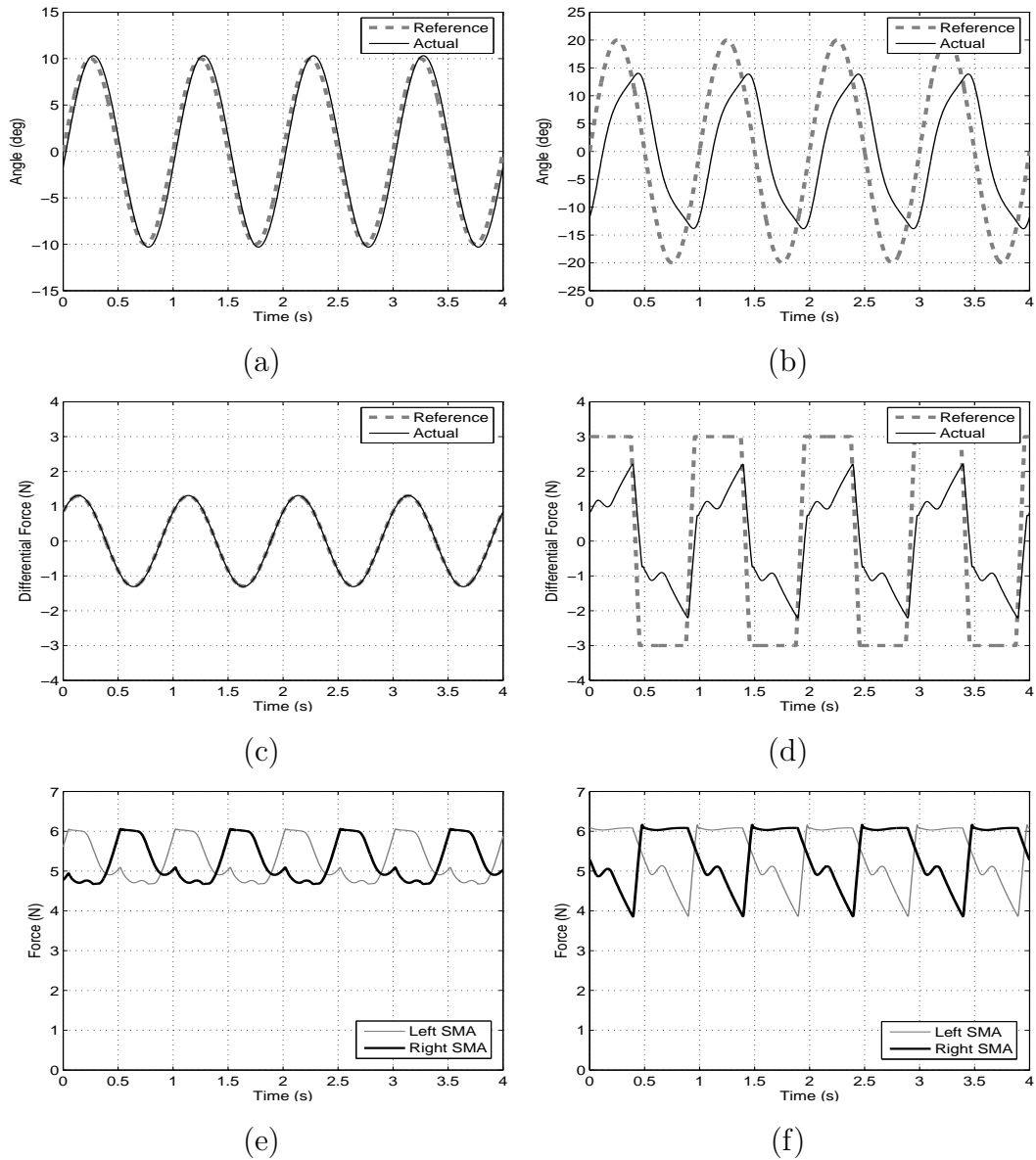
Figure 7.13: (a) Simulated position response for a 1 Hz sine command with 10°
amplitude, (c) its corresponding inner-loop differential force response, and (e)
individual SMA forces. (b) Simulated position response for a 1 Hz sine command
with 20° amplitude, (d) its corresponding inner-loop differential force response,
and (f) individual SMA forces.

7.4 Chapter Summary

This chapter examines the position control of an antagonistic SMA-actuated robotic joint application in the presence of heavy external load. An extended position model has been described and has been useful in the design and tuning of the two-loop position control system. This control system, which is formed by closing an outer position feedback loop around the successfully tested force controller of Chapter 6, demonstrates highly accurate positioning with no limit cycles or steady-state errors.

For experimental step responses, the control system achieves very stable steady-state tracking, with an accuracy of better than 0.035% of the 115° maximum range of the actuator. However, it should be admitted that this claim is based on data for only the central 40° portion of the actuator's motion range. The results also show excellent damping of the transient load dynamics, but at the expense of slower settling times. In terms of tracking continuously varying commands such as triangular and sinusoidal waveforms, the two-loop controller can track the commands accurately at frequencies of 0.2 Hz and 0.5 Hz. However, for 1 Hz commands, its tracking performance is diminished, especially at the peak magnitudes. It has also been observed that coupling effects between the SMA wires are very significant, and that individual wire stresses are quite high in tracking fast-varying commands. Nonetheless, it is also observed that there are no limit cycles, and oscillations are quickly dampened by the controller.

In summary, based on the results presented, the position tracking speed of the proposed two-loop controller is not as fast as the force tracking speed of the force controller. Although the speed of response can be improved using higher position gains or using larger heating currents, this excites the dynamics of the load inertia which may lead to unstable oscillations. However, it must be stressed that the position control system is manipulating a 79 g load, which is considered a very large mass compared to the SMA actuator, and that very accurate position response has been achieved.

CHAPTER 8

Conclusions

8.1   Summary of Contributions

In this thesis, the research on achieving faster and more accurate force and motion control of SMA actuators and the obtained results are documented and discussed. In many applications where space, weight and noise can be an issue, SMA actuators present a potential solution with their high force-to-weight ratio, mechanical compactness, ease of miniaturisation, as well as their clean and silent operation. With improved speed, accuracy and controllability, the possibilities of using SMA actuators in, to name a few, robotics, consumer appliances and bio-medical applications, are greater now.

Investigation of the high-frequency response of SMA Flexinol wires yielded some interesting results. In contrast to the general view, it was observed that high-frequency mechanical response of these SMAs can be induced even in the $500 - 2000$ Hz range at very minuscule strain variations (probably less than one micron). The experimental evidences seemed to show that this is due to the shape memory effect, rather than thermal expansion and contraction. The results opened the door for the possibility of implementing high-bandwidth control systems of SMA actuators. This control method may be able to stabilise system response in the presence of external load inertia.

Force models for a constrained single SMA wire as well as for antagonistic SMA wire pairs were also presented in this work. The modelling experiments were based on frequency response analysis, which was possible as the SMA small-signal responses were observed to be almost linear, repeatable and containing very little hysteresis. Based on the results, the input power to output force relationship for an SMA wire can be approximated as a 1st-order linear system. The experimentally determined force models had been extended for position modelling of SMA wire actuators, of which the effects of strain variations on wire stress and

heating power were considered. The models had been very useful for control system design, tuning and simulation. Comparisons between simulations and experimental closed-loop responses were generally good, although the simulations underestimated the large-signal gains of the actual system, especially in terms of the SMA cooling rates. The modelling, force and position control experiments were conducted using a custom-designed and custom-built experimental test bed with highly accurate sensors and components.

High-gain PID controllers to achieve high-bandwidth control were employed in the force control of a single SMA wire as well as the differential force control of an antagonistic SMA wire actuator pair. To improve actuator speed while preventing overheating of the SMAs, a rapid-heating mechanism was included in the differential force control architecture. In addition, the anti-slack mechanism was implemented to prevent wire slack and keep the SMAs warm and taut for quicker response; the anti-overload mechanism was aimed at monitoring the SMA forces and preventing overstressing. The important results presented for force control in this work are summarised as follows:

i. The differential force response for $\pm 2.5\,\mathrm{N}$ steps achieved very high setpoint accuracy, with errors of less than $0.001\,\mathrm{N}$, which is 0.017% of the $6\,\mathrm{N}$ safe force range available to the antagonistic SMA actuator. This was achieved with high force rates of $50\,\mathrm{Ns^{-1}}$.

ii. The differential force controller resulted in accurate tracking of a $5\,\mathrm{N}$ peak-to-peak magnitude sine command at a frequency of $1\,\mathrm{Hz}$, with a maximum error amplitude of $0.002\,\mathrm{N}$. This was only 0.033% of the $6\,\mathrm{N}$ force range.

iii. For a $5\,\mathrm{N}$ peak-to-peak magnitude sine command at a higher frequency of $2\,\mathrm{Hz}$, the differential force controller still maintained excellent tracking with a maximum error amplitude of $0.02\,\mathrm{N}$. This was 0.33% of the $6\,\mathrm{N}$ force range.

iv. Continuous and aggressive operations demonstrated the excellent performance of the differential force controller with no degradation for more than 1 hour.

v. The control system also demonstrated very good motion disturbance and load inertia rejection. No unstable oscillations nor limit cycles were observed.

This work also addressed the position control of antagonistic SMA actuators, and the difficulty of eliminating limit cycles and unstable oscillations that may be

produced by external load dynamics and antagonistic wire coupling effects. This problem is particularly important for practical actuator applications, as they usually involve continuous motions and displacing a robotic link or a payload. In the experiments, a moving load of 79 g was tested, and it constitutes 1000 times the mass of the SMA actuator. A two-loop position control architecture was proposed, which has a fast, high-bandwidth inner force loop based on the differential force controller, and a slower outer position loop based on PID control.

For $\pm 10°$ steps, the experimental position response achieved a rise time of 0.2 s and a settling time of 1 s. For larger step commands of $\pm 20°$, which is the maximum angle through which the pendulum can swing without hitting the test bed, the results achieved a slower rise time and settling time of 0.5 s and 1.5 s respectively. The most important observation was that the experimental results showed no signs of limit cycles or oscillations, and very high position accuracy had been achieved with only a 0.04° position error amplitude. This value is the resolution of the position encoder, and it constitutes 0.035% of the 115° maximum rotation range of the actuator. This is based on data for only the central 40° portion of the actuator's motion range. The two-loop controller also managed to track various types of continuously varying commands with reasonable accuracy, but with no limit cycles.

To sum up, the research presented in this thesis represents a significant step forward for practical SMA actuator applications. Substantial improvements in terms of speed and accuracy of SMA actuator control have been made compared to past work, whilst some control means of monitoring the state of the actuator have also been provided, which can prevent the overheating and overstressing of the SMA actuators. All of these have been accomplished with free convection cooling and not in a temperature-controlled condition.

8.2 Future Work

Even though this work has resulted in practical control strategies that can improve the response speed and accuracy of SMA actuators immensely, there are several future research directions that can be followed. They are generally in the aspects of shape memory alloy modelling and characterisation, control systems, and actuator and test bed design.

8.2.1 Modelling and Characterisation

The various force and position models proposed in this thesis have been relevant and integral in the design and simulation of control systems, although there were discrepancies between closed-loop simulation and experimental results. The main problem lies in the underestimation of the SMA cooling rates, which in turn increases the predicted average SMA forces. Further work could be done to obtain better approximations of the SMA wire cooling rates under various stress or strain conditions.

Another model improvement that could be made is to obtain temperature-resistance estimations under various stress-strain conditions. A temperature model of the SMA was lacking in Chapter 6 during the simulations of the rapid-heating mechanism. This thermo-electromechanical characterisation would allow us to model the temperature and electrical resistance profiles of the SMAs for control. One method is by measuring the temperature of the SMA wire during heating and cooling using an infra-red thermal imaging camera, in different material conditions, while simultaneously recording its electrical resistance values.

A possible extension work on modelling could be to implement frequency response analysis on other SMA materials instead of Flexinol wires. This would allow us to verify if other SMA wires exhibit similar first-order linear behaviour in their power-force relationship, as well as to compare the response bandwidth of different types of SMAs.

As have been mentioned in Chapter 4, only a narrow range of Flexinol wire diameters have been tested using frequency response analysis. It would be interesting to investigate the frequency response behaviour of a larger range of Flexinol wire diameters as well as other types of SMA wires, to look at how their responses will compare with the results in this thesis.

8.2.2 Control Systems

Several possible control system improvements have appeared during this research and they will be considered in this section.

Firstly, the anti-overload mechanism could be improved by incorporating it as part of the dynamic saturation loop of the differential force controller. Currently it works outside the differential controller. Although it monitors the forces and prevents overstressing the SMA wires, the rapid switchings in heating currents which were observed are inefficient and destabilising to the control system. An-

other way of improving is to use a different, more effective control scheme instead of a proportional controller to eliminate the switchings.

Some investigations into pushing the control boundaries of SMA wires have been carried out, by using higher anti-overload thresholds and larger rapid-heating power limits. The experiments yielded positive results on the continuous and aggressive use of SMAs over long durations. However, these are only initial experiments and it would be useful to explore in this direction. Extensive results, providing quantitative measures of the SMA life time at higher stresses and larger heating currents than the recommended values, could be useful in designing better and faster control systems.

The PID controllers have so far produced satisfactory performance. However, investigating other potential control laws could yield better results. Our observation of the SMA wire actuators suggests that they demonstrate different behaviours in various conditions. Under the same heating conditions, a stretched (and cooler) SMA wire will contract faster and more forcefully, whereas an already contracted (and heated) wire will have a smaller contraction and generate less forces. One possible control scheme is using gain scheduling, which uses a family of controllers or control parameters to achieve satisfactory performance for different operating points of the system. By looking at the states of the actuators (such as the stress, strain, heating current and perhaps temperature profiles), a set of control gains or even controllers could be applied to obtain optimal performance.

For position control in the presence of an external load inertia, the two-loop control architecture with an outer PID position controller and an inner force controller may not be the best solution. A different control architecture could be investigated to improve the speed of response whilst maintaining the high level of position accuracy and eliminating the limit cycles.

Currently all force and position control experiments were conducted in ambient environment with free convection cooling, and one significant factor that affects the speed of actuator response is the cooling rate. The current test bed could be easily modified to allow forced air cooling in a temperature-controlled setting. This would allow us to examine whether forced air cooling is a viable and effective method for further improving the speed of SMA response.

8.2.3   Actuator and Test Bed Design

The SMA actuators that have been investigated in this thesis are SMA wires either as a single actuator or in an antagonistic arrangement. Both of which involves doubling-up of the wires for easier electrical connections as part of the test bed design and to generate large forces than straight wires. Because of this setup, the wire actuators sustain very high stress concentrations at the midpoints, where the wires meet the eyelets of the pulley at the top, and may lead to fracture over long durations at high heating currents. A possible improvement would be to modify the current actuator arrangement to prevent concentrating high stresses at single points. Different actuator arrangements could also be explored for future development, which would involve redesigning the test bed to accommodate the changes.

One possible arrangement is to investigate using parallel SMA wires to increase force output as well as to provide more controllability. Using thinner wires in such parallel setting can generate the same level of forces compared to using a single thicker wire, but this can increase the rate of cooling and thus improve actuator bandwidth. The important factor to be considered for this approach is test bed design (especially in terms of sensing and electrical connections).

A new test rig, with similar or better sensing and experimental capacity but also allowing 2-DOF motion of an SMA-actuated robotic device, could be designed and constructed. The aim is to demonstrate that the two-loop control architecture can perform satisfactorily in a very practical motion control application under heavy loads. More advanced controllers which may be used in the future, can also be tested using this test rig.

APPENDIX A

Properties of Flexinol and NiTi

Flexinol is the trade name of NiTi SMA specifically manufactured and marketed by Dynalloy Inc. Table A.1 lists the technical data for Flexinol wires of various diameters taken from Dynalloy Inc. Table A.2 presents selected properties of NiTi.

Wire Diameter (inches)	Electrical Resistance (ohms/inch)	Maximum Pull Force (gram)	Current at Room Temp. (mA)	Contraction Time[1] (second)	Off Time[2] 70°C Wire (second)	Off Time[2] 90°C Wire (second)
0.0010	45.0	7	20	1	0.1	0.06
0.0015	21.0	17	30	1	0.25	0.09
0.002	12.0	35	50	1	0.3	0.1
0.003	5.0	80	100	1	0.5	0.2
0.004	3.0	150	180	1	0.8	0.4
0.005	1.8	230	250	1	1.6	0.9
0.006	1.3	330	400	1	2.0	1.2
0.008	0.8	590	610	1	3.5	2.2
0.010	0.5	930	1000	1	5.5	3.5
0.012	0.33	1250	1750	1	8.0	6.0
0.015	0.2	2000	2750	1	13.0	10.0
0.020	0.16	3562	4000	1	17.0	14.0

Table A.1: Technical data of Flexinol actuator wires.

If Flexinol actuator wire is used within the guidelines then obtaining repeatable motion from the wire for tens of millions of cycles is reasonable. If higher stresses or strains are imposed, then the memory strain is likely to slowly decrease and good motion may be obtained for only hundreds or a few thousand of cycles. The permanent deformation, which occurs in the wire during cycling, is heavily

---

[1]The contraction time is directly related to current input. The figures used here are only approximate since room temperatures, air currents, and heat sinking of specific devices vary. On small diameter wires (≤ 0.006 in. diameter) currents which heat the wire in 1 second can typically be left on without overheating it.

[2]Approximate cooling time.

a function of the stress imposed and the temperature under which the actuator wire is operating. Flexinol wire has been specially processed to minimize this straining, but if the stress is too great or the temperature too high some permanent strain will occur. Since temperature is directly related to current density passing through the wire, care should be taken to heat, but not overheat, the actuator wire. The above chart gives rough guidelines as to how much current and force to expect with various wire sizes.

Transformation Properties

Transformation Temperature ——————————————————— -210 to $110°$C

Latent Heat of Transformation —————————————————— 5.78 cal.g^{-1}

    Tranformation Strain (for polycrystalline material)

        for a single cycle ————————————————————— max 8%

        for 100 cycles ———————————————————————— 6%

        for 100,000 cycles ——————————————————————- 4%

Hysteresis[3] ————————————————————————— 30 to $50°$C

Physical Properties

Melting Point —————————————————————————— $1300°$C

Density ————————————————————————————- 6.45 gcm^{-3}

Thermal Conductivity

    austenite ———————————————————————— 0.18 Wcm$^{-1°}$C^{-1}

    martensite ——————————————————————— 0.086 Wcm$^{-1°}$C^{-1}

Coefficient of Thermal Expansion

    austenite ————————————————————— 11.0x10^{-6} $°$C^{-1}

    martensite ——————————————————————— 6.6x10^{-6} $°$C^{-1}

Specific Heat ————————————————————————- 0.20 cal.g$^{-1°}$C^{-1}

Corrosion Performance ——————————————————————- excellent

Electrical and Magnetic Properties

Resistivity (resistance = resistivity x length / cross-sectional area)

    austenite ——————————————————————— approx. $100\,\mu\Omega$cm^{-1}

    martensite ——————————————————————- approx. $80\,\mu\Omega$cm^{-1}

Magnetic Permeability ————————————————————— < 1.002

Magnetic Susceptibility ———————————————————- 3.0x10^6 emu g^{-1}

Mechanical Properties

Young's Modulus (highly nonlinear with temperature)

    austenite ——————————————————————————— approx. 83 GPa

    martensite ——————————————————————— approx. 28 to 41 GPa

Yield Strength

    austenite ——————————————————————————— 195 to 690 MPa

    martensite —————————————————————————— 70 to 140 MPa

Ultimate Tensile Strength

    fully annealed ———————————————————————- 895 MPa

    work hardened —————————————————————————— 1900 MPa

Poisson's Ratio ————————————————————————————— 0.33

Elongation at Failure

    fully annealed —————————————————————————— 25 to 50%

    work hardened ——————————————————————————— 5 to 10%

Table A.2: Selected properties of NiTi alloys, taken from Johnson Matthey, Inc.[4]

---

[3]Values listed are for a full martensite to austenite transition. Hysteresis can be significantly reduced by partial transformation or ternary alloys.

[4]Johnson Matthey, Inc. http://www.jmmedical.com. Last accessed 27 March 2007.

APPENDIX A

APPENDIX B

Further Information on the Experimental Test Bed

In this appendix, additional hardware and processing information of the test bed is provided. The major subsystems which are described here are the load cells and their force signal processing, as well as the servo-controlled linear slide system.

B.1 Load Cells and Force Signal Processing

The two load cells in the experimental test bed are S215 single point force sensors from Strain Measurement Devices Inc. They can measure forces in the $\pm 9\,\mathrm{N}$ range, and based on the DS1104 16-bit ADCs and the strain gauge amplifier gain, a resolution of $0.3\,\mathrm{mN}$ can be achieved. The maximum rated force output is 200%, i.e. they overload at $\pm 18\,\mathrm{N}$.

A block diagram depicting one load cell and its force signal processing steps is given in Figure B.1. Due to the high-frequency noise of the load cell as well as the electrical noise from other components of the test bed (e.g. motor amplifier), the force signal from each load cell is pre-filtered with an analog anti-aliasing filter which cuts off at a frequency of $1200\,\mathrm{rad\,s^{-1}}$. The strain gauge amplifier then amplifies the force signal from each load cell at a gain of 150. This gain is chosen to cover the full $18\,\mathrm{N}$ force range (from $-9\,\mathrm{N}$ to $+9\,\mathrm{N}$) without saturation. The signal is then converted to a digital signal via a 16-bit ADC and low-pass filtered using a digital Butterworth filter.

A force overload monitor electronic circuit is incorporated with the strain gauge amplifier hardware to measure and monitor the state of the load cells. There are three LED colour displays: under normal force conditions (less than $9\,\mathrm{N}$), the green LED is switched on; at $9\,\mathrm{N}$, the yellow LED switches on to warn against further force increases; and at 200% maximum rated force output based
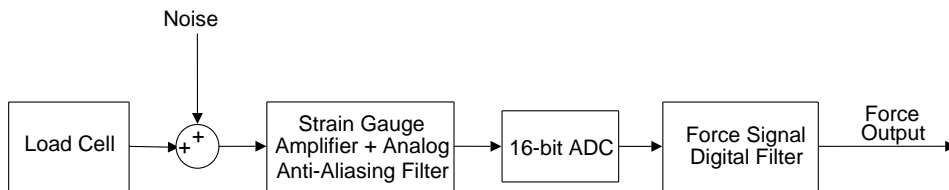
Figure B.1: Load cell and force signal processing.

on the load cell specifications (18 N), the red LED latches on signaling irreversible overload. The damaged load cell will need to be replaced.

Both load cells have a measured mechanical resonance at a frequency of 280 Hz. The bandwidth is chosen to be 140 Hz as the frequency response is fairly flat up to this frequency, as can be seen in Figure B.3. The mechanical resonance of a load cell can be measured by subjecting it to a mechanical impulse, measuring the force output signal, and examining its force signal power spectrum. It has been observed that the force signal exhibits decaying oscillations, which are characteristic of an underdamped second-order system. Therefore the transfer function of the load cell resonance, $R(s)$, can be given as

$$R(s) = \frac{\omega_n^2}{s^2 + 2\zeta\omega_n s + \omega_n^2}, \tag{B.1}$$

where ζ is the damping ratio, and ω_n the undamped natural or resonant frequency. They have been experimentally determined to be 0.04 and $1760\,\mathrm{rad\,s^{-1}}$ (or 280 Hz) respectively. The frequency response of the load cell resonance is given in the Bode diagrams of Figure B.3.

The analog anti-aliasing filter is effectively two analog RC circuits in series, thereby making it a 2nd-order low-pass filter, with a transfer function, $A(s)$, of the form

$$A(s) = \frac{1}{R_1 R_2 C_1 C_2 s^2 + (R_1 C_1 + R_2 C_2 + R_1 C_2)s + 1}, \tag{B.2}$$

where R_1, R_2, C_1 and C_2 are calculated from the measured resistances and capacitances of the analog filter and strain gauge bridge, with the subscripts referring to the first or the second RC circuit in series. The resistance and capacitance values have been measured, of which $R_1 = 10\,\mathrm{k\Omega}$, $R_2 = 11.2\,\mathrm{k\Omega}$, and $C_1 = C_2 = 33.6\,\mathrm{nF}$. The actual anti-aliasing filter is shown in Figure B.2(a) and its equivalent of two cascading RC circuits in Figure B.2(b). The frequency response of this filter is given in Figure B.4.
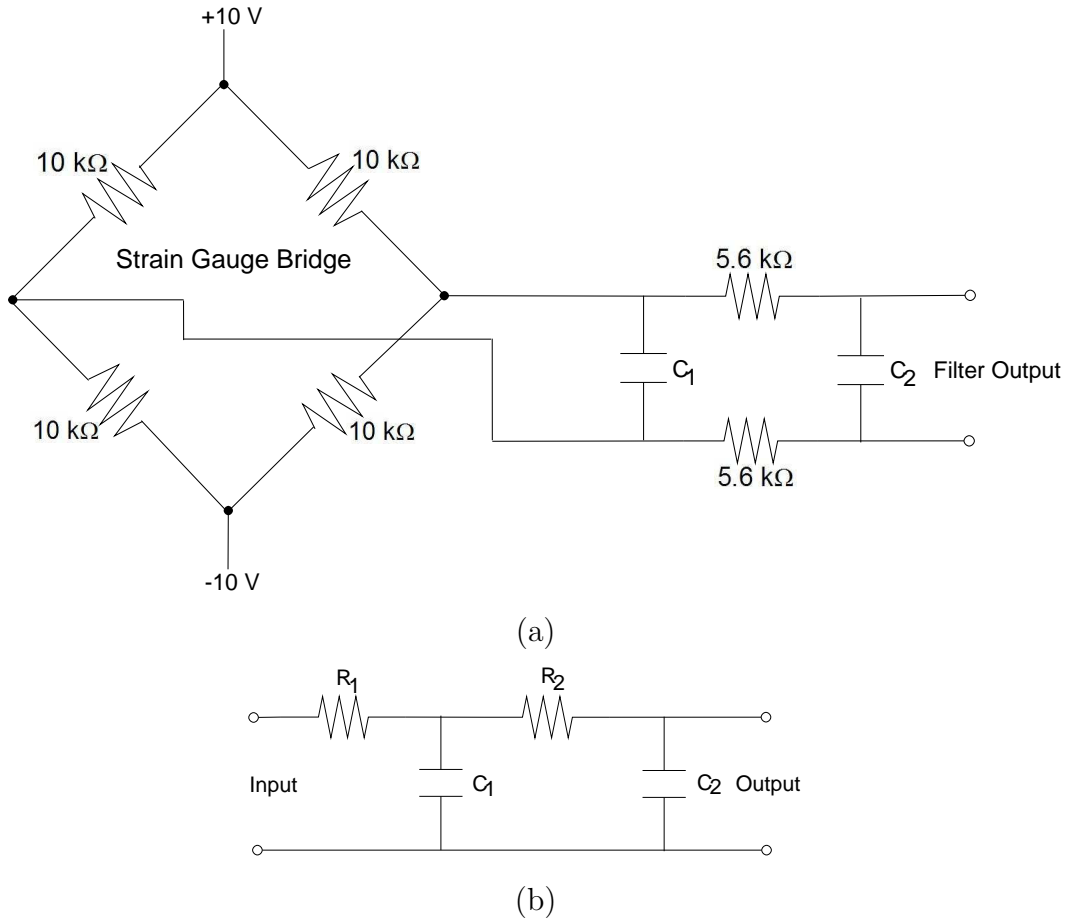
(a)

(b)

Figure B.2: The actual analog anti-aliasing filter (a) and its equivalent (b).

In the modelling experiments of Chapter 4, the implemented force signal digital filter is a 2nd-order low-pass Butterworth filter with a cut-off frequency, ω_c, of $150\,\mathrm{rad\,s^{-1}}$. Its transfer function, $D_1(s)$, is given by

$$D_1(s) = \frac{1}{\frac{1}{\omega_c^2}s^2 + \frac{\sqrt{2}}{\omega_c}s + 1}. \tag{B.3}$$

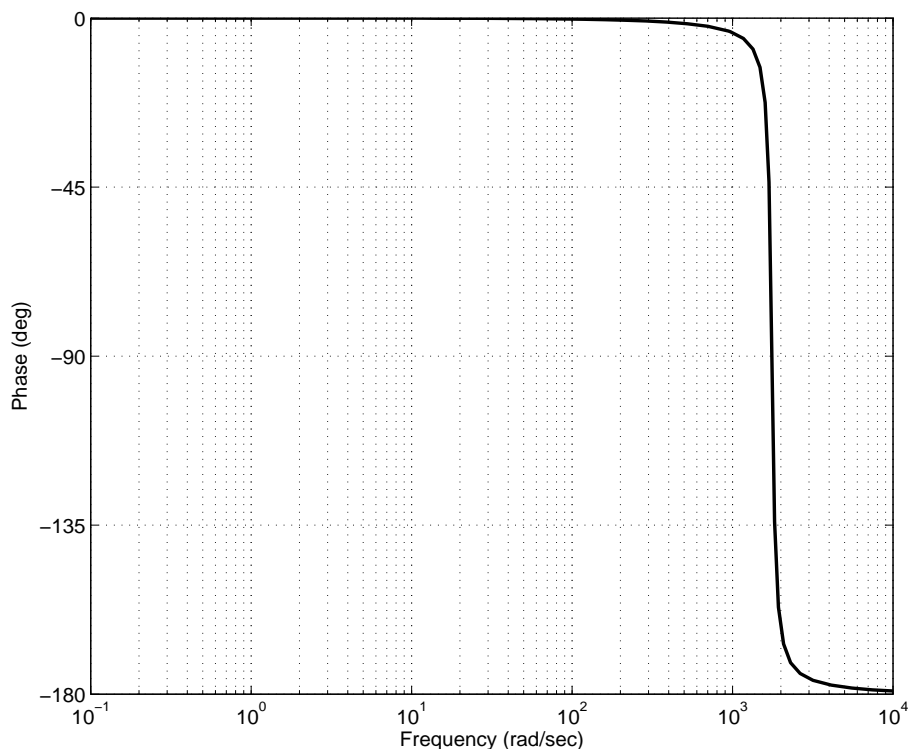In later chapters, a 4th-order low-pass Butterworth filter with a larger ω_c of $600\,\mathrm{rad\,s^{-1}}$ is used for control experiments. The transfer function is given as

$$D_2(s) = \frac{1}{\frac{1}{\omega_c^4}s^4 + \frac{2.6132}{\omega_c^3}s^3 + \frac{2+\sqrt{2}}{\omega_c^2}s^2 + \frac{2.6132}{\omega_c} + 1}. \tag{B.4}$$

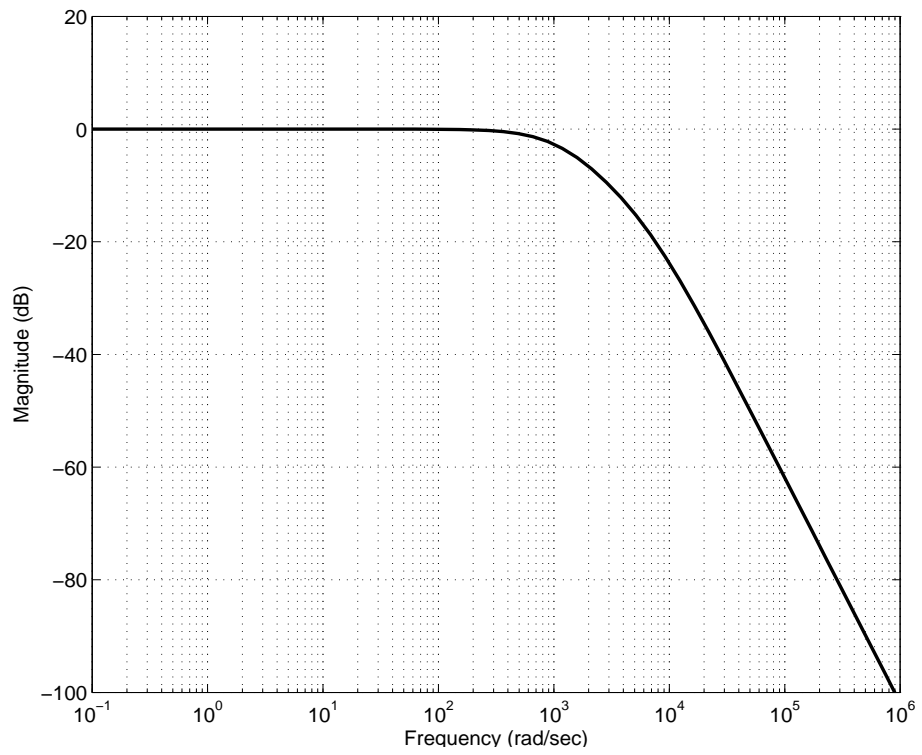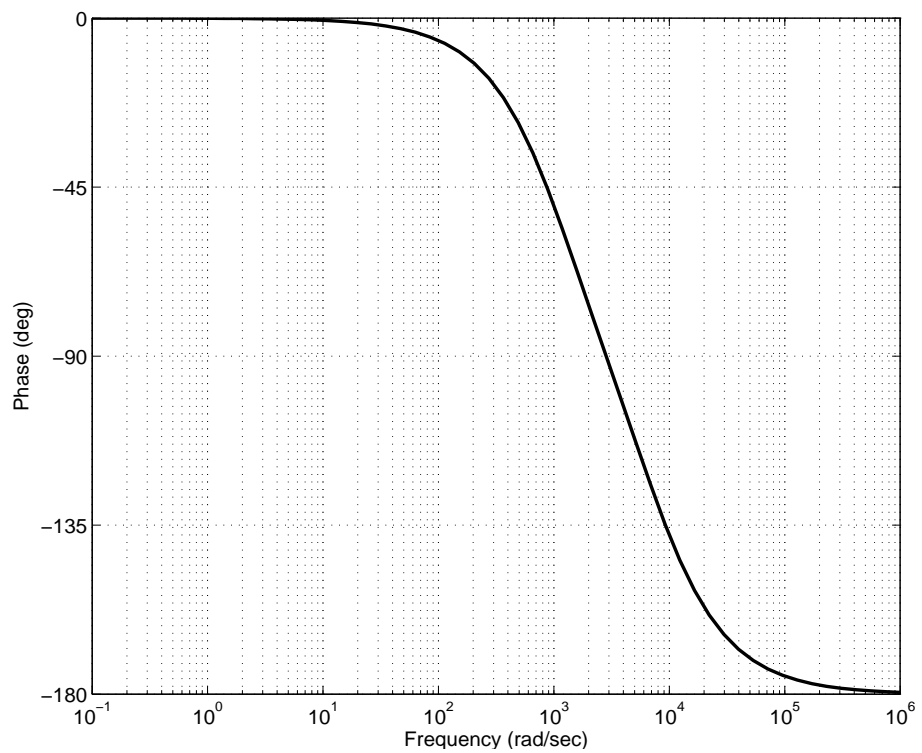Figure B.5 shows the frequency responses for both digital filters.
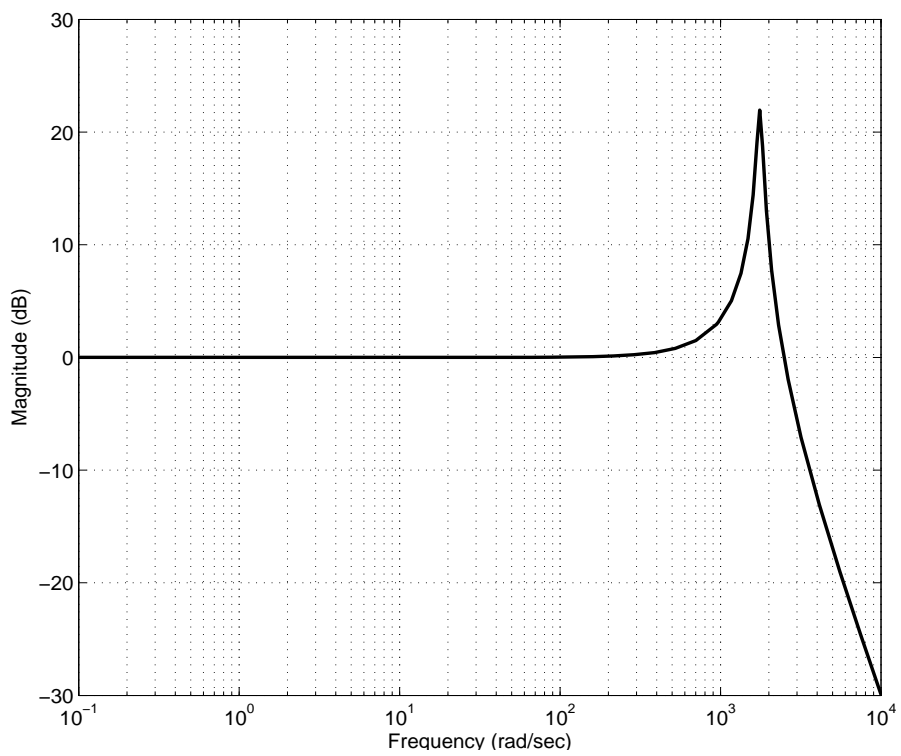
(a)

(b)

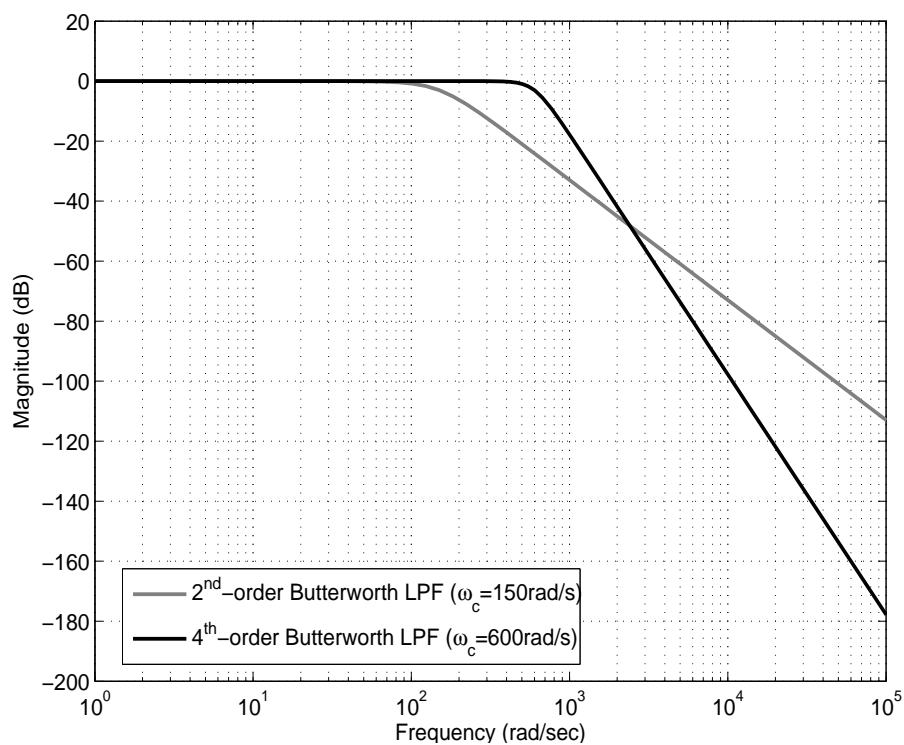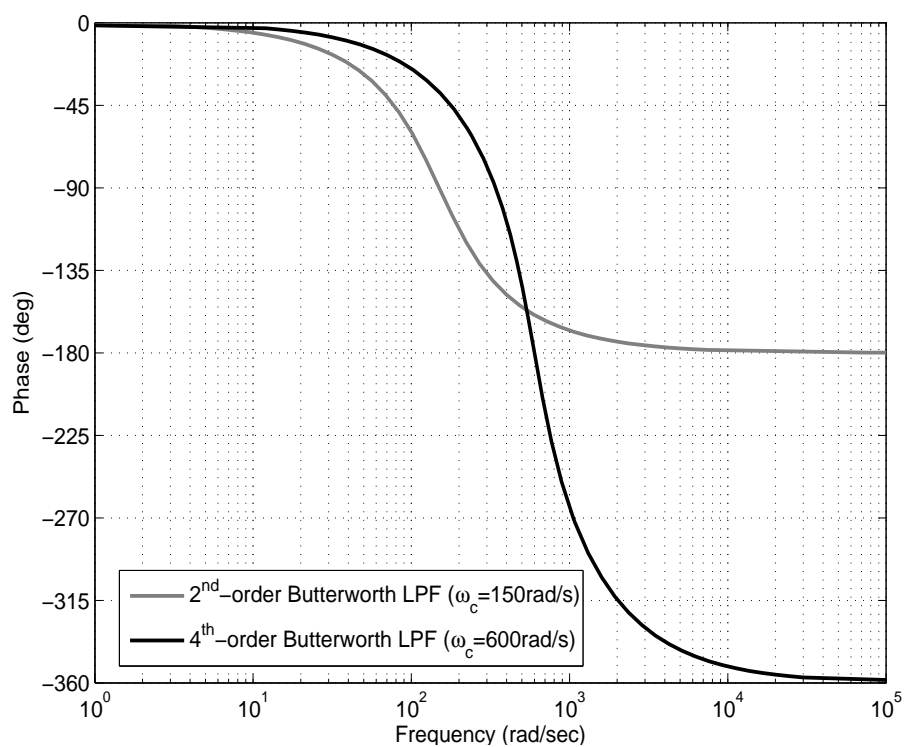Figure B.3: Frequency response of the load cell mechanical resonance.

(a)

(b)

Figure B.4: Frequency response of the force signal analog anti-aliasing filter.

(a)

(b)

Figure B.5: Frequency response of the force signal digital low-pass filter.

B.2 Servo-Controlled Linear Slide

The precision linear slide on the test bed is a Mini Posi-Drive Stage from Del-Tron Precision Inc. Some of its features include:

i. Positive lead screw drive with 3.175 mm/rev pitch

ii. Flexible zero backlash coupling

iii. High repeatability and accuracy (2.5 μm per 25 mm of travel)

iv. Large load capacity (6.8 kg)

v. Suitable range of travel (75 mm)

vi. Adjustable optical limit switches

vii. Adequate recommended speed (30 mm s^{-1}) but can be higher

Because the dSPACE DS1104 system does not provide stepper motor interfaces, a servo motor is required to drive the linear slide. A Pittman brushless DC servo motor, which has a Nema 14 configuration compatible with the Posi-Drive Stage motor mount, is used to directly drive the linear slide. The motor hall sensor with an encoder resolution of 2000 CPR (Counts Per Revolution) allows a linear slide resolution of 1.5875 μm. A Logosol AC/DC servo amplifier (Model LS-5Y-BL) is used for motor control.

The servo-controlled linear slide is used to simulate any desired strain profiles or to induce motion disturbances to the SMA wire(s) in the test bed. A PI controller is chosen for position feedback and the tuned parameters are: proportional gain, $K_P = 31.6$ and integral gain, $K_I = 0.1$. The measured closed-loop frequency response of the linear slide position system is given in Figure B.6. Based on the Bode diagrams, the linear slide has a closed-loop bandwidth of approximately 50 Hz (i.e. the frequency at which the output is attenuated to a factor of 0.707 times the input, or approximately -3 dB).

In the experiments, position error spikes have been observed in the linear slide motion. A snap-shot of the slide position errors is presented in Figure B.7(a). Given the lead screw pitch of 3.175 mm/rev — the linear slide travels 3.175 mm for a complete revolution of the motor rotation, the graph depicts the position errors for a complete 360° cycle. It can be seen from this graph that the error spikes occur at constant intervals. A polar plot of the same data is given in Figure B.7(b). It shows that the spikes happen every 30° rotation of the servo motor. This suggests that the error spikes are caused by a mechanical effect in the linear slide, rather than by the PI controller. One possible cause is friction produced in the ball screw recirculation mechanism.
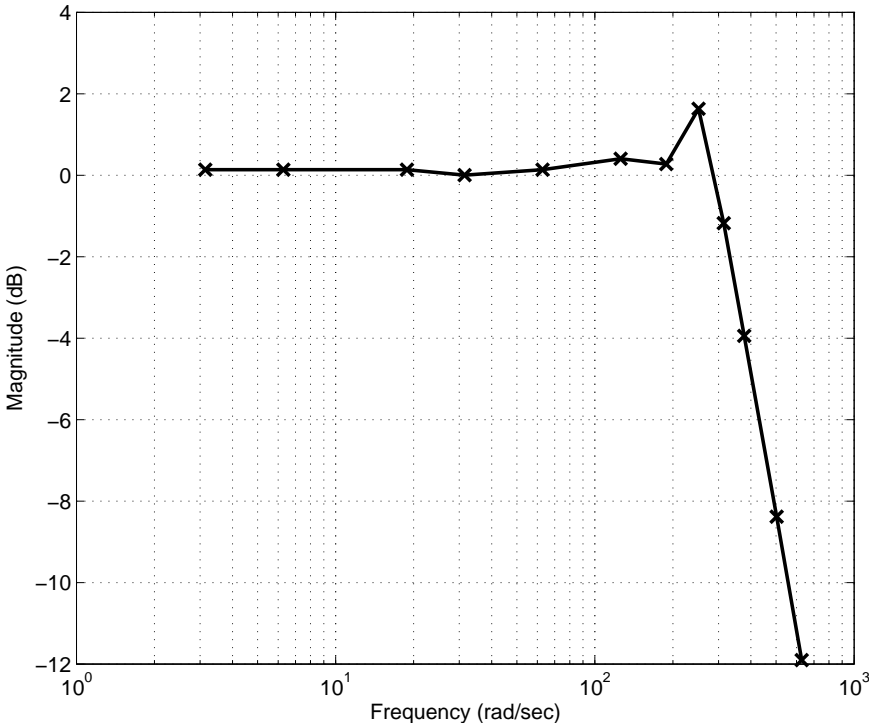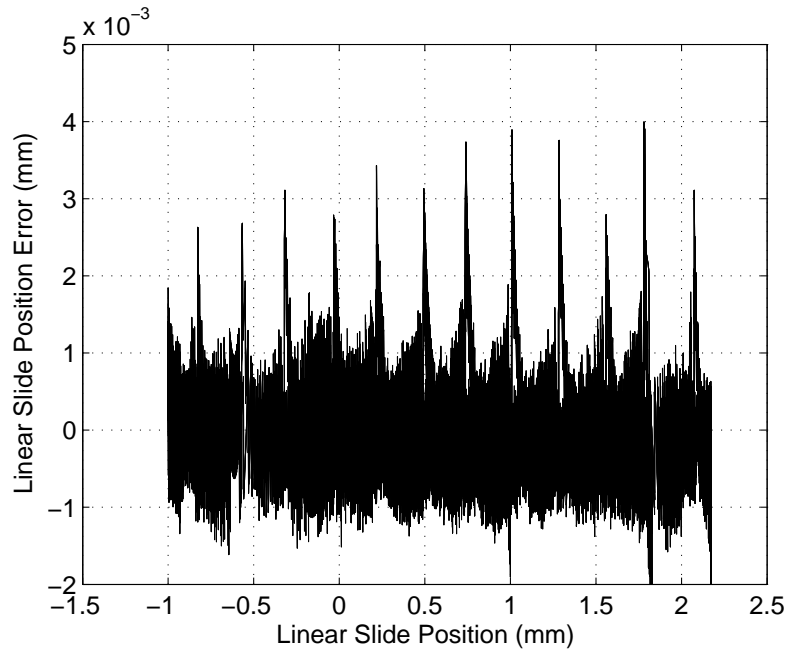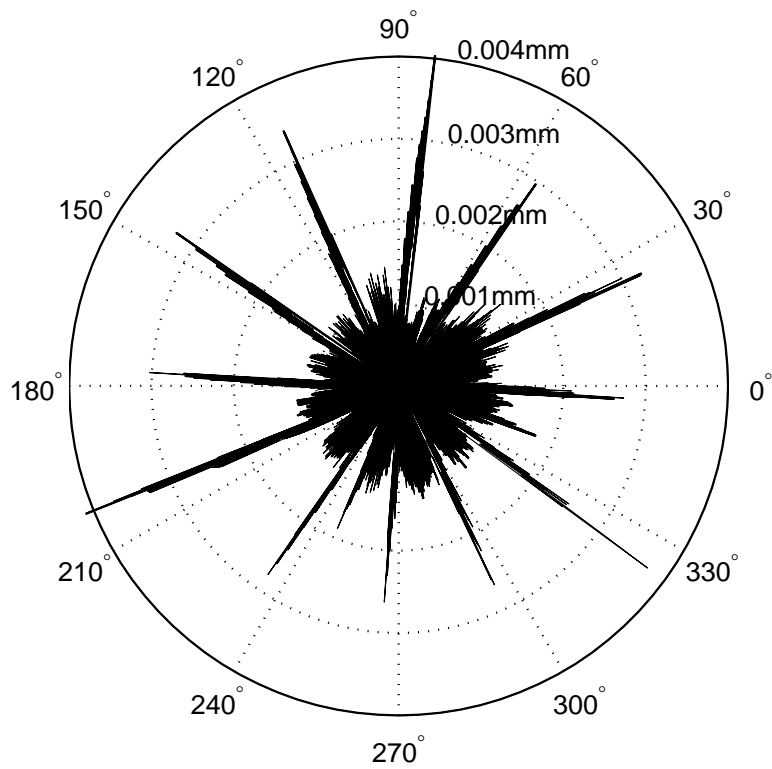
(a)
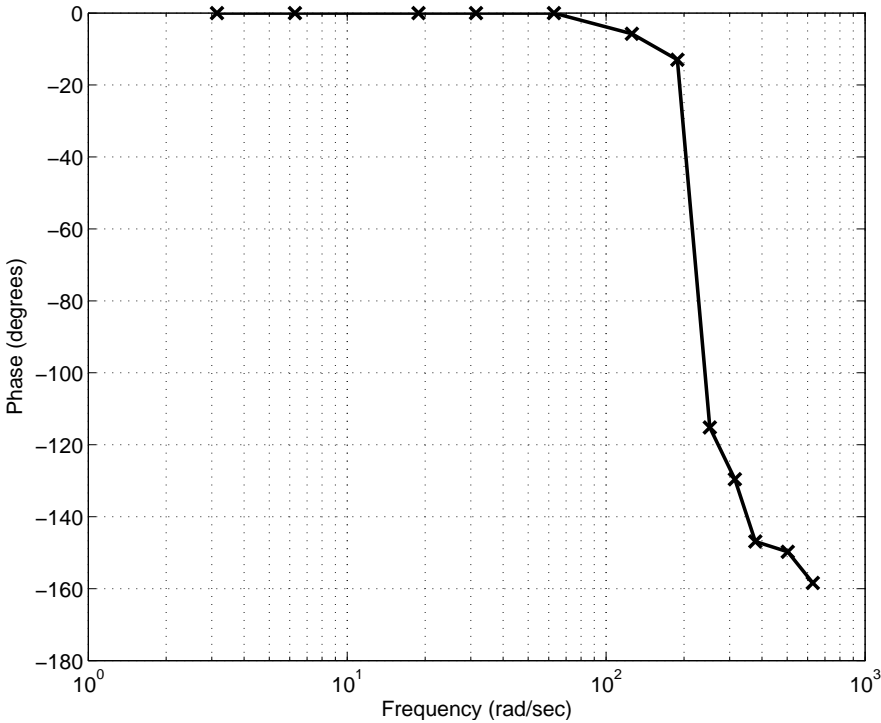
(b)

Figure B.6: Linear slide closed-loop frequency response.

(a)

(b)

Figure B.7: (a) Plot of position error versus linear slide position. (b) Polar plot of the linear slide position error.

The Simulink model of the linear actuator control system is given in Figure B.8. Basically it consists of three parts: initialisation, overload mechanism and servo motor control.

Initialisation steps of the linear actuator system is required before any experiments involving the test bed. The aim is to determine the absolute position of the linear slide with respect to a known zero-position. The position of the lower limit switch is used as the zero-position for all experiments. Once the linear slide position has been determined, the initialisation phase switches over to the motor control phase based on the PI feedback controller to track a desired position command.

In addition, several safety mechanisms have been put in place to prevent linear slide run-off and load cell overload when coupled to the slide via the SMA wire(s):

 i. Mechanical upper and lower rubber end-stops have been installed in the test bed column to prevent linear slide run-off at the end of travel.

 ii. A mechanism based on the 'Out of Travel Range' value (see Figure B.8) automatically overrides any running operation on the test bed when the linear slide travel exceeds a certain pre-determined range. This travel range is based on the position of the limit switches. The mechanism switches off input power to the SMA wire(s) and moves the linear slide downwards until it touches the lower rubber end-stop to remove any residual forces on the load cell.

 iii. A software load cell overload mechanism is implemented (see Figure B.8) which performs the same functions as item ii above, when either load cells exceeds the threshold of 9 N. This is in addition to the load cell overload monitor circuit and LED display.

 iv. A 'Manual Override' switch allows power input to the motor to be cut off at any instant during experiments.

**LINEAR ACTUATOR
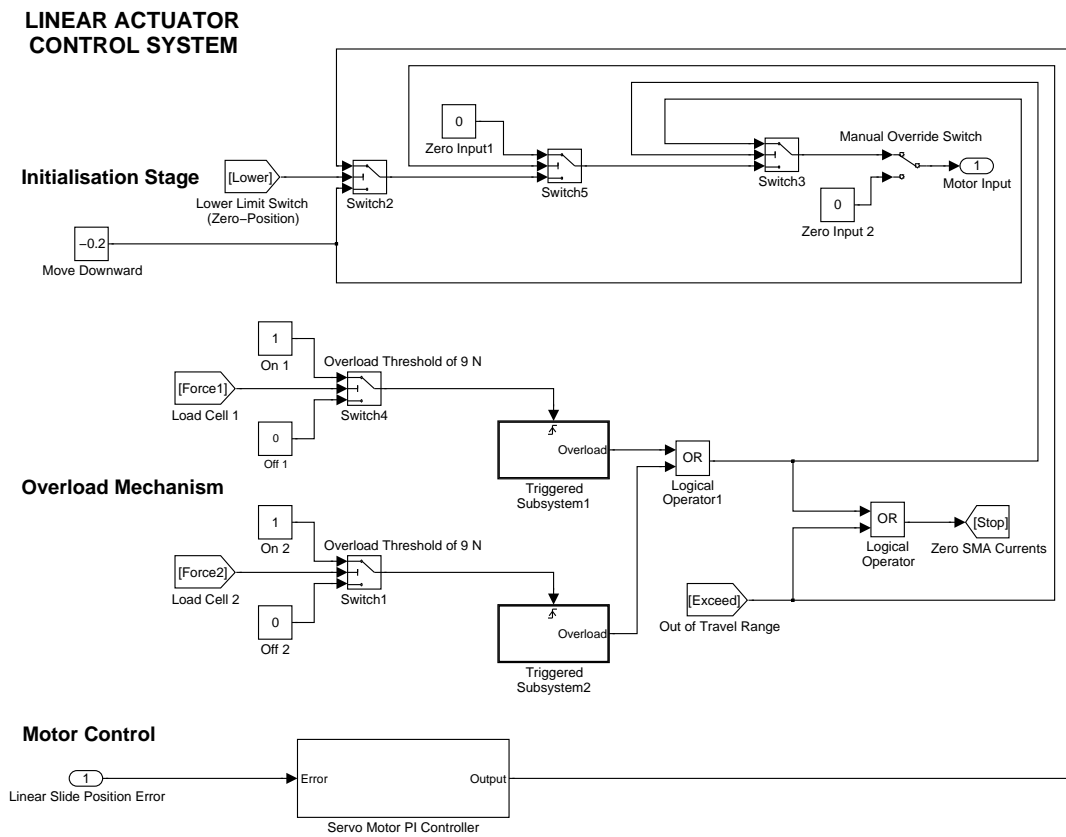CONTROL SYSTEM**

Figure B.8: Simulink model of linear actuator control system.

APPENDIX C

Simulink Models

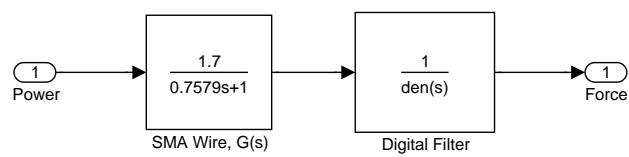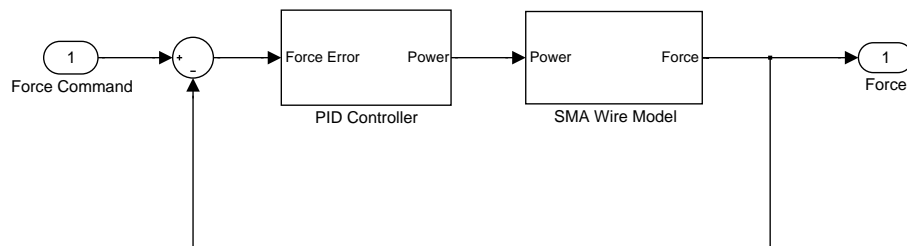
Figure C.1: Open loop SMA force model.

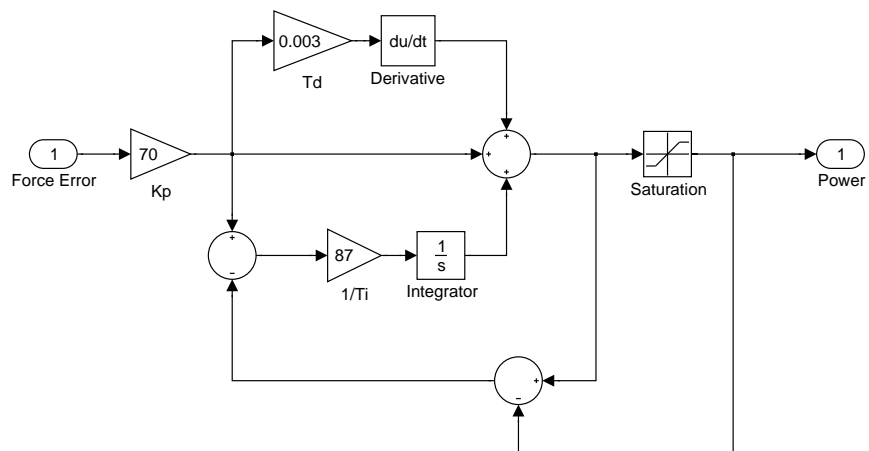Figure C.2: Force control of a single SMA wire.
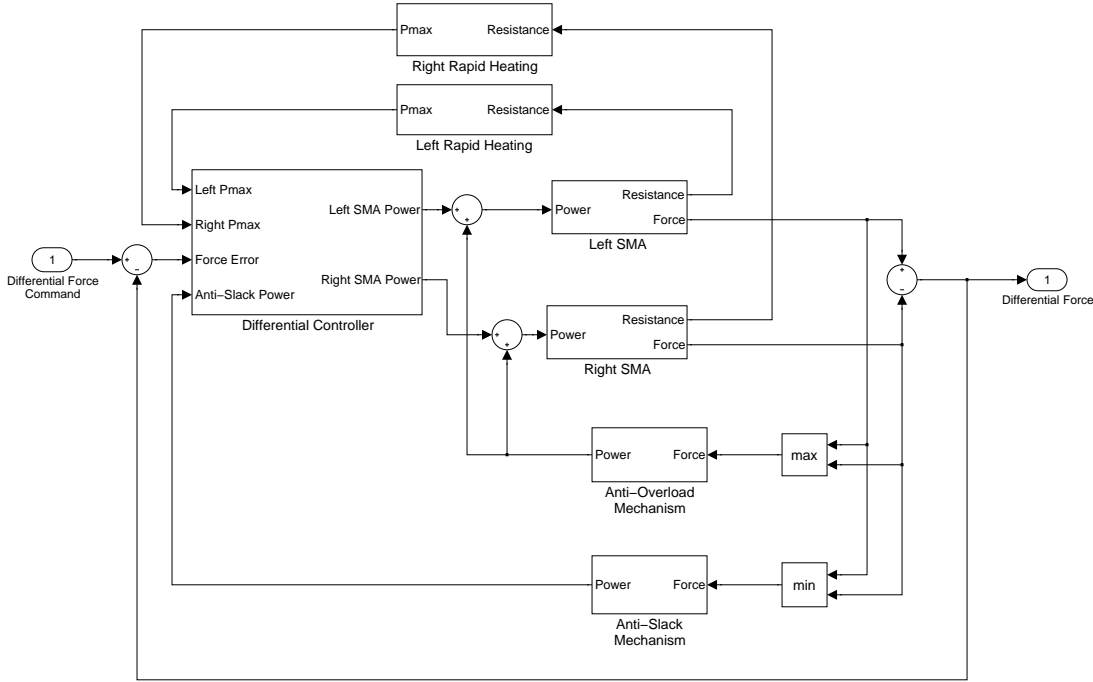

Figure C.3: PID controller.

Figure C.4: Differential force control architecture of antagonisitic SMA actuator.
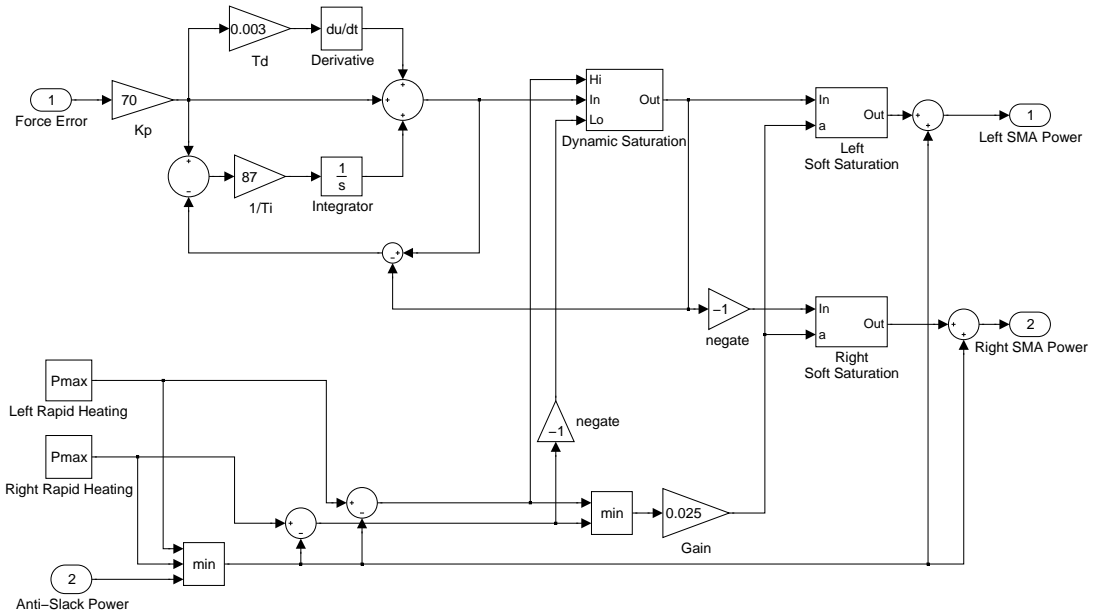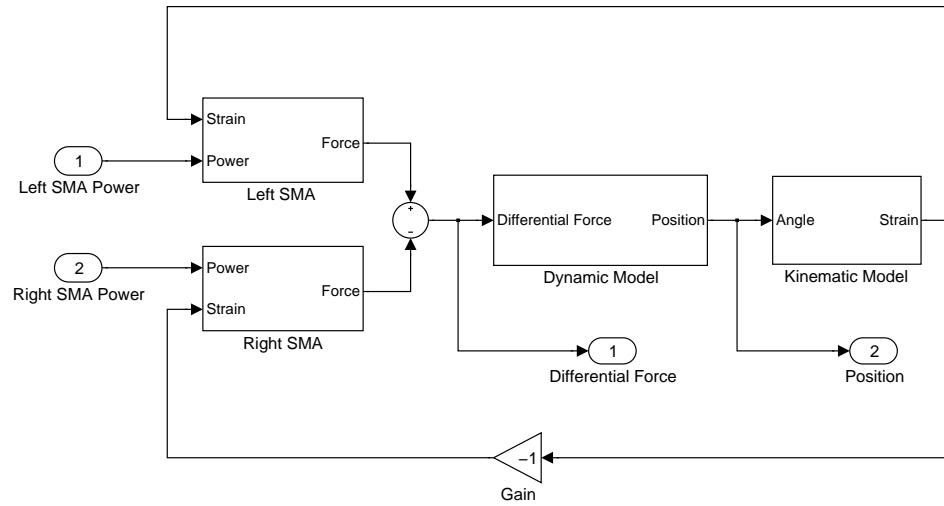

Figure C.5: Differential controller.

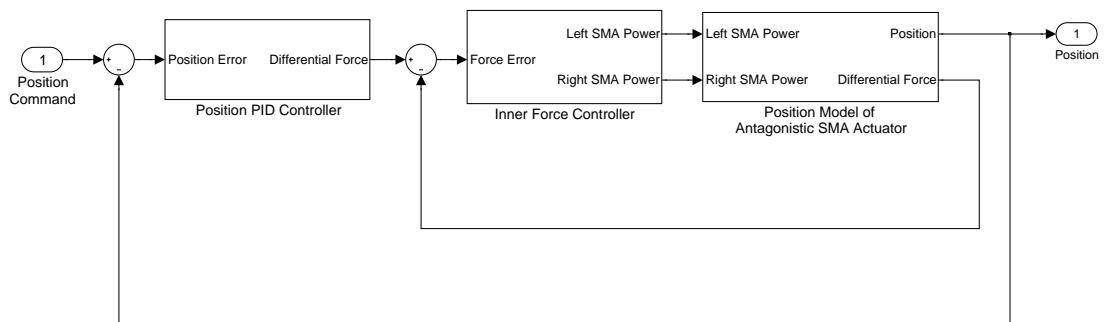Figure C.6: Open loop position model of antagonistic SMA actuator.

Figure C.7: Two-loop position control architecture of antagonistic SMA actuator.

Bibliography

[1] Kyoung Kwan Ahn and Bao Kha Nguyen. Position control of shape memory alloy actuators using self tuning fuzzy PID controller. *International Journal of Control, Automation and Systems*, 4(6):756–762, 2006.

[2] Hashem Ashrafiuon, Mojtaba Eshraghi, and Mohammad H. Elahinia. Position control of a 3-link shape memory alloy actuated robot. *Journal of Intelligent Material Systems and Structures*, 17:381–392, 2006.

[3] M. Berveiller and F. D. Fischer, editors. *Mechanics of Solids with Phase Changes*. SpringerWienNewYork, 1997.

[4] V. Brailovski, S. Prokoshkin, P. Terriault, and F. Trochu, editors. *Shape memory Alloys: Fundamentals, Modeling and Applications*. Université du Québec, École de technologie supérieure, 2003.

[5] L. C. Brinson. One-dimensional thermomechanical constitutive relations for shape memory materials. *Journal of Intelligent Material Systems and Structures*, 1:207–234, 1990.

[6] L. C. Brinson. One-dimensional constitutive behavior of shape memory alloys: Thermomechanical derivation with non-constant material functions and redefined martensite internal variable. *Journal of Intelligent Material Systems and Structures*, 4:229–242, 1993.

[7] Dan Cho. Wrestle a robot. *New Scientist*, 2564:39–41, 12 August 2006.

[8] Kyu-Jin Cho and H. Asaha. Multi-axis SMA actuator array for driving anthropomorphic robot hand. In *Proceedings of the IEEE International Conference on Robotics and Automation*, pages 1356–1361, 2005.

[9] Byung-Jun Choi and Yun-Jung Lee. Preisach model of SMA actuators using proportional relationship of major loop of hysteresis. In *Proceedings*

of the 2002 IEEE/RSJ International Conference on Intelligent Robots and Systems, pages 1986–1991, 2002.

[10] S. B. Choi, Y. B. Han, J. H. Kim, and C. C. Cheong. Force tracking control of a flexible gripper featuring shape memory alloy actuators. *Mechatronics*, 11:677–690, 2001.

[11] John J. Craig. *Introduction to Robotics: Mechanics and Control*. Addison-Wesley Publishing Group, 2nd edition, 1989.

[12] W. Duerig, K. N. Melton, D. Stockel, and C. M. Wayman. *Engineering Aspects of Shape Memory Alloy*. Butterworth-Heinemann Ltd., 1990.

[13] Mohammad H. Elahinia. *Effect of System Dynamics on Shape Memory Alloy Behavior and Control*. PhD thesis, Virginia Polytechnic Institute and State University, 2004.

[14] Mohammad H. Elahinia, Edmond Henneke, and Mehdi Ahmadian. Stress-based sliding mode control of a rotary SMA-actuated manipulator. In *Proceedings of SPIE, Smart Structures and Materials 2004: Modeling, Signal Processing, and Control*, volume 5383, pages 478–489, 2004.

[15] Mohammad H. Elahinia, T. Michael Seigler, Donald J. Leo, and Mehdi Ahmadian. Nonlinear stress-based control of a rotary SMA-actuated manipulator. *Journal of Intelligent Material Systems and Structures*, 15(6):495–508, 2004.

[16] Roy Featherstone and Yee Harn Teh. Improving the speed of shape memory alloy actuators by faster electrical heating. In *Proceedings of the 9th International Symposium on Experimental Robotics*, Singapore, 18-21 June 2004.

[17] Gene F. Franklin, J. David Powell, and Abbas Emami-Naeini. *Feedback Control of Dynamic systems*. Addison-Wesley Publishing Group, 3rd edition, 1994.

[18] Yongqing Fu, Hejun Du, Weimin Huang, Sam Zhang, and Min Hu. TiNi-based thin films in MEMS applications: A review. *Sensors and Actuators A: Physical*, 112:395408, 2004.

[19] Robert B. Gorbet and R. Andrew Russell. A novel differential shape memory alloy actuator for position control. *Robotica*, 13:423–430, 1995.

[20] Robert Benjamin Gorbet. A study of the stability and design of shape memory alloy actuators. Master's thesis, University of Waterloo, 1996.

[21] Robert Benjamin Gorbet. *Control of Hysteretic Systems with Preisach Representations.* PhD thesis, University of Waterloo, 1997.

[22] F. Gori, D. Carnevale, A. Doro Altan, S. Nicosia, and E. Pennestri. A new hysteretic behaviour in the electrical resistivity of flexinol shape memory alloys versus temperature. *International Journal of Thermophysics*, 27(3):866–879, 2006.

[23] Danny Grant. *Accurate and Rapid Control of Shape Memory Alloy Actuators.* PhD thesis, McGill University, 1999.

[24] Danny Grant and Vincent Hayward. Design of shape memory alloy actuator with high strain and variable structure control. In *Proceedings of the IEEE International Conference on Robotics and Automation*, pages 2305–2312, 1995.

[25] Danny Grant and Vincent Hayward. Variable structure control of shape memory alloy actuators. *IEEE Systems and Control Magazine*, 17(3):80–88, 1997.

[26] Danny Grant and Vincent Hayward. Constrained force control of shape memory alloy actuators. In *Proceedings of the 2000 IEEE International Conference on Robotics and Automation*, pages 1314–1320, 2000.

[27] J. D. Harrison. Measurable changes concomitant with the shape memory effect transformation. In T. W. Duerig, K. N. Melton, D. Stockel, and C. M. Wayman, editors, *Engineering Aspects of Shape Memory Alloys*, pages 106–111. Butterworth-Heinemann, 1990.

[28] Toshiyuki Hino and Takashi Maeno. Development of a miniature robot finger with a variable stiffness mechanism using shape memory alloy. In *Proceedings of the International Simposium on Robotics and Automation*, Querétaro, Mexico, 25-27 August, 2004.

[29] S. Hirose, K. Ikuta, and Y. Umetani. A new design method of servo-actuators based on the shape memory effect. In Morecki et. al., editor, *Theory and Practice of Robots and Manipulators*, pages 339–349. MIT Press, 1985.

[30] Dai Honma, Yoshiyuki Miwa, and Nobuhiro Iguchi. Micro robots and micro mechanisms using shape memory alloy. In *The Third Toyota Conference: Integrated Micro Motion Systems, Micro-machining, Control and Applications*, 1984.

[31] Declan Hughes and John T. Wen. Preisach modeling of piezoceramic and shape memory alloy hysteresis. In *Proceedings of the 4th IEEE Conference on Control Applications*, pages 1086–1091, 1995.

[32] Koji Ikuta. Micro/miniature shape memory alloy actuator. In *Proceedings of the IEEE International conference on Robotics and Automation*, volume 3, pages 2156–2161, 1990.

[33] Koji Ikuta, Masahiro Tsukamoto, and Shigeo Hirose. Shape memory alloy servo actuator system with electric resistance feedback and application for active endoscope. In *Proceedings of the IEEE International Conference on Robotics and Automation*, volume 1, pages 427–430, 1988.

[34] Koji Ikuta, Masahiro Tsukamoto, and Shigeo Hirose. Mathematical model and experimental verification of shape memory alloy for designing micro actuator. In *Micro Electro Mechanical Systems, 1991, MEMS '91, Proceedings of IEEE: An Investigation of Micro Structures, Sensors, Actuators, Machines and Robots*, pages 103–108, 1991.

[35] Petros Ioannou and Baris Fidan. *Adaptive Control Tutorial*. SIAM: Society for Industrial and Applied Mathematics, 2007.

[36] V. Kafka. Shape memor: A new concept of explanation and of mathematical modelling. part i: Micromechanical explanation of the causality in the sm processes. *Journal of Intelligent Material Systems and Structures*, 5(6):809–814, 1994.

[37] M. Kohl. *Shape Memory Microactuators*. Springer, 2004.

[38] A. Ktena, D. I. Fotiadis, A. Spanos, P. D.and Berger, and C. V. Massalas. Identification of 1d and 2d preisach models for ferromagnets and shape memory alloys. *International Journal of Engineering Science*, 40:2235–2247, 2002.

[39] A. Ktena, D. I. Fotiadis, P. D. Spanos, and C. V. Massalas. A preisach model identification procedure and simulation of hysteresis in ferromagnets and shape-memory alloys. *Physica B*, 306:84–90, 2001.

[40] Katsutoshi Kuribayashi. A new actuator of a joint mechanism using Ti-Ni alloy wire. *The International Journal of Robotics Research*, 4(4):47–58, 1986.

[41] Katsutoshi Kuribayashi. Improvement of the response of an SMA actuator using a temperature sensor. *The International Journal of Robotics Research*, 10(1):13–20, 1991.

[42] Katsutoshi Kuribayashi. Micro SMA actuator and motion control. In *Proceedings of the 2000 International Symposium on Micromechatronics and Human Science*, pages 35–42, 2000.

[43] Hyo Jik Lee and Jung Ju Lee. Time delay control of a shape memory alloy actuator. *Smart Materials and Structures*, 13:227–239, 2004.

[44] C. Liang and C. A. Rogers. Design of shape memory alloy springs with applications in vibration control. *Journal of Vibration and Acoustics*, 115:129–135, 1993.

[45] C. C. Ma, R. Wang, Q. P. Sun, Y. Zohar, and M. Wong. Frequency response of tini shape memory alloy thin film micro-actuators. In *Proceedings of the 13th International Conference on Micro Electro Mechanical Systems*, pages 370–374, 2000.

[46] L. G. Machado and M. A. Savi. Medical applications of shape memory alloys. *Brazilian Journal of Medical and Biological Research*, 36:683–691, 2003.

[47] D. Madill and D. Wang. Modelling and L2-stability of a shape memory alloy position control system. *IEEE Transactions on Control Systems Technology*, 6(4):473–481, 1998.

[48] Sumiko Majima, Kazuyuki Kodama, and Tadahiro Hasegawa. Modeling of shape memory alloy actuator and tracking control system with the model. *IEEE Transactions on Control Systems Technology*, 9(1):54–59, 2001.

[49] Oohora Masamichi. Drive apparatus, drive system, and drive method. *US Patent Number 20060156027*, Konica Minolta Holdings Inc., 13 July 2006.

[50] Yuji Matsuzaki and Hisashi Naito. Macroscopic and microscopic constitutive models of shape memory alloys based on phase interaction energy function: A review. *Journal of Intelligent Material Systems and Structures*, 15:141–155, 2004.

[51] I. D. Mayergoyz. *Mathematical Models of Hysteresis*. Springer-Verlag, New York, 1991.

[52] István Mihálcz. Fundamental characteristics and design method for nickeltitanium shape memory alloy. *Periodica Polytechnica Ser. Mech. Eng.*, 45(1):75–86, 2001.

[53] N. B. Morgan. Medical shape memory alloy applications — the market and its products. *Materials Sciences and Engineering A*, 378:16–23, 2004.

[54] Michael J. Mosley and Constantinos Mavroidis. Experimental nonlinear dynamics of a shape memory alloy wire bundle actuator. *Journal of Dynamic Systems, Measurement and Control*, 123(1):103–112, 2001.

[55] K. Otsuka and C. M. Wayman, editors. *Shape Memory Materials*. Cambridge University Press, 2002.

[56] Antoni Planes, Francisco-José Pérez-Reche, Edward Vives, and Ma nosa Lluís. Kinetics of martensitic transitions in shape-memory alloys. *Scipta Materialia*, 50:181–186, 2004.

[57] V. A. Plotnikov and D. V. Kokhanenko. Acoustic emission in martensitic transformation in alloys under mechanical loading. *Russian Physics Journal*, 47(7):692–700, 2004.

[58] J. L. Pons, D. Reynaerts, J. Peirs, R. Ceres, and H. Van Brussel. Comparison of different control approaches to drive SMA actuators. In *Proceedings of the 8th International Conference on Advanced Robotics*, pages 819–824, 1997.

[59] O. K. Rediniotis, L. N. Wilson, D. C. Lagoudas, and M. M. Khan. Development of a shape-memory-alloy actuated biomimetic hydrofoil. *Journal of Intelligent Material Systems and Structures*, 13:35–49, 2002.

[60] Dominiek Reynaerts and Hendrik Van Brussel. Design aspects of shape memory actuators. *Mechatronics*, 8:635–656, 1998.

[61] R. Andrew Russell and Robert B. Gorbet. Improving the response of SMA actuators. In *Proceedings of the IEEE International Conference on Robotics and Automation*, volume 3, pages 2299–2304, 1995.

[62] T. Saburi. Ti-Ni shape memory alloys. In K. Otsuka and C. M. Wayman, editors, *Shape Memory Materials*, pages 49–96. Cambridge University Press, 2002.

[63] Brian Selden, Kyu-Jin Cho, and H. Harry Asada. Segmented binary control of shape memory alloy actuator systems using the peltier effect. In *Proceedings of the IEEE International Conference on Robotics and Automation*, pages 4931–4936, 2004.

[64] Ali R. Shahin, Peter H. Meckl, James D. Jones, and Mark A. Thrasher. Enhanced cooling of shape memory alloy wires using semiconductor heat pump modules. *Journal of Intelligent Material Systems and Structures*, 2(1):95–104, 1994.

[65] Daniel D. Shin, Kotekar P. Mohanchandra, and Gregory P. Carman. High frequency actuation of thin film NiTi. *Sensors and Actuators A: Physical*, 111:166–171, 2004.

[66] Daniel D. Shin, Kotekar P. Mohanchandra, and Gregory P. Carman. Development of hydraulic linear actuator using thin film SMA. *Sensors and Actuators A: Physical*, 119(1):151–156, 2005.

[67] S. Sreekala and G. Ananthakrishna. Acoustic emission and shape memory effect in the martensitic transformation. *Physical Review Letters*, 90(13), 2003.

[68] Yuuta Sugiyama and Shinichi Hirai. Crawling and jumping by a deformable robot. *International Journal of Robotics Research*, 25(5-6):603–620, 2006.

[69] K. Tanaka. A thermomechanical sketch of shape memory effect: One-dimensional tensile behaviour. *Res Mechanica, International Journal of Structural Mechanics and Materials Science*, 18:251–263, 1986.

[70] Yoshifumi Tanaka and Akio Yamada. A rotary actuator using shape memory alloy for a robot - analysis of the response with load. In *Proceedings of the IEEE/RSJ International Workshop on Intelligent Robots and Sensors*, pages 1163–1168, 1991.

[71] Yee Harn Teh and Roy Featherstone. Experiments on the performance of a 2-DOF pantograph robot actuated by shape memory alloy wires. In *Proceedings of the 6th Australasian Conference on Robotics and Automation*, Canberra, Australia, 6-8 Dec 2004.

[72] Yee Harn Teh and Roy Featherstone. A new control system for fast motion control of SMA actuator wires. In *The 1st International Symposium on Shape Memory and Related Technologies*, Singapore, 24-26 November 2004.

[73] D. R. Trinkle, R. G. Hennig, S. G. Srinivasan, D. M. Hatch, M. D. Jones, H. T. Stokes, R. C. Albers, and J. W. Wilkins. A new mechanism for the alpha to omega martensitic transformation in pure titanium. *Physical Review Letters*, 91(2), 2003.

[74] N. Troisfontaine, P. Bidaud, and P. Dario. Control experiments on two SMA based micro-actuators. In A. Casals and A. T. de Almeida, editors, *Experimental Robotics V*, pages 490–499. Springer, 1998.

[75] Nelly Troisfontaine, Philippe Bidaud, and Guillaume Morel. A new interphalangeal actuator for dexterous micro-gripper. In *Proceedings of the IEEE International Conference on Robotics and Automation*, pages 1773–1778, 1997.

[76] Jayagopal Uchil. Shape memory alloys - characterization techniques. *Pramana - Journal of Physics*, 58(5):1131–1139, 2002.

[77] Marc van der Wijst. *Shape Control of Structures and Materials with Shape Memory Alloys*. PhD thesis, Technische Universiteit Eindhoven, 1998.

[78] Jan Van Humbeeck. Non-medical applications of shape memory alloys. *Materials Science and Engineering A*, 273-275:134–138, 1999.

[79] Rong Xin Wang, Yitshak Zohar, and Man Wong. Residual stress-loaded titanium-nickel shape-memory alloy thin-film micro-actuators. *Journal of Micromechanics and Microengineering*, 12:323–327, 2002.

[80] Tom Waram. *Actuator Design Using Shape Memory Alloys*. Tom Waram, 2nd (metric) edition, 1993.

[81] Parris S. Wellman, William J. Peine, Gregg Favalora, and Robert D. Howe. Mechanical design and control of a high-bandwidth shape memory alloy

tactile display. In A. Casals and A. T. de Almeida, editors, *Experimental Robotics V*, pages 56–66. Springer, 1998.

[82] Qin Yao, Sheng Jin, and Pei-Sun Ma. The micro trolley based on SMA and its control system. *Journal of Intelligent and Robotic Systems*, 39:199–208, 2004.

[83] Z. W. Zhong and C. K. Yeong. Development of a gripper using SMA wire. *Sensors and Actuators A*, 126(2):375–381, 2006.